

Complexity

Advanced Controls in Complex Clean Energy Devices, Subsystems, and Processes

Lead Guest Editor: Izaskun Garrido

Guest Editors: Jesus A. Romero and Aitor J. Garrido





**Advanced Controls in Complex Clean Energy
Devices, Subsystems, and Processes**

Complexity

Advanced Controls in Complex Clean Energy Devices, Subsystems, and Processes

Lead Guest Editor: Izaskun Garrido

Guest Editors: Jesus A. Romero and Aitor J. Garrido



Copyright © 2019 Hindawi. All rights reserved.



This is a special issue published in “Complexity.” All articles are open access articles distributed under the Creative Commons Attribution License, which permits unrestricted use, distribution, and reproduction in any medium, provided the original work is properly cited.

Editorial Board



- José A. Acosta, Spain
Carlos F. Aguilar-Ibáñez, Mexico
Mojtaba Ahmadiéh Khanesar, UK
Tarek Ahmed-Ali, France
Alex Alexandridis, Greece
Basil M. Al-Hadithi, Spain
Juan A. Almendral, Spain
Diego R. Amancio, Brazil
David Arroyo, Spain
Mohamed Boutayeb, France
Átila Bueno, Brazil
Arturo Buscarino, Italy
Guido Caldarelli, Italy
Eric Campos-Canton, Mexico
Mohammed Chadli, France
Émile J. L. Chappin, Netherlands
Diyi Chen, China
Yu-Wang Chen, UK
Giulio Cimini, Italy
Danilo Comminiello, Italy
Sara Dadras, USA
Sergey Dashkovskiy, Germany
Manlio De Domenico, Italy
Pietro De Lellis, Italy
Albert Diaz-Guilera, Spain
Thach Ngoc Dinh, France
Jordi Duch, Spain
Marcio Eisencraft, Brazil
Joshua Epstein, USA
Mondher Farza, France
Thierry Floquet, France
Mattia Frasca, Italy
José Manuel Galán, Spain
Lucia Valentina Gambuzza, Italy
Bernhard C. Geiger, Austria
Carlos Gershenson, Mexico
- Peter Giesl, UK
Sergio Gómez, Spain
Lingzhong Guo, UK
Xianggui Guo, China
Sigurdur F. Hafstein, Iceland
Chittaranjan Hens, India
Giacomo Innocenti, Italy
Sarangapani Jagannathan, USA
Mahdi Jalili, Australia
Jeffrey H. Johnson, UK
M. Hassan Khooban, Denmark
Abbas Khosravi, Australia
Toshikazu Kuniya, Japan
Vincent Labatut, France
Lucas Lacasa, UK
Guang Li, UK
Qingdu Li, China
Chongyang Liu, China
Xiaoping Liu, Canada
Xinzhi Liu, Canada
Rosa M. Lopez Gutierrez, Mexico
Vittorio Loreto, Italy
Noureddine Manamanni, France
Didier Maquin, France
Eulalia Martínez, Spain
Marcelo Messias, Brazil
Ana Meštrović, Croatia
Ludovico Minati, Japan
Ch. P. Monterola, Philippines
Marcin Mrugalski, Poland
Roberto Natella, Italy
Sing Kiong Ngung, New Zealand
Nam-Phong Nguyen, USA
B. M. Ombuki-Berman, Canada
Irene Otero-Muras, Spain
Yongping Pan, Singapore
- Daniela Paolotti, Italy
Cornelio Posadas-Castillo, Mexico
Mahardhika Pratama, Singapore
Luis M. Rocha, USA
Miguel Romance, Spain
Avimanyu Sahoo, USA
Matilde Santos, Spain
Josep Sardanyés Cayuela, Spain
Ramaswamy Savitha, Singapore
Hiroki Sayama, USA
Michele Scarpiniti, Italy
Enzo Pasquale Scilingo, Italy
Dan Seluşteanu, Romania
Dehua Shen, China
Dimitrios Stamovlasis, Greece
Samuel Stanton, USA
Roberto Tonelli, Italy
Shahadat Uddin, Australia
Gaetano Valenza, Italy
Alejandro F. Villaverde, Spain
Dimitri Volchenkov, USA
Christos Volos, Greece
Qingling Wang, China
Zidong Wang, UK
Yan-Ling Wei, Singapore
Honglei Xu, Australia
Yong Xu, China
Xinggang Yan, UK
Baris Yuçe, UK
Massimiliano Zanin, Spain
Hassan Zargarzadeh, USA
Rongqing Zhang, USA
Xianming Zhang, Australia
Xiaopeng Zhao, USA
Quanmin Zhu, UK

Contents


Advanced Controls in Complex Clean Energy Devices, Subsystems, and Processes

Izaskun Garrido , Jesús A. Romero, and Aitor J. Garrido 
Editorial (2 pages), Article ID 2683151, Volume 2019 (2019)


A Variable Structure Control Scheme Proposal for the Tokamak α Configuration Variable

Aitor Marco , Aitor J. Garrido , Stefano Coda, Izaskun Garrido, and TCV Team
Research Article (10 pages), Article ID 2319560, Volume 2019 (2019)



Design, Modeling, and Experiments of the Vortex-Induced Vibration Piezoelectric Energy Harvester with Bionic Attachments

Zunlong Jin, Guoping Li, Junlei Wang , and Zhien Zhang 
Research Article (13 pages), Article ID 1670284, Volume 2019 (2019)




Performance Sensitivity of a Wind Farm Power Curve Model to Different Signals of the Input Layer of ANNs: Case Studies in the Canary Islands

Sergio Velázquez Medina , José A. Carta, and Ulises Portero Ajenjo
Research Article (11 pages), Article ID 2869149, Volume 2019 (2019)



Proposal of an Adaptive Neurofuzzy System to Control Flow Power in Distributed Generation Systems

Helbert Eduardo Espitia , Iván Machón-González , Hilario López-García, and Guzmán Díaz
Research Article (16 pages), Article ID 1610898, Volume 2019 (2019)






Multiobjective Optimization of a Fractional-Order PID Controller for Pumped Turbine Governing System Using an Improved NSGA-III Algorithm under Multiworking Conditions

Chu Zhang, Tian Peng , Chaoshun Li , Wenlong Fu , Xin Xia, and Xiaoming Xue
Research Article (18 pages), Article ID 5826873, Volume 2019 (2019)

Estimation of Climatic Parameters of a PV System Based on Gradient Method

Rabiah Gammoudi , Houda Brahmi , and Rachid Dhifaoui
Research Article (10 pages), Article ID 7385927, Volume 2019 (2019)


Fuel Cell Output Current Prediction with a Hybrid Intelligent System

José-Luis Casteleiro-Roca , Antonio Javier Barragán , Francisca Segura , José Luis Calvo-Rolle , and José Manuel Andújar 
Research Article (10 pages), Article ID 6317270, Volume 2019 (2019)

A Comparative Analysis of Self-Rectifying Turbines for the Mutriku Oscillating Water Column Energy Plant

Erlantz Otaola , Aitor J. Garrido , Jon Lekube, and Izaskun Garrido
Research Article (14 pages), Article ID 6396904, Volume 2019 (2019)

Meteorological Data-Based Optimal Control Strategy for Microalgae Cultivation in Open Pond Systems

Riccardo De-Luca, Fabrizio Bezzo, Quentin Béchet, and Olivier Bernard 
Research Article (12 pages), Article ID 4363895, Volume 2019 (2019)

Editorial

Advanced Controls in Complex Clean Energy Devices, Subsystems, and Processes

Izaskun Garrido ¹, Jesús A. Romero,² and Aitor J. Garrido ¹

¹Automatic Control Group (ACG), Inst. of Research and Development of Processes (IIDP), Aut. Control and Systems Eng. Dept., University of Basque Country (UPV/EHU), Bilbao, Spain

²TAE Technologies Inc., Foothill Ranch, USA

Correspondence should be addressed to Izaskun Garrido; izaskun.garrido@ehu.es

Received 26 March 2019; Accepted 27 March 2019; Published 15 April 2019

Copyright © 2019 Izaskun Garrido et al. This is an open access article distributed under the Creative Commons Attribution License, which permits unrestricted use, distribution, and reproduction in any medium, provided the original work is properly cited.

One of the mayor challenges facing current society is to transform its energy model, allowing for secure, affordable, and efficient energy. The search for new energy sources with a minimal impact on the environment has brought about new complex technical solutions that require novel control algorithms in their path to commercialization.

This special issue aims to increase the performance and reliability of complex clean energy devices, subsystems, and processes by developing control solutions based on alternative approaches. The articles provide controls that improve the performance and reliability of complex devices or components targeting clean energy. Contributions containing research to predict, diagnose, monitor, and manage the state or condition of engineering assets using various advanced controls have been considered.

We received a total of twenty submissions, and after two rounds of rigorous review, nine papers were accepted.

Z. Jin et al. in their paper titled “Design, Modeling, and Experiments of the Vortex-Induced Vibration Piezoelectric Energy Harvester with Bionic Attachments” propose a bionic attachment structure that widens the bandwidth and efficiency of a piezoelectric energy harvester. Compared with the smooth cylinder which is taken as a carrier, in the harvester with the bionic structure the threshold speed decelerates from 1.8m/s to 1 m/s while the bandwidth increases from 39.3% to 51.4%, while its output power enhances from 0.48 to 0.56 mW. See, for example, [1].

C. Zhang et al. in their paper titled “Multiobjective Optimization of a Fractional-Order PID Controller for Pumped Turbine Governing System Using an Improved NSGA-III

Algorithm under Multiworking Conditions” improve the pump turbine governing system, PTGS. This is the core control system of the pumped storage power station which is responsible for regulating the unit power, which plays an important role in maintaining the grid’s requirements balancing power supply and demand. The fractional-order PID controller under single working conditions is extended to a multiobjective framework. To establish the cost function, the integral of the time absolute error index of PTGS running at low and high working water heads is considered. Finally, an improved nondominated sorting genetic algorithm III based on Latin hypercube sampling and chaos theory (LCNSGA-III) is proposed to solve the optimization problem. See also [2].

E. Otaola et al. in their paper titled “A Comparative Analysis of Self-Rectifying Turbines for the Mutriku Oscillating Water Column Energy Plant” present an analysis the performance of different self-rectifying turbines. This turbine comparison is carried out for the oscillating water column converters located at the Mutriku wave energy power plant. Further details may also be found in [3].

J.-L. Casteleiro et al. in their paper titled “Fuel Cell Output Current Prediction with a Hybrid Intelligent System” present a dynamic model of a real hydrogen fuel cell in order to apply hybrid control strategies. The use of a hybrid scheme improves the performance of neural networks reducing to half the mean squared error obtained for a global model of the fuel cell. See also [4].

R. Gammoudi et al. in their paper titled “Estimation of Climatic Parameters of a PV System Based on Gradient

Method” present a novel formulation for a photovoltaic generator. The model is based in its current-voltage characteristic whose appearance depends on the climatic conditions (temperature and solar radiation). These two parameters are estimated from an experimental curve I_{pv} (V_{pv}), using novel mathematical calculation strategy. Similar approach may be found in [5].

A. Marco et al. in their paper titled “A Variable Structure Control Scheme Proposal for the Tokamak à Configuration Variable” present and apply a Sliding Mode Controller to the plasma current control problem, using the RZIp model for the Tokamak à Configuration Variable (TCV) reactor. See also [6].

H. E. Espitia et al. in their paper titled “Proposal of an Adaptive Neurofuzzy System to Control Flow Power in Distributed Generation Systems” describe the implementation of an adaptive neurofuzzy system for voltage control for a distributed generation system. Previous research may be found in [7].

S. V. Medina et al. in their paper titled “Performance Sensitivity of a Wind Farm Power Curve Model to Different Signals of the Input Layer of ANNs: Case Studies in the Canary Islands” improve the estimation of the power output of a wind farm. A wind farm power curve model is developed using artificial neural networks, and a study is undertaken of the influence on model performance when parameters such as the meteorological conditions (wind speed and direction) of areas other than the wind farm location are added as signals of the input layer of the neural network. Further research on wind farm for Canary Island may be found in [8].

R. De-Luca et al. in their paper titled “Meteorological Data-Based Optimal Control Strategy for Microalgae Cultivation in Open Pond Systems” present a control and optimization strategy for outdoor biofuel production from microalgae. It is based on weather forecast coupled to a detailed predictive model of algal productivity to online optimize the rates of fresh medium injection and culture removal into and from the pond. See also [6].

Conflicts of Interest

The authors declare that there are no conflicts of interest.

Acknowledgments

The guest editorial team would like to thank the invaluable collaboration of the anonymous reviewers, some of whom helped with multiple review assignments. Thanks to their generosity, this issue has been published. Finally, the guest editorial team would also like to thank both the authors of all papers submitted to this special issue and the journal’s editorial board for their efforts regarding this special issue. This work was supported by DPI2015-70075-R (MINECO/FEDER, EU).

Izaskun Garrido
Jesús A. Romero
Aitor J. Garrido

References

- [1] J. Wang, G. Li, S. Zhou, and G. Litak, “Enhancing wind energy harvesting using passive turbulence control devices,” *Applied Sciences*, vol. 9, no. 5, p. 998, 2019.
- [2] J. Hou, C. Li, Z. Tian et al., “Multi-objective optimization of start-up strategy for pumped storage units,” *Energies*, vol. 11, no. 5, 2018.
- [3] A. J. Garrido, E. Otaola, I. Garrido et al., “Mathematical modeling of oscillating water columns wave-structure interaction in ocean energy plants,” *Mathematical Problems in Engineering*, vol. 2015, Article ID 727982, 11 pages, 2015.
- [4] J. L. Casteleiro-Roca, E. Jove, J. M. Gonzalez-Cava et al., “Hybrid model for the ANI index prediction using Remifentanyl drug and EMG signal,” *Neural Computing and Applications*, 2018.
- [5] A. Abbassi, R. Gammoudi, M. Ali Dami, O. Hasnaoui, and M. Jemli, “An improved single-diode model parameters extraction at different operating conditions with a view to modeling a photovoltaic generator: a comparative study,” *Solar Energy*, vol. 155, pp. 478–489, 2017.
- [6] I. Garrido, A. J. Garrido, J. Romero, E. Carrascal, and M. G. Sevillano, “Low effort Li nuclear fusion plasma control using model predictive control laws,” *Mathematical Problems in Engineering*, pp. 1–8, 2015.
- [7] I. Machón-González, J. Rodríguez-Iglesias, H. López-García, L. Castrillón-Peláez, and E. Marañón-Maison, “Knowledge extraction from a nitrification denitrification wastewater treatment plant using SOM-NG algorithm,” *Environmental Technology*, vol. 38, no. 12, pp. 1548–1553, 2016.
- [8] U. Portero, S. Velázquez, and J. A. Carta, “Sizing of a wind-hydro system using a reversible hydraulic facility with seawater. a case study in the Canary Islands,” *Energy Conversion and Management*, vol. 106, pp. 1251–1263, 2015.

Research Article

A Variable Structure Control Scheme Proposal for the Tokamak à Configuration Variable

Aitor Marco ¹, Aitor J. Garrido ², Stefano Coda,³ Izaskun Garrido,² and TCV Team

¹Advanced Design & Analysis Department, IDOM, Bilbao, Spain

²Automatic Control Group, ACG, Institute of Research and Development of Processes, IIDP, Automatic Control and Systems Engineering Department, University of Basque Country (UPV/EHU) Bilbao, Spain

³Ecole Polytechnique Fédérale de Lausanne (EPFL), Swiss Plasma Center (SPC), CH-1015 Lausanne, Switzerland

Correspondence should be addressed to Aitor Marco; aitor.marco@idom.com

Received 25 October 2018; Revised 7 January 2019; Accepted 10 February 2019; Published 14 April 2019

Academic Editor: Yan-Ling Wei

Copyright © 2019 Aitor Marco et al. This is an open access article distributed under the Creative Commons Attribution License, which permits unrestricted use, distribution, and reproduction in any medium, provided the original work is properly cited.

Fusion power is the most significant prospects in the long-term future of energy in the sense that it composes a potentially clean, cheap, and unlimited power source that would substitute the widespread traditional nonrenewable energies, reducing the geographical dependence on their sources as well as avoiding collateral environmental impacts. Although the nuclear fusion research started in the earlier part of 20th century and the fusion reactors have been developed since the 1950s, the fusion reaction processes achieved have not yet obtained net power, since the generated plasma requires more energy to achieve and remain in necessary particular pressure and temperature conditions than the produced profitable energy. For this purpose, the plasma has to be confined inside a vacuum vessel, as it is the case of the Tokamak reactor, which consists of a device that generates magnetic fields within a toroidal chamber, being one of the most promising solutions nowadays. However, the Tokamak reactors still have several issues such as the presence of plasma instabilities that provokes a decay of the fusion reaction and, consequently, a reduction in the pulse duration. In this sense, since long pulse reactions are the key to produce net power, the use of robust and fast controllers arises as a useful tool to deal with the unpredictability and the small time constant of the plasma behavior. In this context, this article focuses on the application of robust control laws to improve the controllability of the plasma current, a crucial parameter during the plasma heating and confinement processes. In particular, a variable structure control scheme based on sliding surfaces, namely, a sliding mode controller (SMC) is presented and applied to the plasma current control problem. In order to test the validity and goodness of the proposed controller, its behavior is compared to that of the traditional PID schemes applied in these systems, using the RZIp model for the Tokamak à Configuration Variable (TCV) reactor. The obtained results are very promising, leading to consider this controller as a strong candidate to enhance the performance of the PID-based controllers usually employed in this kind of systems.

1. Introduction

Traditional nonrenewable energy sources are called to play a minor role in the near future, due to the increasing demand for energy in the world and the limited resources present on the planet. Other factors that have also an impact on this kind of energies are the pollution provoked by the carbon-based fuels, such as petroleum or coal, as well as the nuclear waste and risks originated by the fission reactors. However, nowadays the nonrenewable energies still represent the 86% of the world total primary energy supply [1]. The renewable energies are being developed and improved for

the purpose of increasing their efficiency and ensuring that all the energy needs are covered. The biomass, hydroelectric, solar, and the wind power are some of the most widely used renewable energies, but they suffer from several issues such as intermittency and dispersion, or pollution in the case of biomass. Besides, they usually require subsidies, large areas to be located, and sometimes rare-earth materials.

In this context, the most promising solution to meet the world energy needs is the fusion power, which presents many advantages compared to the fission power: the resources needed are virtually unlimited on Earth, the nuclear waste is limited—just short-live activated materials of the reactor are

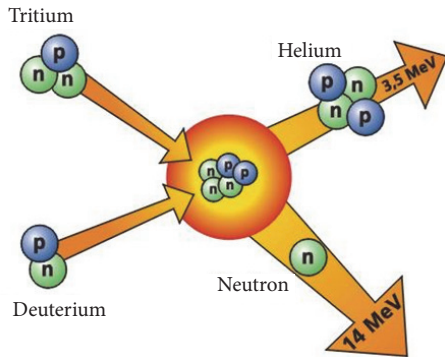


FIGURE 1: D-T fusion reaction.

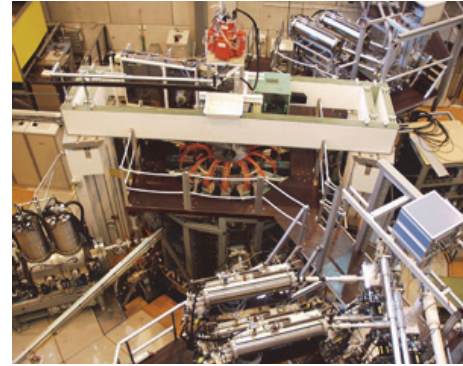


FIGURE 2: TCV reactor.

generated, some of which could be reused as fuel—there is no risk of nuclear explosion or disaster, and the fusion reaction provides the largest amount of energy per kilogram of fuel used. The nuclear fusion consists in artificially provoking the combination of light atom nuclei such as deuterium and tritium (Figure 1). This reaction releases a huge amount of energy, which can be used to heat water and drive a turbine and generate electricity.

The main disadvantages of the fusion power are the large quantity of energy needed to start and hold the reaction and the short duration of the plasma achieved until now. This article tackles this issue by developing advanced controls so as to increase the confinement time and energy availability.

In order to test the feasibility of the nuclear fusion as a power source, an experimental fusion reactor called ITER (International Thermonuclear Experimental Reactor) [2] has been promoted by an international consortium formed by the European Union, China, Japan, India, South Korea, Russia, and the United States. ITER considers a Tokamak fusion reactor that confines the hot plasma in a toroidal chamber using high magnetic fields. The ITER project will test all elements required for the construction of a functional fusion reactor such as the breeder blanket modules, which will provide the tritium obtained from lithium, needed for the D-T reaction. Once the new technologies have been tested, a new reactor, namely, DEMO [3], will be built to demonstrate that the production of energy is feasible.

ITER and DEMO are being planned, developed, and built, while several small Tokamaks serve as a test bench to research the fusion power [4], such as the Globus-M Spherical Tokamak [5] in Russia or the Joint European Torus (JET) [6] in Europe which is the world's largest Tokamak with 38 MW of heating power and 100 m³ of plasma volume. Another interesting operational experimental fusion reactor is the Tokamak à Configuration Variable (TCV) [7], a control-oriented research fusion reactor of the Ecole Polytechnique Fédérale de Lausanne (EPFL), shown in Figure 2, whose main objective is the study of the plasma shape.

Nowadays, the current controller in the TCV and in most of the experimental Tokamaks is the traditional Proportional-Integral-Derivative controller (PID) which has proved to solve the main instabilities problems of the fusion reaction in the Tokamaks but not the major disruptions which are

TABLE 1: TCV coils.

Types	# Coils	Power Source
Toroidal Field Coils	16	1
OH Coils	7	2
Shaping Coils	16	16
In-vessel Vertical fb Coils	2	1

still an inherent issue of them [8–12]. In this context, this article seeks to maximize pulse length by making use of a new control scheme for the plasma current. The model for plasma current, position, and shape to be used is based on the RZIp and extracted from real experimental data of TCV.

The TCV reactor, despite its small size of 1.54 m height by 0.56 width, is a very complex machine, fully loaded of sensors (the so-called diagnostics) and actuators, as it can be seen in Figure 3. Among the diagnostics, there are some for the measurement of the spatial profiles of the electron temperature and density, such as the Thomson Scattering Diagnostic [13], or for the measurement for the plasma currents, temperature, density, and potential, such as the Langmuir probes [14], whose locations are illustrated in Figure 4. The data obtained from some diagnostics (as well as many others related to the plasma physics) are processed and serve as input for the control system, which can actuate over different types of actuators, the Electron Cyclotron Resonance Heating and Current Drive System (ECRH-ECCD), the gas valves, and the coils. The coils are the main actuators for the plasma control, as gathered in Table 1, and there are 4 types with 41 total number of coils fed with 20 independent power sources. Currently, the control system of the TCV is fed with 128 input signals from the diagnostics, which are linearly transformed into 24 observers. This set of observers is composed of the plasma current I_p , the PF coil currents, the difference between the currents in the two Ohmic coil circuits, the vertical position estimator, the radial position estimator, an elongation estimator, and the line-integrated density. With these observables and the reference signals, 24 error signals are generated and serve as input to a PID controller whose outputs are the required voltages for the coils [8, 9]. The scope of this article is to enhance the current PID controller that acts in one of these observers, the plasma current, a relevant parameter to achieve and maintain the fusion reaction. It

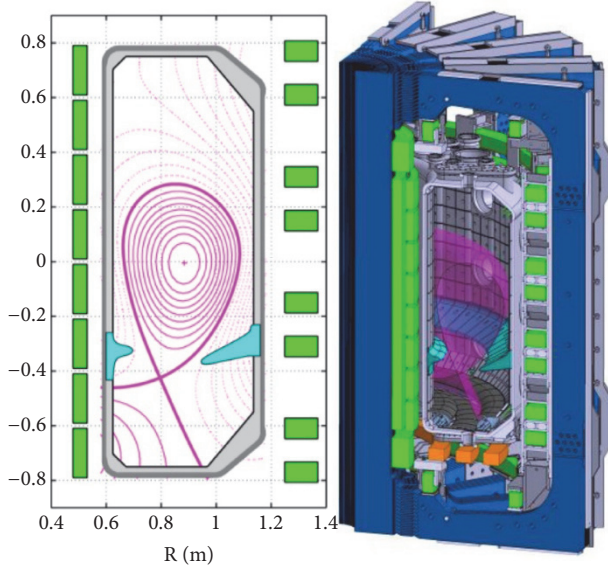


FIGURE 3: TCV reactor section.

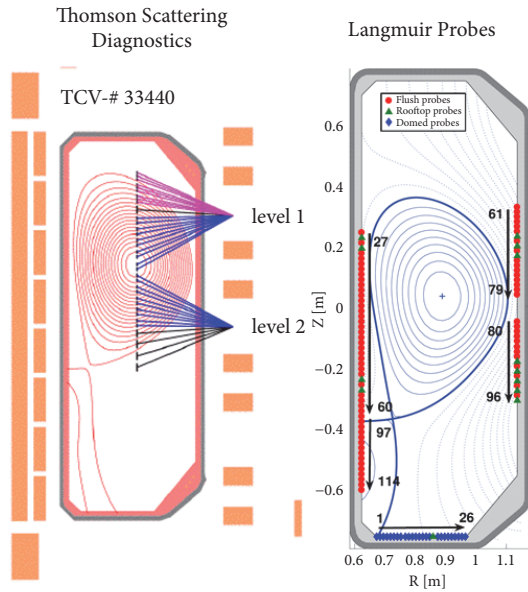


FIGURE 4: TCV diagnostics.

is obvious that better control implies a better response of the system and instability corrections, which may extend the duration of the pulses. The sliding mode control scheme has been studied in this article to enhance the actual control system, which is a variable structure control that presents a robust behavior against plant uncertainties and a finite-time convergence. To test the improvements of this new control scheme, a simulation based on real experimental data has been performed with Simulink.

The remainder of this article is organized as follows: Section 2 introduces the TCV system and explains the RZIp model. In Section 3, the simulation model is presented and the proposed sliding mode control scheme is explained in

detail. The Lyapunov stability is studied for the sliding mode controller in Section 4. Results and comparisons are given in Section 5. Section 6 gathers the concluding remarks.

2. System Description

Tokamaks are devices where the plasma is confined in a toroidal chamber by magnetic fields. These magnetic fields are created by two groups of coils:

- (i) Poloidal field coils: There are coils along the torus that create the poloidal magnetic field. They control the plasma current and stabilize the plasma. In particular, the main coils that act on the plasma current are the OH coils (serving as primary winding like a transformer), which are divided into two sets where the control signals concerning this article will be input.
- (ii) Toroidal field coils: There are coils set in poloidal planes that create a toroidal magnetic field. They control the shape of the plasma.

One of the main issues to overcome in the path to commercialization is the instabilities [15–24]. These instabilities cause disruptions, limiting the maximal achievable time for plasma confinement and making indispensable an optimal control system.

In order to develop the control system, a plant model is required. The TCV is simulated by the RZIp model [15], which considers a rigid plasma radial and vertical displacement. The RZIp model is widely used for simulation purposes and design of real time controllers [19–24].

The state variables of the model are the plasma current, I_e , the structure currents, I_s , and the radial, R , and vertical, z , position of the plasma (1):

$$\dot{\mathbf{q}} = \begin{bmatrix} I_e \\ I_s \\ \dot{\mathbf{r}} \end{bmatrix}, \quad \text{where } \mathbf{r} = \begin{bmatrix} R \\ z \end{bmatrix} \quad (1)$$

The input variables are the effective voltages applied to each plasma element, V_e , and the external poloidal field coil voltages, V_s , (2):

$$\mathbf{U} = \begin{bmatrix} V_e \\ V_s \\ \mathbf{0} \end{bmatrix}. \quad (2)$$

The RZIp model takes into account four vector equations, Kirchoff's voltage law for the plasma elements (3), Kirchoff's voltage law for the structural and poloidal circuits (4), and the force balance for the radial (5) and vertical (6) directions:

$$\frac{d(I_e I_e + M_{es} I_s + REI_e)}{dt} + \Omega_e I_e = V_e, \quad (3)$$

$$\frac{d(I_s I_s + M_{se} I_e)}{dt} + \Omega_s I_s = V_s, \quad (4)$$

$$\frac{d(\mathbf{m}_e \dot{\mathbf{R}})}{dt} = \frac{1}{2} \mathbf{I}'_e \frac{\partial \mathbf{L}_e}{\partial \mathbf{R}} \mathbf{I}_e + \mathbf{I}'_s \frac{\partial \mathbf{M}_{se}}{\partial \mathbf{R}} \mathbf{I}_e + \frac{\mathbf{E} \mathbf{I}_e^2}{2}, \quad (5)$$

$$\frac{d(\mathbf{m}_e \dot{\mathbf{z}})}{dt} = \frac{1}{2} \mathbf{I}'_e \frac{\partial \mathbf{L}_e}{\partial \mathbf{z}} \mathbf{I}_e + \mathbf{I}'_s \frac{\partial \mathbf{M}_{se}}{\partial \mathbf{z}} \mathbf{I}_e. \quad (6)$$

where subindex e denotes the plasma elements, subindex s denotes the structural elements, \mathbf{L} and \mathbf{M} are the self and mutual inductance matrices, $\mathbf{\Omega}$ is the resistance matrix, \mathbf{E} is a constant matrix, and the mass matrix \mathbf{m}_e contains the mass of each plasma current elements. Due to the complexity and nonlinearity of the equations that describe the behavior of the system, it will be linearized and simplified around an operation point using real data from the experiments. In this article, the data used for the model and simulation have been obtained from the shot numbers #49626 and #57587 of the TCV and can be represented by the following state-space system:

$$\dot{\mathbf{x}}_{RZIp} = \mathbf{A} \mathbf{x}_{RZIp} + \mathbf{B} \mathbf{u}_{RZIp} \quad (7)$$

$$\mathbf{y}_{RZIp} = \mathbf{C} \mathbf{x}_{RZIp}.$$

where \mathbf{x}_{RZIp} are the state vector, \mathbf{u}_{RZIp} are the input vector, which are the supplied voltages for the coils, \mathbf{y}_{RZIp} is the output vector that comprises the observers of the system including the plasma current, \mathbf{A} is the state matrix, \mathbf{B} is the input matrix, and \mathbf{C} is the output matrix. As in \mathbf{y}_{RZIp} there are other variables that are out of the scope of this article and are not going to be controlled using the SMC algorithm, and the plasma current output may be obtained from \mathbf{u}_{RZIp} and expressed as $y_{Ip} = C_{Ip} \mathbf{y}_{RZIp}$, where C_{Ip} selects the desired output, so that the state variables can be rewritten as

$$\mathbf{x}_{RZIp} = (C_{Ip} \mathbf{C})^{-1} y_{Ip}. \quad (8)$$

Introducing (8) in (7), the state-space system can be reformulated as

$$\dot{y}_{Ip} = (C_{Ip} \mathbf{C}) \mathbf{A} (C_{Ip} \mathbf{C})^{-1} y_{Ip} + (C_{Ip} \mathbf{C}) \mathbf{B} \mathbf{u}_{RZIp}. \quad (9)$$

The dynamic equation of the plasma current model may be written in a simplified way as

$$\dot{y}_{Ip} = a y_{Ip} + b u_{OH} - d \quad (10)$$

where u_{OH} is the input that controls the plasma current, d is the term that gathers all the uncertainties and noncontrollable inputs, and the state matrix can be reduced to a single scalar as follows:

$$a = (C_{Ip} \mathbf{C}) \mathbf{A} (C_{Ip} \mathbf{C})^{-1}. \quad (11)$$

The tracking error of the plasma current, e_{Ip} , is defined as the difference of plasma current reference, r_{Ip} , and its actual value:

$$e_{Ip} = r_{Ip} - y_{Ip}. \quad (12)$$

Deriving the tracking error and substituting the plasma current model described in (10), the following expression is obtained:

$$\dot{e}_{Ip} = \dot{r}_{Ip} - \dot{y}_{Ip} = a e_{Ip} + u + \delta \quad (13)$$

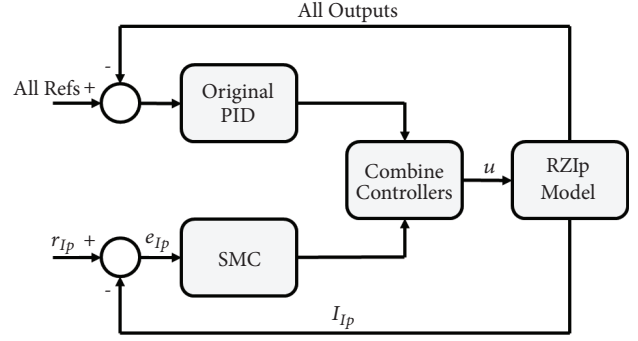


FIGURE 5: General overview of the model.

where the control signal, u , collects the following term:

$$u = -b u_{OH} \quad (14)$$

and the disturbances, uncertainties, and commands are gathered in δ :

$$\delta = d + \dot{r}_{Ip} - a r_{Ip}. \quad (15)$$

3. Sliding Mode Control Scheme

In order to improve the robustness of the TCV control system, the original PID has been enhanced with a sliding mode control for the plasma current, I_p . A schematic view of the general model may be observed in Figure 5, where in the box "SMC" the proposed sliding mode controller will be implemented and the resulting control signals will be combined in the box "Combine Controllers" [19, 24].

The sliding mode controller [25–27] uses a discontinuous control law to lead the system state to a specified sliding surface, σ , and to remain in it. This control law has two main advantages: the first is that the system behaves like a system of reduced order and the second is that the disturbances and uncertainties do not affect the movement on the sliding surface of the system. The development of the sliding control law is divided into two phases.

The first phase is to construct a sliding surface to confine the system dynamics to a sliding manifold with the desired behavior. Let us consider the ideal disturbance-free tracking error expression (13) and suppose that the trajectory of the state has intercepted the sliding surface σ at t_0 , and exists a sliding mode at $t \geq t_0$ implying that $\sigma = 0$ and $\dot{\sigma} = 0$. Deriving σ with respect to time along the trajectory is defined by (13):

$$\dot{\sigma} = \left(\frac{\partial \sigma}{\partial e_{Ip}} \right) \dot{e}_{Ip} = \left(\frac{\partial \sigma}{\partial e_{Ip}} \right) (a e_{Ip} + u_{eq}) = 0 \quad (16)$$

where u_{eq} is the equivalent control, whose action entails that any trajectory starting at $\sigma = 0$ remains on it since $\dot{\sigma} = 0$. This equivalent control can be extracted from (16):

$$u_{eq} = - \left(\frac{\partial \sigma}{\partial e_{Ip}} \right)^{-1} \left(\frac{\partial \sigma}{\partial e_{Ip}} \right) a e_{Ip} = -a e_{Ip}. \quad (17)$$

Therefore, combining (13) and (17), given $\sigma(t_0) = 0$, the dynamics of the system on the sliding surface for $t \geq t_0$ are

$$\dot{e}_{Ip} = ae_{Ip} - ae_{Ip} = 0. \quad (18)$$

In this case, the sliding surface is computed with the error of the plasma current and its integral, taking the form of

$$\sigma = e_{Ip} + B \int e_{Ip} dt \quad (19)$$

where B is the relative weight between the integral of the error and the error of the plasma current.

The second phase is to design a discontinuous control law which is responsible for forcing the system to reach the sliding surface and maintains it there. For this reason, the control signal u is divided into two terms:

$$u = u_{eq} + u_N \quad (20)$$

where the continuous term u_{eq} is the equivalent control defined in (17) and u_N is the discontinuous term. In this particular case, the discontinuous term has been selected as a relay with state dependent gain, presenting the following expression:

$$u_N = -\beta(e_{Ip}) \text{sign}(\sigma) \quad (21)$$

where $\beta(e_{Ip}) > 0$ for all e_{Ip} . The term $\beta(e_{Ip})$ has been defined as

$$u_N = -\left(k_1 |e_{Ip}| + k_2 \left| \int e_{Ip} dt \right| \right) \text{sign}(\sigma). \quad (22)$$

Consequently, the control signal depends on the error of the plasma current and on the absolute value of the error and the integral of the error of the plasma current, and its sign is obtained from the sliding surface. This control signal is given by the following combining (17) and (22):

$$u = -k_c e_{Ip} - \left(k_1 |e_{Ip}| + k_2 \left| \int e_{Ip} dt \right| \right) \text{sign}(\sigma) \quad (23)$$

where k_c , k_1 , and k_2 are tunable parameters.

The discontinuity of the sign function in $\sigma = 0$ leads to an undesirable chattering effect; thus the discontinuous transition is subject to smoothing. In order to obtain this smooth transition, the hyperbolic tangent of the sliding surface has been considered. So, the equation may be rewritten as follows:

$$u = -k_c e_{Ip} - \left(k_1 |e_{Ip}| + k_2 \left| \int e_{Ip} dt \right| \right) \tanh\left(\frac{\sigma}{k_t}\right) \quad (24)$$

where k_t is determined by the order of magnitude of the sliding surface.

Gathering (19) and (24), the sliding mode controller scheme is represented in Figure 6.

4. Lyapunov Stability

Rewrite the expression of the sliding surface σ , defined in (19), as

$$\sigma(t) = e_{Ip}(t) + \int_0^t (k - a) e_{Ip}(\tau) d\tau. \quad (25)$$

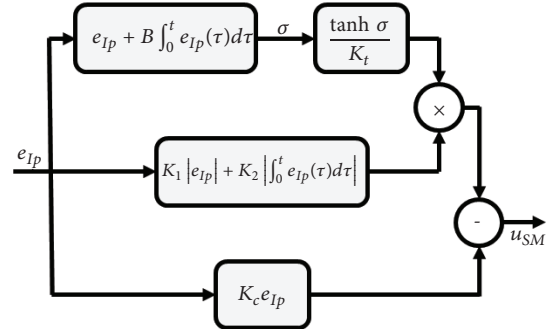


FIGURE 6: Sliding mode scheme.

So its derivative is

$$\dot{\sigma}(t) = \dot{e}_{Ip}(t) + (k - a) e_{Ip}(t). \quad (26)$$

Let us also recall the sliding mode controller law given in (23):

$$u(t) = -k e_{Ip}(t) - \beta \text{sign}(\sigma(t)). \quad (27)$$

In order to ensure the tracking capability, some assumptions shall be established:

- (i) k shall be chosen so that the term $(k - a)$ is strictly positive. Hence $k > a$.
- (ii) β shall be chosen so that $\beta \geq |\delta| \forall t$. To guarantee the robustness of the control action, a switching action is added with a size bigger than the perturbation. This condition implies that the uncertainties of the system are bounded magnitudes.

If the previous assumptions are verified and, using the Lyapunov stability theory, it is possible to demonstrate that the error of the plasma current defined in (12) tends to zero as time tends to infinity.

The Lyapunov function is defined by means of the following expression:

$$V = \frac{1}{2} \sigma \sigma \quad (28)$$

and its time derivative is

$$\begin{aligned} \dot{V} &= \sigma \dot{\sigma} = \sigma (\dot{e}_{Ip} + (k - a) e_{Ip}) = \sigma (k e_{Ip} + \delta + u) \\ &= \sigma (\delta - \beta \text{sign}(\sigma)) \leq -|\sigma| (\beta - |\delta|) \leq 0. \end{aligned} \quad (29)$$

As V is clearly positive definite, \dot{V} is negative definite and when σ tends to infinity, V tends to infinity; then the equilibrium at the origin $\sigma = 0$ is globally asymptotically stable. This is to say, σ tends to zero as time tends to infinity, and all trajectories starting off $\sigma = 0$ must reach it in finite time and then remain on it, being in the so-called sliding mode.

5. Results

In order to validate the control scheme, the sliding mode controller has been simulated with a linearized RZIp model

TABLE 2: Simulated shots.

	#49626	#57587
Starting Time (s)	0.8	1
Duration (s)	0.5	0.5
Starting Ip (A)	-2.4E5	-2.8E5
Starting Radial Pos. (m)	0.872	0.879
Starting Vertical Pos. (m)	0.398	0.262

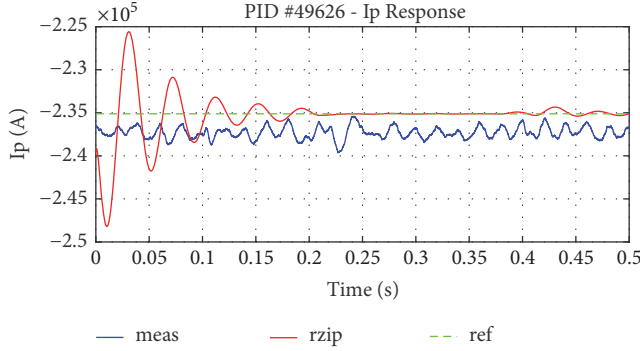


FIGURE 7: PID Response (Shot #49626).

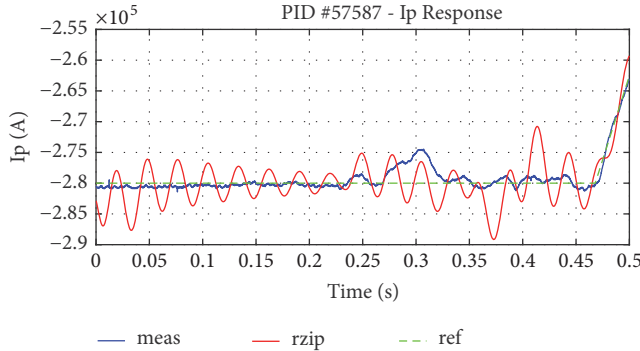


FIGURE 8: PID response (Shot #57587).

of the TCV and two distinct shots, #49626 and #57587, as shown in Table 2. The initial conditions of the system and the reference that the controller has to follow have also been obtained from the experimental data. In addition, to show the improvement of the new control scheme, the original PID controller has been implemented. The plasma current controller acts on the OH coils, which have a physical limit of ± 1400 V, so the output has been saturated in case of overflow.

For a better comparison, the results have been divided into five groups: (A) system response, (B) RMS error, (C) integral error, and (D) control signals.

5.1. System Response. In Figures 7–10, the blue line represents the real measurement of the plasma current, the green dashed line is the reference commanded, and the red line is the response of the simulated system.

It can be clearly seen in Figures 7 and 8 that the original PID produces an underdamped response, which takes a long

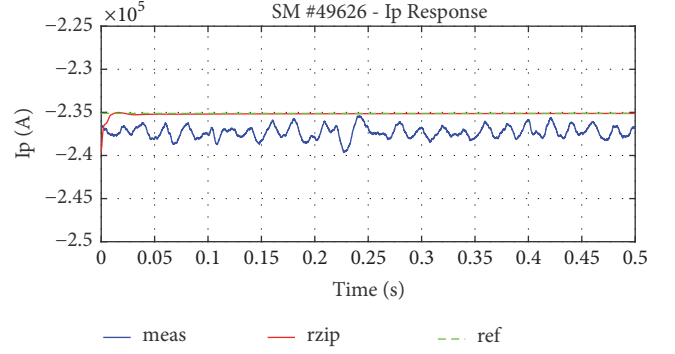


FIGURE 9: Sliding mode response (Shot #49626).

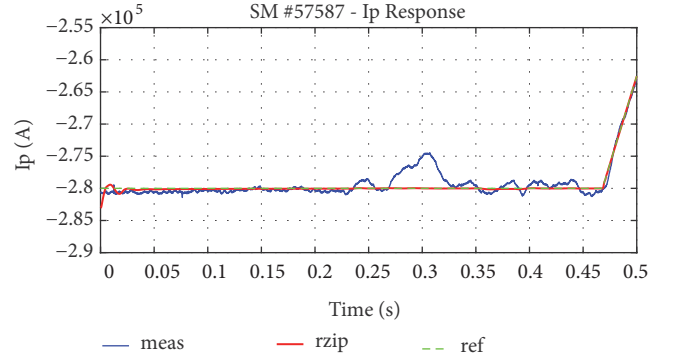


FIGURE 10: Sliding mode response (Shot #57587).

TABLE 3: RMS error.

Shot #	RMS PID	RMS Sliding Mode
49626	2.69E3	2.42E2
57587	3.12E3	2.18E2

time to reach the specified reference. This indicates that the response of the system may be subject to improvement.

The response of the sliding mode controller, shown in Figures 9 and 10, is better than that of the original PID controller because it reaches faster the reference with smaller oscillations. Even more, it may be seen that the response takes about the same time (10 ms) to start correcting the error and has an overshoot much smaller than using the PID.

5.2. RMS Error. One significant quantitative estimator is the Root Mean Square (RMS), which is a measure of the goodness of the controllers. The RMS for a discrete time series of the plasma current error with a fixed-time step can be computed with the following expression:

$$RMS_{e_{ip}} = \sqrt{\frac{1}{N} \sum_{i=1}^N e_{ip,i}^2}. \quad (30)$$

In Table 3, the RMS errors of the PID and the Sliding Mode controlled are depicted. The sliding mode controller reduces the RMS error by one order of magnitude.

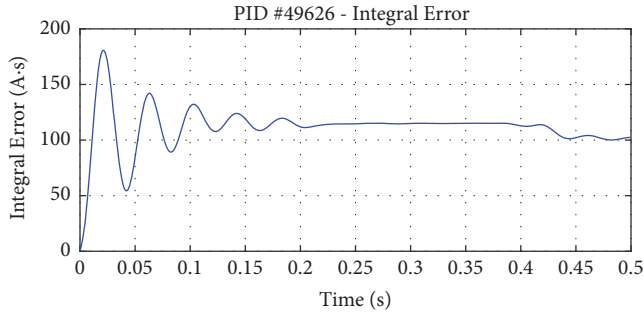


FIGURE 11: PID integral error (Shot #49626).

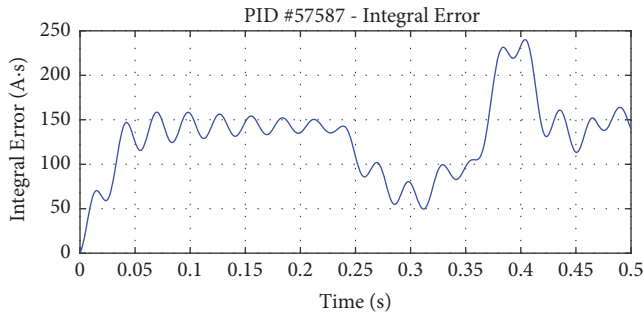


FIGURE 12: PID integral error (Shot #57587).

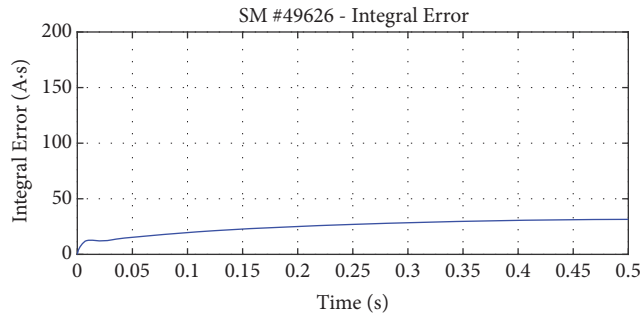


FIGURE 13: Sliding mode integral error (Shot #49626).

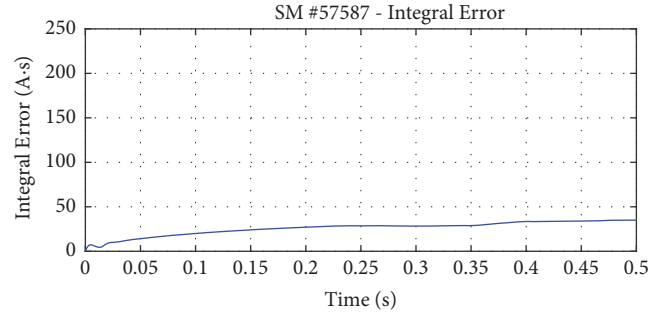


FIGURE 14: Sliding mode integral error (Shot #57587).

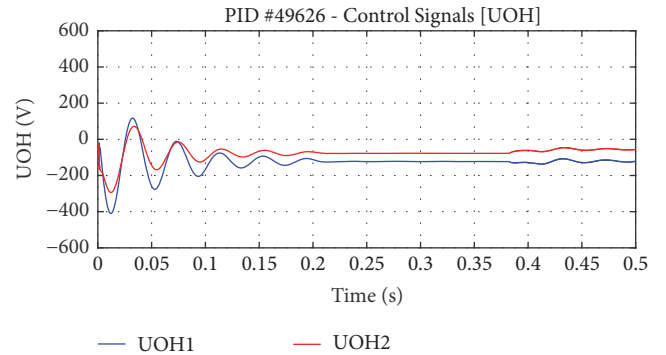


FIGURE 15: PID control signal (Shot #49626).

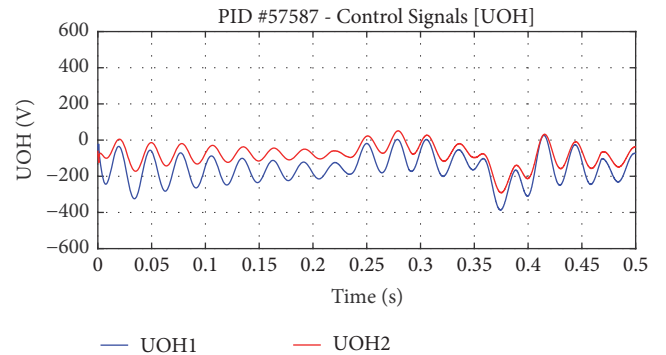


FIGURE 16: PID control signal (Shot #57587).

5.3. Integral Error. The integral error measures how the error accumulates along the time. It is clearly seen from Figures 11 and 12 that with the PID there are oscillations in the integral error.

However, in the integral error in the case of the sliding mode controller, as seen in Figures 13 and 14, there are no oscillations and the values are less than half of the PID's values.

5.4. Control Signals. It is important to keep in mind the feasibility of these controllers. The plasma current is controlled by two sets of OH coils, with a limit of ± 1400 V for both. The difference between the control signals of the two sets is due to the controller of another plasma variable that is acting on them, which does not affect the performance of the plasma current response.

Figures 15 and 16 show the PID control signals, which have many oscillations until they reach the stationary state.

The sliding mode control signals are shown in Figures 17 and 18 where it can be seen that the oscillations are strongly reduced with a control effort smaller than that of the PID controller.

6. Conclusions

The use of optimal and robust control schemes seems to be one of the best ways to ensure an adequate control of the stability of the plasma, so as to extend the duration of the pulses. The traditional PID controllers now implemented within the Tokamak's control system do not allow achieving long enough duration pulses to enable energy production. In

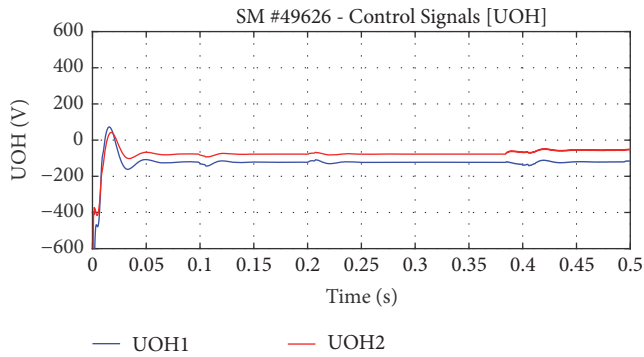


FIGURE 17: Sliding mode control signal (Shot #49626).

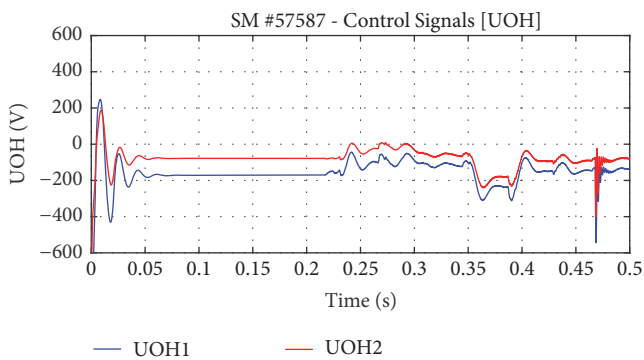


FIGURE 18: Sliding mode control signal (Shot #57587).

this context, new control laws have been developed and tested in order to obtain better results extending the pulse duration and making possible the production of fusion energy. The candidate proposed in this article to enhance the baseline PID-based scheme has been the sliding mode controller, which consists of a variable structure control law with low sensitivity to uncertainties.

As is shown from the results, the plasma current of the systems controlled by the original PID-based controller presents slow and underdamped oscillating responses. In contrast, the proposed sliding mode controller affords excellent results, with an improved fast system response and reduced oscillations of the plasma current, coupled with a more uniform control signal. Furthermore, the RMS errors of the sliding mode controller response show an order of magnitude improvement with respect to the PID ones.

Therefore, in view of the promising results gathered in this article, the next steps are to test them in different TCV scenarios to assure a good response of the controller in several situations and considering other external disturbances in the model that could be studied. In addition, parameter tuning algorithms, such as the Particle Swarm Optimization or the Water Cycle Algorithm, can be proposed.

Finally, the controllers should be tested in a real situation, implementing them at the 2019 experimental campaign of the TCV.

Appendix

The TCV Team is formed by:

S. Coda¹, J. Ahn², R. Albanese³, S. Alberti¹, E. Alessi⁴, S. Allan⁵, H. Anand¹, G. Anastassiou⁶, Y. Andr be¹, C. Angioni⁷, M. Ariola⁸, M. Bernert⁷, M. Beurskens⁹, W. Bin⁴, P. Blanchard¹, T.C. Blanken¹⁰, J.A. Boedo¹¹, T. Bolzonella¹², F. Bouquey², F.H. Braunnm ller¹, H. Bufferand², P. Buratti¹³, G. Calabr ¹³, Y. Camenen¹⁴, D. Carnevale¹⁵, F. Carpanese¹, F. Causa¹³, R. Cesario¹³, I.T. Chapman⁵, O. Chellai¹, D. Choi¹, C. Cianfarani¹³, G. Ciraolo², J. Citrin¹⁶, S. Costea¹⁷, F. Crisanti¹³, N. Cruz¹⁸, A. Czarnecka¹⁹, J. Decker¹, G. De Masi¹², G. De Tommasi³, D. Douai², M. Dunne⁷, B.P. Duval¹, T. Eich⁷, S. Elmore⁵, B. Esposito¹³, M. Faitsch⁷, A. Fasoli¹, N. Fedorczak², F. Felici¹⁰, O. F vrier², O. Ficker²⁰, S. Fietz⁷, M. Fontana¹, L. Frassinetti²¹, I. Furno¹, S. Galeani¹⁵, A. Gallo², C. Galperti¹, S. Garavaglia⁴, I. Garrido²², B. Geiger^{7,9}, E. Giovannozzi¹³, M. Gobbin¹², T.P. Goodman¹, G. Gorini²³, M. Gospodarczyk¹⁵, G. Granucci⁴, J.P. Graves¹, R. Guirlet², A. Hakola²⁴, C. Ham⁵, J. Harrison⁵, J. Hawke¹, P. Hennequin²⁵, B. Hnat^{26,42}, D. Hogewej¹⁶, J.-Ph. Hogge¹, C. Honor ²⁵, C. Hopf⁷, J. Hor c k²⁰, Z. Huang¹, V. Igochine⁷, P. Innocente¹², C. Ionita Schrittwieser¹⁷, H. Isliker²⁷, R. Jacquier¹, A. Jardin², J. Kamleitner¹, A. Karpushov¹, D.L. Keeling⁵, N. Kirneva^{28,29}, M. Kong¹, M. Koubiti¹⁴, J. Kovacic³⁰, A. Kr mer-Flecken³¹, N. Krawczyk¹⁹, O. Kudlacek^{7,12}, B. Labit¹, E. Lazzaro⁴, H.B. Le¹, B. Lipschultz³², X. Llobet¹, B. Lomanowski³³, V.P. Loschiavo³, T. Lunt⁷, P. Maget², E. Maljaars¹⁰, A. Malygin¹, M. Maraschek⁷, C. Marini¹, P. Martin¹², Y. Martin¹, S. Mastrostefano⁸, R. Maurizio¹, M. Mavridis²⁷, D. Mazon², R. McAdams⁵, R. McDermott⁷, A. Merle¹, H. Meyer⁵, F. Militello⁵, I.G. Miron³⁴, P.A. Molina Cabrera¹, J.-M. Moret¹, A. Moro⁴, D. Moulton⁵, V. Naulin³⁵, F. Nespoli¹, A.H. Nielsen³⁵, M. Nocente²³, R. Nouailleras², S. Nowak⁴, T. Odr cil⁷, G. Papp⁷, R. Papr k²⁰, A. Pau³⁶, G. Pautasso⁷, V. Pericoli Ridolfini⁸, P. Piovesan¹², C. Piron¹², T. Pisokas²⁷, L. Porte¹, M. Preynas¹, G. Ramogida¹³, C. Rapson⁷, J. Juul Rasmussen³⁵, M. Reich⁷, H. Reimerdes¹, C. Reux², P. Ricci¹, D. Rittich⁷, F. Riva¹, T. Robinson⁵, S. Saarelma⁵, F. Saint-Laurent², O. Sauter¹, R. Scannell⁵, Ch. Schlatter¹, B. Schneider¹⁷, P. Schneider⁷, R. Schrittwieser¹⁷, F. Sciortino³⁷, M. Sertoli⁷, U. Sheikh¹, B. Sieglin⁷, M. Silva¹, J. Sinha¹, C. Sozzi⁴, M. Spolaore¹², T. Stange⁹, T. Stoltzfus-Dueck³⁸, P. Tamain², A. Teplukhina¹, D. Testa¹, C. Theiler¹, A. Thornton⁵, L. Toph j³⁵, M.Q. Tran¹, C. Tsironis⁶, C. Tsui^{1,11}, A. Uccello⁴, S. Vartanian², G. Verdoolaege³⁹, K. Verhaegh³², L. Vermare²⁵, N. Vianello^{1,12}, W.A.J. Vijvers¹⁶, L. Vlahos²⁷, N.M.T. Vu⁴⁰, N. Walkden⁵, T. Wauters⁴¹, H. Weisen¹, M. Wischmeier⁷, P. Zestanakis⁶ and M. Zuin¹².

¹Ecole Polytechnique F d rale de Lausanne (EPFL), Swiss Plasma Center (SPC), CH-1015 Lausanne, Switzerland

²CEA, IRFM, F-13108 Saint Paul Lez Durance, France

³University of Napoli 'Federico II', Consorzio CREATE, Via Claudio 21, 80125 Napoli, Italy

⁴IFP-CNR, via R. Cozzi 53, 20125 Milano, Italy

⁵CCFE, Culham Science Centre, Abingdon, Oxon OX14 3DB, UK

⁶National Technical University of Athens, Athens, Greece

⁷Max-Planck-Institut für Plasmaphysik, D-85748 Garching, Germany

⁸University of Napoli Parthenope, Consorzio CREATE, Via Claudio 21, 80125 Napoli, Italy

⁹Max-Planck-Institut für Plasmaphysik, Teilinstitut Greifswald, D-17491 Greifswald, Germany

¹⁰Eindhoven University of Technology, P.O. Box 513, NL-5600 MB Eindhoven, Netherlands

¹¹University of California, San Diego, Energy Research Center, La Jolla, CA 92093, USA

¹²Consorzio RFX, Corso Stati Uniti 4, 35127 Padova, Italy

¹³Unità Tecnica Fusione, ENEA C. R. Frascati, via E. Fermi 45, 00044 Frascati (Roma), Italy

¹⁴Aix-Marseille Université, CNRS, PIIM, F13013 Marseille, France

¹⁵University of Rome Tor Vergata, via del Politecnico 1, 00133 Rome, Italy

¹⁶FOM Institute DIFFER ‘Dutch Institute for Fundamental Energy Research’ Eindhoven, Netherlands

¹⁷Institut für Ionen- und Angewandte Physik, Universität Innsbruck, Technikerstraße 25, 6020 Innsbruck, Austria

¹⁸Instituto de Plasmas e Fusão Nuclear, Instituto Superior Técnico, Universidade de Lisboa, Lisbon, Portugal

¹⁹Institute of Plasma Physics and Laser Microfusion, Hery 23, 01-497 Warsaw, Poland

²⁰Institute of Plasma Physics AS CR, Za Slovankou 1782/3, 182 00 Praha 8, Czechia

²¹Fusion Plasma Physics, EES, KTH, SE-10044 Stockholm, Sweden

²²Faculty of Engineering, University of the Basque Country (UPV/EHU), Paseo Rafael Moreno 3, Bilbao 48013, Spain

²³Department of Physics ‘G. Occhialini’, University of Milano-Bicocca, Piazza della Scienza 3, 20126 Milano, Italy

²⁴VTT Technical Research Centre of Finland Ltd, P.O. Box 1000, FI-02044 VTT, Finland

²⁵Laboratoire de Physique des Plasmas, CNRS UMR7648, Ecole Polytechnique, 91128 Palaiseau, France

²⁶Rudolf Peierls Centre for Theoretical Physics, University of Oxford, Oxford, UK

²⁷Aristotle University of Thessaloniki, Thessaloniki, Greece

²⁸Institute of Physics of Tokamaks, National Research Center ‘Kurchatov Institute’, 123182 Kurchatov Sq., 1, Moscow, Russia

²⁹National Research Nuclear University MEPhI (Moscow Engineering Physics Institute), 115409, Kashirskoe Sh., 31, Moscow, Russia

³⁰Jožef Stefan Institute, Jamova 39, SI-1000 Ljubljana, Slovenia

³¹Forschungszentrum Jülich GmbH, Institut für Energie- und Klimaforschung, Plasmaphysik, 52425 Jülich, Germany

³²Department of Physics, York Plasma Institute, University of York, Heslington, York YO10 5DD, UK

³³Department of Physics, Durham University, Durham DH1 3LE, UK

³⁴National Institute for Laser, Plasma and Radiation Physics, P.O. Box MG-36, Bucharest, Romania

³⁵Department of Physics, Technical University of Denmark, Bldg 309, DK-2800 Kgs Lyngby, Denmark

³⁶Department of Electrical and Electronic Engineering, University of Cagliari, Piazza d’Armi, 09123 Cagliari, Italy

³⁷Plasma Science and Fusion Center, Massachusetts Institute of Technology, Cambridge, MA 02139, USA

³⁸Princeton University, Princeton, NJ 08544, USA

³⁹Department of Applied Physics, UG (Ghent University), St-Pietersnieuwstraat 41 B-9000 Ghent, Belgium

⁴⁰Laboratoire de Conception et d’Intégration des Systèmes, Institut Polytechnique de Grenoble, BP54 26902 Valence Cedex 09, France

⁴¹Laboratory for Plasma Physics, Koninklijke Militaire School-Ecole Royale Militaire, Renaissancelaan 30 Avenue de la Renaissance, B-1000 Brussels, Belgium

⁴²Culham Centre for Fusion Energy, Abingdon, UK.

Data Availability

The data used to support the findings of this study are available from the corresponding author upon request.

Conflicts of Interest

The authors declare that there are no conflicts of interest.

Acknowledgments

This work was supported by the MINECO through the Research Project DPI2015-70075-R (MINECO/FEDER, EU). The authors would like to thank the collaboration of the Spanish National Fusion Laboratory (EURATOM-CIEMAT) through Agreement UPV/EHUCIEMAT08/190 and EUSKAMPUS—Campus of International Excellence.

References

- [1] Key World Energy Statistics, 2017, <https://www.iea.org/publications/freepublications/publication/KeyWorld2017.pdf>.
- [2] N. Holtkamp, “An overview of the ITER project,” *Fusion Engineering and Design*, vol. 82, no. 5–14, pp. 427–434, 2007.
- [3] S. Ciattaglia et al., “The European DEMO fusion reactor: Design status and challenges from balance of plant point of view,” in *Proceedings of the 2017 IEEE International Conference on Environment and Electrical Engineering and 2017 IEEE Industrial and Commercial Power Systems Europe (EEEIC / I&CPS Europe)*, pp. 1–6, Milan, Italy, June 2017.
- [4] Y. Mitrishkin, P. Korenev, A. Prokhorov, N. Kartsev, and M. Patrov, “Plasma control in tokamaks. Part 1. controlled thermonuclear fusion problem. Tokamaks. Components of control systems,” *Advances in Systems Science and Applications*, vol. 18, no. 2, pp. 26–52, 2018.
- [5] V. K. Gusev et al., “Review of Globus-M spherical tokamak results,” *Nuclear Fusion*, vol. 55, no. 10, Article ID 104016, 2015.
- [6] X. Litaudon et al., “Overview of the JET results in support to ITER,” *Nuclear Fusion*, vol. 57, no. 10, Article ID 102001, 2017.

- [7] S. Coda et al., "Overview of the TCV tokamak program: scientific progress and facility upgrades," *Nuclear Fusion*, vol. 57, Article ID 102011, 2017.
- [8] B. Duval, J. Moret, A. Rodrigues, L. Pereira, and C. Varandas, "Digital Control System for the TCV Tokamak," *IEEE Transactions on Nuclear Science*, vol. 53, no. 4, pp. 2179–2186, 2006.
- [9] H. Le, F. Felici, J. Paley et al., "Distributed digital real-time control system for TCV tokamak," *Fusion Engineering and Design*, vol. 89, no. 3, pp. 155–164, 2014.
- [10] M. Ariola and A. Pironti, *Magnetic Control of Tokamak Plasmas*, Springer, 2nd edition, 2016.
- [11] Y. Mitrishkin, A. Prokhorov, P. Korenev, and M. Patrov, "Hierarchical robust switching control method with the Improved Moving Filaments equilibrium reconstruction code in the feedback for tokamak plasma shape," *Fusion Engineering and Design*, vol. 138, pp. 138–150, 2019.
- [12] Y. V. Mitrishkin, N. M. Kartsev, E. A. Pavlova, A. A. Prokhorov, P. S. Korenev, and M. I. Patrov, "Plasma control in tokamaks. Part 2. Magnetic Plasma control systems," *Advances in Systems Science and Applications*, vol. 18, no. 3, pp. 39–78, 2018.
- [13] G. Farias, S. Dormido-Canto, J. Vega et al., "Iterative noise removal from temperature and density profiles in the TJ-II Thomson scattering," *Fusion Engineering and Design*, vol. 89, no. 5, pp. 761–765, 2014.
- [14] O. Février, C. Theiler, H. De Oliveira, B. Labit, N. Fedorczyk, and A. Baillod, "Analysis of wall-embedded Langmuir probe signals in different conditions on the Tokamak à Configuration Variable," *Review of Scientific Instruments*, vol. 89, no. 5, p. 053502, 2018.
- [15] A. S. Sharma, *Tokamak modeling and control [Doctoral Thesis]*, January 2002.
- [16] I. Garrido, J. A. Romero, A. J. Garrido, D. Lucchin, E. Carrascal, and G. Sevillano-Berasategui, "Internal inductance predictive control for Tokamaks," in *Proceedings of the World Automation Congress (WAC '14)*, pp. 628–633, August 2014.
- [17] M. G. Sevillano, I. Garrido, A. J. Garrido et al., "Observer-based real-time control for the poloidal beta of the plasma using diamagnetic measurements in tokamak fusion reactors," in *Proceedings of the IEEE Conference on Decision and Control*, pp. 7536–7542, December 2011.
- [18] I. Garrido, A. J. Garrido, J. Romero, E. Carrascal, M. G. Sevillano, and O. Barambones, "Low effort Li nuclear fusion plasma control using model predictive control laws," *Mathematical Problems in Engineering*, vol. 2015, Article ID 527420, 8 pages, 2015.
- [19] I. Garrido, A. Garrido, S. Coda, H. Le, and J. Moret, "Real time hybrid model predictive control for the current profile of the tokamak à configuration variable (TCV)," *Energies*, vol. 9, no. 8, p. 609, 2016.
- [20] A. S. Sharma, D. J. N. Limebeer, I. M. Jaimoukha, and J. B. Lister, "Modeling and control of TCV," *IEEE Transactions on Control Systems Technology*, vol. 13, no. 3, Article ID 841647, pp. 356–369, 2005.
- [21] I. Garrido, A. J. Garrido, O. Barambones, P. Alkorta, and F. J. Maseda, "Tokamak state-space control modeling," in *Proceedings of the 2008 Canadian Conference on Electrical and Computer Engineering - CCECE*, pp. 001437–001442, Niagara Falls, ON, Canada, May 2008.
- [22] M. G. Sevillano-Berasategui, I. Garrido, A. J. Garrido, and O. Barambones, "Review of tokamak codes," in *Proceedings of the 5th International Conference on Electrical Engineering, Computing Science and Automatic Control (CCE)*, pp. 45–50, Mexico City, Mexico, November 2008.
- [23] I. Garrido, A. Garrido, G. Sevillano, M. Alberdi, M. Amundarain, and O. Barambones, "Space-state modeling and control of tokamak reactors," *IFAC Proceedings Volumes*, vol. 42, no. 13, Part 1, pp. 431–436, 2009.
- [24] I. Garrido, S. Coda, H. Le et al., "Hierarchical model predictive control in fusion reactors," in *Proceedings of the 2016 World Automation Congress (WAC)*, pp. 1–6, Rio Grande, PR, USA, July 2016.
- [25] C. Vecchio, *Sliding mode control: theoretical developments and applications to uncertain mechanical systems [Doctoral Thesis]*, 2008.
- [26] A. Levant, "Sliding order and sliding accuracy in sliding mode control," *International Journal of Control*, vol. 58, no. 6, pp. 1247–1263, 1993.
- [27] A. Levant, "Higher-order sliding modes, differentiation and output-feedback control," *International Journal of Control*, vol. 76, no. 9–10, pp. 924–941, 2003.

Research Article

Design, Modeling, and Experiments of the Vortex-Induced Vibration Piezoelectric Energy Harvester with Bionic Attachments

Zunlong Jin,^{1,2} Guoping Li,^{1,2} Junlei Wang ,^{1,2} and Zhien Zhang ²

¹School of Chemical Engineering and Energy, Zhengzhou University, Zhengzhou 450001, China

²Engineering Research Center of Energy Saving Technology and Equipment of Thermal Energy System, Ministry of Education, Zhengzhou 450001, China

Correspondence should be addressed to Junlei Wang; just4pipi@126.com

Received 25 November 2018; Revised 12 January 2019; Accepted 17 March 2019; Published 4 April 2019

Academic Editor: Dimitri Volchenkov

Copyright © 2019 Zunlong Jin et al. This is an open access article distributed under the Creative Commons Attribution License, which permits unrestricted use, distribution, and reproduction in any medium, provided the original work is properly cited.

Since the energy demand increases, the sources of fluid energy such as wind energy and marine energy have attracted widespread attention, especially vortex-induced vibrations excited by wind energy. It is well known that the lock-in effect in vortex-induced vibration can be applied to the piezoelectric energy harvester. Although numerous researches have been conducted on piezoelectric energy harvesting devices in recent years, a common problem of low bandwidth and harvesting efficiency still exists. In order to increase the response amplitude and decrease the threshold wind speed of vortex-induced vibration, a bionic attachment structure is proposed based on the experimental method. In the present work, twelve models are designed according to the size of pits and hemispheric protrusions which are added to the surface of a flexible smooth cylinder. Compared with the smooth cylinder which is taken as a carrier, the harvester with the bionic structure shows stronger energy capture performance on the whole. As the threshold speed decelerates from 1.8m/s to 1 m/s, the bandwidth, on the contrary, increases from 39.3% to 51.4%. Particularly, for the 10 mm pits structure with 5 columns, its peak voltage can reach 47 V, and its peak power can reach 1.21 mW with a resistance of 800 k Ω , 0.57 mW higher than that of the smooth cylinder. Comparatively speaking, the hemispherical projections structure figures with a much more different energy capturing characteristic. Starting from the column, the measured voltage of the hemispherical bionic harvester is much smaller than that of the smooth cylinder, with a peak voltage less than 15 V and a reducing bandwidth. However, compared with the smooth cylinder, hemispheric projections with 3 columns have a better energy capture effect with a measured voltage of 35V, a resistance of 800k Ω , and a wind speed of 3.097 m/s. Besides, its output power also enhances from 0.48 to 0.56 mW.

1. Introduction

Energy policy has become a key strategy in the recent decades in the world [1], and researches focus on energy has been extended in many fields, e.g., environmental protection [2–4], industrial catalysis [5–7], and energy storage [8–13]. Additionally, in recent years, under the background of big data technology [14, 15], some new types of low-power consumption technologies like MEMs and WSNs [16, 17] have been introduced into many areas. As a widespread phenomenon in the natural environment, fluid flow contains a lot of energy, which will provide great convenience for power systems to transform the kinetic energy of fluid into electricity, especially for those that need electronic

components with lower power. Over the past few years, a new technology based on vortex-induced vibration has been widely developed to extract energy from wind and oceanic or other fluid flow energy; in brief, the source of energy is responsible for the vibration. Nevertheless, as a destructive phenomenon in the engineering structure for a long time, vortex-induced vibration requires a nonlinear bluff body structure such as a cylinder of smooth surface. In engineering, when the fluid flows through the surface of the bluff body [18–20], the flow will separate on the surface of the bluff body at the same time, and then the vortex begins to shed alternately around the bluff body under the action of the shear layer, thus generating periodic fluid force which will act on the surface of the cylinder. The bluff body begins to oscillate

when the frequency of the vortex shedding corresponds to the natural frequency of the elastic structural oscillations. As the fluid dynamics theory emerges, an effective drag reduction method called bionic drag reduction has been found, which can not only reduce the resistance, but also be widely used in energy collection. It is green, simple, and feasible for the bionic structure to extend the bandwidth and increase the voltage in the energy harvesting system. Since the last decade, the bionic structure drag reduction has become much more prevalent, motivating more and more scholars to do a lot of simulation and experimental researches in this field from different perspectives.

Emerging in the 1980s, nonsmooth surface bionic drag reduction has grown rapidly in recent years. Zhu and Zhang [21] built a H-shaped cantilevered structure. Though D-shaped cross section can increase the drag force with the natural resonant vibration frequency, it can strengthen the vortex shedding and the beam deflection. Until now, a square column has been studied the most as the choosing bluff body in galloping piezoelectric energy harvesting. Lim and Lee [22] used wind tunnel tests and flow patterns to study the drag reduction of the flow field around the cylinder on the surface of the convex ring. Wind tunnel tests show that the convex ring on the cylinder ($d = 0.0167D$ in a pitch interval of $0.165D$) can reduce resistance by 9% under the condition that the Reynolds number (Re) is 1.2×10^5 based on the diameter of the cylinder. Wang et al. [23] numerically simulated a concave cylinder with the subcritical Reynolds number ($Re = 4 \times 10^4$) on nonsmooth cylindrical flow reduction problem. The sensitivity analysis of the structure parameters including the depth, internal shape, and distribution of the pit was also conducted, the results of which show that the concave cylinder has a good drag reduction effect and will work best when $h = 0.015D$. The average resistance coefficients of cylindrical concave pit and circular cylinder of diamond distribution pit texture are both 0.923, lower than that of the spherical pit cylinder with 0.94 and that of rectangle with 0.973, respectively. Some scholars have applied the bionic concept to vortex-induced vibration piezoelectric energy harvesting (VIVPEH). Allen and Smits [24] proposed an “eel” shaped flow energy harvester. Experiments were performed to investigate the possibility of using flexible piezoelectric membranes as power generation devices in the ocean. Membranes are excited by the von Kármán vortex street forming behind a bluff body which can transform the flow energy into piezoelectric energy. Bernitsas and his coworkers [25, 26] studied fluid-induced vibrations of smooth cylinders with PTC module, and they divided the galloping into two categories: soft galloping and hard galloping. The former one refers to the gradual increase of the flow velocity when the object is transformed from vortex-induced vibration to galloping by means of self-excitation; the latter one means that the bluff body cannot change from self-excitation to galloping, but it can be converted to galloping by external excitation at a high flow rate. At present, PTC has been successfully applied in VIVACE flow-induced vibration. Based on the morphology of the heterocercal tail of thresher sharks and the ionic polymer-metal composites, Cha et al. [27] designed a bionic fish tail to collect energy

from its impact and then proposed a modeling framework for underwater vibration of bionic tail. It is worth mentioning that the feasibility of the model to obtain energy is verified experimentally and theoretically. Akaydin et al. [28] experimentally studied a self-excited energy harvester, which refers to a column attached to the free end of a cantilever beam and partially covered by piezoelectric sheets. The energy harvester is tested in a wind tunnel, generating about 0.1 mW of nonrectified power when the wind speed is 1.192 m/s. The resonant mechanical and electrical efficiency is calculated as 0.72%, while the power of each device is 23.6 mW/m^3 , and the piezoelectric volume is 233 W/m^3 . Recently, in order to obtain stronger and more standard eddy current, Pan et al. [29] studied a circular cylinder with an opening and concave surface through experiment and simulation, which simulates two kinds of vortex type systems, respectively, by using two kinds of vortex generator. The results indicate an increase of the induction frequency of the modified cylinder from 2.7 to 2.9 Hz and the peak voltage from 0.35 to 0.41 V. At present, as the derivation direction of vortex-induced vibration with bionic structure becomes more and more diverse, a large number of scholars commit themselves to exploring the nonlinearity [30–33], multi-degree of freedom [34], and multicylinder string juxtaposition [35–37]. To sum up, the bionic structure is indeed a feasible and effective method to improve the bandwidth and output voltage of the energy harvester based on vortex-induced vibration.

In this paper, the VIVPEH characteristics of the bionic cylinder are studied experimentally. In Section 2, the physical and mathematical models of VIVPEH are given. It is noted that the bionic structure model is guaranteed to have the same mass as the corresponding smooth cylinder model. The model verified by experiment in Section 3 is focused on the analysis of the wake oscillator model based on the vortex-induced vibration. The influence of bionic structure model on the performance of harvester is discussed from measuring voltage, bandwidth, and efficiency in Section 4, while the conclusions are given in Section 5.

2. Physical and Mathematical Models

To the best of our knowledge, reducing the resistance in fluid-induced vibration by using the bionic nonsmooth surface structure has been successfully applied in bionic drag reduction technology [38–40]. Based on bionics and mechanical-electric conversion mechanism, the concept of bionics is adopted for the design of bluff body in this paper.

2.1. Physical Model. Many organisms in nature have evolved nonsmooth structures that can help reduce resistance, such as shark scales and the surface of the planthopper’s chest. Of course, this pit or convex-clad structure has also been applied to the design of many materials with the golf ball being the most remarkable. As the golf ball moves through the concave structure on the surface, the airflow generates a small vortex near the pit [41]. With the adsorption force of the vortex, the airflow near the sphere begins to move closer to the wall, causing the separation point of the boundary

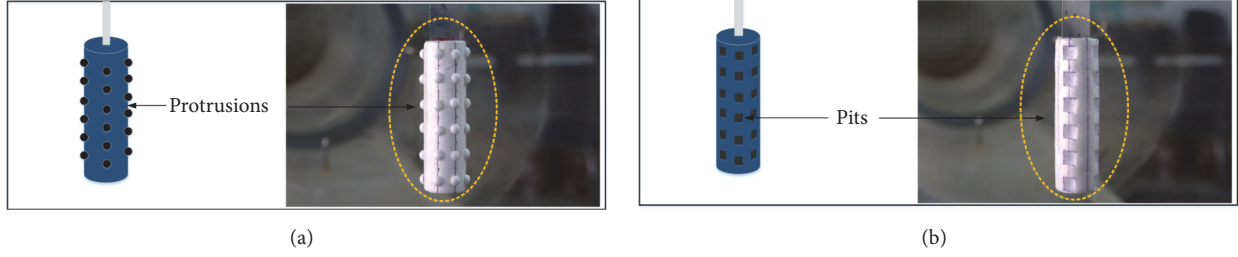


FIGURE 1: Physical model of bluff bodies with bionic structure. (a) Schematic of the protrusions; (b) schematic of the pits.

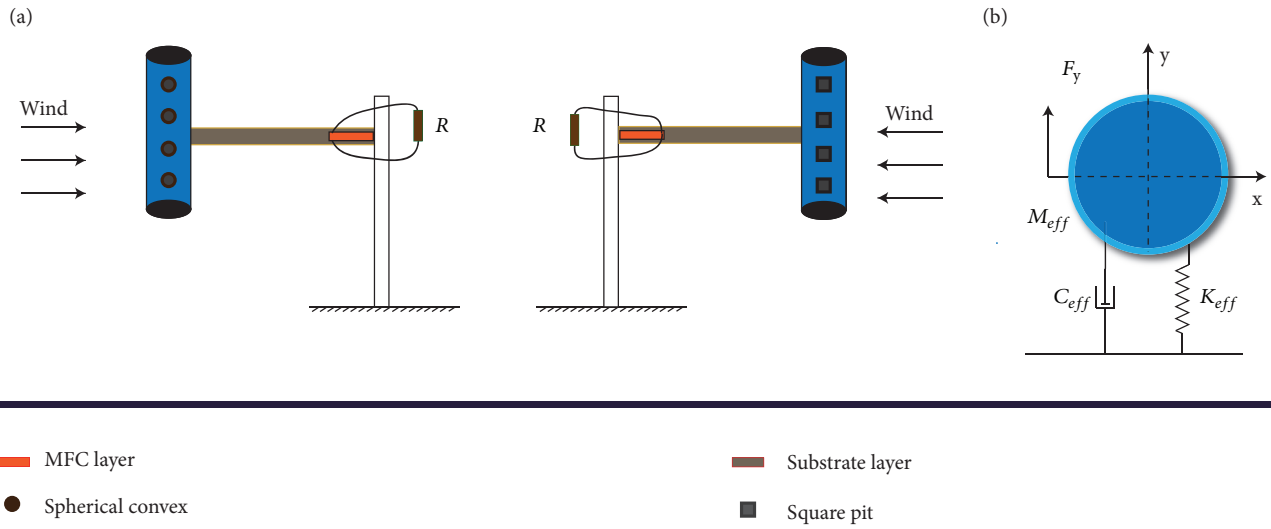


FIGURE 2: Schematic diagram of VIVPEH with bionic structure: (a) physical diagram in the wind tunnel test; (b) equivalent schematic diagram.

layer to move backward. The vortex area at the rear of the sphere and the pressure difference between the front and the back decline gradually, and so does the pressure difference resistance compared with the smooth sphere. Serving as a bionic structure for fluid vibration experiments in this paper, the size of pits and hemispheric convex is 6 mm, 8 mm, and 10 mm; the number of pits in each smooth cylinder is 3, 4, 5, and 6; and there are twelve bionic structures with pits and hemispheric protrusions, respectively. The physical model is shown in Figure 1.

Based on vortex-induced motions, the mechanism of generating device can be divided into piezoelectric [42–44], electromagnetic, and electrostatic [45–47], among which, piezoelectric type is used and valued the most. Most piezoelectric energy harvesters use a cantilever beam of one or two piezoelectric ceramic layers [48]. The cantilever beam is generally placed on the body of a vibrating structure, and the strain of the piezoelectric layer caused by the vibration can result in an alternating output voltage through the electrode. Figures 2(a) and 2(b) show the schematic diagram of the presented VIVPEH with bionic structure. As shown in Figure 2(a), the wind speed is perpendicular to the cylindrical section, the whole system of which can be simplified as a

single degree of freedom system (1DOF). Here, Figure 2(b) can also be called the efficient M - C - K vibration system.

In fact, it is feasible to introduce the load resistance into the cantilever energy collection system for equivalent analysis. Besides, another requirement is that the converter is used to adjust the output voltage to maximize the power of the charging and storage device, and to meet the charging demand of small batteries or capacitors [49–51]. For cylinders with bionic structures, it is abstract to study the flow-induced vibration of bluff body directly. Hence, it can be simplified as a mass-spring-damping system on a single degree of freedom.

2.2. Mathematical Model. As shown in Figure 2, there is a cantilever which can vibrate when the bluff body is interacted by the coming wind. As the piezoelectric sheet is coherent in the bottom of the cantilever, a distributed model is used here to simulate the vibration of the cantilever. The distributed parameter model of the energy harvester can be obtained according to the following formula.

$$\ddot{\eta}(t) + 2\zeta\omega_n\dot{\eta}(t) + \omega_n^2\eta(t) = F_{VIV}(t) \quad (1)$$

Here $\eta(t)$ is the model coordinate, and the force caused by vortex-induced vibration can be presented as

$$F_{VIV}(t) = 0.25C_{L0}\phi(L)\rho DLU^2q(t) - 0.5C_D\rho DLU\phi^2(L)\dot{\eta}(t) \quad (2)$$

where C_{L0} , C_D are constants which can be tested by a wind tunnel test, $\phi(x)$ is the model shape function of the cantilever, and $q(t)$ is the variable in the Van Del Pol wake oscillator model for describing the vortex-induced vibration effect which could be determined by

$$\ddot{q}(t) + \varepsilon\omega_f[q^2(t) - 1]\dot{q}(t) + \omega_f^2q(t) = \frac{A}{D}\phi(L)\ddot{\eta}(t) \quad (3)$$

where ε and A are also constants which can be tested by wind tunnel test. By adding $\eta(t)\phi(L) = y(t)$, $M_{eff} = 1/\phi^2(L)$, $C_{eff} = 2\zeta\omega_n/\phi^2(L)$, $K_{eff} = \omega_n^2/\phi^2(L)$, the reduced lumped parameter model can be obtained as follows.

$$M_{eff}\ddot{y}(t) + C_{eff}\dot{y}(t) + 0.5C_D\rho DLU\dot{y}(t) + K_{eff}y(t) = 0.25C_{L0}\rho DLU^2q(t) \quad (4)$$

$$\ddot{q}(t) + \varepsilon\omega_f[q^2(t) - 1]\dot{q}(t) + \omega_f^2q(t) = \frac{A}{D}\ddot{y}(t) \quad (5)$$

By adding the electromechanical coupling governing equation:

$$\frac{V(t)}{R} + C_p\dot{V}(t) + \theta\dot{y}(t) = 0 \quad (6)$$

the whole governing equations of the present energy harvest system could be obtained.

$$M_{eff}\ddot{y}(t) + C_{eff}\dot{y}(t) + 0.5C_D\rho DLU\dot{y}(t) + K_{eff}y(t) - \theta V(t) = 0.25C_{L0}\rho DLU^2q(t)$$

$$\frac{V(t)}{R} + C_p\dot{V}(t) + \theta\dot{y}(t) = 0 \quad (7)$$

$$\ddot{q}(t) + \varepsilon\omega_f[q^2(t) - 1]\dot{q}(t) + \omega_f^2q(t) = \frac{A}{D}\ddot{y}(t)$$

Equation (7) is called the concentrated parameter model of nonlinear harvester: M_{eff} and K_{eff} are the equivalent mass; C_{eff} is the system damping, which is related to damping coefficient ζ , K_{eff} is the system equivalent stiffness which depends on the physical properties of the cantilever beam. $y(t)$ is the displacement of bluff body vibrating, and $V(t)$ is the output voltage. C_p is the capacitance, θ is the piezoelectric coupling coefficient, and $F(t)$ is the fluid-dynamical force. It is worth noting that damping coefficient ζ is defined as the ratio of system damping to critical damping, which is expressed as follows.

$$\zeta = \frac{C_{system}}{C_c} = \frac{C_{system}}{2\sqrt{M_{eff}K_{eff}}} \quad (8)$$

The symbol ζ can also be obtained by the free decay experiment. Equation (3) can be rewritten as follows.

$$\zeta = \frac{In\delta}{\sqrt{4\pi^2 + (In\delta)^2}} \quad (9)$$

Here, δ is the ratio of the two adjacent amplitudes in the free decay experiment. Considering the natural frequency $\omega_n = \sqrt{K_{eff}/M_{eff}}$, the system damping C_{system} obtained by the formula is given as below.

$$C_{system} = 2M_{eff}\omega_n \frac{In\delta}{\sqrt{4\pi^2 + (In\delta)^2}} \quad (10)$$

The resistors with different resistance values are connected into the circuit to obtain the optimal load, and the measured data can be used to obtain the open circuit ω_{noc} and short circuit ω_{nsc} frequency by Fourier transform. In this point, the piezoelectric coupling coefficient θ is obtained through the following formula.

$$\theta = \sqrt{(\omega_{noc}^2 - \omega_{nsc}^2)M_{eff}C_p} \quad (11)$$

Finally, the average power expression $P_{avg} = \int_{U_1}^{U_2} (V_{amplitude}/\sqrt{2})^2/RdU$ is used to obtain the power of harvester, in which V_{max} is the maximum voltage harvested under the maximum tip deflection y_{max} .

3. Experimental Setup and the Theoretical Validation

Figure 3 shows all the instruments needed for this experiment, while the schematic diagram of the bionic structure energy collection system is shown in Figure 1. The entire experiment is implemented in a wind tunnel with the wind speed controlled by frequency conversion device and the conversion relation between frequency and wind speed expressed as $U = 0.137f + 0.18$. The range of wind speed is set at 0 to 7 m/s in the experiment.

The device includes an aluminum cantilever beam with MFC on the root, and the cantilever beam and its column are arranged in "1" shape and placed vertically with a total weight of 5.73 g. With a total length of 168 mm, the cantilever beam is split into two parts which are inserted into the bluff body and exposed to air with a ratio of 0.68 (6.8mm:10mm). The data acquisition instrument is used for signal processing to acquire frequency components. At different wind speeds and resistive loads, a two-channel digital oscilloscope is used to determine the harvester amplitude and peak voltage values. The peak power can be calculated simply from the voltage in the circuit and the corresponding load. In order to ensure the same quality as smooth cylinder, it is essential to have a quality inspection of the cylinder with concave pits and hemispheric convex during the experiment, that is, to add a mass block. The model parameters of concave pits and hemispheric convex are shown in Tables 1 and 2, respectively.

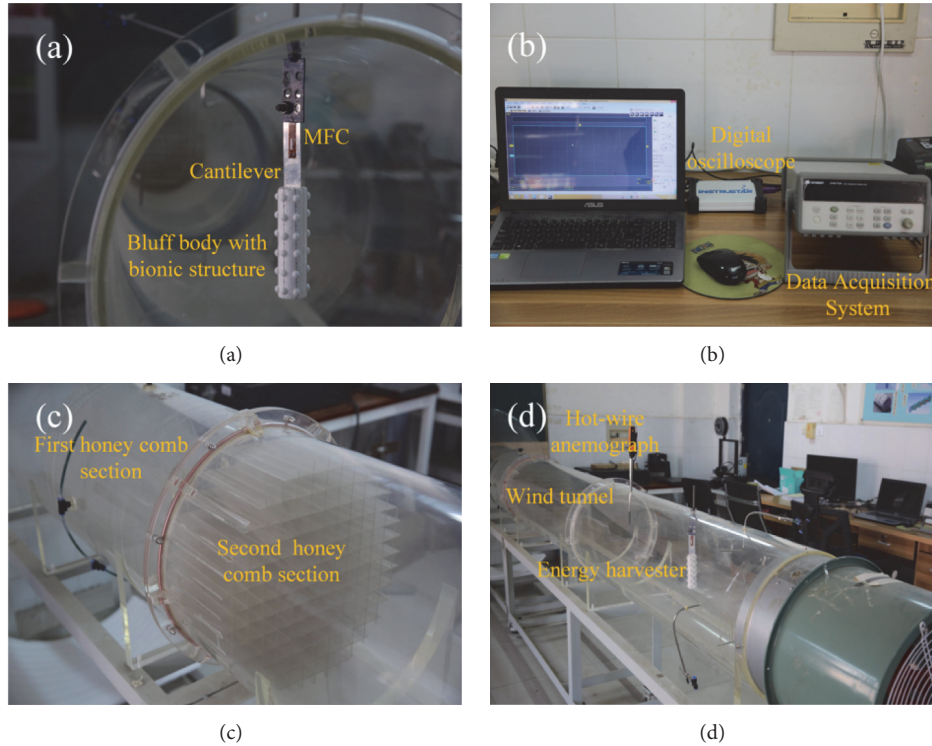


FIGURE 3: Entire experimental setup. (a) The fabricated energy harvester; (b) the data acquisition system; (c) honey comb for air stability; (d) the global views of the wind tunnel.

As is seen in Tables 1 and 2, the maximum mass of the bionic model is 2.48 g and 2.90 g, demonstrating that the mass of other models can be achieved by adding mass blocks. Of course, the same is true for the smooth cylinder. Here, the side length of the pit and the diameter of the hemispherical projection are denoted by L and d , respectively.

Aiming to validate the present aero-electromechanically coupled model, a VIVPEH prototype is prepared and tested in the wind tunnel (Figure 3). The VIVPEH prototype comprises an aluminum cantilever beam bonded with a piezoelectric transducer connected to an electrical load resistance (R_L), and an equilateral smooth cylinder bluff body. The frontal characteristic dimension of the equilateral triangular bluff body is 0.032 m. The identified effective parameters of the VIVPEH are listed in Table 3. Figure 4 shows the comparison of experimental and theoretical results for VIVPEH with smooth cylinder shaped bluff body in an open circuit condition. As shown in Figure 4, in general, the output voltage increases first and then decreases when the wind speed increases. Though the measured data is slightly higher than the theoretical prediction, the theoretical solution and experimental results are generally consistent with each other. The discrepancy is probably attributed to the error caused by the aerodynamic force coefficient of the bluff body. Computed by theoretical method and used in the vortex-induced vibration model, it could be slightly different due to some degree of uncertainty in the experiment. The time history diagrams of peak voltage calculated by

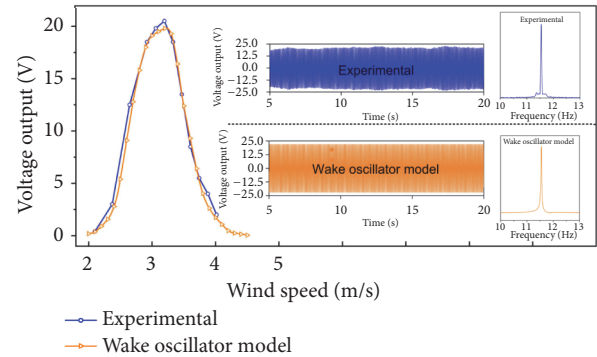


FIGURE 4: Comparison of experimental and theoretical results for VIVPEH with smooth cylinder shaped bluff body.

experiment and theory are shown in the middle of Figure 4, in which the peaks are 20.8 V and 20 V, respectively. On the right is the natural frequency, clearly showing that the experimental result is reasonably close to the theoretical calculating value.

4. Results and Discussions

To highlight the comparison with a smooth cylinder, an experimental analysis on the smooth cylinder is needed. One of the important parameters mentioned in the previous

TABLE 1: Mass parameters of convex pit models.

Size	3 columns	4 columns	5 columns	6 columns
6mm	2.48g	2.06g	2.16g	2.00g
8mm	2.30g	2.10g	1.91g	2.18g
10mm	2.00g	2.10g	1.91g	2.05g

TABLE 2: Mass parameters of hemispheric convex models.

Size	3 columns	4 columns	5 columns	6 columns
6mm	2.50g	2.57g	2.51g	2.50g
8mm	2.64g	2.50g	2.55g	2.57g
10mm	2.90g	2.61g	2.60g	2.54g

TABLE 3: Material parameters involved in the system.

Material parameter	value
Elastic coefficient (K_{eff})($N \cdot m^{-1}$)	34.07
Capacity (C_p)(nF)	15.7
Active diameter (D_a)(mm)	32
Active height (H)(mm)	118
Active mass (m_c)(g)	2.48/2.90
Equivalent mass (M_{eff})(g)	6.44/6.86
Density (ρ)($kg \cdot m^{-3}$)	27.38/31.25
System damping (C_{eff})($N \cdot s \cdot m^{-1}$)	0.0098
Piezoelectric coupling coefficient (θ)($N \cdot V^{-1}$)	1.183×10^{-5}

section is obtained by the free decay experiment. The natural frequencies ω_n are obtained by the free decay experiment of the smooth cylinder, as shown in Figure 5.

Figure 5(a) shows the time history voltage and displacement: the free decay test of vortex-induced vibration requires initial disturbance to grow until it reaches a locked area and ends up in a stable state. Corresponding to the wave peak, the horizontal coordinate shown as 11.50 Hz is the natural frequency of the system. In order to analyze the influence of bionic structures on the performance of the harvester, the characteristics of smooth, pit, and convex bluff body under different wind speeds and different resistance values are compared in detail, and the resistance values are set as 400 k Ω , 500 k Ω , 600 k Ω , 700 k Ω , 800 k Ω , and 900 k Ω .

4.1. Performance Analysis on Bionic Bluff Body with Pit Shape.

The time step curve and the measured voltage under different wind speeds are shown in Figures 6 and 7, respectively. It can be seen from Figure 7 that from three columns to six columns, the voltage rises at first and then declines as the wind speed grows, which verifies the characteristics of VIV; the VIV can be separated into three regions: presynchronization region, lock-in region, and postsynchronization region [52]. Through the overall comparison with the smooth bluff body, the starting vibration wind speed of the bionic structure decreases from 1.8 to 1 m/s, showing that energy can also be

harvested at low wind speed. When the size of the square pits on the surface of the cylinder is 6mm, 8mm, and 10mm, the voltage peak also reaches 40, 45, and 47 V, successively, 10 to 15 V higher than that of a smooth cylinder, and the bandwidth also increases from 39.3% to 51.4%. But it is not always suitable to have a bigger or smaller size of the pit for some specific structures, and there is an optimal size. The following is a concrete analysis of each column of pits: in the case of 3 columns, it is obvious that the 10 mm pit has the best vibration effect and plays a reinforcing role in the whole vibration stage with its measured voltage reaching 40 V. In the 4 columns, the voltage curves of the 6 mm and 10mm pits are always above the smooth cylinder, and the bandwidth is also extended. Although the 10 mm pit has an inhibitory effect in the early stage, the voltage in the later stage increases rapidly, even exceeding the voltage values of 6 mm and 10 mm pits. For 5 columns, the 6 mm and 10 mm pits have a weak effect, but the 8 mm pits increase significantly when the wind speed reaches 2.8 m/s. For 6 columns, 8 mm pits show a significant inhibition effect on energy harvesting, and 6mm and 10 mm pits are better than smooth cylinder as the voltage is above 45 V. Therefore, in the engineering field, it is of great significance for the above four models to raise the efficiency of energy collection without increasing the processing materials.

Figures 8(a) and 8(b) are the voltage-wind speed curves of the pit structure and the smooth cylinder, respectively. With

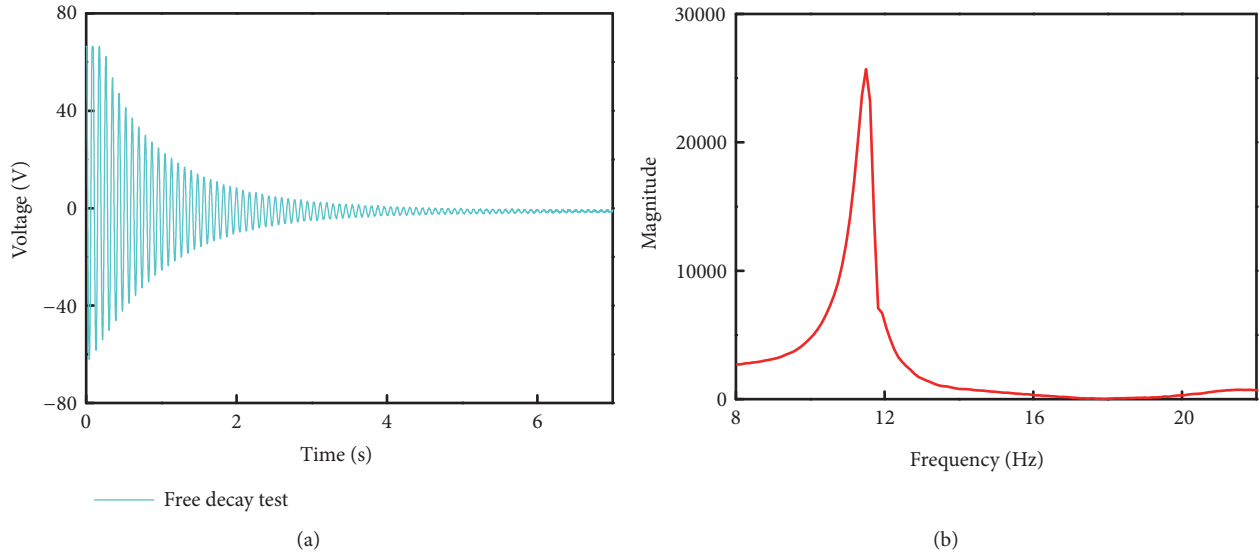


FIGURE 5: Free decay test of the energy harvester: (a) time history response curve; (b) fast Fourier transforming result.

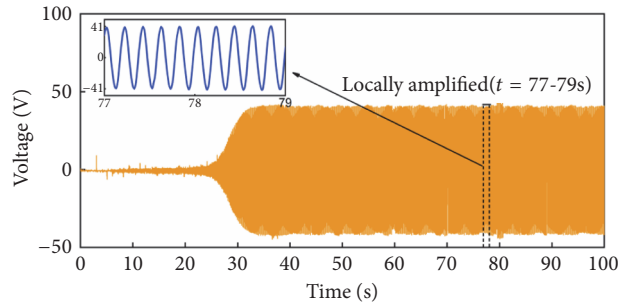


FIGURE 6: Time history curve of voltage output.

the structure of 4 columns with one side 8mm long selected, it can be seen from Figure 7 that as the wind speed expedites, the voltage and power increase gradually with a constant resistance, but they then descend slowly when reaching their peaks. For the pit structure, the maximum peak voltage is 46 V with a wind speed of 2.92 m/s and a resistance of 900 k Ω , and the maximum peak power is 1.21 mW with a resistance of 800k Ω . The voltage and power begin to decrease when their resistance surpasses 800k Ω . Regardless of voltage or power, the pit structure is higher than the smooth blunt body under the same wind speed and resistance. The optimal resistance measured for the maximum power is 800 k Ω . For the smooth bluff body, the peak voltage is lower than 35 V, about 10 V less than the bionic structure voltage, and the maximum power is only 0.64mW. It can be demonstrated in Figure 8 that the optimal load is around 800 k Ω , which can also be calculated from the time constant in a RC circuit $R_{opt} = 1/\omega_n$. $C_P = 881.5$ k Ω , where ω_n is the natural frequency, and $\omega_n = 2\pi f_n$, $f_n = 11.5$ Hz. It is obvious that the resistance measured is very close to the actual value.

4.2. Performance Analysis on Bionic Bluff Body with Spherical Convex. As it is mentioned in the second section, the convex object model also needs quality inspection, and the quality after verification is 2.90 g. The natural frequency of the vibration changes along with the quality of the bluff body. Therefore, it is also necessary to conduct free decay experiments on the smooth cylinder of 2.90 g and to obtain the natural frequency of the system $f_n = 11.2$ Hz. The output voltage of the bionic structure with different hemispheres of different sizes is measured in the wind tunnel, as shown in Figure 9.

For the 3 columns of convex bionic structure, the hemispherical enhances the amplitude of vortex-induced vibration for the diameter from 6 to 10 mm. Specifically, the output voltage of the 10 mm hemisphere is the largest with its measured voltage close to 50V, 100% higher than that of the smooth cylinder. The enhancement effect is 10 mm>8 mm>6 mm in turn, as shown in Figure 9(a). Figures 9(b) and 9(c) both show strong inhibitory effects, and the measured voltage of the bionic structure is much smaller than that of

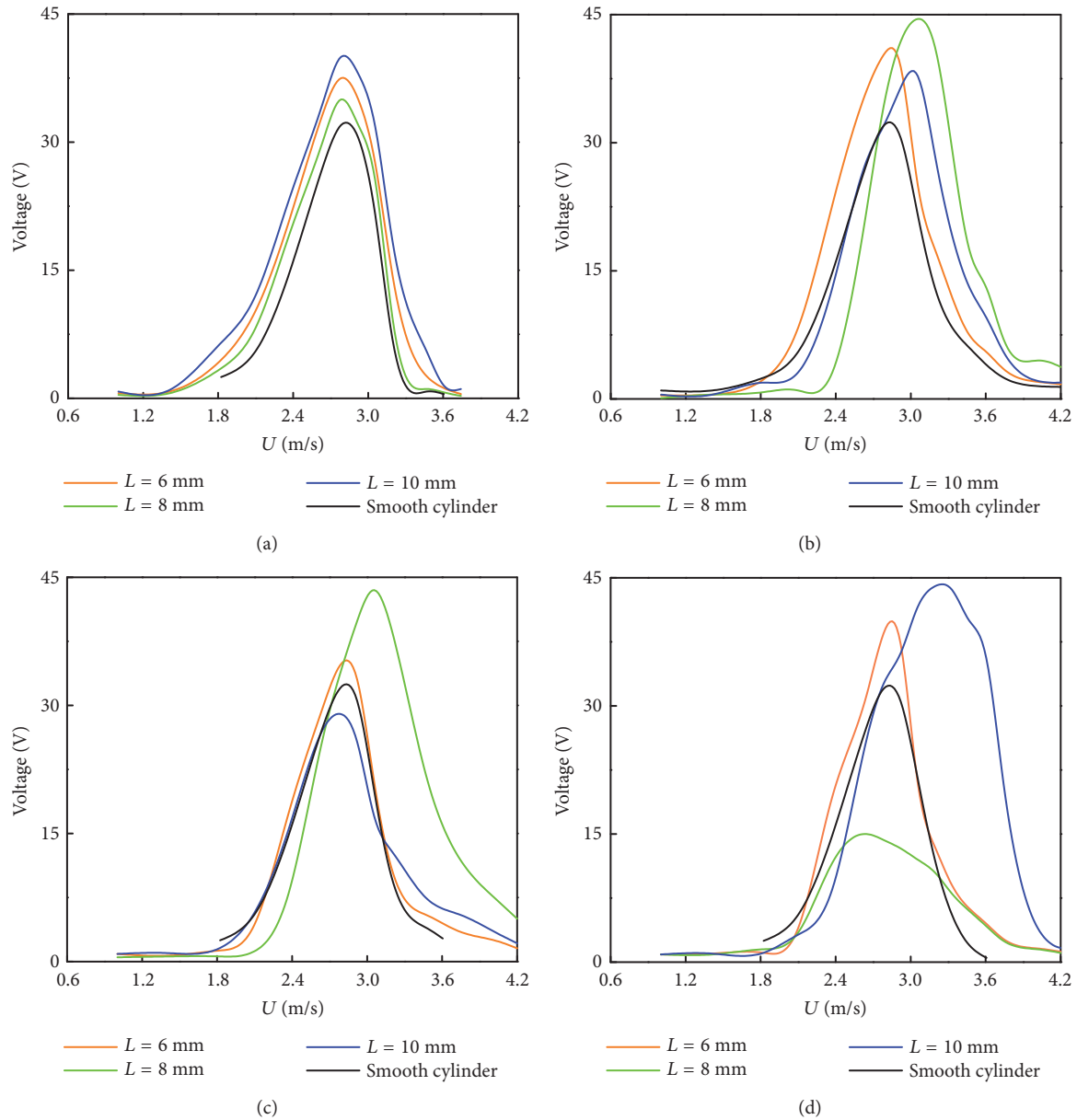


FIGURE 7: Measured piezoelectric energy harvester data (no resistance): (a) peak voltage versus wind speed of 3 columns of pits; (b) peak voltage versus wind speed of 4 columns of pits; (c) peak voltage versus wind speed of 5 columns of pits; (d) peak voltage versus wind speed of 6 columns of pits.

the smooth cylinder, which means that the 4-column and 5-column hemisphere models have no sense for enhancing the flow-induced vibration. On the contrary, it is of great significance in mitigating the damage of buildings affected by the wind. The relationship between the measured voltage and the wind speed of a 6-column hemispherical bionic cylinder is shown in Figure 9(d). Figure 9(d) shows that 10 mm to 6 mm exhibits different degrees of enhancement or inhibition for flow-induced vibration, but the measured voltage increases first and then decreases as the wind speed accelerates, which is in line with the curve of vortex-induced vibration. In detail, the 10 mm hemisphere acts as reinforcement, and the 6 to 8 mm hemisphere suppresses the vibration

of the bluff body. Figures 10(a)–10(d) show the power-wind speed curve of two energy harvesting machines, and three columns of 10 mm hemispherical bionic bluff bodies are selected. Figure 10 shows that the threshold wind speed of both energy harvesters is 1.7 m/s. The maximum peak voltage is close to 35 V with a resistance of 800 k Ω and a wind speed of 3.097 m/s. Compared with the smooth structure, the peak power increases from 0.48 to 0.56 mW with the resistance 800 k Ω . Corresponding to the pit model, the optimal load of the hemispheric model is also around 800 k Ω ; therefore, it can be considered that the added mass of the hemispheric model is tiny compared with that of the pit model, which can also be verified in Figure 10.

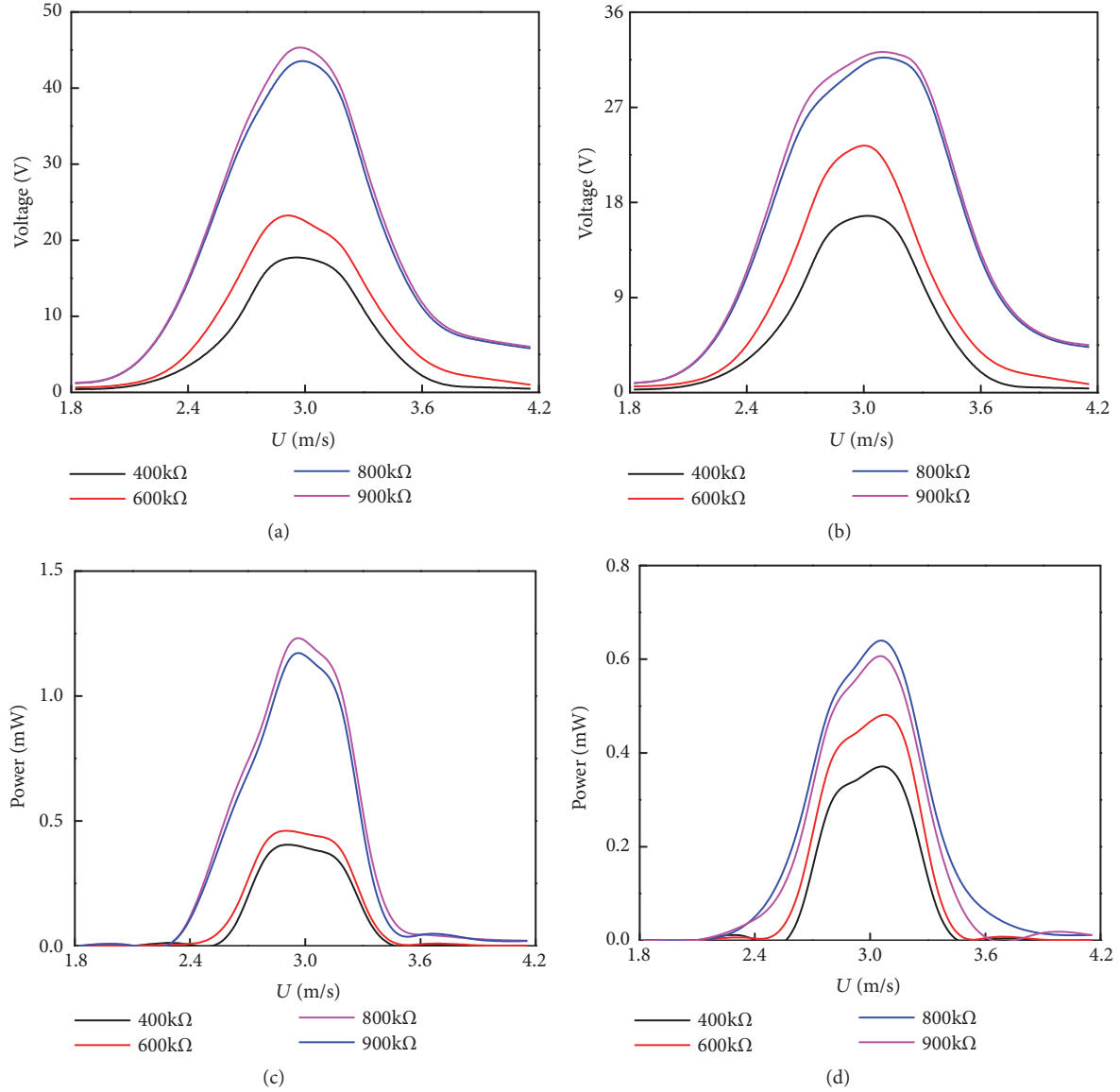


FIGURE 8: The power-wind and voltage-wind curve of the energy harvester of the pit bionic and smooth structure: (a) the voltage-wind curve of the pit structure; (b) the voltage-wind curve of the smooth cylinder; (c) the power-wind curve of the pit structure; (d) the power-wind curve of the smooth cylinder.

5. Conclusions

The piezoelectric energy harvesting characteristics of smooth cylinders with pits and hemispherical protrusions are comprehensively evaluated by experimental methods. The relationship between maximum voltage and resonance frequencies of each model under different wind speeds is studied under the condition of the same equivalent mass. The experimental result demonstrates an effect on the performance of the harvester exerted by the size and distribution of the square pit and hemispherical convex hull. In terms of the pit structure, the locking area is concentrated on 2 to 3.5 m/s. The 6 to 10mm square pit can reduce the threshold wind speed; meanwhile, it has a different effect on the enhancement

of vibration, which is closely related to the number of pit columns. For example, the measured voltage of 4 columns and 5 columns of 8 mm pits can reach about 47 V, while the voltage of 6 columns of 8 mm pits is much lower than that of the smooth cylinders. As for convex structures, the 10 mm hemispherical convex structures of 3 columns and 6 columns have excellent effects on increasing amplitude of vibration, according to the piezoelectric principle; namely, the higher the amplitude is, the higher the measuring voltage will be. The measured voltage is close to 50 V, completely higher than that of the smooth cylinder. The power output of 10 mm convex structure is 0.56 mW, slightly higher than the smooth cylinder under the same conditions. On the contrary, 4-column and 5-column hemispheric convex

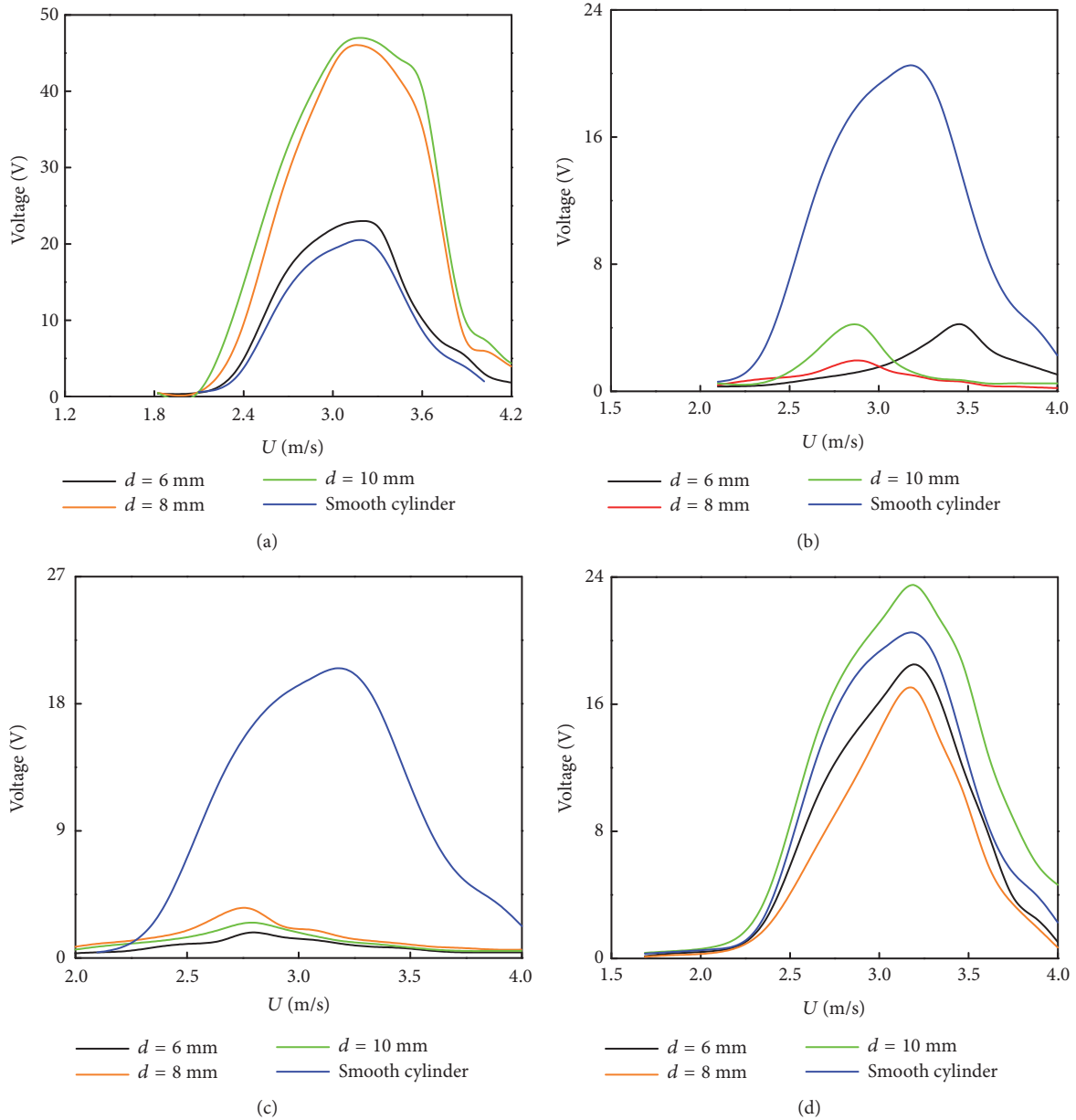


FIGURE 9: Measured piezoelectric energy harvester data (no resistance): (a) peak voltage versus wind speed of 3-column hemisphere protrusion; (b) peak voltage versus wind speed of 4-column hemisphere protrusion; (c) peak voltage versus wind speed of 5-column hemisphere protrusion; (d) peak voltage versus wind speed of 6-column hemisphere protrusion.

structures have obvious inhibiting effects on the flow-induced vibration of bluff body, which can be used for vibration reduction. For wind tunnel experiments with load resistance, the measured voltage increases with the load resistance, and the optimal load of both bionic energy collection systems is around 800 k Ω . In summary, the bionic structure energy harvesting system design can serve as a good method to obtain high voltage from wind-induced vibration. Finally, it should be mentioned that the parametric study is performed for our present bionic structures. A comparison to other methods and more efficient bionic structures for

improving performance will be further studied in the future work.

Data Availability

The data sets used to support the findings of this study are included within the article.

Conflicts of Interest

The authors declare that they have no conflicts of interest.

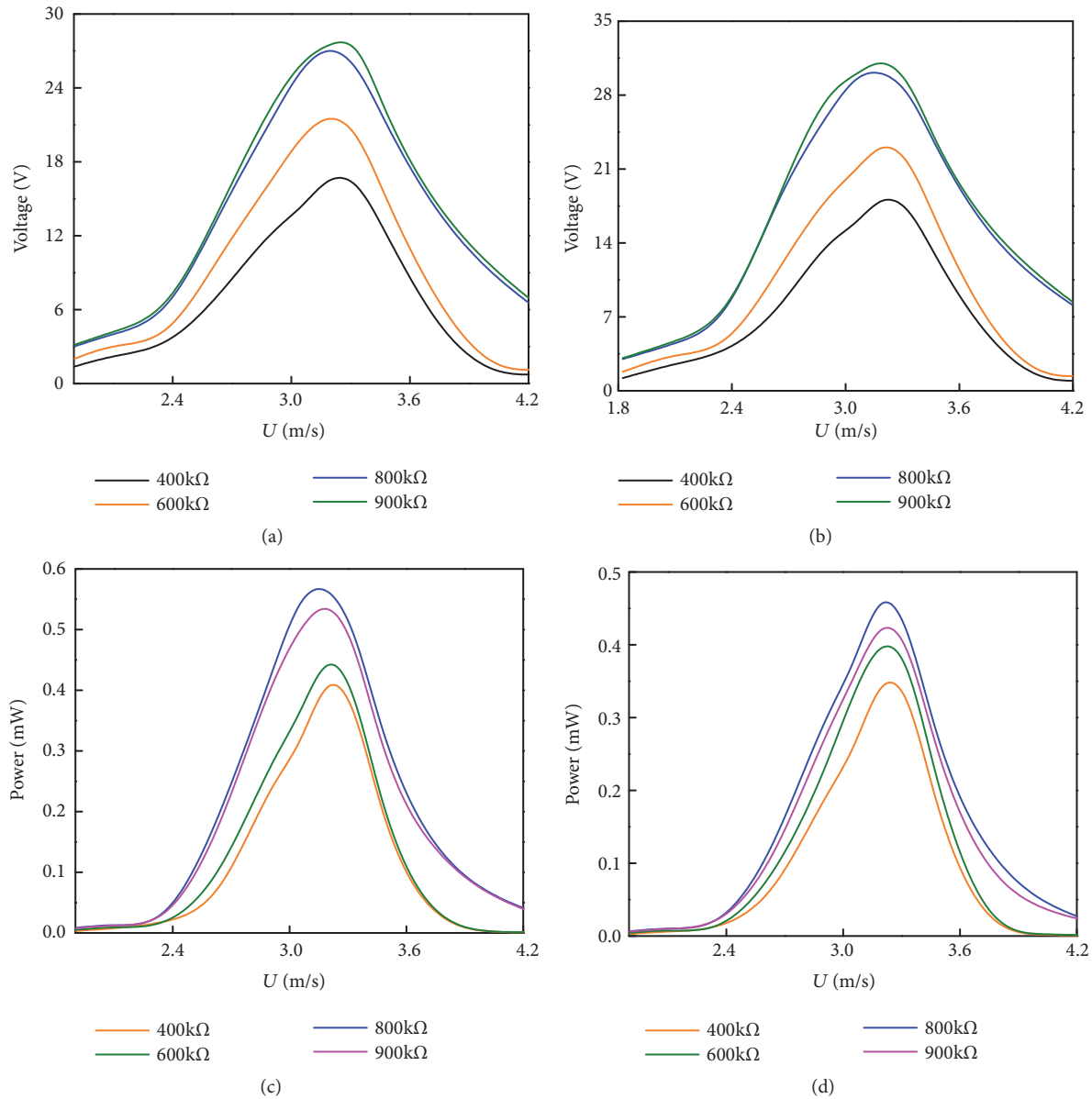


FIGURE 10: Comparison of voltage and power response between smooth cylinder and hemisphere protrusion structure: (a) voltage response of smooth cylinder; (b) voltage response of hemisphere; (c) power response of hemisphere protrusion structure; (d) power response of smooth cylinder structure.

Acknowledgments

We gratefully appreciate the financial support for this project from the National Natural Science Foundation of China (Nos. 21676257 and 51606171).

References

- [1] L. Yu and Y. P. Li, "A flexible-possibilistic stochastic programming method for planning municipal-scale energy system through introducing renewable energies and electric vehicles," *Journal of Cleaner Production*, vol. 207, pp. 772–787, 2019.
- [2] S. F. Tang, D. L. Yuan, and Y. D. Rao, "Percarbonate promoted antibiotic decomposition in dielectric barrier discharge plasma," *Journal of Hazardous Materials*, vol. 366, pp. 669–676, 2019.
- [3] Z. E. Zhang, Y. F. Li, W. X. Zhang, J. L. Wang, M. R. Soltanian, and A. G. Olabi, "Effectiveness of amino acid salt solutions in capturing CO₂: A review," *Renewable & Sustainable Energy Reviews*, vol. 98, pp. 179–188, 2018.
- [4] Q. N. Sun, Y. J. Yang, Z. X. Zhao et al., "Elaborate design of polymeric nanocomposites with Mg(ii)-buffering nanochannels for highly efficient and selective removal of heavy metals from water: case study for Cu(ii)," *Environmental Science: Nano*, vol. 5, no. 10, pp. 2440–2451, 2018.

- [5] H. Li, L. Luo, P. Kunal et al., "Oxygen Reduction Reaction on Classically Immiscible Bimetallics: A Case Study of RhAu," *The Journal of Physical Chemistry C*, vol. 122, no. 5, pp. 2712–2716, 2018.
- [6] G. Yang, J. Wang, H. W. Zhang, H. Jia, Y. Zhang, and F. Gao, "Applying bio-electric field of microbial fuel cell-upflow anaerobic sludge blanket reactor catalyzed blast furnace dusting ash for promoting anaerobic digestion," *Water Research*, vol. 149, pp. 215–224, 2019.
- [7] H. Li, K. Shin, and G. Henkelman, "Effects of ensembles, ligand, and strain on adsorbate binding to alloy surfaces," *The Journal of Chemical Physics*, vol. 149, no. 17, Article ID 174705, 8 pages, 2018.
- [8] C. W. Duan, Y. Z. Cao, L. X. Hu, D. Fu, and J. L. Ma, "Synergistic effect of TiF₃ on the dehydriding property of a-AlH₃ nanocomposite," *Materials Letters*, vol. 238, pp. 254–257, 2019.
- [9] K. Wang, S. Z. Zhou, Y. T. Zhou, J. Ren, L. W. Li, and Y. Lan, "Synthesis of Porous Carbon by Activation Method and its Electrochemical Performance," *International Journal of Electrochemical Science*, pp. 10766–10773, 2018.
- [10] Y. L. Hou, Y. Tie, C. Li, T. Sapanathan, and M. Rachik, "Low-velocity impact behaviors of repaired CFRP laminates: Effect of impact location and external patch configurations," *Composites Part B: Engineering*, vol. 163, pp. 669–680, 2019.
- [11] K. P. Wu, K. Du, and G. R. Hu, "A novel design concept for fabricating 3D graphene with the assistant of anti-solvent precipitated sulphates and its Li-ion storage properties," *Journal of Materials Chemistry A*, vol. 6, no. 8, pp. 3444–3453, 2018.
- [12] K. P. Wu, D. W. Liu, and Y. Tang, "In-situ single-step chemical synthesis of graphene-decorated CoFe₂O₄ composite with enhanced Li ion storage behaviors," *Electrochimica Acta*, vol. 263, pp. 515–523, 2018.
- [13] C. X. Duan, J. B. Huo, F. E. Li, M. H. Yang, and H. X. Xi, "Ultrafast room-temperature synthesis of hierarchically porous metal-organic frameworks by a versatile cooperative template strategy," *Journal of Materials Science*, vol. 53, no. 24, pp. 16276–16287, 2018.
- [14] L. Kang, H. L. Du, H. Zhang, and W. L. Ma, "Systematic research on the application of steel slag resources under the background of big data," *Complexity*, 2018.
- [15] K. J. Yu, B. Y. Qu, and C. T. Yue, "A performance-guided JAYA algorithm for parameters identification of photovoltaic cell and module," *Applied Energy*, vol. 237, pp. 241–257, 2019.
- [16] K. Yin, S. Yang, X. R. Dong, D. K. Chu, X. Gong, and J. A. Duan, "Femtosecond laser fabrication of shape-gradient platform: underwater bubbles continuous self-driven and unidirectional transportation," *Applied Surface Science*, vol. 471, pp. 999–1004, 2019.
- [17] Y. L. Zhang, Y. S. Hu, X. G. Guo, and F. Wang, "Micro Energy Harvester With Dual Electrets on Sandwich Structure Optimized by Air Damping Control for Wireless Sensor Network Application," *IEEE Access*, vol. 6, pp. 26779–26788, 2018.
- [18] J. L. Wang, L. H. Tang, L. Y. Zhao, and Z. E. Zhang, "Efficiency investigation on energy harvesting from airflows in HVAC system based on galloping of isosceles triangle sectioned bluff bodies," *Energy*, vol. 172, pp. 1066–1078, 2019.
- [19] J. L. Wang, G. P. Li, M. Zhang et al., "Energy harvesting from flow-induced vibration: a lumped parameter model," *Energy Sources, Part A: Recovery, Utilization, and Environmental Effects*, vol. 40, no. 24, pp. 2903–2913, 2018.
- [20] J. L. Wang, S. X. Zhou, Z. E. Zhang, and D. Yurchenko, "High-performance piezoelectric wind energy harvester with Y-shaped attachments," *Energy Conversion and Management*, vol. 181, pp. 645–652, 2019.
- [21] J. Zhu and W. Zhang, "Coupled analysis of multi-impact energy harvesting from low-frequency wind induced vibrations," *Smart Materials and Structures*, vol. 24, no. 4, Article ID 045007, 2015.
- [22] H. C. Lim and S. J. Lee, "Flow control of a circular cylinder with O-rings," *Fluid Dynamics Research*, vol. 35, no. 2, pp. 107–122, 2004.
- [23] G. R. Wang, C. J. Liao, G. Hu, L. Zhong, and M. Zhang, "Numerical simulation analysis and the drag reduction performance investigation on circular cylinder with dimples at sub-critical reynolds number," *Jixie Qiangdu/Journal of Mechanical Strength*, vol. 39, no. 5, pp. 1119–1125, 2017.
- [24] J. J. Allen and A. J. Smits, "Energy harvesting EEL," *Journal of Fluids and Structures*, vol. 15, no. 3-4, pp. 629–640, 2001.
- [25] H. Park, R. A. Kumar, and M. M. Bernitsas, "Enhancement of flow-induced motion of rigid circular cylinder on springs by localized surface roughness at $3 \times 10^4 \leq Re \leq 1.2 \times 10^5$," *Ocean Engineering*, vol. 72, pp. 403–415, 2013.
- [26] E. S. Kim, M. M. Bernitsas, and R. A. Kumar, "Multicylinder flow-induced motions: enhancement by passive turbulence control at $28,000 < Re < 120,000$," *Journal of Offshore Mechanics and Arctic Engineering*, vol. 135, no. 2, Article ID 021802, 2013.
- [27] Y. Cha, M. Verotti, H. Walcott, S. D. Peterson, and M. Porfiri, "Energy harvesting from the tail beating of a carangiform swimmer using ionic polymer-metal composites," *Bioinspiration & Biomimetics*, vol. 8, no. 3, Article ID 036003, 2013.
- [28] H. D. Akaydin, N. Elvin, and Y. Andreopoulos, "The performance of a self-excited fluidic energy harvester," *Smart Materials and Structures*, vol. 21, no. 2, Article ID 025007, 2012.
- [29] F. F. Pan, Z. K. Xu, P. Pan, and L. Jin, "Piezoelectric energy harvesting from vortex-induced vibration using a modified circular cylinder," in *Proceedings of the International Conference on Electrical Machines and Systems*, pp. 1–5, 2017.
- [30] S. X. Zhou and L. Zuo, "Nonlinear dynamic analysis of asymmetric tristable energy harvesters for enhanced energy harvesting," *Communications in Nonlinear Science and Numerical Simulation*, vol. 61, pp. 271–284, 2018.
- [31] S. X. Zhou, J. Y. Cao, D. J. Inman, J. Lin, S. S. Liu, and Z. Z. Wang, "Broadband tristable energy harvester: modeling and experiment verification," *Applied Energy*, vol. 133, pp. 33–39, 2014.
- [32] D. M. Huang, S. X. Zhou, and G. Litak, "Theoretical analysis of multi-stable energy harvesters with high-order stiffness terms," *Communications in Nonlinear Science and Numerical Simulation*, vol. 69, pp. 270–286, 2019.
- [33] M. H. Yao, Y. Niu, and Y. X. Hao, "Nonlinear dynamic responses of rotating pretwisted cylindrical shells," *Nonlinear Dynamics*, vol. 95, no. 1, pp. 151–174, 2019.
- [34] S. X. Zhou, J. D. Hobeck, J. Y. Cao, and D. J. Inman, "Analytical and experimental investigation of flexible longitudinal zigzag structures for enhanced multi-directional energy harvesting," *Smart Materials and Structures*, vol. 26, no. 3, Article ID 035008, 2017.
- [35] S. X. Zhou and J. L. Wang, "Dual serial vortex-induced energy harvesting system for enhanced energy harvesting," *AIP Advances*, no. 7, Article ID 075221, 2018.

- [36] K. Muralidharan, S. Muddada, and B. S. V. Patnaik, "Numerical simulation of vortex induced vibrations and its control by suction and blowing," *Applied Mathematical Modelling*, vol. 37, no. 1-2, pp. 284–307, 2013.
- [37] J. L. Wang, L. F. Geng, M. Zhang et al., "Broadening band of wind speed for aeroelastic energy scavenging of a cylinder through buffeting in the wakes of a squared prism," *Shock and Vibration*, vol. 2018, 2018.
- [38] L. M. Tian, L. Q. Ren, Q. P. Liu, Z. W. Han, and X. Jiang, "The mechanism of drag reduction around bodies of revolution using bionic non-smooth surfaces," *Journal of Bionic Engineering*, vol. 4, no. 2, pp. 109–116, 2007.
- [39] Y. Q. Gu, G. Zhao, J. X. Zheng, Z. Y. Li, W. B. Liu, and F. K. Muhammad, "Experimental and numerical investigation on drag reduction of non-smooth bionic jet surface," *Ocean Engineering*, vol. 81, pp. 50–57, 2014.
- [40] J. L. Wang, G. F. Zhao, M. Zhang, and Z. E. Zhang, "Efficient study of a coarse structure number on the bluff body during the harvesting of wind energy," *Energy Sources, Part A: Recovery, Utilization, and Environmental Effects*, vol. 40, no. 15, pp. 1788–1797, 2018.
- [41] S. K. Kumar, C. Bose, S. F. Ali, S. Sarkar, and S. Gupta, "Investigations on a vortex induced vibration based energy harvester," *Applied Physics Letters*, vol. 111, no. 24, Article ID 243903, 2017.
- [42] L. C. Zhao, H. X. Zou, G. Yan et al., "A water-proof magnetically coupled piezoelectric-electromagnetic hybrid wind energy harvester," *Applied Energy*, vol. 239, pp. 735–746, 2019.
- [43] X. F. He, X. K. Yang, and S. L. Jiang, "Enhancement of wind energy harvesting by interaction between vortex-induced vibration and galloping," *Applied Physics Letters*, vol. 112, no. 3, Article ID 033901, 2018.
- [44] M. Zhang and J. L. Wang, "Experimental study on piezoelectric energy harvesting from vortex-induced vibrations and wake-induced vibrations," *Journal of Sensors*, vol. 2016, 2016.
- [45] X. Q. Zhao, J. Cai, Y. Guo, C. B. Li, J. L. Wang, and H. W. Zheng, "Modeling and experimental investigation of an AA-sized electromagnetic generator for harvesting energy from human motion," *Smart Material and Structures*, vol. 27, no. 8, Article ID 085008, 2018.
- [46] P. D. Mitcheson, T. C. Green, and E. M. Yeatman, "Power processing circuits for electromagnetic, electrostatic and piezoelectric inertial energy scavengers," *Microsystem Technologies*, vol. 13, no. 11-12, pp. 1629–1635, 2007.
- [47] T. N. Kato and H. Takabe, "Electrostatic and electromagnetic instabilities associated with electrostatic shocks: Two-dimensional particle-in-cell simulation," *Physics of Plasmas*, vol. 17, no. 3, Article ID 032114, 2010.
- [48] H. C. Liu, J. W. Zhong, C. K. Lee, S. W. Lee, and L. W. Lin, "A comprehensive review on piezoelectric energy harvesting technology: Materials, mechanisms, and applications," *Applied Physics Reviews*, vol. 5, no. 5, Article ID 041306, 2018.
- [49] S. X. Zhou, J. Y. Cao, A. Erturk, and J. Lin, "Enhanced broadband piezoelectric energy harvesting using rotatable magnets," *Applied Physics Letters*, vol. 102, no. 17, Article ID 173901, 2013.
- [50] G. B. Hu, L. H. Tang, and R. Das, "Internally coupled meta-material beam for simultaneous vibration suppression and low frequency energy harvesting," *Journal of Applied Physics*, vol. 123, no. 5, Article ID 055107, 2018.
- [51] Z. S. Chen, J. He, J. H. Liu, and Y. P. Xiong, "Switching delay in self-powered nonlinear piezoelectric vibration energy harvesting circuit: mechanism, effects and solution," *IEEE Transactions on Power Electronics*, vol. 34, no. 3, pp. 2427–2440, 2019.
- [52] J. L. Wang, J. Y. Ran, and Z. E. Zhang, "Energy harvester based on the synchronization phenomenon of a circular cylinder," *Mathematical Problems in Engineering*, vol. 2014, 2014.

Research Article

Performance Sensitivity of a Wind Farm Power Curve Model to Different Signals of the Input Layer of ANNs: Case Studies in the Canary Islands

Sergio Velázquez Medina ¹, José A. Carta,² and Ulises Portero Ajenjo³

¹Department of Electronics and Automatics Engineering, Universidad de Las Palmas de Gran Canaria, Campus de Tafira s/n, 35017 Las Palmas de Gran Canaria, Canary Islands, Spain

²Department of Mechanical Engineering, University of Las Palmas de Gran Canaria, Campus de Tafira s/n, 35017 Las Palmas de Gran Canaria, Canary Islands, Spain

³School of Industrial and Civil Engineering, University of Las Palmas de Gran Canaria, Campus de Tafira s/n, 35017 Las Palmas de Gran Canaria, Canary Islands, Spain

Correspondence should be addressed to Sergio Velázquez Medina; sergio.velazquezmedina@ulpgc.es

Received 18 October 2018; Revised 11 February 2019; Accepted 11 March 2019; Published 26 March 2019

Guest Editor: Aitor J. Garrido

Copyright © 2019 Sergio Velázquez Medina et al. This is an open access article distributed under the Creative Commons Attribution License, which permits unrestricted use, distribution, and reproduction in any medium, provided the original work is properly cited.

Improving the estimation of the power output of a wind farm enables greater integration of this type of energy source in electrical systems. The development of accurate models that represent the real operation of a wind farm is one way to attain this objective. A wind farm power curve model is proposed in this paper which is developed using artificial neural networks, and a study is undertaken of the influence on model performance when parameters such as the meteorological conditions (wind speed and direction) of areas other than the wind farm location are added as signals of the input layer of the neural network. Using such information could be of interest, either to study possible improvements that could be obtained in the performance of the original model, which uses exclusively the meteorological conditions of the area where the wind farm is located, or simply because no reliable meteorological data for the area of the wind farm are available. In the study developed it is deduced that the incorporation of meteorological data from an additional weather station other than that of the wind farm site can improve by up to 17.6% the performance of the original model.

1. Introduction

The power curve of a wind turbine (WT) is a model that relates the electrical power generated by the WT to the wind speed. This characteristic of a WT is of fundamental importance in power output estimation processes. A precise knowledge of the power curve of a WT is vital to optimise the efficiency of these processes and is indispensable for massive wind power integration in electrical systems [1–6].

Manufacturers of WTs provide certified power curve models based on the IEC 61400-12-1 standard [7]. To obtain this certification for the full operating range of the WT within an acceptable period of time, these curves are usually certified using wind simulation systems and not directly at the site where the WT will be definitively located. The power curve of

a WT that is obtained in this way is therefore static. That is to say, it is independent of the actual meteorological conditions of the site where it is to be located, of the surrounding conditions of the terrain (roughness) and of the variations that it may undergo over time or of changes to the operation of the WT due to aging of the system.

Other procedures have been proposed in the literature to establish the power curve models of a WT. These include, for example, polynomial and exponential type parametric models. These define the operating curve of a WT according to various design values including, amongst others, rotor diameter, blade design, start-up speed, rated speed, etc. [8–13]. Carrillo et al. [12] and Lydia et al. [9] reviewed the different types of parametric models defined in the literature, comparing them according to their fit with the power curve

of the manufacturer defined in accordance with IEC 61400-12-1. Carrillo et al. [12] point out in their study that one of the major drawbacks of this type of generic power curve model is the difficulty of confirming that these models are an exact representation of each of the different WT technologies.

Nonparametric models have also been developed to define the power curve of a single WT using artificial intelligence methods [14, 15].

Terrain roughness is one of the factors that most impacts the uncertainty of the energy estimation process of a WT [16, 17]. Terrain roughness additionally needs to be considered according to the direction the wind is coming from [18]. In this respect, in the power curve model development process and for a better estimation of the electrical power of the WT, it is considered important to also take into account wind direction as well as wind speed.

Currently, the integration of wind power in the markets and electrical systems is done through the installation of wind farms (WF) comprised of groups of WTs [19–21]. In these cases, the uncertainty in the estimation of the electrical power of a WT, obtained from the individual power curve model, is increased as a result of the additional wake effect generated between the different WTs in the WF [17, 18, 22–24]. This effect depends on the relative location of each WT with respect to the others, on the predominant wind direction and on the distance between the WTs [18].

This additional uncertainty as a consequence of the integration of a WT in a WF can be corrected through the development of global WF power curve models.

Mingdi You et al. [25] developed a linear power curve of a WT as an integral component of a WF. For development of the individualised model, both wind speed and direction are taken into account. With respect to wind direction, the idea is to divide the spectrum of possible directions into a specific number of ranges, developing a different WT power curve for each of them. Sixteen sectors at most are used, which is equivalent to developing the same model for the data corresponding to a 22.5° range of directions. To estimate the different parameters of the model, these authors used information about the neighbouring WTs. For this reason, according to the authors, the reliability of this model is limited to its use in WFs with a large number of WTs (tens or hundreds).

All the parametric models published in the literature are based exclusively on identifying the power curve of individual WTs.

Marvuglia and Messineo [26] compared three WF power curve models developed on the basis of artificial intelligence techniques. All of these models use the historic wind speed and global power output data of a real WF. They do not consider wind direction as a signal of the input layer.

For estimation of the meteorological conditions of a specific site, studies have been published in the literature in which meteorological data from different areas have been used to optimize the estimation process [27, 28]. For the specific case of the generation of power curve models of WTs or WFs, none of the models found in the literature take into account meteorological conditions (wind speed and direction) of areas other than those of the wind farm. Using

such information could be of interest, either to study possible improvements that could be obtained in the performance of the original model which uses exclusively the meteorological conditions of the area where the wind farm is located, or simply because no reliable meteorological data for the area of the wind farm are available.

The research work undertaken in the present study aims to cover this gap found in the body of knowledge. For this purpose, an adaptive wind farm power curve model (ADWFPC) is proposed using regression techniques based on artificial neural networks (ANNs). The following original studies have been carried out:

- (i) A study of the improvements in the model efficiency when meteorological data corresponding to weather stations other than the reference weather station of the wind farm is additionally incorporated in the input layer of the neural network.
- (ii) A study of the possibility of using exclusively information from a weather station other than the reference station to generate the adaptive wind farm power curve model.

This case studies the option of generating the power curve model based on real data from other weather stations instead of using estimated meteorological data for the area where the wind farm is situated. Using estimated meteorological data introduces additional uncertainty in the estimation process of the wind farm power output, namely, the uncertainty associated with the model used for the estimation of the meteorological data.

The model was applied to two real WFs located on two islands of the Canary Archipelago (Spain).

2. Materials

The models were generated using real electricity production data of two WFs on two islands of the Canary Archipelago (Spain). The electricity production data corresponded to time instants when all the WTs in the corresponding WF were available for operation.

Wind farm 1 (WF-1) (Figure 1) is located on the east coast of the island of Gran Canaria, very close to the sea and in a flat area with very few natural obstacles in the vicinity. WF-1 has 4 Gamesa G47-660kW wind turbines. These are distributed in two lines virtually perpendicular to the dominant wind direction of the area: the line which connects WT1 with WT2 and the line which joins WT3 with WT4. The distance between WTs in the same line and between lines is 1.6 and 5.5 times the rotor diameter, respectively.

Wind farm 2 (WF-2) (Figure 2) is located inland on Lanzarote island in an area of variable orography. It has 9 Gamesa G52-850kW wind turbines. Unlike WF-1, all the WTs of WF-2 are practically distributed along a single line (line which connects WT1 with WT9) perpendicular to the dominant wind direction. The distance between the different WTs, measured along that line, is variable, ranging between 2 and 3 times the rotor diameter.



D: Rotor diameter

-----Perpendicular to the dominant wind direction.

FIGURE 1: Distribution of the four wind turbines of WF-1 on Gran Canaria island [29].

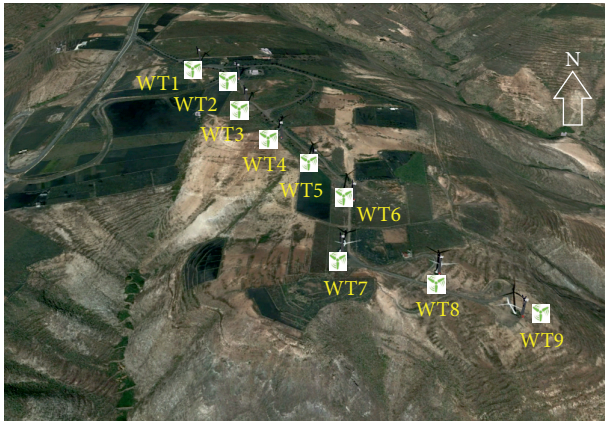


FIGURE 2: Distribution of wind turbines of WF-2 on Lanzarote [29].

As is clear from the above description, and as can be seen in Figures 1 and 2, the two WFs used for this study differ in terms of the distribution pattern of their respective WTs.

Shown in Table 1 are the geographic coordinates of the WTs of the two WFs.

The meteorological data (wind speeds and directions) were recorded at 9 weather stations (WS) installed on four of the seven main islands that make up the Canary Archipelago (Figure 3). These were numbered from WS-1 to WS-9. The reference stations are WS-1 and WS-9 in, respectively, WF-1 and WF-2.

The data used are from 2008 and have a mean hourly frequency.

The meteorological data series were provided by the Technological Institute of the Canary Islands (ITC, Instituto

TABLE 1: Geographic coordinates of the wind turbines.

Code	X(m.)	Y(m.)	Z(m.)
Wind Farm 1			
WF1-WT1	461764	3086314	3
WF1-WT2	461839	3086301	1
WF1-WT3	461681	3086067	5
WF1-WT4	461753	3086038	2
Wind Farm 2			
WF2-WT1	645043	3219819	486
WF2-WT2	645147	3219752	478
WF2-WT3	645186	3219638	473
WF2-WT4	645264	3219548	464
WF2-WT5	645333	3219462	456
WF2-WT6	645403	3219369	448
WF2-WT7	645406	3219213	440
WF2-WT8	645554	3219194	425
WF2-WT9	645664	3219133	405

Tecnológico de Canarias) [30], the Spanish State Meteorological Agency (AEMET, Agencia Española de Meteorología) [31], and the owners of the WFs. The ITC is a public research and development company which pertains to the Canary Government. Among its many lines of research are the analysis of renewable resources and the undertaking of projects such as the wind map of the Canary Islands [32, 33].

Table 2 shows the general data of each of the WSs: the code assigned to each of them, the height above ground level, the geographic coordinates, and the mean annual wind speed for 2008.

Figure 4 shows the distribution of real wind directions for the reference WSs (WS-1 and WS-9) of the WFs.

Table 3 shows the linear correlation coefficients (CC) (1) between the mean hourly wind speeds of the different WSs. The range of CCs obtained is between 0.10 and 0.87. The lowest value was obtained between WS-3 and WS-9. The highest CCs were observed between WS-1 and WS-2 and between WS-2 and WS-7.

$$CC = \frac{\sum_{i=1}^m (V_{1i} - \bar{V}_1) \times (V_{2i} - \bar{V}_2)}{\sqrt{\sum_{i=1}^m (V_{1i} - \bar{V}_1)^2} \times \sqrt{\sum_{i=1}^m (V_{2i} - \bar{V}_2)^2}} \quad (1)$$

where

CC is Pearson's correlation coefficient between the wind speeds of two weather stations.

V_{1i} and V_{2i} are the wind speed data of the two weather stations for hour "i."

m is the number of data available in the year.

\bar{V}_1 and \bar{V}_2 are the mean wind speed values for the available data series of the two weather stations.

3. Methodology

3.1. *Architecture Used for the Neural Network.* The architecture used for the ANNs was comprised of three layers with

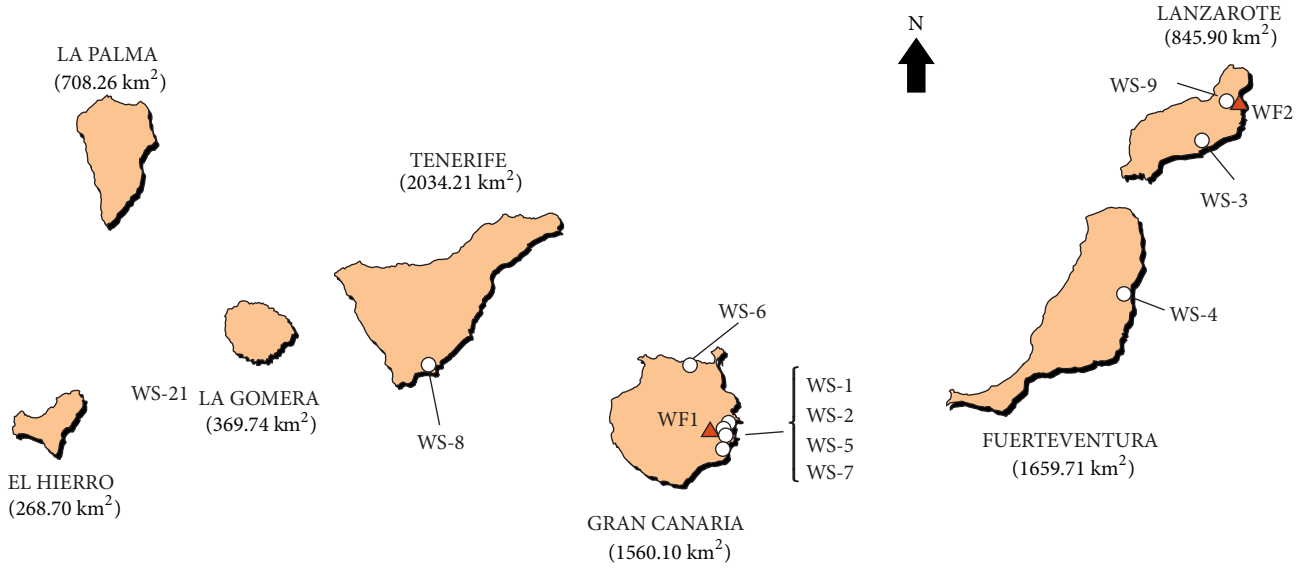


FIGURE 3: Location of the weather stations (WS) and wind farms (WF) used in the study.

TABLE 2: Weather stations used in the study.

Code	Height (m a.g.l.)	X(m.) (north)	Y(m.) (west)	Z(m.) (m.)	Annual mean wind speed(m/s)
WS-1	40	461811	3086432	16	8.3
WS-2	10	461905	3081754	3	7.7
WS-3	10	611130	3147885	24	5.6
WS-4	10	636430	3203469	10	5.4
WS-5	13	461882	3100217	5	6.9
WS-6	10	433517	3111235	472	8.5
WS-7	10	458351	3090136	186	6.0
WS-8	10	345575	3102967''	51	6.0
WS-9	40	645405	3219587	457	8.4

feedforward connections. More specifically, multilayer perceptron topologies (MLPs) were used [34, 35]. This architecture has shown its capacity to satisfactorily approximate any continuous transformation [34, 35] and has been proposed by various authors [36, 37]. A total of 20 neurons were used for the hidden layer. It was verified that model efficiency was not improved with more neurons in this layer. The number of neurons in the input layer varies depending on the case under study. In all the cases considered, the output layer comprised just a single neuron.

The designed architectures were trained using the back-propagation algorithm with sigmoidal activation function [34, 35] and the Levenberg-Marquard method [34, 38] for mean square error minimisation.

The different tests were performed using Matlab software tools for neural networks (the licence was acquired by the Group for Research on Renewable Energy Systems of the University of Las Palmas de Gran Canaria).

3.2. Description of the Study Cases. Figure 5 is a schematic description of the general methodology for generation of ADWFPCs using ANNs. The input layer neurons correspond to the meteorological information (wind speed and/or direction) of one or various WSs. The output layer will have a single neuron which corresponds to the WF power output.

All the available data are divided randomly into three parts to be used in the training, validation and test stages (Figure 5). The proportion of data used for the training, validation, and test stages was 70%, 15%, and 15%, respectively.

The training data subset was used to estimate the weights of the ANN. The validation data subset was used to check the progress of the training of the ANNs, optimizing their parameters. Based on this, and using the data reserved for the test stage, the hourly WF power output is estimated. To assess model precision, a comparison of the data estimated in the test stage with the observed data is undertaken. That is, it constitutes an independent measure of the functioning of the ANN after its training.

TABLE 3: Linear correlation coefficients between the wind speeds recorded at the different weather stations.

	WS-1	WS-2	WS-3	WS-4	WS-5	WS-6	WS-7	WS-8	WS-9
WS-1	1	0.84	0.27	0.34	0.74	0.73	0.77	0.50	0.50
WS-2	0.81	1	0.19	0.25	0.79	0.74	0.87	0.44	0.54
WS-3	0.27	0.19	1	0.70	0.16	0.16	0.18	0.16	0.10
WS-4	0.34	0.25	0.70	1	0.20	0.21	0.22	0.20	0.11
WS-5	0.74	0.79	0.16	0.20	1	0.49	0.78	0.21	0.44
WS-6	0.73	0.74	0.16	0.21	0.49	1	0.61	0.62	0.54
WS-7	0.77	0.87	0.18	0.22	0.78	0.61	1	0.39	0.46
WS-8	0.50	0.44	0.16	0.20	0.21	0.62	0.39	1	0.34
WS-9	0.50	0.54	0.10	0.11	0.44	0.54	0.46	0.34	1

The results obtained were analysed in the present paper for the following cases.

Case 1. This case considers the original model which uses exclusively, as signals of the input layer of the ANN, meteorological data of the reference station of the wind farm. The results obtained in this case were differentiated according to whether only the wind speed data were used, or both the wind speed and wind direction data were used simultaneously (Figure 6(a) vs. Figure 6(b)).

Case 2. Analysis of improvements in the precision of the adaptive model when the data from a WS other than the reference station of the WF is additionally incorporated in the ANN input layer.

Figure 7 shows a schematic representation of the ANN for this case. Unlike the adaptive model of Case 1, this ANN will have an input layer of 4 neurons.

A total of 9 WSs were used in this study (including each reference WS of the two WFs). Each WF reference station was combined with the seven WSs with no connection to either of the two WFs. This means the generation of 7 different models for each of the two WFs.

Case 3. Analysis of the performance of the adaptive model when only the data from a WS other than the reference station of the WF is used in the input layer.

This case was considered because it is possible that there may be no reliable reference station meteorological data available [39]. With this in mind, adaptive models were generated using meteorological data from WSs other than the reference station. The precision of these models was compared with that of the adaptive model obtained following option (b) of Case 1 (Figure 6(b)).

Figure 8 shows a schematic representation of the ANN model for this case. The number of neurons in the different layers is the same as in Case 1, option (b).

3.3. Metrics Used to Compare the Different Models. The metrics defined in (2), (3), and (4) were used to compare the precision of the different models that were generated. These

metrics are commonly used in analyses of model efficiency [40–42].

$$\text{MARE} = \frac{1}{n} \sum_{i=1}^n \frac{|P_i - \hat{P}_i|}{P_i}; \quad \begin{cases} P_i > 0 \\ \hat{P}_i > 0 \end{cases} \quad (2)$$

where

MARE is the mean absolute relative error.

P_i is the observed value of the wind farm power output for the time instant i .

\hat{P}_i is the estimated value of the wind farm power output for the time instant i .

n is the number of data used in the test stage.

$$R = \frac{\sum_{i=1}^n (P_i - \bar{P}) \times \left(\hat{P}_i - \bar{\hat{P}} \right)}{\sqrt{\sum_{i=1}^n (P_i - \bar{P})^2} \times \sqrt{\sum_{i=1}^n \left(\hat{P}_i - \bar{\hat{P}} \right)^2}} \quad (3)$$

where

R is Pearson's correlation coefficient between the estimated and observed values of the wind farm power output.

\bar{P} is the mean of the observed values of the power output for the data series of the test stage (Figure 5).

$\bar{\hat{P}}$ is the mean of the estimated values of the power output for the data series of the test stage (Figure 5).

$$I_oA = 1 - \frac{\sum_{i=1}^n \left(\hat{P}_i - P_i \right)^2}{\sum_{i=1}^n \left(\left| \hat{P}_i - \bar{P} \right| + \left| P_i - \bar{P} \right| \right)^2} \quad (4)$$

where

I_oA (Index of Agreement) evaluates the index of agreement between the values estimated by the model and the observed values of the wind farm power output [40].

4. Results and Discussion

4.1. Discussion of Results for Case 1 (C1). Table 4 shows the results obtained for the different metrics.

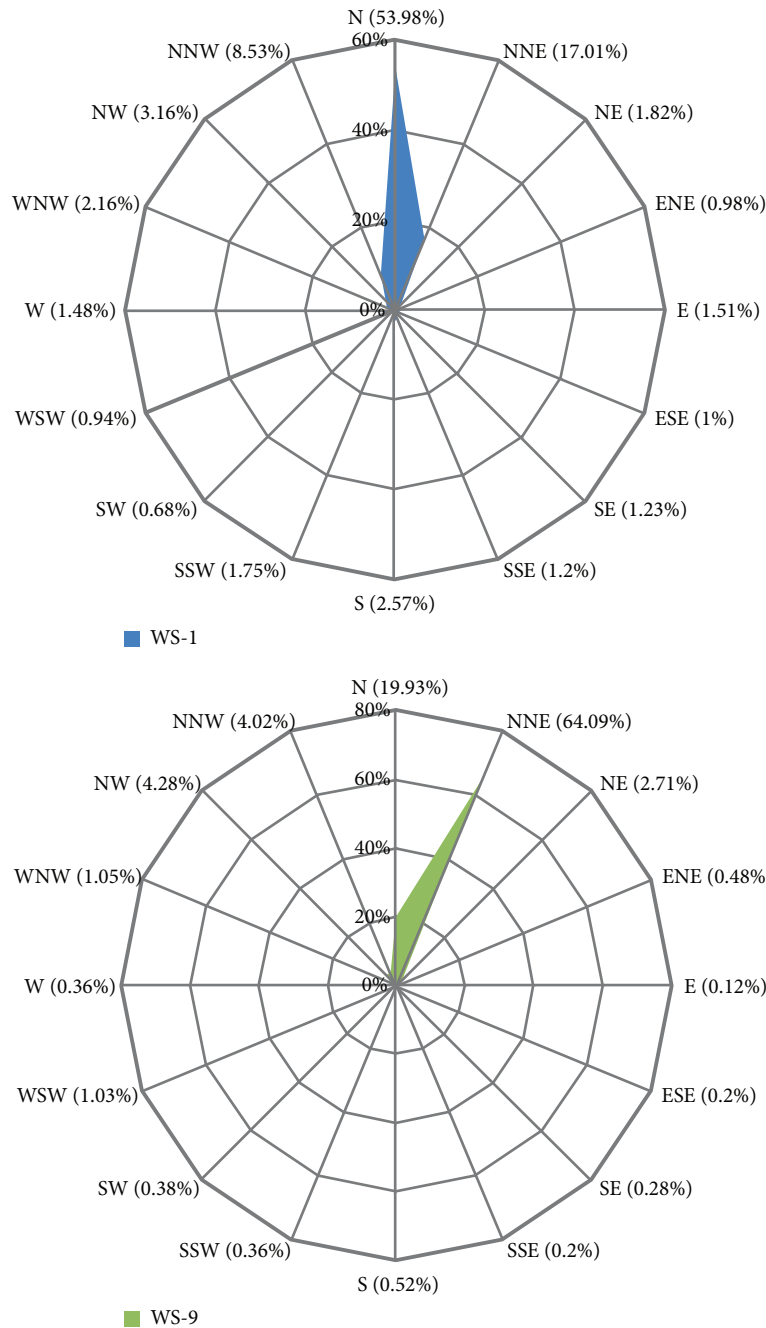


FIGURE 4: Annual wind direction frequency distribution for WS-1 and WS-9.

TABLE 4: Comparison of the results of the models generated according to (a) and (b) of Figure 6.

Wind farm	Input layer signal (wind speed)			Input layer signals (wind speed and direction)		
	MARE	R	IoA	MARE	R	IoA
CI-WF-1	0.2492	0.9174	0.9546	0.2438	0.9236	0.9591
CI-WF-2	0.1094	0.9716	0.9855	0.0991	0.9803	0.99

In the simulation of the models generated for the two WFs, it can be seen that the reliability of the model obtained for WF-2 is higher than that for WF-1. This difference in model performance is due to the greater difficulty in the learning stage of WF-1 which has a more complex distribution of WTs on the ground: there are various lines of WTs and the distances are relatively small, both between WTs on the same line and between lines.

Another of the conclusions that can be drawn from the data shown in Table 4 is that, when incorporating wind direction in the input layer of the ANN, the new models that

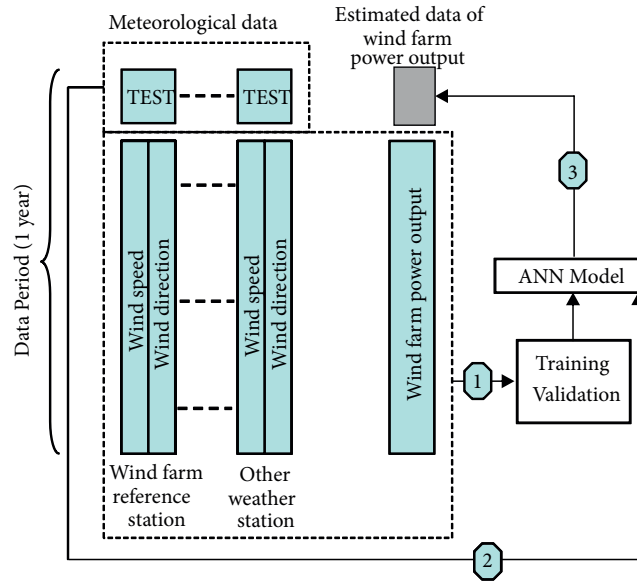


FIGURE 5: General layout of the methodology followed to obtain the adaptive wind farm power curves.

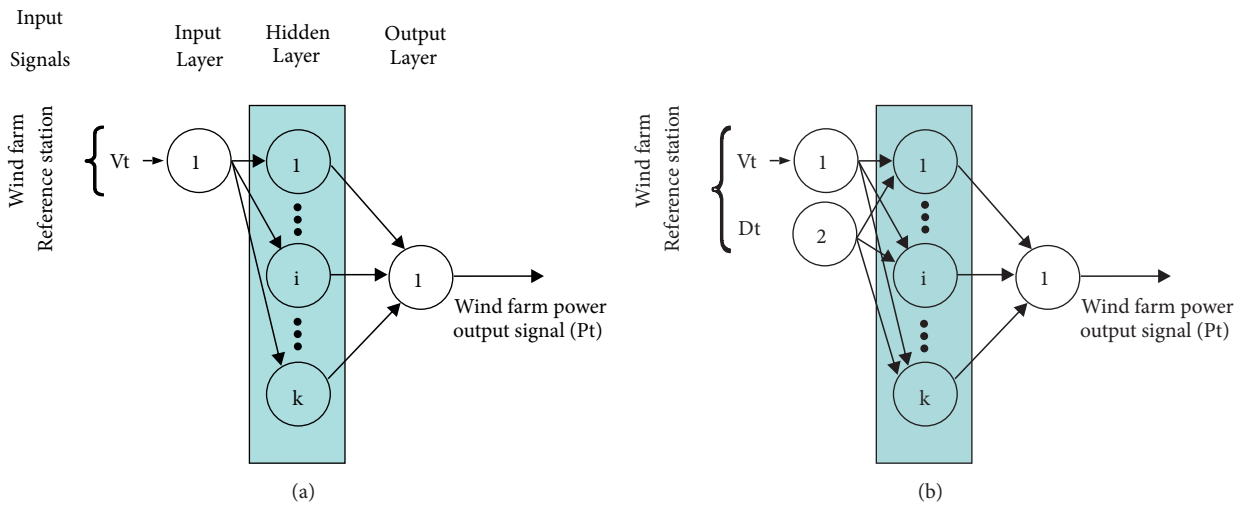


FIGURE 6: Schematic representation of the ANNs of the ADWFPC model when only wind speed is used in the input layer (option (a)) vs. when wind speed and direction are used (option (b)).

are generated for the WFs perform better than the original model. It can also be seen that the degree of improvement differs depending on whether the new model is applied to WF-1 or WF-2. For WF-1, and in relation to the MARE metric, a 2.2% improvement is found and for WF-2 the improvement is 4.3 times greater (9.4%).

4.2. Discussion of the Results for Case 2 (C2). The different simulations analysed in Case 2 were coded as shown in Table 5. The simulations coded as “C2-WF1 S0” and “C2-WF2 S0” correspond to the adaptive models obtained according to Case 1 (Figure 6(b)). These were compared with the remaining simulations, the wind farm power curve models which were obtained according to Case 2 (Figure 7).

Figures 9 and 10 show, respectively, the “MARE” and correlation coefficient “R” results obtained when applying the different models. For WF-1, it can be seen that the results obtained with the models developed for all the simulations of Case 2 were better than those obtained according to Case 1, option (b) (Table 4). The degree of improvement is independent of the correlation coefficient (Table 3) that exists between the reference WS of the WF and the additional WS. That is, a better value for the correlation coefficient does not directly imply a better degree of improvement. An example of this can be seen by comparing the results of the simulations C2-WF1 S3 and C2-WF1 S6.

For WF-2, the results obtained initially for Simulation 0 are already quite good, with a “MARE” below 0.1 and an IoA of 0.99. Even so, some of the models developed according

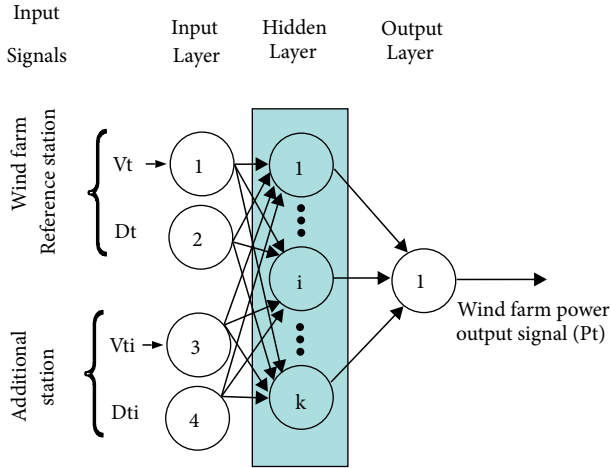


FIGURE 7: Schematic representation of the ANN of the ADWFPC model when the wind speed and direction data of a station other than the reference station of the wind farm are additionally incorporated.

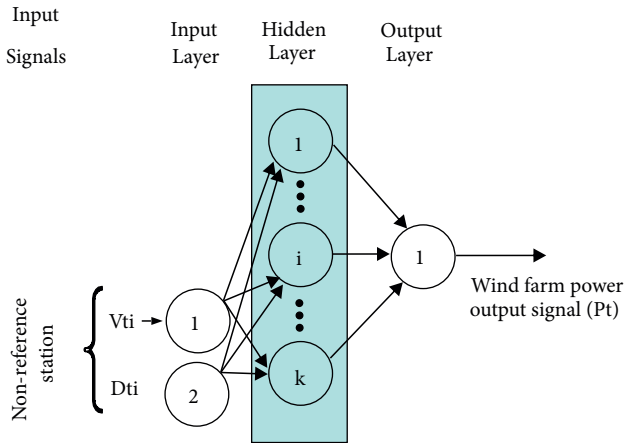


FIGURE 8: Schematic representation of the ANN used to generate the ADWFPC model when only using in the input layer the wind speed and direction of a WS other than the reference station of the WF.

to Case 2 improved on the initial result. More specifically, the “MARE” and “R” results with the Case 2 models for the C2-WF2 S4 and the C2-WF2 S6 were better than those obtained with the Case 1 models, option (b). As with WF-1, it is concluded that the degree of improvement in model efficiency is independent of the CC that exists between the reference WS of the WF and the additional WS.

Figure 11 shows the results obtained for “IoA” (4). The results follow the same general pattern seen for “MARE” and “R.” That is, for the case of WF-1, the results obtained with all the models of Case 2 were better than the initial result obtained with a single station (C2-WF1 S0). Similarly, it can be seen for WF-2 that the results obtained for C2-WF2 S4 and C2-WF2 S6 were better than the initial result.

4.3. *Discussion of the Results for Case 3.* For Case 3 and for each of the WFs, the adaptive models were generated using

TABLE 5: Simulations studied in Case 2.

Simulations for WF1	Simulations for WF2	Additional WS
C2-WF1 S0	C2-WF2 S0	None
C2-WF1 S1	C2-WF2 S1	WS-2
C2-WF1 S2	C2-WF2 S2	WS-3
C2-WF1 S3	C2-WF2 S3	WS-4
C2-WF1 S4	C2-WF2 S4	WS-5
C2-WF1 S5	C2-WF2 S5	WS-6
C2-WF1 S6	C2-WF2 S6	WS-7
C2-WF1 S7	C2-WF2 S7	WS-8

the meteorological data of a WS other than the reference stations. A total of 7 models were therefore obtained for each WF. Model performance according to Case 3 was then compared with that of the adaptive model obtained according to Case 1, option (b) (Figure 6(b)). For this purpose, the ratio was calculated between the IoA obtained for each of the models of Case 3 (C3-IoA) and that obtained for each of the models of Case 1 (C1-IoA). The results are shown in Figure 12. Represented on the x-axis is the CC between the WS used to generate the model other than the reference WSs and the actual reference WS of the WF.

It can be seen that the higher the CC the greater the degree of similarity between the ADWFPC models obtained according to Cases 1 and 3. For CC values above 0.7, the degree of similarity, expressed as the ratio between the IoAs, is above 0.9.

5. Conclusions

From the study undertaken in the present paper it can be deduced that when the meteorological data from an additional weather station other than the reference station of the wind farm (Case 2 of this study) are incorporated in the input layer of the neural network, the model performance can improve the results obtained for the original model (Case 1). For WF-1, model performance increased in 100% of the cases. It was also observed that the degree of improvement is independent of the correlation coefficient (CC) between the corresponding reference weather station of the wind farm and the additional weather station.

The conclusions obtained from the comparison of the models developed according to Cases 1 and 2 can serve as a reference for optimization of the performance of already developed power curve models in which only data from the reference weather station of the wind farm are used.

When the meteorological data from a weather station other than the reference station were used instead of the data of the actual reference station of the wind farm in the input layer of the ANN (Case 3), the degree of similarity between the results of the adaptive model obtained in this way and the results obtained with the adaptive model according to Case 1, option (b) (Figure 6(b)), increases with the CC between the wind speeds of the reference station and the nonreference station. For a CC over 0.7, the degree of similarity between the adaptive models obtained according to Cases 1 and 3 was

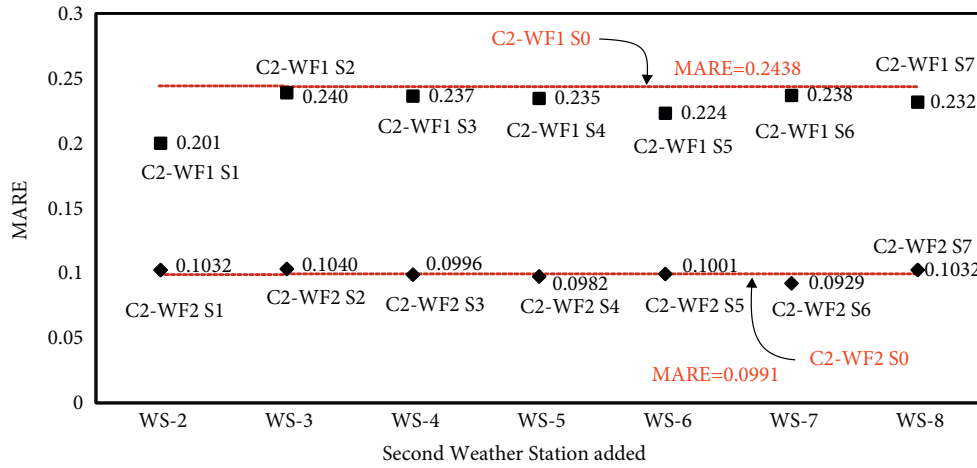


FIGURE 9: Comparison of the “MARE” results for Case 2 and Case 1 (C2-WF S0).

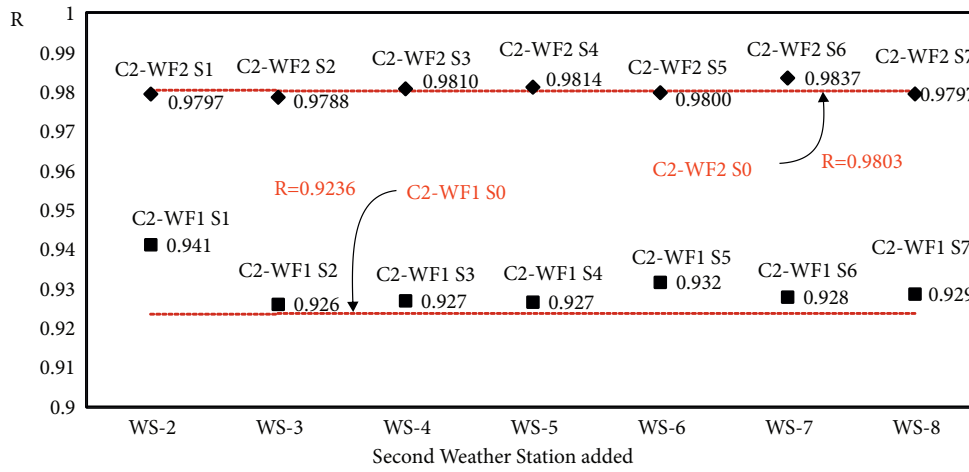


FIGURE 10: Comparison of the “R” results for Case 2 and Case 1 (C2-WF S0).

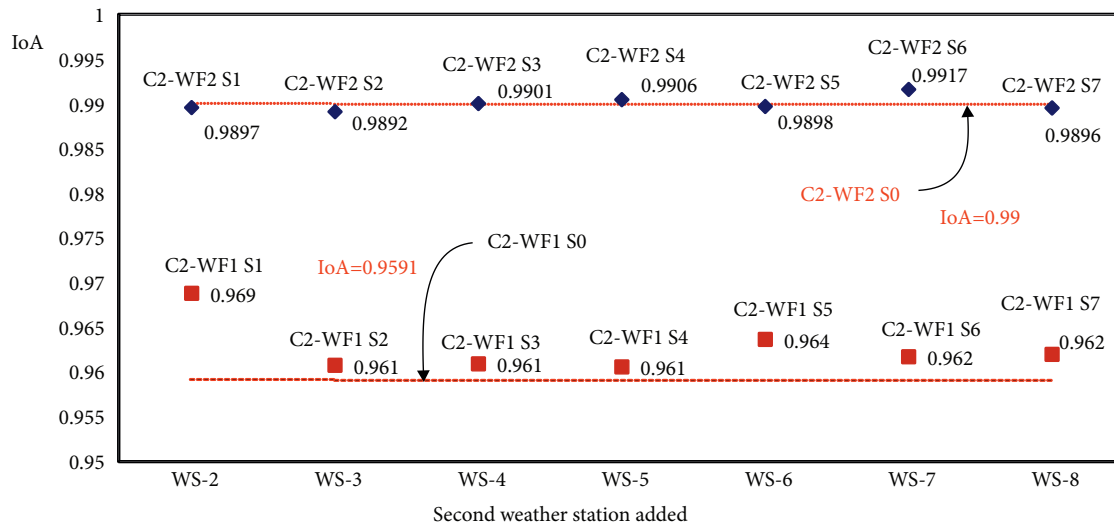


FIGURE 11: Comparison of the “IoA” results for Case 2 and Case 1 (C2-WF S0).

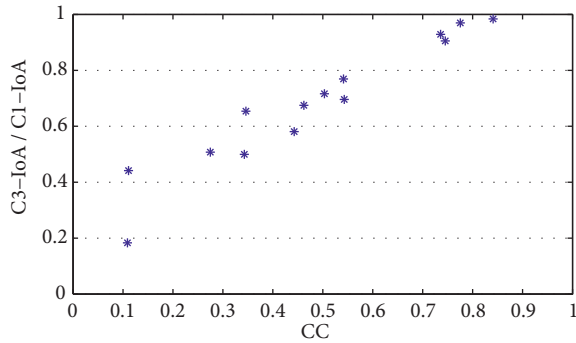


FIGURE 12: Comparison of the precision of the adaptive models calculated according to Cases 1 and 3.

above 0.9 (Figure 12). In this respect, it is possible to know the additional uncertainty when the power curve model is generated with data other than the data of the reference weather station of the wind farm.

Nomenclature

ANN:	Artificial neural network
CC:	Pearson's correlation coefficient between the wind speeds of different weather stations
IoA:	Index of Agreement
MARE:	Mean absolute relative error
ADWFPC:	Adaptive wind farm power curve
R:	Pearson's correlation coefficient between the estimated and observed values of the electrical power of a wind farm
WF-1:	Wind farm 1
WF-2:	Wind farm 2
WS:	Weather station
WT:	Wind turbine.

Data Availability

The wind farms data used to support the findings of this study were supplied by the owners under confidential terms and conditions and so cannot be made freely available. Requests for access to these data should be made to the following: Wind farm 1: Owner: Soslares Canarias, S.L. (<https://empresite.eleconomista.es/SOSLAIRES-CANARIAS.html>) Wind farm 2: Owner: Eólicas de Lanzarote, S.L. (<https://empresite.eleconomista.es/EOLICAS-LANZAROTE.html>). The meteorological data used to support the findings of this study are available from the corresponding author upon request.

Disclosure

No funding sources had any influence on study design, collection, analysis, or interpretation of data, manuscript preparation, or the decision to submit for publication.

Conflicts of Interest

The authors declare that there are no conflicts of interest.

Acknowledgments

This research has been cofunded by ERDF funds, INTERREG MAC 2014-2020 programme, within the ENERMAC project (MAC/1.1a/117).

References

- [1] A. V. Ntomaris and A. G. Bakirtzis, "Stochastic scheduling of hybrid power stations in insular power systems with high penetration," *IEEE Transactions on Power Systems*, vol. 31, no. 5, pp. 3424–3436, 2016.
- [2] D. Dhungana and R. Karki, "Data constrained adequacy assessment for wind resource planning," *IEEE Transactions on Sustainable Energy*, vol. 6, no. 1, pp. 219–227, 2015.
- [3] Y. Kuang, Y. Zhang, B. Zhou et al., "A review of renewable energy utilization in islands," *Renewable & Sustainable Energy Reviews*, vol. 59, pp. 504–513, 2016.
- [4] U. Portero, S. Velázquez, and J. A. Carta, "Sizing of a wind-hydro system using a reversible hydraulic facility with seawater. A case study in the Canary Islands," *Energy Conversion and Management*, vol. 106, pp. 1251–1263, 2015.
- [5] S. Wang, X. Zhang, L. Ge, and L. Wu, "2-D wind speed statistical model for reliability assessment of microgrid," *IEEE Transactions on Sustainable Energy*, vol. 7, no. 3, pp. 1159–1169, 2016.
- [6] I. González-Aparicio and A. Zucker, "Impact of wind power uncertainty forecasting on the market integration of wind energy in Spain," *Applied Energy*, vol. 159, pp. 334–349, 2015.
- [7] International Electrotechnical Commission (IEC), "Power performance measurements of electricity producing wind turbines," IEC 61400-12-1, 2005.
- [8] G. Bai, B. Fleck, and M. J. Zuo, "A stochastic power curve for wind turbines with reduced variability using conditional copula," *Wind Energy*, vol. 19, no. 8, pp. 1519–1534, 2016.
- [9] M. Lydia, S. S. Kumar, A. I. Selvakumar, and G. E. Prem Kumar, "A comprehensive review on wind turbine power curve modeling techniques," *Renewable & Sustainable Energy Reviews*, vol. 30, pp. 452–460, 2014.
- [10] A. Feijóo and D. Villanueva, "Wind farm power distribution function considering wake effects," *IEEE Transactions on Power Systems*, vol. 32, no. 4, pp. 3313–3314, 2017.
- [11] A. Feijóo and D. Villanueva, "Four-parameter models for wind farm power curves and power probability density functions," *IEEE Transactions on Sustainable Energy*, vol. 8, no. 4, pp. 1783–1784, 2017.
- [12] C. Carrillo, A. F. Obando Montaña, J. Cidrás, and E. Díaz-Dorado, "Review of power curve modelling for wind turbines," *Renewable & Sustainable Energy Reviews*, vol. 21, pp. 572–581, 2013.
- [13] D. Villanueva and A. Feijóo, "Normal-based model for true power curves of wind turbines," *IEEE Transactions on Sustainable Energy*, vol. 7, no. 3, pp. 1005–1011, 2016.
- [14] F. Pelletier, C. Masson, and A. Tahan, "Wind turbine power curve modelling using artificial neural network," *Journal of Renewable Energy*, vol. 89, pp. 207–214, 2016.

- [15] T. Ouyang, A. Kusiak, and Y. He, "Modeling wind-turbine power curve: a data partitioning and mining approach," *Journal of Renewable Energy*, vol. 102, pp. 1–8, 2017.
- [16] S. Jung, O. A. Vanli, and S.-D. Kwon, "Wind energy potential assessment considering the uncertainties due to limited data," *Applied Energy*, vol. 102, pp. 1492–1503, 2013.
- [17] L. Wang, A. C. Tan, M. Cholette, and Y. Gu, "Comparison of the effectiveness of analytical wake models for wind farm with constant and variable hub heights," *Energy Conversion and Management*, vol. 124, pp. 189–202, 2016.
- [18] S. Grassi, S. Junghans, and M. Raubal, "Assessment of the wake effect on the energy production of onshore wind farms using GIS," *Applied Energy*, vol. 136, pp. 827–837, 2014.
- [19] L. Martínez-Villaseñor, H. Ponce, J. A. Marmolejo-Saucedo, J. M. Ramírez, and A. Hernández, "Analysis of constraint-handling in metaheuristic approaches for the generation and transmission expansion planning problem with renewable energy," *Complexity*, vol. 2018, Article ID 1438196, 22 pages, 2018.
- [20] M. Deissenroth, M. Klein, K. Nienhaus, and M. Reeg, "Assessing the plurality of actors and policy interactions: agent-based modelling of renewable energy market integration," *Complexity*, vol. 2017, Article ID 7494313, 24 pages, 2017.
- [21] J. M. Torres and R. M. Aguilar, "Using deep learning to predict complex systems: a case study in wind farm generation," *Complexity*, vol. 2018, Article ID 9327536, 10 pages, 2018.
- [22] H. Jadhav and R. Roy, "Effect of turbine wake on optimal generation schedule and transmission losses in wind integrated power system," *Sustainable Energy Technologies and Assessments*, vol. 7, pp. 123–135, 2014.
- [23] S. Pookpant and W. Ongsakul, "Design of optimal wind farm configuration using a binary particle swarm optimization at Huasai district, Southern Thailand," *Energy Conversion and Management*, vol. 108, pp. 160–180, 2016.
- [24] L. Wang, A. C. Tan, M. E. Cholette, and Y. Gu, "Optimization of wind farm layout with complex land divisions," *Journal of Renewable Energy*, vol. 105, pp. 30–40, 2017.
- [25] M. You, B. Liu, E. Byon, S. Huang, and J. Jin, "Direction-dependent power curve modeling for multiple interacting wind turbines," *IEEE Transactions on Power Systems*, vol. 33, no. 2, pp. 1725–1733, 2018.
- [26] A. Marvuglia and A. Messineo, "Monitoring of wind farms' power curves using machine learning techniques," *Applied Energy*, vol. 98, pp. 574–583, 2012.
- [27] J. A. Carta, S. Velázquez, and P. Cabrera, "A review of measure-correlate-predict (MCP) methods used to estimate long-term wind characteristics at a target site," *Renewable & Sustainable Energy Reviews*, vol. 27, pp. 362–400, 2013.
- [28] J. A. Carta, P. Cabrera, J. M. Matías, and F. Castellano, "Comparison of feature selection methods using ANNs in MCP-wind speed methods. A case study," *Applied Energy*, vol. 158, pp. 490–507, 2015.
- [29] Canary Government, "Sistema de información territorial de Canarias (IDECanarias)" (Spanish), 2018, <http://visor.grafcan.es/visorweb/>.
- [30] Canary Government, "Technological institute of the Canary Islands (ITC - Instituto Tecnológico de Canarias)," 2018, <http://www.itccanarias.org/web/>.
- [31] Spanish Government, "Spanish state meteorological agency (AEMET - Agencia Española de Meteorología)," 2018, <http://www.aemet.es/es/en>.
- [32] Technological Institute of the Canary Islands (ITC - Instituto Tecnológico de Canarias), "Valoración de recursos energéticos renovables" (Spanish), 2018, http://www.itccanarias.org/web/actividades/eerr/recursos_energeticos.jsp?lang=en.
- [33] Technological Institute of the Canary Islands (ITC - Instituto Tecnológico de Canarias), "Recurso Eólico de Canarias" (Spanish), 2018, <http://www.itccanarias.org/recursoeolico/>.
- [34] J. C. Principe, N. R. Euliano, and W. C. Lefebvre, "Neural and adaptive systems," in *Fundamentals through Simulations*, John Wiley & Sons, Inc., New York, NY, USA, 1st edition, 2000.
- [35] T. Masters, *Practical Neural Network Recipes in C++*, Morgan Kaufmann Publishers, Calif, USA, 1st edition, 1993.
- [36] A. Oztopal, "Artificial neural network approach to spatial estimation of wind velocity," *Energy Conversion and Management*, vol. 47, pp. 395–406, 2006.
- [37] M. Monfared, H. Rastegar, and H. M. Kojabadi, "A new strategy for wind speed forecasting using artificial intelligent methods," *Journal of Renewable Energy*, vol. 34, no. 3, pp. 845–848, 2009.
- [38] N. R. Draper and H. Smith, *Applied Regression Analysis*, John Wiley & Sons, Inc, 1966.
- [39] Y. Zhao, L. Ye, W. Wang, H. Sun, Y. Ju, and Y. Tang, "Data-driven correction approach to refine power curve of wind farm under wind curtailment," *IEEE Transactions on Sustainable Energy*, vol. 9, no. 1, pp. 95–105, 2018.
- [40] C. J. Willmott, S. M. Robeson, and K. Matsuura, "A refined index of model performance," *International Journal of Climatology*, vol. 32, no. 13, pp. 2088–2094, 2012.
- [41] P. Brandimarte, *Quantitative Methods: An Introduction for Business Management*, Wiley, NJ, USA, 1st edition, 2011.
- [42] D. S. Wilks, *Statistical Methods in the Atmospheric Sciences*, Academic Press, USA, 3rd edition, 2011.

Research Article

Proposal of an Adaptive Neurofuzzy System to Control Flow Power in Distributed Generation Systems

Helbert Eduardo Espitia ¹, Iván Machón-González ²,
Hilario López-García,² and Guzmán Díaz²

¹Facultad de Ingeniería, Universidad Distrital Francisco José de Caldas, Bogotá, Colombia

²Departamento de Ingeniería Eléctrica, Electrónica de Computadores y Sistemas, Universidad de Oviedo, Campus de Viesques, Gijón/Xixón, Spain

Correspondence should be addressed to Helbert Eduardo Espitia; heespitiac@udistrital.edu.co

Received 21 October 2018; Revised 30 January 2019; Accepted 7 February 2019; Published 5 March 2019

Guest Editor: Aitor J. Garrido

Copyright © 2019 Helbert Eduardo Espitia et al. This is an open access article distributed under the Creative Commons Attribution License, which permits unrestricted use, distribution, and reproduction in any medium, provided the original work is properly cited.

Systems of distributed generation have shown to be a remarkable alternative to a rational use of energy. Nevertheless, the proper functioning of them still manifests a range of challenges, including both the adequate energy dispatch depending on the variability of consumption and the interaction between generators. This paper describes the implementation of an adaptive neurofuzzy system for voltage control, regarding the changes observed in the consumption within the distribution system. The proposed design employs two neurofuzzy systems, one for the plant dynamics identification and the other for control purposes. This focus optimizes the controller using the model achieved through the identification of the plant, whose changes are produced by charge variation; consequently, this process is adaptively performed. The results show the performance of the adaptive neurofuzzy system via statistical analysis.

1. Introduction

The increasing demands of energy, together with the associated costs, enhance the necessity of creating new energetic alternatives covering aspects such as the economic generation of energy and uninterrupted production. Distributed Generation (DG) has become an attractive method that offers electricity to consumers. This focus lowers the costs of installation of generators and the production of electricity; in addition, the electrical efficiency can also be improved using cogeneration [1]. Distributed energy resources have demonstrated potential advantages for use in energy generation and distribution [2].

Conventionally, electric energy systems consist of large interconnections characterized by a centralized high voltage generation and transmission over long distances. In recent years, a DG approach is being implemented to reduce energy losses in transmissions [3]. According to [4], electricity DG units located in adequate places (near to users) allow reducing

transmission losses and increasing the flexibility to the generation system using local renewable energy sources. A microgrid integrates heterogeneous distributed energy resources within the distribution system [5]. Microgrids represent a challenge that requires control techniques, automation, and computation for generation and distribution [6].

In terms of energy systems, resources of distributed energy, such as fuel cells, microturbines, wind generation, and photovoltaic systems, have a wide range of advantages [7, 8]. For instance, demands can be efficiently mitigated, increasing the reliability against failures in energy systems and improving the quality of those systems through sophisticated control schemes. The concept of microgrid has been proposed for solving common interconnection problems of individual DG in different energy systems [9]. A microgrid is defined as an independent grid power of low or medium voltage of distribution that operates in three different modes: connected to a power grid, isolated (autonomous), and transition mode [10].

Generator systems require to operate in the boundaries of design as complexity increases and doubts arise in terms of functioning, which also makes necessary more requirements in control systems [11, 12].

In relation to applied computational intelligence in energy distribution systems, reference [13] shows the design of an automatic voltage regulator using machine learning; this system is tested in distribution systems with 6 and 118 nodes. A related work can be seen in [14], where is proposed the use of reinforcement learning technique to implement a decentralized voltage control of the distribution network. Reinforcement learning is a method used to improve the agent action through several trials in an unknown environment.

According to [15], state estimation is fundamental to energy management in distribution systems; in this way, the authors develop a state estimation using artificial neural networks, to observe the system performance. The tests are made in distribution systems with 33 and 69 nodes where connection/disconnection of DG and load variation is considered.

An approach for power flow and voltage regulation using multiagents is proposed in [16, 17]. The attractive characteristic of multiagents is the distributive operation; related to this issue, [18] proposed a tool for agent simulation for decentralized control strategies in electrical distribution systems; this tool allows observing the emergent behavior produced by agents. Additionally, in [19] is presented a proposal based on consensus protocol for cooperative voltage control applied to wind farms. Another related work is shown in [20] where optimal control strategies are proposed for distributed photovoltaic systems which manage the energy flow among the energy system in a power grid to charge electric vehicles.

About other related applications of computational intelligence, [21] proposes the identification of a permanent magnet synchronous generator using neuronal networks. Regarding applications using fuzzy logic, reference [22] shows a fuzzy predictive control for a gas turbine used for the power generation process. Authors emphasize the relevance of advanced control strategies to satisfy the control demands of energy generation. Meanwhile, in [23] is proposed an adaptive fuzzy logic system for load frequency control of multiarea power system. Load frequency control consists of regulating the distribution system frequency in a specified value and maintains the interchange power between areas [23].

According to the above, the DG is a remarkable alternative for the generation of electricity; however, advanced control techniques are required for its operation. In this way, a proposal of a neurofuzzy adaptive approach for the regulation of voltage in a distribution system controlling the power flow is presented in this document. This adaptive control system allows having a distributed implementation of controllers such that without direct communication each controller can assimilate the effects of other controllers as well as load variations in the distribution system. In order to have a frame of reference, a description of the characteristics of the

neurofuzzy adaptive control and the model of a neurofuzzy controller used are provided below.

1.1. Characteristics of the Neurofuzzy Adaptive Control. From a biological perspective, adaptability refers to a capacity present in organisms, which allows them to survive in a particular environment; once the adaptation occurs, they prosper and produce offspring; otherwise, they may disappear [24]. According to [25] and [26], this principle may be applied in both optimization and adaptive intelligent control systems. Also [25] displays a proposal using bioinspired optimization algorithms in adaptive control systems. Moreover, in [26] the author points out that intelligent control represents the study to achieve automatic control through the emulation of biologic intelligent systems (biomimetic).

Taking into account [27], adaptive control systems are appropriate for monitoring and controlling systems with variable and unknown parameters. Besides, considering the training techniques associated with optimization methods, evolutionary algorithms have shown to be a useful tool to approach an optimum global value. However, they require several executions and a high number of evaluations of the objective function. Meanwhile, methods based on gradient calculations manifest a rapid convergence, although they are highly susceptible to the initial search point and show convergence towards local minima [28].

According to [25], techniques based on gradient calculations offer practical and effective methods to undertake online optimization in order to achieve all parameter adjustments in the control system. The basic approach consists of adjusting parameters iteratively to minimize the error. However, local minima are usually presented since, in general, the objective function that characterizes the error is not convex. According to [29], the gradient calculation is widely utilized in algorithms for neuronal systems, particularly the descending gradient method which is used for the Backpropagation algorithm for neuronal networks training [30].

Considering the above, an adequate option for improving the performance of the adaptive control system employing gradient-based algorithms consists of a suitable preliminary configuration for both identification of the plant and control; meanwhile, a fuzzy system allows the establishment of a preliminary structure and configuration of the system that is used for identification of the plant and the optimization of the control. This also allows dealing with the problems present when setting neuronal networks as well as parameter initialization [31]. In general, when using neuronal networks, the initial configuration is random, while a fuzzy system permits a previously set configuration based on a preliminary knowledge of the system. The initial configuration of fuzzy systems can be designed considering the general system behavior; then, training data is used to adjust the model of the plant and the controller. According to [27], when it comes to highly complex systems with uncertainty and variability, the adaptive feature is remarkably important.

The proposal made in this paper uses the compact fuzzy system shown in Section 3 which allows establishing an initial configuration (Figure 12); in this way, the optimization is

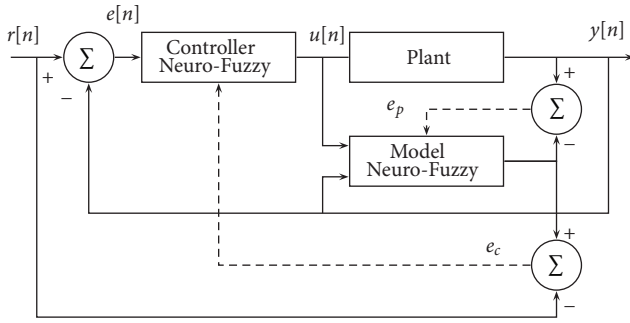


FIGURE 1: Control using a neurofuzzy system.

made via the gradient-descend method described in Section 4. This fuzzy system and optimization process are used in the control structure.

1.2. General Model of a Neurofuzzy Controller. Two neuro-fuzzy systems are implemented in this architecture, one for the controller and the other for the plant model. In such a scheme, firstly the plant identification is made and later the training of the controller. Figure 1 displays the neurofuzzy systems used.

As shown in Figure 1, the plant model has $u[n]$ as input and $y[n]$ as output signal, resulting in a structure given by (1).

$$y[n+1] = f_p(y[n], y[n-1], \dots, y[n-N_y], u[n], u[n-1], \dots, u[n-N_u]) \quad (1)$$

Meanwhile, for the input controller, the error signal is $e[n]$, the output to action control is $u[n]$, resulting in a general equation for the controller as

$$u[n+1] = f_c(u[n], u[n-1], \dots, u[n-N_u], e[n], \dots, e[n-N_e]) \quad (2)$$

where N_y represents the number of output delays, N_u the input delays, and N_e the error signal delays. Generally, the number of delays implemented increases with the order of the plant. Furthermore, the plant identification (distribution system) is necessary to perform the controller optimization.

The control model shown in Figure 1 is used for the distribution system, because the plant identification permits acquiring system information such as power flow, the interaction between generators and load variation. This characteristic, combined with an adaptive process, allows the controller adjustment when changes occur in the distribution system. The following section describes the adaptive process.

2. Description of the Neurofuzzy Adaptive System for the Generation System

Regarding the above, to implement an adaptive control system, the structure of the control system and the training methods must allow the parameter adjustments in the

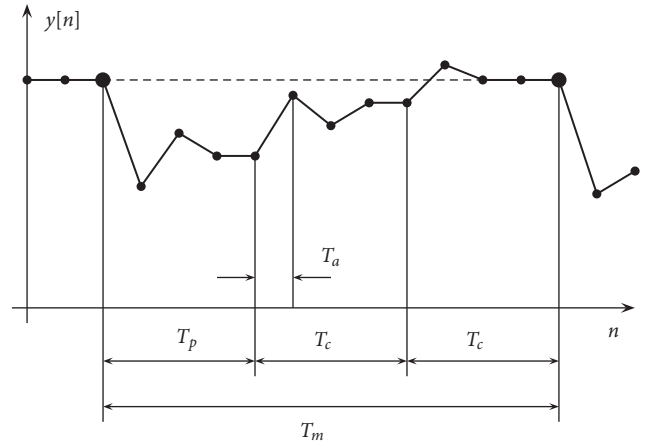


FIGURE 2: Times involved in the adaptation and control process.

required time according to the application. As previously highlighted, for plant identification and controller optimization, evolutionary algorithms may be implemented; however, the number of iterations is higher than a gradient-based algorithm [28, 32].

Fuzzy systems allow modeling nonlinear processes and obtaining information from a dataset using training algorithms. Unlike neuronal systems, those based on fuzzy logic allow an easy use of the knowledge of experts as a direct initial point for their optimization [33]. Meanwhile, fuzzy systems based on Boolean relations show a compact scheme, which facilitates the calculations associated with the inference process, having compact structures for the identification of the plant as well as the controller [34, 35].

2.1. Adaptive Control Process. For the implementation of the adaptive control system, the plant is first identified, then the training of the neurofuzzy controller is performed; this scheme integrates the model of the plant with the controller.

The time lapses involved during a cycle of the adaptation process appear in Figure 2, where T_p corresponds to the time of the controller operation after a change is present in the system; T_c represents the time when the system operates with the controller adjustment; T_m is the time interval in which the system presents variation. Finally, T_a is the time available to perform the adaptation process to identify the plant and the optimization of the controller. Moreover, in this specific case it is necessary to have adequate algorithms for the adaptation process in this lapse.

A graphical example of the neurofuzzy adaptive control process is presented using a radial net similar to the one considered in [36]. Summarizing, the adaptive process is as follows.

2.1.1. Initial Configuration. Here, based on knowledge of the system behavior, a general structure of fuzzy controller and plant model is established. Then, the plant identification is made, taking the nominal model (open loop) of the distribution network. Therefore, using the plant fuzzy model, the controller training is performed. Figures 3 and 4 show

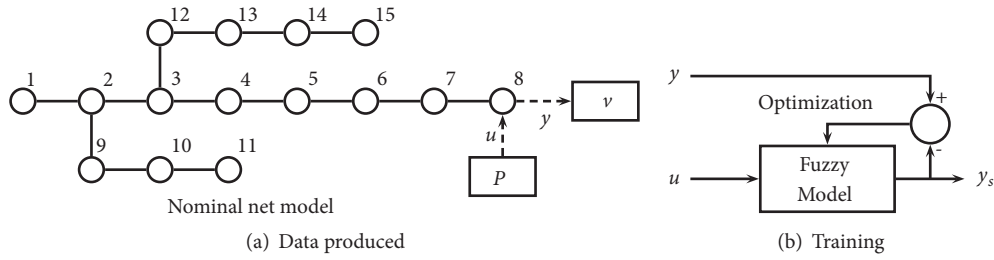


FIGURE 3: Plant identification using the grid nominal model.

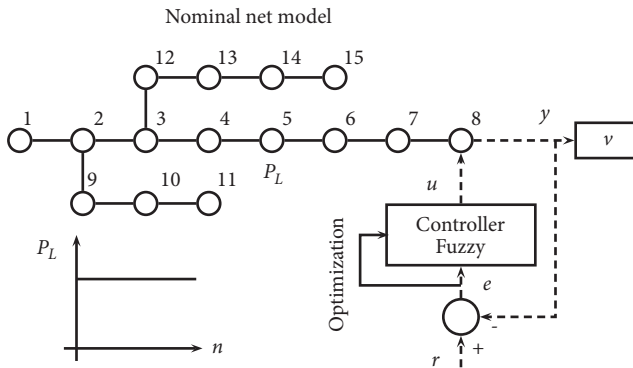


FIGURE 4: Training of the controller with the net nominal model.

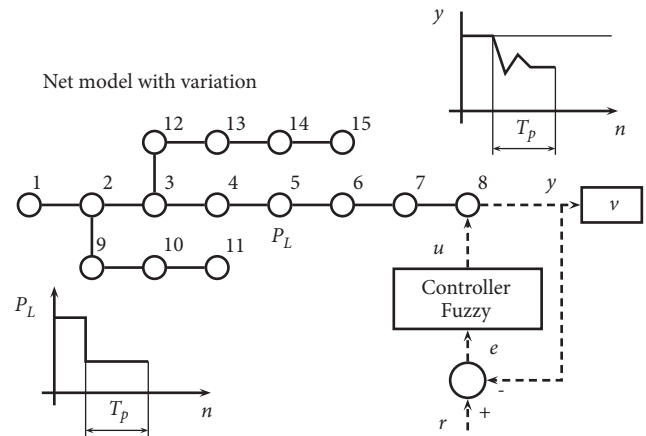


FIGURE 5: Operation of the control system when load variation occurs.

a representation of the process; in this way both initial configurations of the controller and the neurofuzzy model of the plant are obtained.

2.1.2. *Data Acquisition.* In this process, input-output data of the plant are obtained during the functioning of the system. An example of this step is given in Figure 5.

2.1.3. *Plant Adjustment.* The acquired data allow a new training of the neurofuzzy model of the plant in a way that parameters are adapted to the new data. Figure 6 displays this process.

2.1.4. *Controller Training.* With the new adjusted plant model, the training of the controller (optimization) is performed. Figure 7 shows the process example.

2.1.5. *Optimized Controller Operation.* During this process, the new controller (optimized) is activated to correct the variation in the system. Figure 8 shows an example of this process.

2.1.6. *Repeat Process.* The process is repeated from step 2 for the next time interval in a way that an iterative process for identification and training of the controller is performed. The example of this process is displayed in Figure 9.

Regarding the limited amount of data produced during the charge variation and the system response after the controller optimization, the process of plant identification and

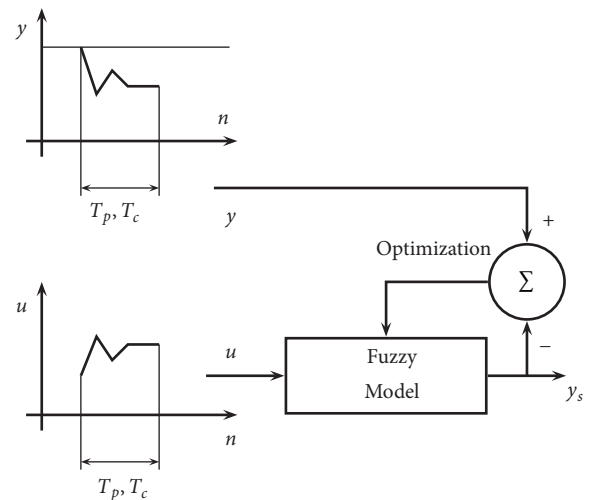


FIGURE 6: Plant model adjustment.

controller training is iteratively undertaken. It is noticeable the importance of establishing an initial search point to identify the plant and to optimize the controller when charge variation is present this is achieved with the neurofuzzy systems determined in the first point of the process.

2.2. *General Architecture for the Plant Model.* According to [37], an approach to obtain a model system consists of the

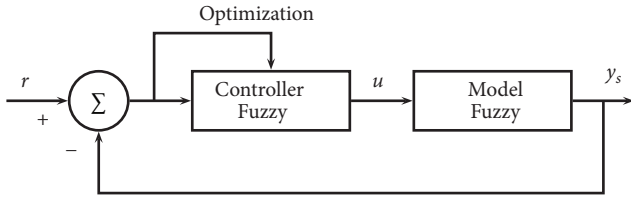


FIGURE 7: Controller training with the fuzzy plant model.

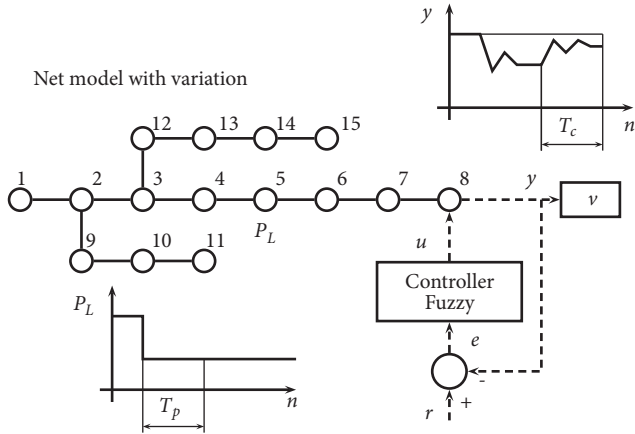


FIGURE 8: Operation of the system after the respective controller adjustment.

estimation of a structure working the same function of the plant. The input and output samples are taken from the plant to perform the identification using the neurofuzzy system in a way to perceive these signals as a nonlinear function. Figure 10 displays the basic scheme to identify the plant.

Considering Figure 10 the model for output $y_s[n + 1]$ is

$$y_s[n + 1] = f_p(y_s[n], \dots, y_s[n - N_y], u[n], \dots, u[n - N_u], \mathbf{H}_p) \quad (3)$$

where N_y is the number of previous output samples, N_u the number of previous input samples, and \mathbf{H}_p the system vector parameter to be optimized.

2.3. *General Architecture for Controller.* Considering $e[n]$ as the input of neurofuzzy controller, this can be represented as shown in Figure 11.

The controller equation with this structure is

$$u[n] = f_c(e[n], e[n - 1], \dots, e[n - N_e], u[n - 1], \dots, u[n - N_u], \mathbf{H}_c) \quad (4)$$

where N_e is the number of previous error samples and \mathbf{H}_c is the vector parameter for neurofuzzy controller.

3. Compact Fuzzy System for Control and Identification

The proposed compact fuzzy system used for identification and control is obtained modifying a linear system (in discrete

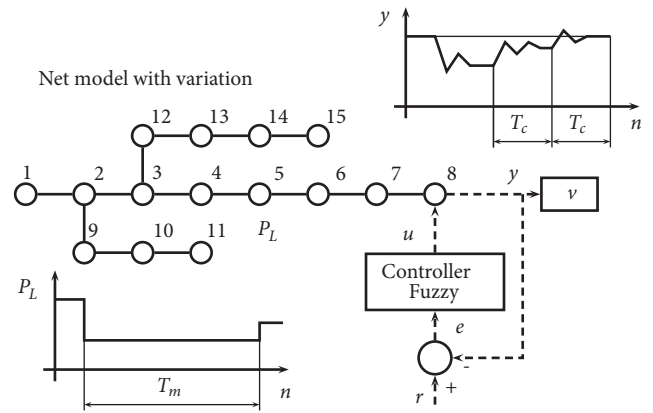


FIGURE 9: System operation after the second controller optimization.

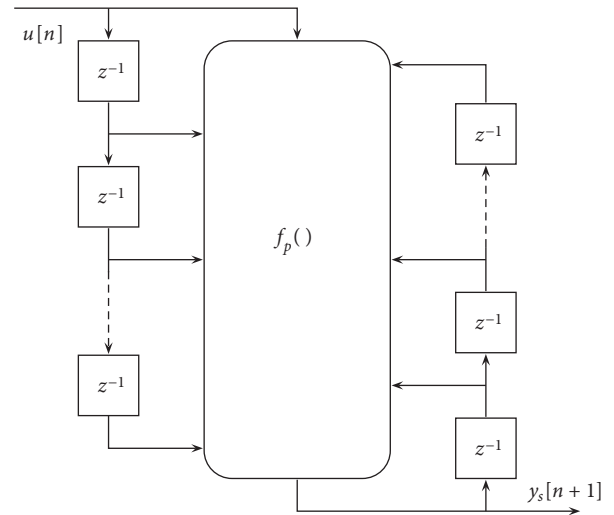


FIGURE 10: Scheme used for the plant identification.

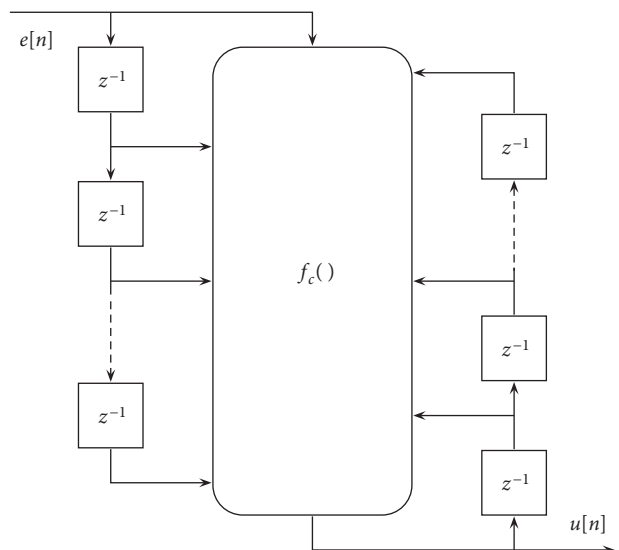


FIGURE 11: General architecture of the controller.

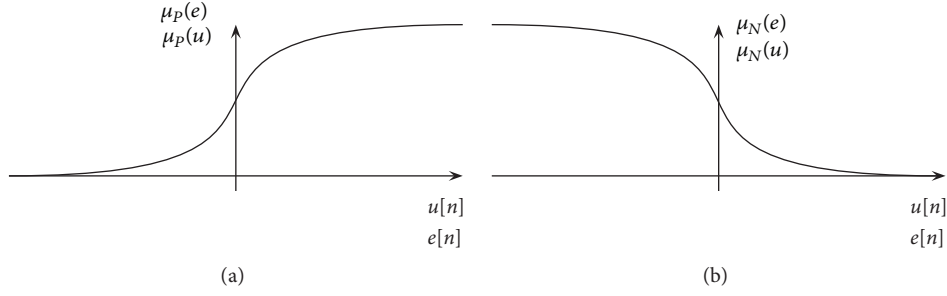


FIGURE 12: Membership functions employed.

time) using fuzzy sets to model nonlinear relations. The neurofuzzy architecture is obtained considering a general linear discrete-time system whose transfer function is

$$C(z) = \frac{U(z)}{E(z)} = \frac{b_0 + b_1 z^{-1} + b_2 z^{-2} + \dots + b_{N_e} z^{-N_e}}{1 + a_1 z^{-1} + a_2 z^{-2} + \dots + b_{N_u} z^{-N_u}} \quad (5)$$

The system equation in discrete time is

$$\begin{aligned} u[n] = & b_0 e[n] + b_1 e[n-1] + b_2 e[n-2] + \dots \\ & + b_j e[n-j] + \dots + b_{N_e} [n-N_e] - a_1 u[n-1] \\ & - a_2 u[n-2] - \dots - a_i u[n-i] - \dots \\ & - a_{N_u} u[n-N_u] \end{aligned} \quad (6)$$

where coefficients a_i , b_j are constant, while for the fuzzy system these constant values are replaced by nonlinear relations given by fuzzy membership so that

$$\begin{aligned} u[n] = & f_{e,0}(e[n]) + f_{e,1}(e[n-1]) + f_{e,2}(e[n-2]) \\ & + \dots + f_{e,N_e}(e[n-N_e]) - f_{u,1}(u[n-1]) \\ & - f_{u,2}(u[n-2]) - \dots - f_{u,N_u}(u[n-N_u]) \end{aligned} \quad (7)$$

The fuzzy sets displayed in Figure 12 are considered to implement the fuzzy system; particularly, Figure 12(a) presents a sigmoidal fuzzy set for modeling positive values in the universe of discourse; meanwhile, Figure 12(b) represents negative values.

Considering the fuzzy sets of Figure 12 and the general structure given by (7), Figure 13 provides the scheme of the proposed compact fuzzy system, where $g[n]$ is the input, $f[n]$ the output, p and q the number of output and input samples, respectively. According to Figures 10 and 11, the controller is implemented taking $f[n] = u[n]$ and $g[n] = e[n]$; meanwhile, the plant model uses the configuration $f[n] = y[n]$ and $g[n] = u[n]$.

Considering Figure 13 the fuzzy output system can be calculated as

$$f[n] = \sum_{i=1}^{p+q} \sum_{j=1}^2 v_{ij} \mu_{ij}(x_i) \quad (8)$$

where $x_i \in \{f[n-1], f[n-2], \dots, f[n-p], g[n], g[n-1], \dots, f[n-q], \dots\}$. Each input x_i has an associated function f_i given by

$$f_i = \sum_{j=1}^2 v_{ij} \mu_{ij}(x_i) = v_{i1} \mu_{i1}(x_i) + v_{i2} \mu_{i2}(x_i) \quad (9)$$

Meanwhile, the membership function $\mu_{ij}(x_i)$ is

$$\mu_{ij}(x_i) = \frac{1}{1 + e^{-\sigma_{ij}(x_i - \gamma_{ij})}} \quad (10)$$

Thus, the group of parameters corresponds to $\mathbf{H} \in \{v_{ij}, \gamma_{ij}, \sigma_{ij}\}$, which are the parameters to be optimized (adaptation parameters), being v_{ij} the virtual actuators, γ_{ij} the midpoint value of the sigmoidal function, and σ_{ij} the curve steepness. For plant identification \mathbf{H} corresponds to \mathbf{H}_p and \mathbf{H}_c to controller.

4. Fuzzy Systems Optimization Process

The gradient-descend method is used to implement the optimization; such process is performed until the desired value is achieved in the objective function. Consequently, Figure 14 shows the optimization scheme, by which the system is first evaluated with the parameters to be optimized. Then, the objective function is calculated using the system response. Finally, using gradient calculations, the system parameters adjustment is developed.

In this process the objective function is

$$J = \frac{1}{2} \sum_{n=1}^N [y_d[n] - y_s[n]]^2 \quad (11)$$

where N is the number of total data, y_d is the desired output, and y_s is the neurofuzzy system response. For identification process y_d corresponds to the plant data, y_s is the neurofuzzy output, and \vec{x} corresponds to the neurofuzzy vector parameter \mathbf{H}_p . Meanwhile, for controller optimization y_d corresponds to the reference $r[n]$, y_s is the simulated system control output, and \vec{x} is the controller vector parameter \mathbf{H}_c .

4.1. Gradient-Descend Method. This algorithm calculates the gradient of the objective function for a current position in the search space; then, the gradient of the objective function f is

$$\vec{G} = \vec{\nabla} f(\vec{x}) \quad (12)$$

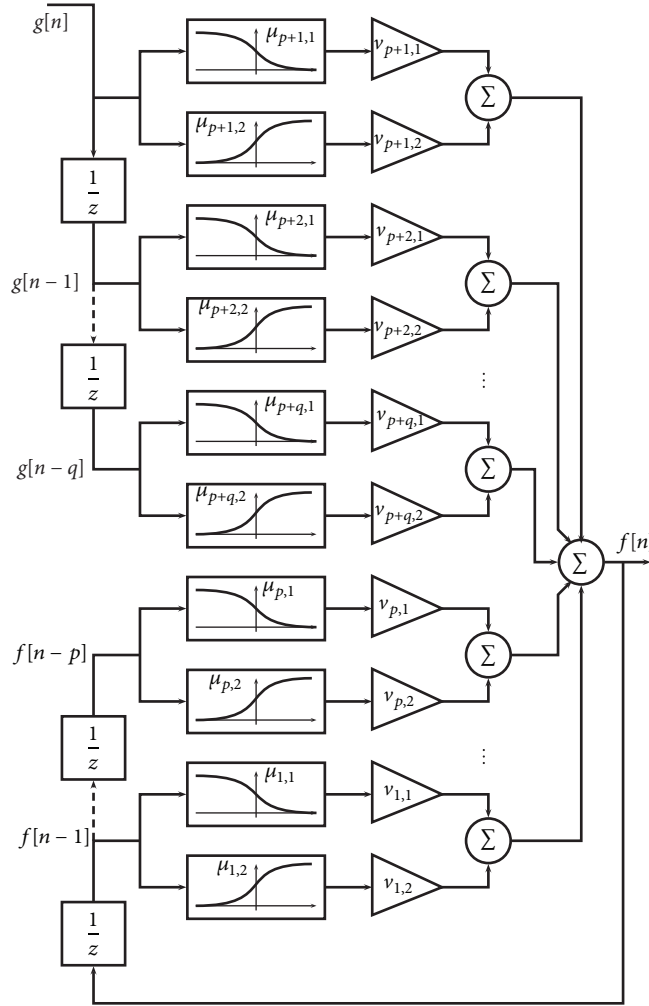


FIGURE 13: Compact fuzzy system.

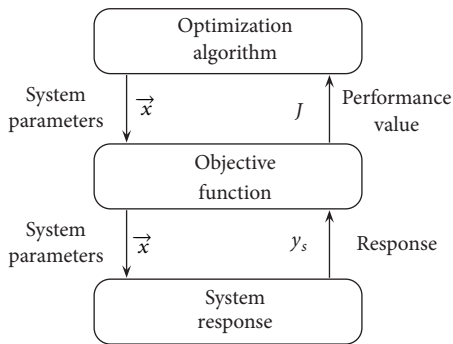


FIGURE 14: Optimization process.

Geometrically, vector \vec{G} points to the direction where the objective function has a bigger descent. If the step is small enough in the direction of $-\vec{G}$, then the value of the objective function in this new point will be smaller. The next position is calculated through

$$\vec{x}_{k+1} = \vec{x}_k - \eta \vec{G} \quad (13)$$

Here, $\eta \in \mathbb{R}^+$ is the descent rate. It is also possible to implement a sequence of values η_k which diminishes as k increases (for convergence). Using a higher learning rate the algorithm will move farther in a single step, taking the risk of going above a minimum.

Bold driver is another known variation of the algorithm; this technique modifies the learning rate while the objective function is minimized [38]. An implementation of this algorithm employs the following rule to update η :

$$\eta_{k+1} = \begin{cases} 1.1\eta_k, & \text{if } \Delta f \leq 0; \\ 0.5\eta_k, & \text{if } \Delta f > 0. \end{cases} \quad (14)$$

where $\Delta f = f(\vec{x}_k) - f(\vec{x}_{k-1})$ represents the change in the value of the objective function between steps $k - 1$ and k . If $\Delta f > 0$, then $\vec{x}_k = \vec{x}_{k-1}$ and it is reduced to half the learning rate, ensuring the algorithm avoids moving in an ascendant way [38]. In addition, the learning rate is

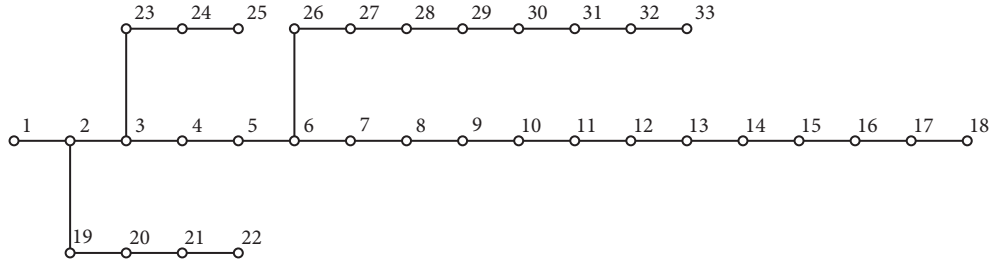


FIGURE 15: Model for the network considered.

continually increasing as the objective function decreases. Generally, the methods that use gradients as stopping criteria take a tolerance value $\epsilon \in \mathbb{R}^+$ so that

$$|\Delta f| \leq \epsilon \quad (15)$$

5. Energy Distribution System

5.1. Distribution Network Operator. Power distribution networks are a key constituent in the infrastructure as they permit carrying electricity to business and homes, offering a continuous service which is an essential function of the Distribution Network Operators (DNOs). The incorporation of Distributed Generation (DG) in the distribution networks carries out important effects in the distribution systems operation. The current distribution networks are designed to be passive, which leaves the transport of electricity with minimum surveillance, supervision, and control; likewise, these networks have been designed without the capacity to manage generators with lower voltage. Although DG introduces new challenges to DNOs, it also brings opportunities as economic benefits derived from more active networks [39].

5.2. Power Flow Calculation. In electrical engineering, the power flow study is an important tool for numeric analysis in energy systems [40]. Such studies are implemented to ensure that energy transfer from generators to consumers is stable, reliable, and economic. Moreover, flow power calculations allow determining power and tension values in a system of energy according to the capacity of regulation of the generators, condensers, and transformers [41]. The efficiency of the algorithms to establish the flow of power is fundamental whenever numerous estimations of this flow are required. In this regard, the Backward/Forward Sweep BFS is the most widely used technique for flow power calculation in radial topology networks.

5.3. Energy Distribution Model. Figure 15 shows the radial network model considered for the distribution system which also includes the nodes identification.

The system, which is taken from [42], consists of 33 nodes. The impedance values for the lines of the distribution system are shown in Table 1. Meanwhile, power charges are shown in Table 2. In the case of one generator, this is located in node 18 and the variable charge in node 17. For three generators these are placed in the nodes 18, 22, and 33. Additionally, variable

loads are held in the nodes 17, 21, and 32. Finally, the node of reference corresponds to number 1.

6. Methodology for the Analysis of Statistical Results

Given the stochastic nature of the system, variability of results may appear when a particular configuration of the control system is implemented. A test is performed to observe if a relevant difference in the results obtained is present (regarding the aspects to be compared); then, a statistical hypothesis is performed as follows:

- (i) H_0 Null hypothesis: the results obtained by the control systems exhibit equal average values.
- (ii) H_1 Alternative hypothesis: the results obtained by the control systems show no equal average values.

When formulating this hypothesis, there exists the possibility of making mistakes as shown in Table 3 in which error type I occurs when the null hypothesis is rejected even though it is true; meanwhile, for type II error the null hypothesis is accepted even though it is false [43].

Usually, the hypothesis test is performed considering a level of significance referred to as p -value which is the probability of making a type I error. Under this orientation, the null hypothesis is rejected if the statistical p -value test is equal to or less than an established significance level, which is in general 5% [43].

6.1. Statistical Tests. The statistical test can be classified as parametric or nonparametric in terms of their application. Parametric tests are robust but based on normality and data equality variance. On the other hand, suppositions are not required in nonparametric tests but information is missed in their process as the comparison is made with the representation of data on an ordinal scale [43].

Figure 16 shows the suggested methodology for the hypothesis test as follows:

- (i) Kolmogorov-Smirnov: this test is applied to determine the data normality. Besides, other alternative tests are the Shapiro-Wilk and the Anderson-Darling.
- (ii) Levene: through this test the variance equality (homoscedasticity) is established; another alternative is the Bartlett test.

TABLE I: Network impedances.

Line	Input bus	Output bus	Resistance	Reactance
1	1	2	0.0922	0.0470
2	2	3	0.4930	0.2511
3	3	4	0.3660	0.1864
4	4	5	0.3811	0.1941
5	5	6	0.8190	0.7070
6	6	7	0.1872	0.6188
7	7	8	0.7114	0.2351
8	8	9	1.0300	0.7400
9	9	10	1.0440	0.7400
10	10	11	0.1966	0.0650
11	11	12	0.3744	0.1238
12	12	13	1.4680	1.1550
13	13	14	0.5416	0.7129
14	14	15	0.5910	0.5260
15	15	16	0.7463	0.5450
16	16	17	1.2890	1.7210
17	17	18	0.7320	0.5740
18	2	19	0.1640	0.1565
19	19	20	1.5042	1.3554
20	20	21	0.4095	0.4784
21	21	22	0.7089	0.9373
22	3	23	0.4512	0.3083
23	23	24	0.8980	0.7091
24	24	25	0.8960	0.7011
25	6	26	0.2030	0.1034
26	26	27	0.2842	0.1447
27	27	28	1.0590	0.9337
28	28	29	0.8042	0.7006
29	29	30	0.5075	0.2585
30	30	31	0.9744	0.9630
31	31	32	0.3105	0.3619
32	32	33	0.3410	0.5302

- (iii) Welch: this test is used to compare several distributions. It is an extension of the T-student; this test requires data normality.
- (iv) ANOVA: this test compares several distributions and requires normality and homoscedasticity.
- (v) Kruskal-Wallis: it is a nonparametric test to compare several distributions; this test requires no previous suppositions.

Multiple tests of comparison are performed when having significant differences in experimental groups to determine such differences [44].

As in Figure 16, the same methodology is applied when assumptions of normality and homoscedasticity are fulfilled; here, Duncan and Newman-Keuls, Bonferroni, Scheff or HSD of Tukey contrasts can be used [43, 44]. Meanwhile, when these assumptions are not fulfilled, nonparametric contrasts of Nemenyi, Holm, and Bonferroni-Dunn are used [45–47].

The outcome of comparing the groups corresponds to “comparison intervals” which allow determining the difference between groups. A way to show such a result consists of graphically displaying the average ranking in each group and an equivalent interval; thus, with this representation, two groups are considered as different if their intervals are not overlapped [48].

7. Experimental Results

These results are directed to show the ability of adaptation of the neurofuzzy system proposed; whereby, the comparison is made with the fuzzy controller without adaptation.

According to [26], there are different alternatives to control, from the formal and traditional ones to those based on flexible computation and bioinspired systems. In addition, [27] this approach consists of showing the ability of adaptation present in these systems.

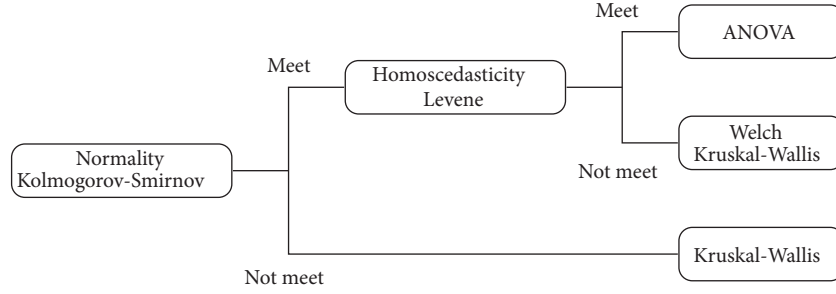


FIGURE 16: Methodology to determine the hypothesis test.

TABLE 2: Grid power charges.

Bus	Real	Reactive
1	0	0
2	100	60
3	90	40
4	120	80
5	60	30
6	60	20
7	200	100
8	200	100
9	60	20
10	60	20
11	45	30
12	60	35
13	60	35
14	120	80
15	60	10
16	60	20
17	60	20
18	90	40
19	90	40
20	90	40
21	90	40
22	90	40
23	90	50
24	420	200
25	420	200
26	60	25
27	60	25
28	60	20
29	120	70
30	200	600
31	150	70
32	210	100
33	60	40

The performance value used for comparison is the mean square error (MSE) which is also used as objective function for the controller optimization; the MSE value can be determined as

TABLE 3: Type I and II errors.

Decision \ Real condition	H_0 true	H_0 false
Reject H_0	Type I error	Right
Accept H_0	Right	Type II error

$$MSE = \frac{1}{N} \sum_{n=1}^N (r[n] - y[n])^2 \quad (16)$$

7.1. Experiments Configuration. Three aspects are considered to carry out the experimental design to observe the characteristics of the adaptive control system. A first comparison consists of regarding the controller performance with and without the adaptive process. Secondly, the configuration used for the control system considers the number of input and output delays (Figures 10 and 11). Considering the data of charge variation for each hour and using a scale of minutes, then, $T_m = 60min$ and $T_p = T_c = 20min$ are taken. On the other hand, the controller and the model of the plant have different configurations depending on the inputs and feedback. Table 4 shows the experimental configurations considered for both adaptive and nonadaptive cases.

Considering the stochastic characteristics of the system, each configuration must be executed several times to be statistically valid; thus, the analysis described in Section 6 can be performed [43].

A 10 times simulation of 10 hours is performed to determine the experimental data for each configuration; thereby, each simulation obtained consists of 600 minutes and 10 load changes. Likewise, data of charge are randomly generated with data distributed (uniformly) in values from 0 to 1000KW.

7.2. Results Using One Generator. In this case, the generator is located at node 18 and the charge (variable) at node 17. After carrying out the respective executions for each configuration, MSE is calculated. The results summary is shown in Table 5, including minimum and maximum values, standard deviation STD, and average value.

The respective tests are performed using the acquired data from the experiments. Table 6 shows both the results of the normality test in each experimental group and the accomplishment of the normality requirement.

TABLE 4: Experimental configurations.

Inputs	Feedbacks	Nonadaptive	Adaptive
1	2	CS1AD0	CS1AD1
2	2	CS2AD0	CS1AD1
1	3	CS3AD0	CS1AD1
2	3	CS4AD0	CS1AD1

TABLE 5: Summary of statistical values in the obtained results.

Configuration	Minimum	Maximum	STD	Mean
CS1AD0	0.0007138	0.0013849	0.0001969	0.00095738
CS2AD0	0.0007061	0.0013707	0.00019503	0.00094726
CS3AD0	0.00071098	0.0013793	0.00019609	0.00095358
CS4AD0	0.00070439	0.0013672	0.00019449	0.00094491
CS1AD1	7.3672×10^{-5}	0.00014293	2.0351×10^{-5}	9.8719×10^{-5}
CS2AD1	7.3218×10^{-5}	0.00014205	2.024×10^{-5}	9.8079×10^{-5}
CS3AD1	7.3305×10^{-5}	0.00014222	2.0249×10^{-5}	9.825×10^{-5}
CS4AD1	7.2702×10^{-5}	0.00014104	2.0086×10^{-5}	9.7411×10^{-5}

TABLE 6: Summary of normality test.

Configuration	p -value
CS1AD0	0.6230
CS2AD0	0.6223
CS3AD0	0.6231
CS4AD0	0.6225
CS1AD1	0.6258
CS2AD1	0.6241
CS3AD1	0.6262
CS4AD1	0.6247

The homoscedasticity test produces a p -value of 8.3068×10^{-6} which indicates that the equality variance requirement is not accomplished. Considering the results of homoscedasticity and normality test, a Kruskal-Wallis test is undertaken to determine if there exists a representative difference between the experimental groups. Then a p -value of 1.9486×10^{-10} is obtained, which indicates the presence of differences between groups. In this way, Figure 17 shows the nonparametric test of Bonferroni performed for multiple comparisons; the level of significance considered is 0.05.

If the intervals of two groups in Figure 17 are overlapped, then there is no statistical difference between them. These results show a better controller response when the process of adaptation is used.

7.2.1. Simulation Results. The configuration CS2AD1 is taken to qualitatively show the behavior of the control system. Figure 18 graphically displays the system response with the conventional controller and the adaptive system also shows that the controller adjusts the value of the system output to the reference value after a charge variation. Figure 18(a) shows the voltage regulation and Figure 18(b) displays the control signal corresponding to the amount of power to be delivered.

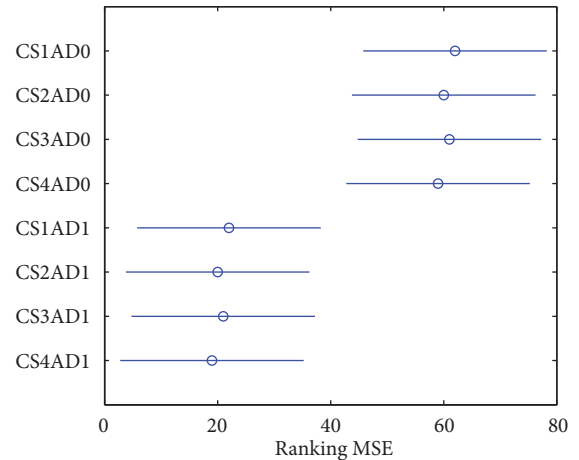


FIGURE 17: Multiple comparisons results.

Figure 19 shows the detailed adjustments made by the adaptive system. In the simulation, it is noticeable the time when the progressive adjustments of the controller are made to correct the change present when the charge has variance.

7.3. Results for Three Generators. A key aspect in the distributed generation systems is the capacity to plug and unplug several generators in the distribution network showing no major alterations among voltage values in the nodes. In order to observe the performance in the neuroadaptive control, different generators are included in the distribution network as shown in Figure 15. Consequently, three generators located in the following nodes are considered:

- (i) Generator 1: Node 18.
- (ii) Generator 2: Node 25.
- (iii) Generator 3: Node 33.

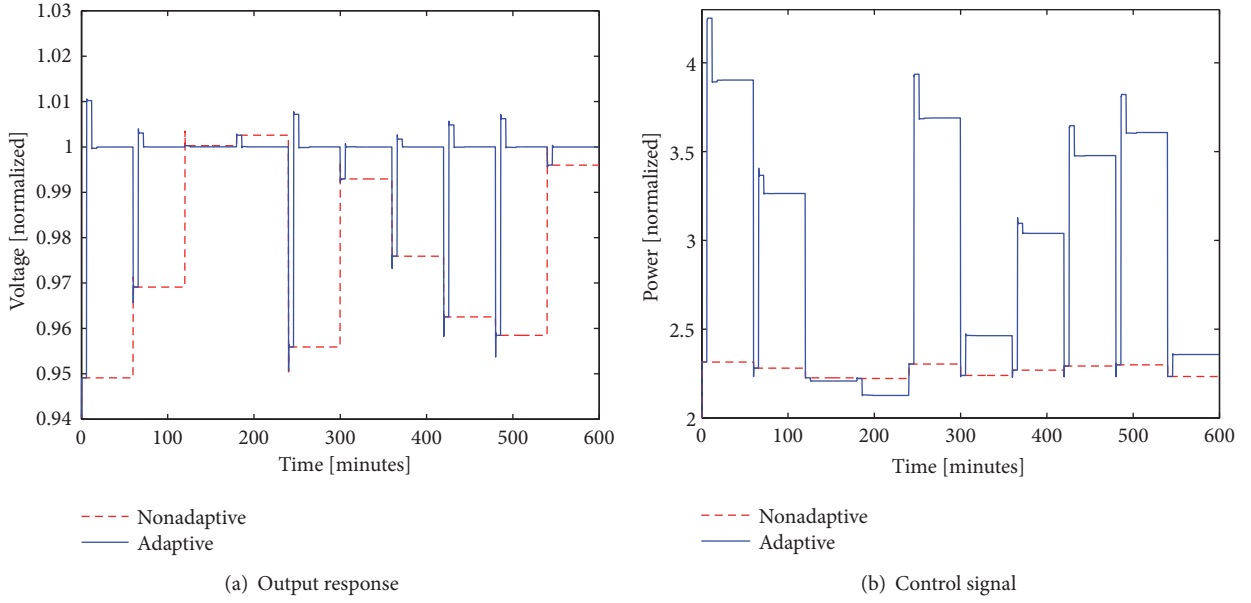


FIGURE 18: Control system response with and without adaptation process.

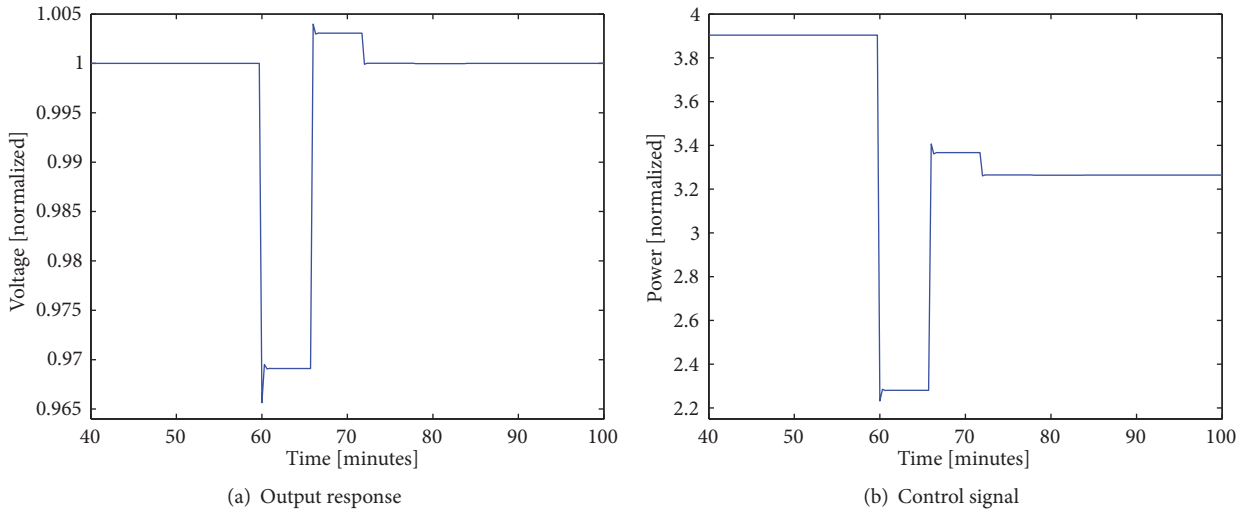


FIGURE 19: Detailed system response of the adaptive control system.

Meanwhile, there are nodes considered for charge variation:

- (i) Variable charge 1: Node 17.
- (ii) Variable charge 2: Node 24.
- (iii) Variable charge 3: Node 32.

Data for charge variation are evenly generated at random with values between 0KW and 1000KW. The experimental groups are taken in the same way as in the implementation for one generator. Considering that each generator has an associated value of mean square error (MSE), then the performance index used for the statistical analysis is the sum of MSE for three generators:

$$MSE_T = MSE_{G1} + MSE_{G2} + MSE_{G3} \quad (17)$$

Table 7 shows the minimum and maximum values, standard deviation STD, and average results for the 10 executions of each configuration.

With the data obtained the statistical tests can be made. The normality test results are shown in Table 8 in which the normality requirement is accomplished.

The p -value obtained for the homoscedasticity test is 8.3068×10^{-6} ; this indicates that equality of variance is not met. Regarding the results in the normality and homoscedasticity tests, the Kruskal-Wallis test is performed; as a result, the outcome value is 1.9486×10^{-10} . This shows the difference between experimental groups. The Bonferroni nonparametric test of multiple comparisons is then performed to establish differences between groups, using a significance level of 0.05. The results are displayed in Figure 20, where the

TABLE 7: Summary of statistical values of the results.

Configuration	Minimum	Maximum	STD	Mean
CS1AD0	0.0015202	0.0030316	0.00051718	0.0022923
CS2AD0	0.0015496	0.0030854	0.00052539	0.0023342
CS3AD0	0.001546	0.0030808	0.00052423	0.00233
CS4AD0	0.0015356	0.0030595	0.00052081	0.0023144
CS1AD1	8.3829×10^{-5}	0.00016181	2.6401×10^{-5}	0.00012498
CS2AD1	8.5712×10^{-5}	0.00016511	2.713×10^{-5}	0.00012664
CS3AD1	8.4852×10^{-5}	0.00016398	2.6979×10^{-5}	0.00012559
CS4AD1	8.4648×10^{-5}	0.00016333	2.687×10^{-5}	0.00012521

TABLE 8: Summary of normality test.

Configuration	p -value
CS1AD0	0.6230
CS2AD0	0.6223
CS3AD0	0.6231
CS4AD0	0.6225
CS1AD1	0.6258
CS2AD1	0.6241
CS3AD1	0.6262
CS4AD1	0.6247

statistical results show that the adaptive system has a better performance. No overlapping is present for the comparison intervals of adaptive and nonadaptive configurations. The configurations for the adaptive cases obtain lower values of MSE.

7.3.1. Simulation Results. The CS2AD1 configuration is used to show the control system simulation. Figure 21 shows the system response for three generators using adaptive control. Figures 21(a) and 21(b) show the voltage regulation and the control signals, respectively.

Meanwhile, Figure 22 presents the simulation when nonadaptive process is performed. It is worth noting that in Figure 21 the adaptive controller makes adjustments of the output system once the charge variation has occurred.

Figure 23 shows the adjustments made for the adaptive system when charge variation is present. It highlights that several adjustments are required to adjust the output. Figure 23(a) shows the voltage regulation detail and Figure 23(b) displays the respective control signals detail.

8. Discussion

This article is focused on showing the capabilities of the adaptive control system proposed to manage the flow of energy in a distribution system. It is seen that the proposed system is a good alternative to manage the power flow in the distribution network. However, there are several aspects of the distribution system which should be studied in subsequent works.

Taking into account the above, in this work the profile of the voltages throughout the network is not considered. Only

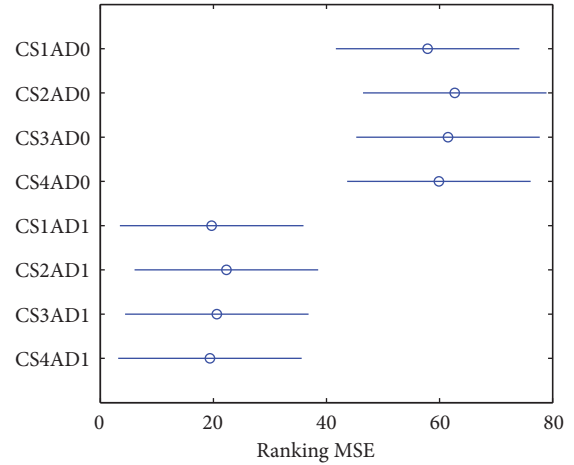


FIGURE 20: Results of multiple comparisons.

the voltages on the points are considered where the generators are located. This type of application might be studied in greater detail in future developments.

The charge and the generation power are considered only with the real component; therefore, for future works it is possible to include a complex power for load and generators.

Additionally, the generators connection in the grid is considered where the greatest voltage drop occurs. However, a further study can contemplate different locations of these, including their dynamic connection and disconnection.

9. Conclusions

The scheme of the neurofuzzy system was proposed considering the general structure of a discrete-time system. It is also noteworthy that the considered plant presents parameter variations as well as generators interaction.

The proposed neurofuzzy scheme allows the adjustment of the controller after a charge variation. The system works satisfactorily in three generators, which is important in systems of distributed generation.

The statistical analysis reflects a better performance when the adaptation process is made; it is also observed that there are no differences in the configuration sets considered (input-output delays) in the neurofuzzy system. For the simulation

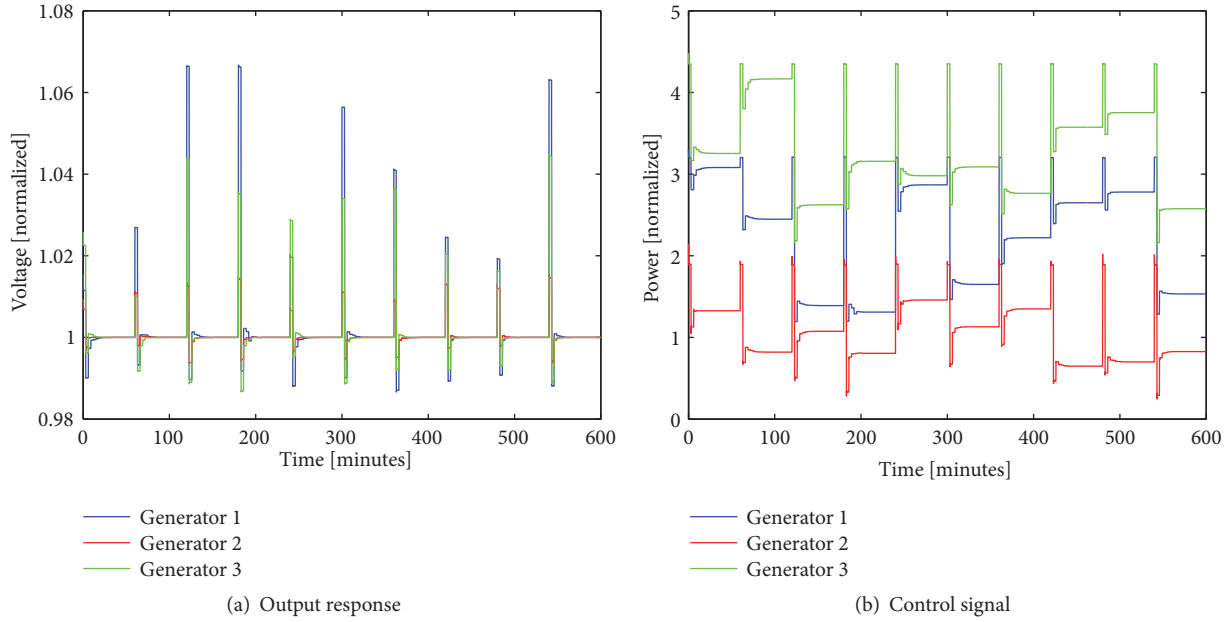


FIGURE 21: The response of the control system with adaptation process.

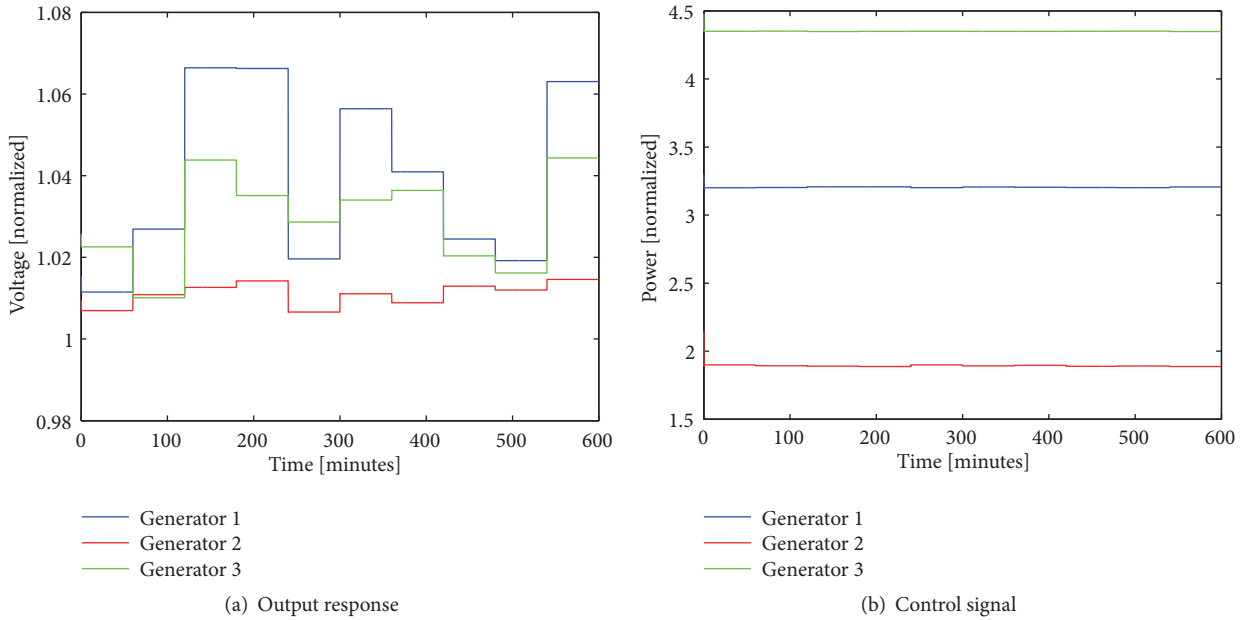


FIGURE 22: The response of the control system without the adaptation process.

case, when three generators are used, the several adjustments made after a load variation are worth highlighting.

The plant identification is highly relevant for the proper functioning of the adaptive control system; therefore, the progressive adjustment is made to identify the plant and controller optimization.

The strategy proposed allows handling the low amount of data available to identify the plant when the variation of the

charge is present. For that reason, it is also important to make iterative controller adjustments.

Data Availability

The data of this study are included within the supplementary information files.

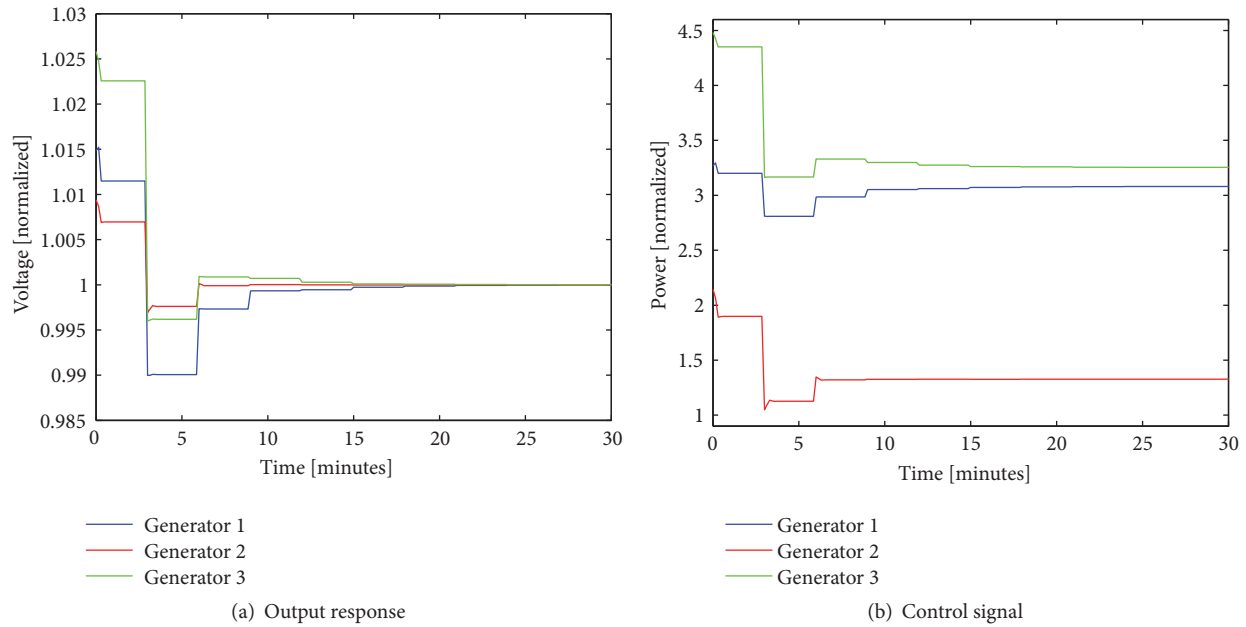


FIGURE 23: Detail of the adaptive control system response.

Conflicts of Interest

The authors declare that they have no conflicts of interest.

Acknowledgments

The proposal presented in this article is the result of a Ph.D. thesis at the Universidad de Oviedo. There is an additional acknowledgment of Universidad Distrital Francisco José de Caldas.

Supplementary Materials

The files correspond to the experimental results of Section 7, using one and three generators with the neurofuzzy system configurations shown in Table 4. Each file contains the results for the output signal and the control action. (*Supplementary Materials*)

References

- [1] R. C. Dugan, T. E. McDermott, and G. J. Ball, "Planning for distributed generation," *IEEE Industry Applications Magazine*, vol. 7, no. 2, pp. 80–88, 2001.
- [2] S. Abdollahy, O. Lavrova, and A. Mammoli, "Coordinated collaboration between heterogeneous distributed energy resources," *Journal of Solar Energy*, vol. 2014, Article ID 135106, 8 pages, 2014.
- [3] L. Mehigan, J. P. Deane, B. P. Ó. Gallachóir, and V. Bertsch, "A review of the role of distributed generation (DG) in future electricity systems," *Energy*, vol. 163, pp. 822–836, 2018.
- [4] Y. Ok and M. Atak, "Allocation of distributed energy systems at district-scale over wide areas for sustainable urban planning with a MILP model," *Mathematical Problems in Engineering*, vol. 2018, Article ID 4208415, 14 pages, 2018.
- [5] M. Rahimian, L. D. Iulo, and J. M. P. Duarte, "A review of predictive software for the design of community microgrids," *Journal of Engineering*, vol. 2018, Article ID 5350981, 13 pages, 2018.
- [6] C. Essayeh, M. Raiss El-Fenni, and H. Dahmouni, "Cost-effective energy usage in a microgrid using a learning algorithm," *Wireless Communications and Mobile Computing*, vol. 2018, Article ID 9106430, 11 pages, 2018.
- [7] H. Jiayi, J. Chuanwen, and X. Rong, "A review on distributed energy resources and MicroGrid," *Renewable & Sustainable Energy Reviews*, vol. 12, no. 9, pp. 2472–2483, 2008.
- [8] A. Khorshidi, M. Zolfaghari, and M. Hejazi, "Dynamic modeling and simulation of microturbine generating system for stability analysis in microgrid networks," *International Journal of Basic Sciences & Applied Research*, vol. 3, no. 9, pp. 663–670, 2014.
- [9] R. H. Lasseter and P. Paigi, "Microgrid: a conceptual solution," in *Proceedings of the IEEE 35th Annual Power Electronics Specialists Conference (PESC '04)*, pp. 4285–4290, June 2004.
- [10] A. G. Tsikalakis and N. D. Hatziargyriou, "Centralized control for optimizing microgrids operation," *IEEE Transactions on Energy Conversion*, vol. 23, no. 1, pp. 241–248, 2008.
- [11] T. H. Mohamed, A.-M. Mohammed Abdel-Rahim, A. A.-E. Hassan, and T. Hiyama, "Wide-area power system oscillation damping using model predictive control technique," *IEEE Transactions on Power and Energy*, vol. 131, no. 7, pp. 536–541, 2011.
- [12] Q. Liu, T. Mohamed, T. Kerdphol, and Y. Mitani, "PID-MPC based automatic voltage regulator design in wide-area interconnected power system," *International Journal of Emerging Technology and Advanced Engineering*, vol. 4, no. 8, pp. 412–417, 2014.
- [13] N. Tomin, V. Kurbatsky, D. Panasetsky, D. Sidorov, and A. Zhukov, "Voltage/VAR Control and Optimization: AI approach," *IFAC-PapersOnLine*, vol. 51, no. 28, pp. 103–108, 2018.

- [14] S. Takayama and A. Ishigame, "Autonomous decentralized control of distribution network voltage using reinforcement learning," *IFAC PapersOnLine*, vol. 51, no. 28, pp. 209–214, 2018.
- [15] F. Ahmad, M. Tariq, and A. Farooq, "A novel ANN-based distribution network state estimator," *International Journal of Electrical Power & Energy Systems*, vol. 107, pp. 200–212, 2019.
- [16] F. Z. Harmouch, N. Krami, and N. Hmina, "A multiagent based decentralized energy management system for power exchange minimization in microgrid cluster," *Sustainable Cities and Society*, vol. 40, pp. 416–427, 2018.
- [17] A. Bedawy and N. Yorino, "Reactive power control of DGs for distribution network voltage regulation using multi-agent system," *IFAC-PapersOnLine*, vol. 51, no. 28, pp. 528–533, 2018.
- [18] S. Kolen, S. Dähling, T. Isermann, and A. Monti, "Enabling the analysis of emergent behavior in future electrical distribution systems using agent-based modeling and simulation," *Complexity*, vol. 2018, Article ID 3469325, 16 pages, 2018.
- [19] Y. Guo, H. Gao, and Q. Wu, "Distributed cooperative voltage control of wind farms based on consensus protocol," *International Journal of Electrical Power & Energy Systems*, vol. 104, pp. 593–602, 2019.
- [20] Q. Zhong, Y. Sun, and L. Peng, "A novel control strategy on multiple-mode application of electric vehicle in distributed photovoltaic systems," *Complexity*, vol. 2018, Article ID 1640395, 11 pages, 2018.
- [21] H. E. Espitia and G. D. Gonzalez, "Identification of a Permanent Magnet Synchronous Generator using neuronal networks," in *Proceedings of the Workshop on Engineering Applications - International Congress on Engineering (WEA '15)*, pp. 1–5, Bogotá, Colombia, October 2015.
- [22] G. Hou, L. Gong, X. Dai, M. Wang, and C. Huang, "A novel fuzzy model predictive control of a gas turbine in the combined cycle unit," *Complexity*, vol. 2018, Article ID 6468517, pp. 1–18, 2018.
- [23] H. Yousef, "Adaptive fuzzy logic load frequency control of multi-area power system," *International Journal of Electrical Power & Energy Systems*, vol. 68, pp. 384–395, 2015.
- [24] A. Silverstein, V. Silverstein, and L. Silverstein, *Adaptation*, Twenty-First Century Books, 2007.
- [25] K. M. Passino, "Biomimicry of bacterial foraging for distributed optimization and control," *IEEE Control Systems Magazine*, vol. 22, no. 3, pp. 52–67, 2002.
- [26] K. Passino, *Biomimicry for Optimization, Control, and Automation*, Springer-Verlag, London, UK, 2005.
- [27] I. D. Landau, R. Lozano, M. M'Saad, and A. Karimi, *Adaptive Control, Algorithms, Analysis and Applications*, Springer, 2011.
- [28] R. Salomon, "Evolutionary algorithms and gradient search: Similarities and differences," *IEEE Transactions on Evolutionary Computation*, vol. 2, no. 2, pp. 45–55, 1998.
- [29] F. Ahmad, N. A. M. Isa, M. K. Osman, and Z. Hussain, "Performance comparison of gradient descent and genetic algorithm based artificial neural networks training," in *Proceedings of the 10th International Conference on Intelligent Systems Design and Applications (ISDA '10)*, pp. 604–609, December 2010.
- [30] V. N. P. Dao and R. Vemuri, "A performance comparison of different back propagation neural networks methods in computer network intrusion detection," *Differential Equations and Dynamical Systems*, vol. 10, 2002.
- [31] H. T. Nguyen, N. R. Prasad, C. L. Walker, and E. A. Walker, *A First Course in Fuzzy and Neural Control*, Chapman & Hall/CRC, 2003.
- [32] T. Weise, "Global optimization algorithms - theory and application," *Self-Published Thomas Weise*, 2009.
- [33] B. Del Brio and A. Sanz, *Redes Neuronales y Sistemas Difusos*, Alfaomega, Segunda Edición, 2006.
- [34] H. E. Espitia and J. J. Soriano, "Sistema de inferencia difusa basado en relaciones Booleanas," *Ingeniería*, vol. 15, no. 2, pp. 52–66, 2010.
- [35] H. E. Espitia, H. R. Chamorro, and J. J. Soriano, "Fuzzy controller design using concretion based on boolean relations (CBR)," in *Proceedings of the 12th UK Workshop on Computational Intelligence (UKCI '12)*, pp. 1–6, September 2012.
- [36] H. E. Espitia, G. Diaz Gonzalez, and S. I. Diaz, "Adaptive model for a variable load in a distribution network using a neuro-fuzzy system," in *Proceedings of the IEEE Workshop on Power Electronics and Power Quality Applications (PEPQA '17)*, pp. 1–7, Bogota, Colombia, May 2017.
- [37] O. Nelles, *Nonlinear System Identification: from Classical Approaches to Neural Networks and Fuzzy Models*, Springer Science & Business Media, 2013.
- [38] F. Van Den Bergh, *An Analysis of Particle Swarm Optimizers [PhD. Thesis]*, University of Pretoria, Doctor of Philosophy, 2001.
- [39] K. L. Anaya and M. G. Pollitt, *Distributed Generation: Opportunities for Distribution Network Operators, Wider Society and Generators*, Cambridge Working Paper in Economics CWPE-1505, 2015.
- [40] C. Sreenivasulu, G. Madhusudhana, and B. V. Sanker, "Reliable load flow solution for controlling power network by FACTS devices," *International Journal of Emerging Technology and Advanced Engineering*, vol. 3, no. 1, 2013.
- [41] K. Krushna and S. V. Jaya, "Three-phase unbalanced radial distribution load flow method," *International Refereed Journal of Engineering and Science*, vol. 1, no. 1, pp. 39–42, 2012.
- [42] G. Diaz, J. Gomez-Aleixandre, and J. Coto, "Direct backward/forward sweep algorithm for solving load power flows in AC droop-regulated microgrids," *IEEE Transactions on Smart Grid*, vol. 7, no. 5, pp. 2208–2217, 2016.
- [43] D. Montgomery, *Diseño y Análisis de Experimentos*, Limusa Wiley, 2003.
- [44] A. J. Arriaza, F. M. Fernández, A. López, M. Muñoz, S. Pérez, and A. Sánchez, "Estadística básica con R y R-Commander," *Servicio de Publicaciones de la Universidad de Cádiz*, 2008.
- [45] J. Demsar, "Statistical comparisons of classifiers over multiple data sets," *Journal of Machine Learning Research*, vol. 7, pp. 1–30, 2006.
- [46] S. Garcí and F. Herrera, "An extension on statistical comparisons of classifiers over multiple data sets for all pairwise comparisons," *Journal of Machine Learning Research*, vol. 9, 2008.
- [47] L. Moreno, *Texto y software en diseños experimentales no paramétricos más importantes*, Tesis profesional, Universidad de las Américas Puebla, México, 2005.
- [48] Y. Hochberg and A. Tamhane, *Multiple Comparison Procedures*, Wiley, New York, NY, USA, 1987.

Research Article

Multiobjective Optimization of a Fractional-Order PID Controller for Pumped Turbine Governing System Using an Improved NSGA-III Algorithm under Multiworking Conditions

Chu Zhang,^{1,2} Tian Peng ,¹ Chaoshun Li ,² Wenlong Fu ,³
Xin Xia,¹ and Xiaoming Xue¹

¹College of Automation, Huaiyin Institute of Technology, Huaian 223003, China

²School of Hydropower and Information Engineering, Huazhong University of Science and Technology, Wuhan 430074, China

³College of Electrical Engineering & New Energy, China Three Gorges University, Yichang 443002, China

Correspondence should be addressed to Tian Peng; husthydropt@126.com and Chaoshun Li; cslu@hust.edu.cn

Received 1 November 2018; Revised 19 December 2018; Accepted 6 February 2019; Published 27 February 2019

Guest Editor: Izaskun Garrido

Copyright © 2019 Chu Zhang et al. This is an open access article distributed under the Creative Commons Attribution License, which permits unrestricted use, distribution, and reproduction in any medium, provided the original work is properly cited.

In order to make the pump turbine governing system (PTGS) adaptable to the change of working conditions and suppress the frequency oscillation caused by the “S” characteristic area running at middle or low working water heads, the traditional single-objective optimization for fractional-order PID (FOPID) controller under single working conditions is extended to a multiobjective framework in this study. To establish the multiobjective FOPID controller optimization (MO-FOPID) problem under multiworking conditions, the integral of the time multiplied absolute error (ITAE) index of PTGS running at low and high working water heads is adopted as objective functions. An improved nondominated sorting genetic algorithm III based on Latin hypercube sampling and chaos theory (LCNSGA-III) is proposed to solve the optimization problem. The Latin hypercube sampling is adopted to generate well-distributed initial population and take full of the feasible domain while the chaos theory is introduced to enhance the global search and local exploration ability of the NSGA-III algorithm. The experimental results on eight test functions and a real-world PTGS have shown that the proposed multiobjective framework can improve the Pumped storage units' adaptability to changeable working conditions and the proposed LCNSGA-III algorithm is able to solve the MO-FOPID problem effectively.

1. Introduction

With the continuous expansion of the power system scale, the power grid's requirements for power quality, safety, and intelligence have been constantly improving. Pumped storage units (PSUs) have played an important role in maintaining the balance of power supply and demand because of their fast start-up and shutdown speed, flexible working condition conversion, excellent peak-load regulation, and frequency regulation ability [1–3]. Pump turbine governing system is the core control system of the pumped storage power station which is responsible for stabilizing the unit frequency and regulating the unit power [4, 5]. Due to the huge flow inertia

of the long-distance water pipeline and the existence of the unstable “S” characteristic area, the optimal control of PTGS is highly complex [6]. Therefore, it is of great theoretical value and practical significance to explore optimization methods for PTGS and research new control laws. The control quality of PSU and the dynamic response performance of PTGS can then be improved.

The classical Proportional-Integral-Derivative (PID) controller is widely used in the optimal control of PTGS because of its simple and reliable structure and easy adjustment of control parameters [7–10]. However, due to the strong non-linear characteristics of different parts of PSU and the changeable working conditions, the traditional PID controller often

fails to realize the global optimization of PTGS. The control problems of phase modulation instability and no-load frequency fluctuation are becoming increasingly prominent. As an extension of the classical PID controller, the fractional-order PID controller (FOPID) has attracted the attention of many scholars for its better adaptability and flexibility and greater potential to obtain better control performance [11–15]. Li et al. [16] proposed an improved gravitational search algorithm using the Cauchy and Gaussian mutations to adjust the parameters of the FOPID controller automatically. A number of tests have shown that the FOPID controller can improve the dynamic characteristics and stability of regulation frequency of PSUs. In Xu et al. [17], a robust nonfragile FOPID controller was proposed for PTGS. The parameters of the FOPID controller were selected using the bacterial foraging algorithm and multiscenario analysis functions. The FOPID controller turned out to have obtained higher robustness and stability compared with the traditional PID controller. And it can fully track the nonlinear characteristics of PTGS in the “S” area. Xu et al. [18] proposed an adaptively fast fuzzy fractional-order PID (AFFFOPID) control method for PSUs by combining a fuzzy fractional-order PD controller with a fuzzy fractional-order PI controller. Experiments of PTGS at various water heads under unload running condition have shown that the controller can effectively improve the performance and control quality of PSUs during the transient process.

Apart from the advantages of the FOPID compared with the PID controller, one of the most important and challenge issues of the employment of FOPID controller in PTGS is the optimal optimization of its parameters. With the continuous development of optimization algorithms and control theory in recent years, scholars have combined the FOPID controller with intelligent algorithms to achieve the optimal tuning of control parameters and improvement of control laws for PTGS [19]. The related works on optimal optimization for PID controller or hydroturbine governing system (HTGS) can also provide meaningful reference for the research of FOPID controller for PTGS. Fang et al. [20] developed an improved particle swarm optimization (PSO) algorithm for optimal tuning of PID control parameters for water turbine governor. Simulation results have demonstrated the stable convergence characteristic and good computational ability of the developed optimization stagey. Kou et al. [21] proposed a novel BFO-PSO algorithm by introducing PSO into the framework of the bacterial foraging optimization (BFO) algorithm to improve the control performance of the PID controller for HTGS. The advantages of the proposed algorithm to the BFO and PSO algorithms have been demonstrated through experiments at real working conditions. Wang et al. [22] proposed a three-stage start-up strategy for PSUs by opening guide vanes to a large opening degree firstly and then reducing the opening degree and finally switching to the PID controller. The switching time and PID control parameters are optimized synchronously using an integrated optimization scheme based on artificial sheep algorithm (ASA). Simulation results under various water heads have shown that the control strategy can shorten the start-up time and reduce the speed oscillation.

Some researchers have paid attention to multiobjective designing to consider multiobjectives that reflect the specific characteristics of the control system [23, 24]. Zamani et al. [25] developed a multiobjective cuckoo search approach to optimize the parameters of a FOPID controller. Sánchez et al. [26] proposed a multiobjective optimization strategy for identifying the optimal solution for a robust FOPID controller. Zhao et al. [27] proposed a parameter tuning scheme based on two *lbests* multiobjective PSO (2LB-MOPSO) to minimize the integral squared error and balanced robust performance criteria of a robust PID controller simultaneously. Chen et al. [28, 29] put forward a parameter tuning scheme to optimize the integral of the squared error (ISE) and the integral of the time multiplied squared error (ITSE) performance indices of PTGS simultaneously. The adaptive grid PSO (AGPSO) and the chaotic nondominated sorting genetic algorithm II (NSGA II) were adopted to realize the optimal control of the PID and the FOPID controllers, respectively. The proposed multiobjective PID and FOPID controller turned out to have achieved better control effects than the compared methods.

It is noticed that most of the research works on optimal control of the PID or FOPID controllers are designed under a single working condition. The traditional multiobjective optimization control usually adopts a set of objective functions to obtain the Pareto optimal solutions for a certain condition and then select the compromise optimal solution. The traditional multiobjective optimization control is essentially an optimization scheme for single working conditions. However, the characteristics of the controlled object of PTGS are not only related to the nonlinear characteristics of the pump turbine, the penstock system, the generator, and the other parts of PTGS but also vary with the changes of the working conditions. The optimal control of a single working condition is often at the expense of the deterioration of some other working conditions. The optimal control of PTGS under multiworking conditions should be a process of overall trade-off and cannot be limited to the pursuit of the optimal control under a certain working condition. In order to enhance the adaptability of PTGS to the change of working conditions, a multiobjective optimization framework which takes into account the integral of the time multiplied absolute error (ITAE) index of PTGS running at multiworking conditions is constructed. The nondominated sorting genetic algorithm III based on the Latin hypercube sampling and chaos theory (LCNSGA-III) is proposed to optimize the control parameters of the FOPID controller for PTGS under multiworking conditions.

The rest of this paper is arranged as follows: Section 2 gives a brief introduction to the multiobjective optimization problem; Section 3 builds the mathematical model of MO-FOPID under multiworking conditions; Section 4 proposes the LCNSGA-III algorithm based on Latin hypercube sampling and the chaos theory to solve the MO-FOPID problem; Section 5 employs eight benchmark functions and a real-world PTGS to verify the effectiveness of the LCNSGA-III algorithm and the developed multiobjective optimization framework; Section 6 gives the conclusions.

2. Multiobjective Optimization Problem (MOOP)

The purpose of the single-objective (SO) optimization problem is to obtain the optimal solution by searching for the minimum or maximum value of one single objective function. However, optimization problems in scientific research or engineering application usually contain not only one objective. These objectives are sometimes in concordance with each other, but sometimes there are conflicts between them. The objective of the multiobjective optimization problem (MOOP) is to search for the optimal solutions of all objectives, which is also known as the Pareto optimal solution [30]. A typical MOOP with D decision variables, N objective functions, and $m+k$ constraints can be described as follows:

$$\begin{aligned} \min \quad & F(X) = (\min f_1(x), \min f_2(x), \dots, \min f_i(x), \\ & \dots, \min f_N(x)) \\ \text{st.} \quad & \begin{cases} g_i(X) \geq 0, & i = 1, 2, \dots, m \\ h_j(X) = 0, & i = 1, 2, \dots, k \end{cases} \\ & X = [x_1, x_2, \dots, x_d, \dots, x_D,] \\ & x_{d_{\min}} \leq x_d \leq x_{d_{\max}} \quad d = 1, 2, \dots, D \end{aligned} \quad (1)$$

where X is the decision variable in D dimensions; $F(X)$ is the objective function in N dimensions; $g_i(X)$ represents the i th inequality equation; $h_j(X)$ represents the i th equality equation; $x_{d_{\min}}$ and $x_{d_{\max}}$ represent the upper and lower bounds of the d th decision variable, respectively.

To define the Pareto optimal solution, four definitions are given as follows.

Pareto Dominance Relationship. A vector $X^* = [x_1^*, x_2^*, \dots, x_d^*, \dots, x_D^*]$ is said to dominate $X = [x_1, x_2, \dots, x_d, \dots, x_D]$ (known as $X^* < X$) if and only if the following two conditions are satisfied:

$$\begin{aligned} \forall n, \quad & f_n(X^*) \leq f_n(X), \quad n = 1, 2, \dots, N, \\ \exists n_0, \quad & f_{n_0}(X^*) < f_{n_0}(X), \quad 1 \leq n_0 \leq N. \end{aligned} \quad (2)$$

Pareto Optimal Solution. Pareto optimal solution is a solution that cannot be dominated by any solution in the feasible region S which means that if and only if $\neg \exists X \in S : X < X^*$, X^* is the Pareto optimal solution.

Pareto Optimal Set. For a given MOOP, the Pareto optimal set P^* can be defined as

$$P^* = \{X^* \in S \mid \neg \exists X \in S : X < X^*\} \quad (3)$$

Pareto Optimal Front. For a given MOOP, the Pareto optimal front Pf^* can be described as

$$\begin{aligned} Pf^* = \{u = F(x) = (f_1(x), f_2(x), \dots, f_N(x))^T \mid X \\ \in P^*\} \end{aligned} \quad (4)$$

3. Problem Formulation of the MO-FOPID Problem under Multiworking Conditions

To formulate the multiobjective FOPID controller optimization problem (MO-FOPID) under multiworking conditions, the fractional calculus theory and fractional-order PID (FOPID) controller are first introduced.

3.1. Introduction to Fractional Calculus Theory and FOPID Controller. Fractional calculus theory is an extension of the traditional calculus theory to the fractional systems. The fractional calculus theory can describe complex systems in an easy way with a clear physical meaning. Among the various fractional calculus operators, the Laplacian transformation defined by Caputo is the most usual mathematical expression for calculating the fractional-order time derivatives and has been widely used in fractional-order PID controller [28, 31]. Given a continuous derivable function $f(t)$, Caputo's fractional derivative of order α can be defined as

$${}_0D_t^\alpha f(t) = \frac{1}{\Gamma(n-\alpha)} \int_0^t \frac{f^n(\tau)}{(t-\tau)^{\alpha+1-n}} d\tau \quad (5)$$

where ${}_0D_t^\alpha$ denotes the fractional calculus operator and $\Gamma(\cdot)$ denotes the Euler Gamma function.

Fractional calculus equations usually need to be transformed into algebraic equations. The Laplacian transformation of (5) under zero initial condition can be expressed as

$$\int_0^\infty e^{-st} D^\alpha f(t) dt = s^\alpha F(s) \quad (6)$$

In recent years, with the further research and development of fractional calculus theory, the combination of fractional calculus theory and modern control theory is becoming more and more popular. Controllers based on fractional calculus have been implemented and applied in many research fields [12, 25]. The Oustaloup recursive filter and its improved version have been widely adopted to realize the discretization approximation of the fractional calculus operator. The expression of the Oustaloup filter is as follows:

$$s^\alpha \approx K \prod_{k=-N}^N \left(\frac{s + \omega'_k}{s + \omega_k} \right) \quad (7)$$

where $\omega_k = \omega_b(\omega_h/\omega_b)^{(k+N+(1+\alpha)/2)/(2N+1)}$; $\omega'_k = \omega_b(\omega_h/\omega_b)^{(k+N+(1-\alpha)/2)/(2N+1)}$; $K = \omega_h^\alpha$; α denotes the order of the fractional calculus; $(2N+1)$ is the order of filter; (ω_b, ω_h) denotes the expected fitting range; N , ω_b , and ω_h are determined according to the accuracy requirement of the numerical approximation.

The FOPID controller proposed by Professor Podlubny [32] is an extension of the classical PID controller. Compared with the classical PID controller, the range of control rate of the FOPID controller is much wider. The transfer function of the FOPID controller is as follows:

$$\frac{U(s)}{E(s)} = K_p + \frac{K_i}{s^\lambda} + K_d s^u \quad (8)$$

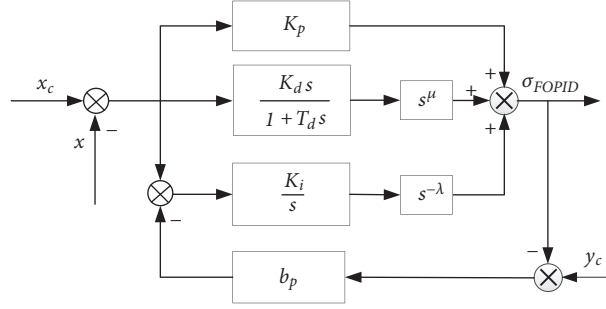


FIGURE 1: The structure of the FOPID controller for pumped turbine governing system.

where E denotes the control deviation; U denotes the controller output; K_p , K_i , and K_d represent the gain parameter, the integral order, and the differential order, respectively. The traditional PID controller is a special case of the FOPID controller when $\lambda = 1$ and $\mu = 1$. Because the integral and differential orders are variational, the FOPID controller has better adaptability and flexibility and bigger potential to obtain better control performance [33]. The structure of the FOPID controller for PTGS is shown in Figure 1. In Figure 1, x_c denotes the given unit speed; x denotes the unit speed; b_p denotes the permanent slip coefficient; T_d denotes the differential time constant; K_p , K_i , and K_d represent the proportional, integral, and differential gain coefficients of the controller, respectively; λ and μ denote the integral and differential orders of the controller, respectively.

3.2. Description of the PTGS System. PTGS is a complex nonlinear time-varying system of hydraulic, mechanical, and electrical connections. PTGS mainly contains five parts, namely, a controller, an electrohydraulic servomechanism system, a pump turbine, a generator, and a penstock system, where the controller and the servomechanism system consist of the speed governor of PTGS [4]. A PID controller has always been employed as part of the speed governor of PTGS. In this study, the FOPID controller is designed for PTGS. The FOPID controller has been described in Section 3.1. In what follows, transfer functions of the other four connectors are illuminated.

(1) Servomechanism System. Servomechanism is the actuator of the governor of PSU. It is made up of an auxiliary servomotor and a main servomotor of which the transfer functions are as follows:

$$G(s) = \frac{K_v}{1 + T_{y1}s} \quad (9)$$

$$G_v(s) = \frac{1}{T_y s}$$

where T_{y1} and K_v are the time constant and scale factor of the auxiliary servomotor, respectively, and T_y represents the main servomotor open-loop time constant.

(2) Pump Turbine. To reflect the complex nonlinear characteristics among water, machine, and electricity during the operation process accurately, the pump turbine model based on characteristic curves is constructed. The model of pump turbine is as follows:

$$M_{11} = f_M(a, N_{11}) \quad (10)$$

$$Q_{11} = f_Q(a, N_{11})$$

where M_{11} , Q_{11} , and N_{11} represent the unit torque, unit flow, and unit speed, respectively; a is the guide vane opening; f_M and f_Q denote the functions of the moment and flow characteristic curves, respectively. Because of the strong nonlinear characteristics of the flow and moment characteristic curves, the improved Suter transform is introduced to transfer the flow and moment characteristic curves into WH and WM characteristic curves, respectively [4]. The WH and WM characteristic curves of a pump turbine in a pumped storage power station in China using the improved Suter transform have been illustrated in Zhou et al. [4]. In this study, the WH and WM characteristic curves in two dimensions in [4] have been changed to three dimensions. The three-dimensional WH and WM characteristic curves are illustrated as in Figure 2.

(3) Generator. The common first-order model [6, 16, 18] is adopted in this study to balance the pump turbine torque and the generator torque. The transfer function of the first-order model is as follows:

$$G_g(s) = \frac{1}{T_a s + e_n} \quad (11)$$

where T_a and e_n are the inertia time constant and self-adjusting factor of the generator, respectively.

(4) Penstock System. Because of the fluid and tube wall elastic effects on the penstock, the second-order elastic water hammer model is exploited in this study by applying the second-order Taylor expansion on the nonlinear hyperbolic tangent function. The transfer function of the second-order elastic water hammer model is as follows:

$$G_h(s) = \frac{H(s)}{Q(s)} = \frac{-T_w s}{1 + 0.5 f T_r s + 0.125 T_r^2 s^2} \quad (12)$$

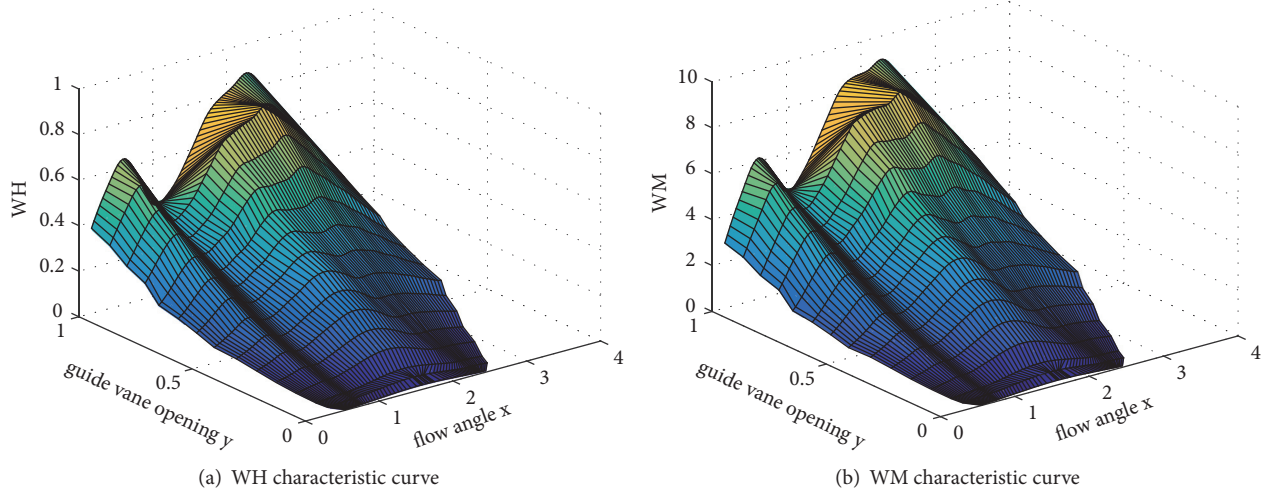


FIGURE 2: Three-dimensional surface of the characteristic curves of pump turbine.

where T_w denotes water flow inertia time constant, f represents the water head loss coefficient, and T_r is the reflection time of water hammer wave.

3.3. Multiobjective Optimization of FOPID Controller for PTGS. For single-optimization of the FOPID controller under a certain working condition, the ITAE [34, 35] is usually employed as the objective function to obtain satisfactory transient dynamic performance of the system. The ITAE index is defined as follows:

$$\text{ITAE} = \int_0^T t |e(t)| dt \quad (13)$$

where $e(t)$ denotes the relative deviation of the rotational speed of PTGS. The ITAE index considers the stable time and overshoot of the dynamic response of PTGS simultaneously. It can evaluate the speed and stability of the system at the same time. The smaller the ITAE, the better the speed and stability of the system.

When operating at the working condition of low water head, the PSU is easy to fall into the “S” characteristic region, resulting in oscillation of the unit speed near the rated frequency. The working condition of medium or high water head, in the other way, is the most common working condition in the operation process of PSU. The optimal control of PTGS under different working conditions should be considered and researched to make the PTGS system better adapt to the changeable working environment. However, the ITAE for PTGS at working condition of low head (referred as ITAE_1) and that of high head (referred as ITAE_2) usually influence and restrict each other. In this study, the single-objective optimization of the FOPID controller for PTGS is expanded to multiobjective theoretical framework to find a compromise solution and ensure that the PTGS system can achieve relatively better control performance under changeable working conditions. To formulate the MO-FOPID problem, the ITAE_1 and ITAE_2 are adopted as objective functions. The five parameters of the FOPID

controller for PTGS including the proportional coefficient K_p , the integral coefficient K_i , the differential coefficient K_d , the integral order λ , and the differential order μ are taken as decision variables. The MO-FOPID problem can then be formulated as

$$\text{Min} \quad \begin{cases} f_1 = \text{ITAE}_1 = f_1(K_p, K_i, K_d, \lambda, \mu) \\ f_2 = \text{ITAE}_2 = f_2(K_p, K_i, K_d, \lambda, \mu) \end{cases} \quad (14)$$

$$\text{subject to} \quad \begin{cases} K_{p\min} \leq K_p \leq K_{p\max} \\ K_{i\min} \leq K_i \leq K_{i\max} \\ K_{d\min} \leq K_d \leq K_{d\max} \\ \lambda_{\min} \leq \lambda \leq \lambda_{\max} \\ \mu_{\min} \leq \mu \leq \mu_{\max} \end{cases} \quad (15)$$

where $f_1(\cdot)$ and $f_2(\cdot)$ are functions of $K_p, K_i, K_d, \lambda, \mu$ at working condition of low water head and high water head, respectively. X_{\min} and X_{\max} are the lower and upper bounds of $K_p, K_i, K_d, \lambda, \mu$ of the FOPID controller, respectively.

4. Nondominated Sorting Genetic Algorithm-III Based on Latin-Hypercube Sampling and Chaos Theory (LCNSGA-III)

An improved version of NSGA-III based on Latin-hypercube sampling and chaos theory is developed to solve the proposed MO-FOPID problem under multiworking conditions.

4.1. Brief Introduction to NSGA-III. The NSGA-III algorithm [36], first introduced by Deb and Jain in 2014, is a novel reference-point-based nondominated sorting genetic algorithm following the NSGA-II framework. Unlike the crowding distance operator exploited in NSGA-II [37], NSGA-III employed a reference point-based mechanism to make the Pareto optimal front well-distributed. The step-to-step

procedures of the NSGA-III algorithm can be expressed as follows.

Step 1. Calculate the number of reference points (H) to be placed on the hyper-plane.

$$H = \binom{C + g - 1}{g} \quad (16)$$

where C represents the number of objective functions and g denotes the number of divisions (For $C = 3$ and $g = 4$, H is calculated as 15).

Step 2. Generate NP individuals in the feasible region randomly to form the initial population of the NSGA-III algorithm, and record it as P_k . Set the iteration number as $k = 1$.

Step 3. Generate the offspring population Q_k using the simulation binary crossover (SBX) operator and polynomial mutation operator.

Step 4. Let $R_k = Q_k \cup P_k$ and calculate the fitness value of each individual in R_k .

Step 5. Identify the nondominated level F_1, F_2, \dots, F_t for each individual in R_k using the nondominated sorting operator.

Step 6. Normalize the objectives and associate the solutions in R_k with the reference points. Delete the useless reference points and preserve solutions with higher rankings according to the niche preservation strategy to construct the next generation of population P_{k+1} .

Step 7. If $k < G_{\max}$, skip to Step 3; else stop iteration and output the Pareto optimal set.

The crossover and mutation operators in Step 3 and the nondominated sorting operator in Step 5 of the NSGA-III algorithm are the same as those of the NSGA-II algorithm. In Step 6, the NSGA-III algorithm generates the next population using the reference point-based selection mechanism other than the crowding distance operator of NSGA-II. Readers can refer to [36] for more details about NSGA-III. The improvements of the NSGA-III algorithms including the Latin hypercube sampling-based initialization technique and the chaotic crossover and mutation operators are introduced in the following subsections.

4.2. Latin Hypercube Sampling Based Initialization Technique.

NSGA-III generates the initial values of the decision variables in the feasible region randomly to form the initial population of the algorithm. However, a large number of individuals may assemble into a local area of the feasible region because of the random initiation, leading to premature convergence in the iterative process. In order to make the individuals of the initial population well-distributed in the feasible region, the Latin hypercube sampling based initialization technique [38] is introduced to NSGA-III to improve its search performance.

The brief steps to generate the initial population of NSGA-III using Latin hypercube sampling are as follows.

Step 1. Suppose the size of the population is N and each individual in the population contains L discrete elements. The range of the discrete element x_l , $l = 1, 2, \dots, L$ of individual x can be divided into N equal mini zones:

$$x_{l,\min} = x_l^0 < x_l^1 < \dots < x_l^j < \dots < x_l^N = x_{l,\max} \quad (17)$$

where $P(x_l^j < x < x_l^{j+1}) = 1/N$ and the value space of x can be divided into N^L small hypercubes finally.

Step 2. Generate a matrix M of which the dimension is $N \times L$, and every column of M is the full permutation of $\{1, 2, \dots, N\}$.

Step 3. Generate an individual in each row of M randomly; an initial population with N individuals is then generated.

4.3. Chaotic Crossover and Mutation Operators. The NSGA-III algorithm generates a random number r_c to determine whether to apply the crossover operator or not. The SBX operator is implemented when $r_c < \eta_c$, where η_c represents the crossover distribution index. For two parent individuals $x_{p1} = \{x_{p1}^1, \dots, x_{p1}^i, \dots, x_{p1}^n\}$ and $x_{p2} = \{x_{p2}^1, \dots, x_{p2}^i, \dots, x_{p2}^n\}$, the NSGA-III algorithm generates two offspring individuals $x_{c1} = \{x_{c1}^1, \dots, x_{c1}^i, \dots, x_{c1}^n\}$ and $x_{c2} = \{x_{c2}^1, \dots, x_{c2}^i, \dots, x_{c2}^n\}$ according to the following:

$$x_{c1}^i = \frac{1}{2} \left[(1 - \beta) x_{p1}^i + (1 + \beta) x_{p2}^i \right] \quad (18)$$

$$x_{c2}^i = \frac{1}{2} \left[(1 + \beta) x_{p1}^i + (1 - \beta) x_{p2}^i \right]$$

where β represents the crossover coefficient. β can be calculated according to the following:

$$\beta = \begin{cases} (2u)^{1/(\eta_c+1)}, & u \leq 0.5 \\ \left(\frac{1}{2(1-u)} \right)^{1/(\eta_c+1)}, & \text{else} \end{cases} \quad (19)$$

where $u = \text{rand}(\cdot)$ is a random number uniformly generated in $[0, 1]$.

The NSGA-III algorithm generates a random number r_m to determine whether to apply the mutation operator or not. The polynomial mutation operator is implemented when $r_m < \eta_m$, where η_m represents the mutation distribution index. For the feasible solution x_s , the mutation individual is generated using the polynomial mutation operator:

$$x_s^* = x_s + (x_s^u - x_s^l) \times \delta_s \quad (20)$$

where x_s^* represents the mutation individual; x_s^u and x_s^l represent the upper and lower bounds of x_s , respectively; δ_s is the mutation coefficient; δ_s can be calculated as follows:

$$\delta_s = \begin{cases} (2u_s)^{1/(\eta_m+1)} - 1, & u_s < 0.5 \\ 1 - (2 \times (1 - u_s))^{1/(\eta_m+1)}, & \text{else} \end{cases} \quad (21)$$

where $u_s = \text{rand}(\cdot)$ is a random number uniformly generated in $[0, 1]$.

The standard NSGA-III algorithm has excellent computational efficiency and stability. However, the NSGA-III algorithm sometimes may fall into the local optimal solution because of the insufficient exploration of the feasible region. Because of the ergodicity and stochasticity of chaotic sequences [39], the chaotic map which can generate chaotic sequences is introduced into the crossover and mutation operators of NSGA-III to enhance its global search and local exploration ability [40]. In this study, the tent map [41] is employed to improve the crossover and mutation operators of NSGA-III.

The tent chaotic map with uniform distribution probability density can be expressed as

$$cx^{(k+1)} = \begin{cases} cx^{(k)} & cx^{(k)} < 0.5 \\ 0.5 & \\ 2 \cdot (1 - cx^{(k)}) & \text{else} \end{cases} \quad (22)$$

where $x^{(k)} \in (0, 1)$ denotes the chaotic variable generated in the k th iteration.

According to (19) and (21), the crossover and mutation operators of the standard NSGA-III algorithm need to generate two random numbers u and u_s in $[0, 1]$, respectively. The two numbers u and u_s are generated using the tent chaotic map in the LCNSGA-III algorithm. The two random numbers u and u_s are generated according to the following:

$$u = cx^{(k+1)} \quad (23)$$

$$u_s = cx^{(k+1)} \quad (24)$$

4.4. The Flowchart of LCNSGA-III for MOOPs. Based on the above introduction of LCNSGA-III, the Latin hypercube sampling, and the chaotic crossover and mutation operators, the flowchart of LCNSGA-III for MOOPs is shown in Figure 3.

4.5. Implementation of LCNSGA-III for Solving the MO-FOPID Problem under Multiworking Conditions. The above LCNSGA-III algorithm is used to optimize the FOPID controller for PTGS under multiworking conditions. The schematic diagram of the MO-FOPID problem optimized by LCNSGA-III under multiworking conditions is shown in Figure 4. In Figure 4, x_c denotes the rotational speed (or frequency) and y_c denotes the given guide vane opening. Since the frequency of the rotational speed is 50 Hz and the frequency disturbance is 2 Hz, the frequency perturbation is set as 4% of the rated frequency.

5. Numerical Experiments and Analysis

5.1. Experiments for Benchmark Functions

5.1.1. Benchmark Functions and Performance Metrics. In order to validity the effectiveness of the newly developed LCNSGA-III algorithm based on Latin-hypercube sampling

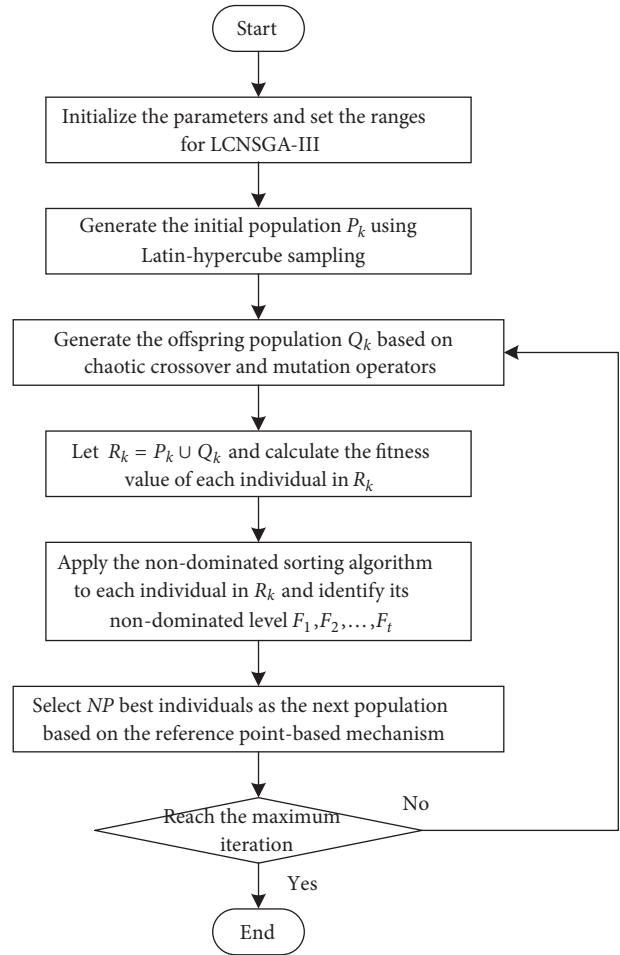


FIGURE 3: Flowchart of LCNSGA-III for MOOPs.

and chaotic map, a total number of eight test functions including the ZDT1-4, 6 [42] and the DTLZ1-2, 5 [43] (shown in Table 1) are employed to test its performance. Among the eight test functions for MOOPs, the ZDT benchmark functions are two-objective MOOPs. The dimension of the decision variables and the number of the test functions of the DTLZ benchmark functions can be adjusted. In this study, the number of the objective functions of the DTLZ test functions is selected as three to display the Pareto front of three-objective MOOPs. Four other typical multiobjective algorithms including NSGA-II, NSGA-III, MOEA/D, and PESA-II [30, 44] are adopted as control group. The performances of the multiobjective evolutionary algorithms (MOEAs) are evaluated and compared using the widely used evaluation metrics of generational distance (GD) and Spread. GD is adopted to measure the mean value of the distance between the Pareto solution set and the real Pareto front. Spread is employed to describe the distribution uniformity of the Pareto optimal set [40]. GD can be expressed as follows:

$$GD = \frac{1}{N} \sqrt{\sum_{i=1}^N D_i^2} \quad (25)$$

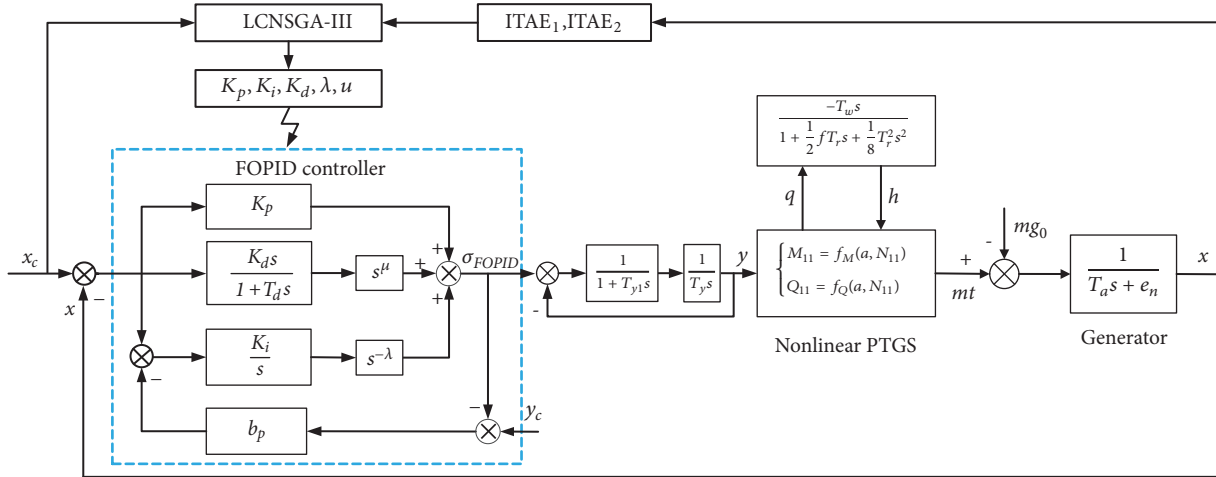


FIGURE 4: Schematic diagram of the MO-FOPID problem optimized by LCNSGA-III under multiworking conditions.

where D_i denotes the Euclidean distance between the i th non-dominated solution and the nearest nondominated solution on the real Pareto front and N denotes the size of the Pareto optimal set. The smaller the GD, the closer the Pareto solution set to the real Pareto front and the better the convergence accuracy.

Spread can be expressed as follows:

$$\text{Spread} = \frac{\sum_{j=1}^M d_j^e + \sum_{i=1}^N |d_i - \bar{d}|}{\sum_{j=1}^M d_j^e + N \cdot \bar{d}} \quad (26)$$

where d_i denotes the distance between i th solution with its neighboring solution; \bar{d} is the mean of d_i ; d_j^e denotes the Euclidean distance between the extreme solution of the real Pareto front and the boundary solution of the obtained Pareto optimal set; M denotes the number of objective functions. The smaller the Spread, the better the distribution of the solutions.

5.1.2. Results Analysis. The parameters of the five algorithms for MOOPs with two objectives are set as follows: the population size is set as 100 while the number of iterations is set as 300. The parameters of the five algorithms for MOOPs with three objectives are set as follows: the population size is set as 150 while the number of iterations is 500. The crossover and mutation probability of the five algorithms are set as 0.7 and 0.3, respectively. The neighborhood size of MOEA/D is set as 20 [45, 46]. All the experiments are implemented in Matlab environment. Because of the random initialization of the MOOPs, all the experiments have been repeated ten times independently to eliminate the effectiveness of randomness. The average GD and Spread of the five algorithms for the eight benchmark functions are given in Tables 2 and 3, respectively. Numbers in bold represent the optimal GD and Spread among the five algorithms for the eight benchmark functions.

As can be seen from Table 2, the GD of the Pareto optimal solution obtained by the newly developed LCNSGA-III is the

best out of the total eight benchmark functions. Although the GD of LCNSGA-III algorithm is slightly worse than that of NSGA-II and NSGA-III to optimize ZDT4 and DTLZ1, the Spread of LCNSGA-III is prominent. The Spread of LCNSGA-III performs best to optimize the ZDT1, ZDT4, and DTLZ5 benchmark problems. And the Spread for LCNSGA-III does not differ much from those for the other five MOOPs except DTLZ1, which indicates that the LCNSGA-III algorithm can obtain good convergence performance for the eight benchmark functions. The Pareto optimal front obtained by LCNSGA-III to optimize the eight benchmark functions is shown in Figure 5 (ZDT1-4) and Figure 6 (ZDT6, DTLZ1-2, 5) (Grey points denote the true Pareto front while blue ones denote the obtained Pareto front), respectively. As depicted in Figures 5 and 6, the Pareto front obtained by LCNSGA-III to optimize the eight benchmark MOOPs can approximate the real Pareto front perfectly and the distributions of the Pareto optimal sets are uniform. As a result, the LCNSGA-III algorithm has prominent convergence performance and optimization ability compared with the other algorithms.

5.2. Experiments for Nonlinear PTGS

5.2.1. Experiments Design and Results. In order to fully verify the performance and effectiveness of the LCNSGA-III algorithm in solving the MO-FOPID problem under multiworking conditions, the nonlinear model of PTGS with different controllers (PID and FOPID) and water heads (198m, 205m, and 210m) under no-load conditions is simulated on MATLAB environment. The frequency perturbation is set as 4% of the rated frequency and the simulation time is set as 50s. A total number of ten schemes have been designed to obtain the optimal parameters. The ten schemes can be divided into four categories as follows:

(1) The backtracking search algorithm (BSA) [47] is exploited to optimize the parameters of PID controller under a single working condition of different water heads (198m, 205m, and 210m). The ITAE of PTGS under a certain working condition is selected as the objective function for

TABLE 1: Eight test functions for MOOPs.

Name	Functions	Dimension of decision variable	Feasible region	Type of Pareto Front
ZDT1	$f_1(X) = x_1,$ $f_2(X) = g \cdot \left(1 - \sqrt{\frac{f_1}{g}}\right)$ $g(X) = 1 + 9 \cdot \sum_{i=2}^n \frac{x_i}{(n-1)}$	30	[0, 1]	High dimension, convex
ZDT2	$f_1(X) = x_1,$ $f_2(X) = g \cdot \left(1 - \left(\frac{f_2}{g}\right)^2\right)$ $g(X) = 1 + 9 \cdot \sum_{i=2}^n \frac{x_i}{(n-1)}$	30	[0, 1]	High dimension, convex
ZDT3	$f_1(X) = x_1$ $f_2(X) = g \cdot \left(1 - \sqrt{\frac{f_1}{g}}\right) - \left(\frac{f_1}{g}\right) \sin(10\pi f_1)$ $g(X) = 1 + 9 \cdot \sum_{i=2}^n \frac{x_i}{(n-1)}$	30	[0, 1]	Discontinuous, convex
ZDT4	$f_1(X) = x_1$ $f_2(X) = g \cdot \left(1 - \sqrt{\frac{f_1}{g}}\right)$ $g(X) = 1 + 10(n-1) + \sum_{i=2}^n [x_i^2 - 10 \cos(4\pi x_i)]$	10	$x_1 \in [0, 1]$ $x_i \in [-5, 5]$ $i = 2, 3, \dots, n$	Multi-modal, convex
ZDT6	$f_1(X) = 1 - \exp(-4x_1) \sin^6(6\pi x_1)$ $f_2(X) = g \cdot \left(1 - \left(\frac{f_1}{g}\right)^2\right)$ $g(X) = 1 + 9 \cdot \left[\sum_{i=2}^n \frac{x_i}{(n-1)}\right]^{0.25}$	10	[0, 1]	Inhomogeneous
DTLZ1	$f_1(X) = \frac{1}{2} x_1 x_2 \cdots x_{M-1} (1 + g(x_M))$ $f_2(X) = \frac{1}{2} x_1 x_2 \cdots (1 - x_{M-1}) (1 + g(x_M))$ \vdots $f_{M-1}(X) = \frac{1}{2} x_1 (1 - x_2) (1 + g(x_M))$ $f_M(X) = \frac{1}{2} (1 - x_1) (1 + g(x_M))$ $g(X_M) =$ $100 \left(x_M + \sum_{x_i \in x_M} * (x - 0.5)^2 + \cos(20\pi(x - 0.5)) \right)$	7	[0, 1]	Linear, multimodal
DTLZ2	$f_1(X) = (1 + g(x_M)) \cos\left(\frac{x_2\pi}{2}\right) \cdots \cos\left(\frac{x_{M-1}\pi}{2}\right)$ $f_2(X) = (1 + g(x_M)) \cos\left(\frac{x_1\pi}{2}\right) \cdots \cos\left(\frac{x_{M-1}\pi}{2}\right)$ \vdots $f_M(X) = (1 + g(x_M)) \sin\left(\frac{x_1\pi}{2}\right)$ $g(X_M) = \sum * (x - 0.5)^2$	12	[0, 1]	Complex nonconvex
DTLZ5	<p>replace the x_i in DTLZ2 with θ_i</p> $\theta_i = \frac{\pi}{4(1+q(r))} (1 + 2g(r) x_i)$ $g(x_M) = \sum_{x_i \in x_M} x_i^{0.1}$	12	[0, 1]	Space arc

TABLE 2: Comparison of GD for eight benchmark functions.

Benchmark functions	Multi-objective optimization algorithms				
	PESA-II	MOEA/D	NSGA-II	NSGA-III	LCNSGA-III
ZDT1	7.72E-05	3.66E-04	5.77E-05	7.95E-05	3.80E-05
ZDT2	3.37E-04	8.27E-04	3.11E-05	6.77E-05	2.84E-05
ZDT3	6.14E-05	1.90E-03	4.23E-05	7.48E-05	3.56E-05
ZDT4	1.41E-02	2.05E-03	2.00E-04	2.52E-04	3.15E-04
ZDT6	1.09E-02	7.38E-04	4.30E-05	7.84E-05	3.63E-05
DTLZ1	1.97E-02	3.01E-04	4.75E-04	2.25E-04	4.33E-04
DTLZ2	9.77E-04	4.18E-04	9.30E-04	4.14E-04	3.78E-04
DTLZ5	1.50E-04	7.88E-05	1.32E-04	1.55E-04	5.34E-05

TABLE 3: Comparison of Spread for eight benchmark functions.

Benchmark functions	Multi-objective optimization algorithms				
	PESA-II	MOEA/D	NSGA-II	NSGA-III	LCNSGA-III
ZDT1	9.67E-01	4.53E-01	4.25E-01	3.47E-01	3.24E-01
ZDT2	9.83E-01	6.73E-01	4.68E-01	2.15E-01	2.99E-01
ZDT3	1.01E+00	6.79E-01	5.87E-01	7.52E-01	6.65E-01
ZDT4	1.02E+00	5.51E-01	4.31E-01	3.93E-01	3.30E-01
ZDT6	1.04E+00	1.55E-01	4.15E-01	1.13E-01	1.20E-01
DTLZ1	8.02E-01	3.11E-02	4.95E-01	3.40E-02	3.51E-01
DTLZ2	3.88E-01	1.73E-01	5.21E-01	1.74E-01	3.01E-01
DTLZ5	9.20E-01	2.03E+00	6.61E-01	9.78E-01	4.58E-01

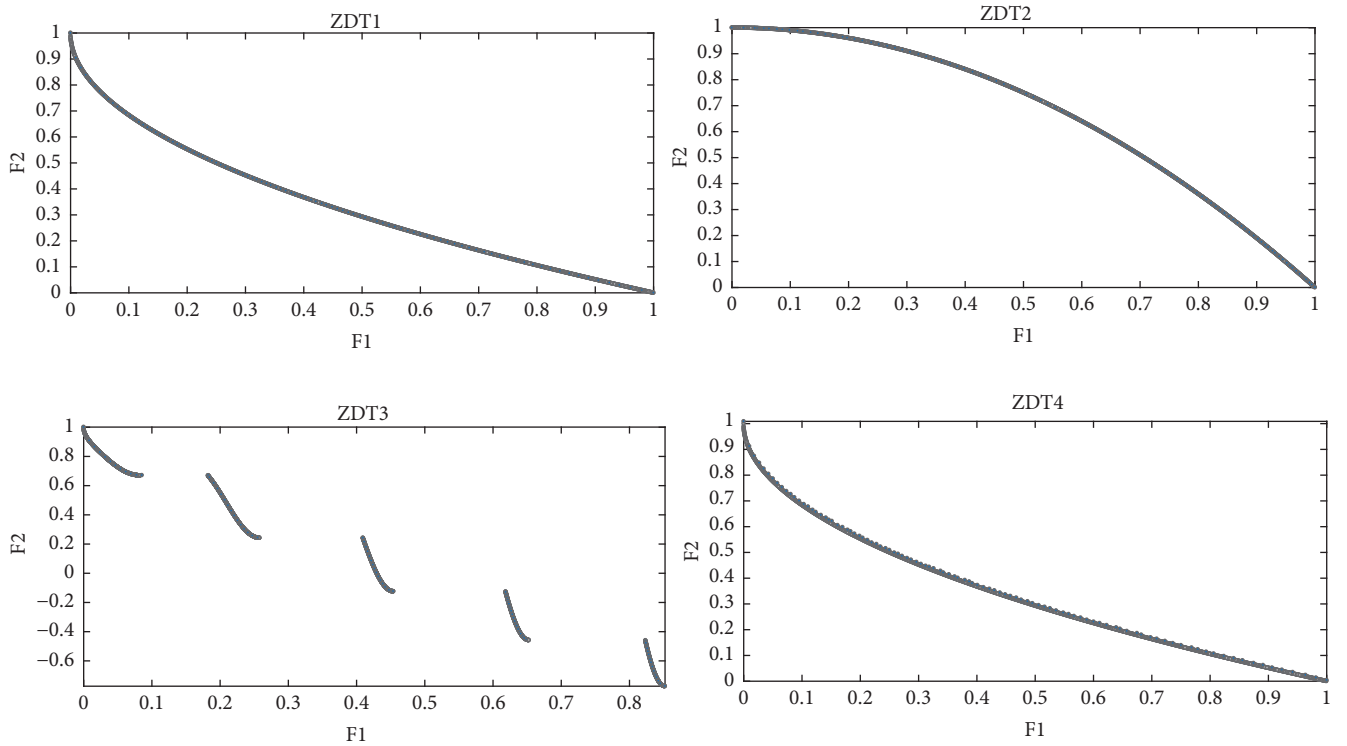


FIGURE 5: Pareto optimal solutions obtained by LCNSGA-III for ZDT1-4.

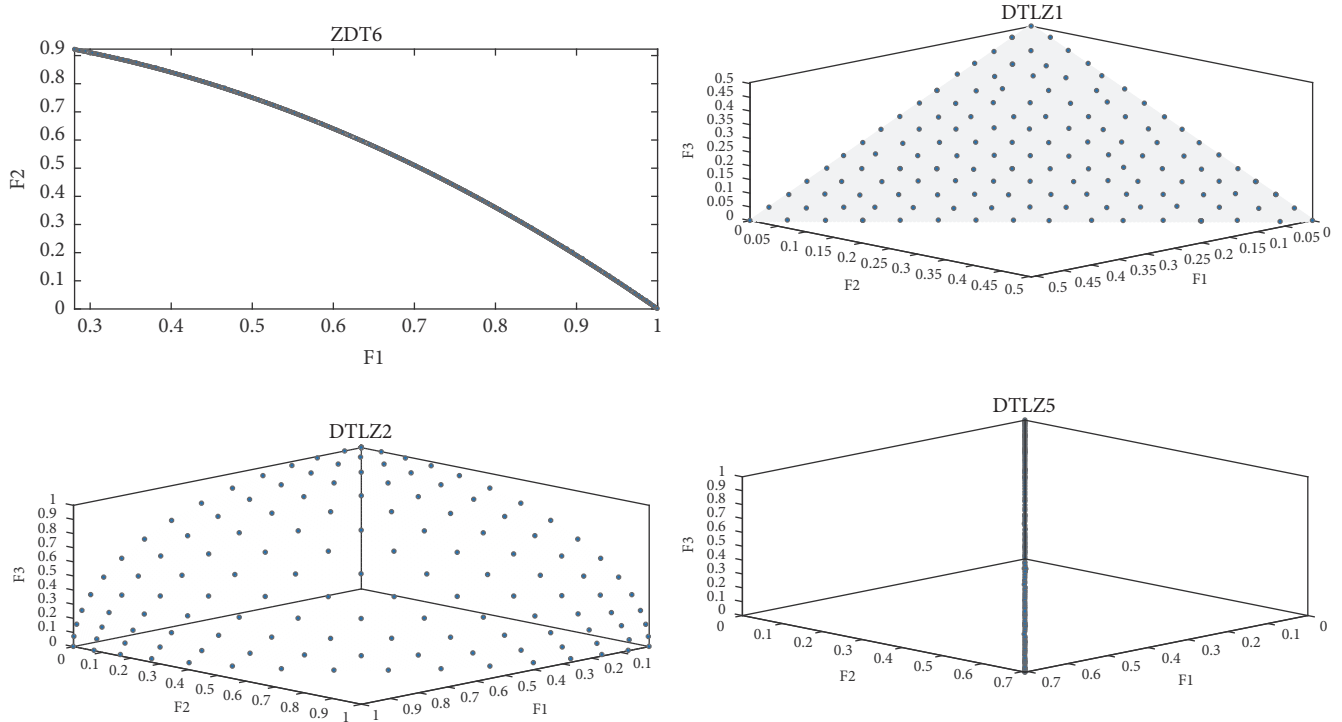


FIGURE 6: Pareto optimal solutions obtained by LCNSGA-III for ZDT6, DTLZ1-2, 5.

single-objective optimization. The experiments are simplified as S-198-PID, S-205-PID, and S-210-PID, respectively. The optimized control parameters are applied on the other two working conditions to test the adaptability of different schemes in tracking the dynamic responses of PTGS. (e.g., for scheme S-198-PID, the working condition running at 198m water head is used for training while those at 205m and 210m are used for testing);

(2) The BSA algorithm is exploited to optimize the parameters of FOPID controller under a single working condition of different water heads (198m, 205m, and 210m). The experiments are simplified as S-198-FOPID, S-205-FOPID, and S-210-FOPID, respectively. The optimized control parameters are applied on the other two working conditions to test the adaptability of different schemes in tracking the dynamic responses of PTGS;

(3) The NSGA-III algorithm is adopted to optimize the parameters of PID or FOPID controller under two working conditions (198m and 210m). The ITAE of PTGS at working conditions of 198m and 210m water head is selected as the objective functions for multiobjective optimization, and the compromise optimal solution among the Pareto optimal set is selected. The experiments are simplified as NSGA-III-PID and NSGA-III-FOPID for the PID and FOPID controller, respectively. The compromise optimal control parameters are applied on the working condition of 205m water head to test the adaptability of different schemes in tracking the dynamic responses of PTGS;

(4) The LCNSGA-III algorithm is adopted to optimize the parameters of PID or FOPID controller under two working conditions (198m and 210m). The experiments are simplified

as LCNSGA-III-PID and LCNSGA-III-FOPID for the PID and FOPID controller, respectively. The compromise optimal control parameters are applied on the working condition of 205m water head to test the adaptability of different schemes in tracking the dynamic responses of PTGS.

The parameters of PTGS are set as follows: the ranges of K_p , K_i , and K_d of the PID and FOPID controllers are all set as $[0, 15]$ and the ranges of λ and u are all set as $[0, 2]$. The parameters of the BSA algorithm are set as follows: the population size is set as 50, the number of iterations is 200, and the control parameter F is set as the default value. The parameters of the NSGA-III and LCNSGA-III algorithms are as follows: the population size is set as 50; the iteration number is 300; the crossover probability is 0.7; the mutation probability is 0.3.

Apart from ITAE, the integral of the ITSE [29], the stable time (ST) and the overshoot (OSO) is adopted to evaluate the performance of different schemes. The ITSE index is defined as follows:

$$\text{ITSE} = \int_0^T t (e(t))^2 dt \quad (27)$$

In this study, the best compromise solution is selected according to the subjective weighting method based on experts' preferences of weights. The optimal control parameters of the ten schemes for PTGS are shown in Table 4. The performance indices including ITAE, ITSE, ST, and OSO of the ten schemes under different working water heads are shown in Table 5. In Table 5, for scheme S-198-PID, the results for 198m water head are training results while those for 205m and 210m heads are testing results. For scheme S-205-PID, the

TABLE 4: Optimal control parameters for nonlinear PTGS using different schemes.

Schemes	Optimal parameters				
	K_p	K_i	K_d	λ	μ
S-198-PID	5.05	0.72	2.08	/	/
S-205-PID	8.00	1.00	2.91	/	/
S-210-PID	6.97	0.87	5.00	/	/
S-198-FOPID	9.00	0.52	0.82	0.49	0.97
S-205-FOPID	1.36	0.58	1.74	0.64	0.98
S-210-FOPID	8.91	0.56	1.98	0.77	0.99
NSGA-III-PID	9.92	1.04	1.62	/	/
NSGA-III-FOPID	8.90	0.52	1.02	0.57	0.98
LCNSGA-III-PID	14.72	0.97	0.81	/	/
LCNSGA-III-FOPID	10.62	0.58	1.12	0.56	0.98

TABLE 5: Performance indices for nonlinear PTGS using different schemes at different water heads.

Experiments	198m				205m				210m			
	ITAE	ITSE	ST (s)	OSO (%)	ITAE	ITSE	ST (s)	OSO (%)	ITAE	ITSE	ST (s)	OSO (%)
S-198-PID	5.68	0.04	49.9	17.7	4.10	0.02	35.6	15.0	3.16	0.02	35.5	12.4
S-205-PID	37.28	0.17	/	25.4	2.69	0.02	29.3	22.9	1.93	0.02	20.1	20.5
S-210-PID	54.29	0.35	/	22.8	37.88	0.21	/	11.7	1.34	0.02	18.6	9.3
S-198-FOPID	2.10	0.02	27.6	3.6	1.50	0.02	26.1	0.5	1.87	0.02	27.1	0.9
S-205-FOPID	23.29	0.10	/	10.5	1.11	0.02	25.0	0.5	1.48	0.01	28.2	0.7
S-210-FOPID	20.11	0.08	/	7.9	1.81	0.02	25.7	3.3	0.96	0.02	17.0	0.3
NSGA-III-PID	5.88	0.04	/	37.1	2.82	0.03	23.2	34.5	2.04	0.02	23.7	32.4
NSGA-III-FOPID	2.18	0.02	27.4	5.6	1.52	0.02	24.1	3.0	1.41	0.02	26.6	0.9
LCNSGA-III-PID	5.43	0.04	/	33.3	2.76	0.03	18.4	30.4	1.90	0.02	18.4	27.6
LCNSGA-III-FOPID	1.90	0.02	27.6	5.5	1.37	0.02	23.3	2.3	1.42	0.01	25.9	1.1

results for 205m water head are training results while those for 198m and 210m heads are testing results. For scheme S-210-PID, the results for 210m water head are training results while those for 198m and 205m heads are testing results. The single-objective schemes are designed to compare with the multiobjective schemes to highlight the effectiveness of multiobjective schemes in optimizing PTGS. “/” means that the system is unstable and when the fluctuation of frequency is smaller than 0.003, it is considered to be stable.

5.2.2. Comparison of PID and FOPID Controllers under Different Working Conditions. From Table 5, it is known that the FOPID controller generally achieves better performance than the corresponding PID controller in terms of ITAE, ITSE, ST, and OSO for 198m, 205m, and 210m working water heads. The ITAE, ITSE, ST, and OSO for the FOPID controller are either smaller or in coincidence with those of the PID controller. For example, the improved percentages of scheme S-198-FOPID compared with scheme S-198-PID are 63.0%, 50.0%, 44.7%, and 79.7% in terms of ITAE, ITSE, ST, and OSO, respectively in the training stage (198m). The improved percentages in the testing stage (205m) are 63.4%, 26.7%, and 96.7% in terms of ITAE, ST, and OSO, respectively. The ITSE for S-198-FOPID and scheme S-198-PID in the testing stage (205m) is the same. To further compare the effects of different controllers in capturing the dynamic performances of PTGS,

the test unit frequency at 198m, 205m, and 210m working water heads using different controllers is illustrated in Figures 7–9, respectively. As can be seen from Figures 7–9, the FOPID controller for PTGS can obtain smaller overshoot ITAE, ITSE, ST, and OSO in most cases. For working condition of 198m water head which is easy to fall into the “S” area, the unit frequency oscillates a lot using PID controller. The FOPID controller, in the other way, can effectively restrain the strong nonlinear characteristics of PTGS and significantly improve the control quality.

5.2.3. Analysis of Controllers Optimized under a Single Working Condition. It is noticed from Table 5 that for controllers optimized at a single working condition, the performance is only good for the training working condition, but the test working conditions. It can also be seen from Table 5 and Figures 7–9 that the S-210-FOPID scheme can obtain good control performance when PTGS is running at 210m water head, but not 198m. For schemes S-198-PID and S-198-FOPID, PTGS can obtain good control performance at 205m and 210m working water heads, which conforms to the actual physical phenomenon that the control parameters suitable for low water head may also suitable for middle or high water heads. However, due to the lack of comprehensive consideration for complex working conditions, the adaptability and robustness of the PID and FOPID controllers optimized

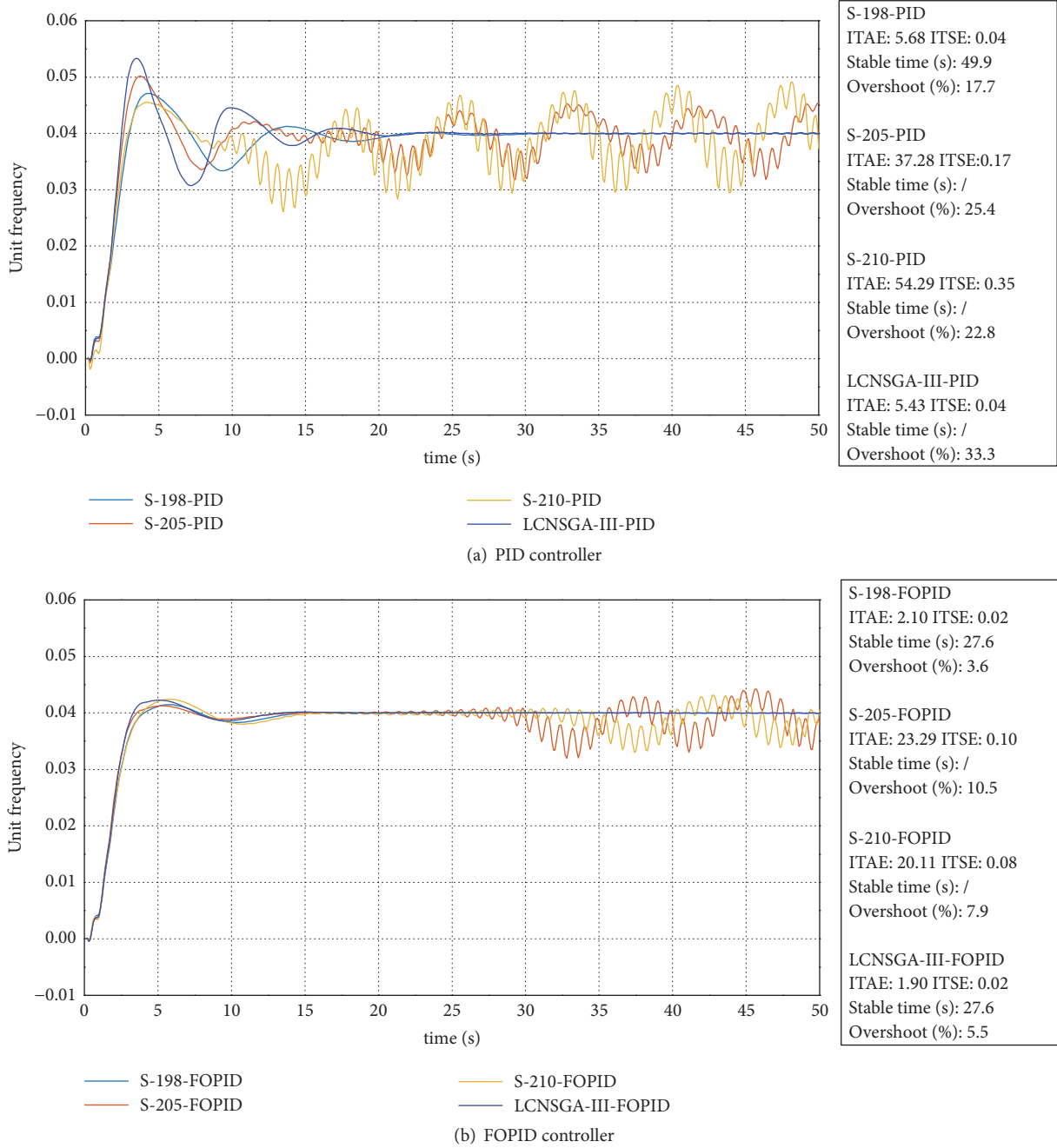


FIGURE 7: Unit frequency obtained at 198m working water head.

at complex operating conditions simultaneously using multiobjective optimization algorithms should be studied and investigated.

5.2.4. *Analysis of Controllers Optimized under Multiworking Conditions.* The Pareto fronts obtained by LCNSGA-III-PID and LCNSGA-III-FOPID are shown in Figure 10. From Figure 10, it can be noticed that the Pareto front of LCNSGA-III-FOPID can dominate that of LCNSGA-III-PID, which further demonstrate the superiority of the FOPID controller. It can also be noticed from Figure 10 that the $ITAE_1$ for

low water head (198m) and the $ITAE_2$ for high water head (210m) are two conflicting indices. The optimal solution for working condition at low water head is not the best one for working condition at high water head. The employment of multiobjective optimization algorithms to optimize the two objectives simultaneously can help researchers find the compromise optimal solutions. Compare the ITAE indices for S-198-PID and S-210-PID in Table 5 with the Pareto front obtained by LCNSGA-III-PID; in Figure 10, it can be found that the ITAE indices for the two schemes are the nearest to the two edge solutions of the Pareto front of

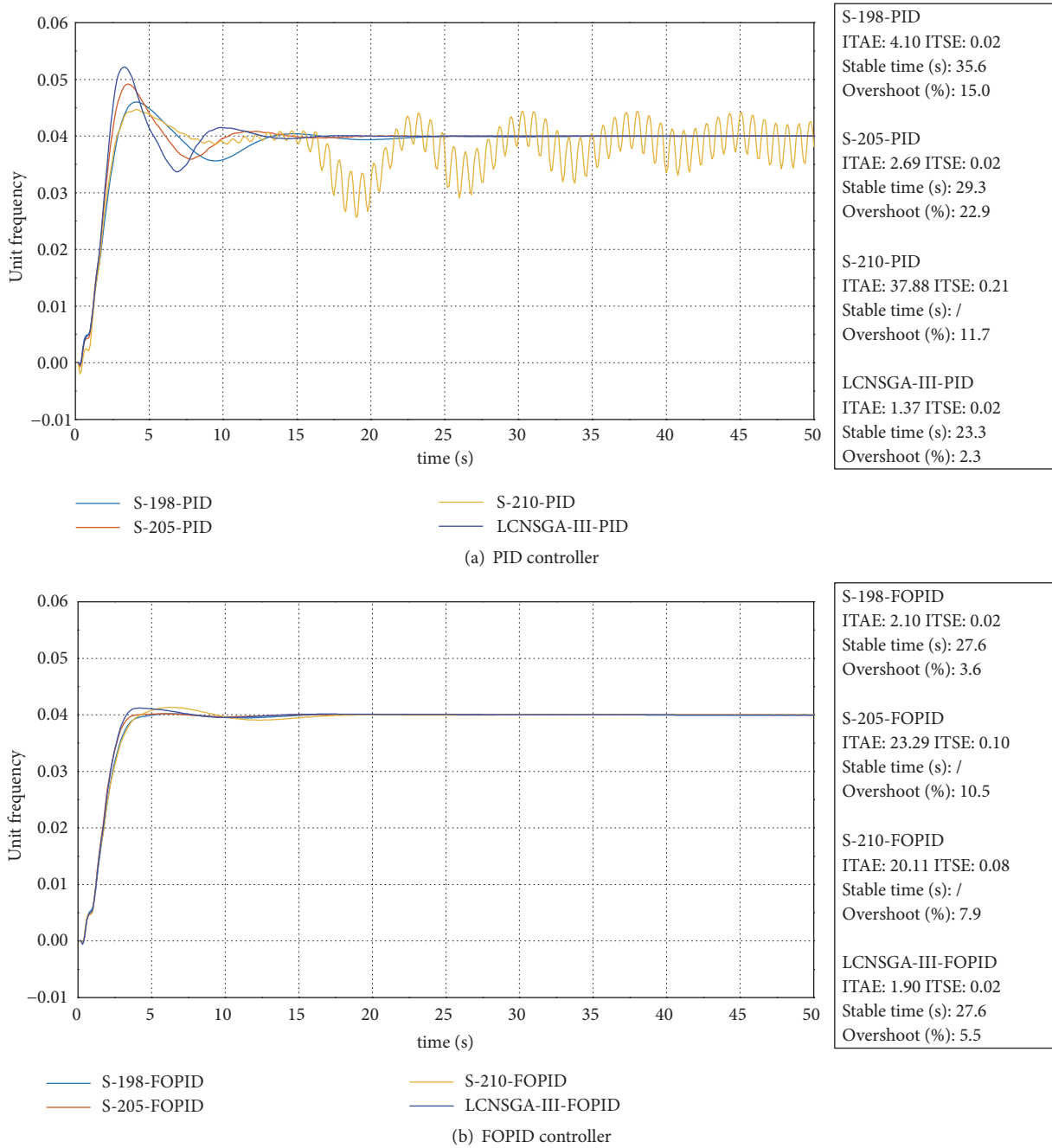


FIGURE 8: Unit frequency obtained at 205m working water head.

LCNSGA-III-PID. Similar phenomenon also exists between the solutions obtained by S-198-FOPID and S-210-FOPID and the Pareto optimal solutions obtained by LCNSGA-III-FOPID, which demonstrates that the pursuing for a single objective (high or low water head) is at the cost of the other objective (corresponding low or high water head). What is more, compared with the schemes for single working conditions, the adaptability and robustness of the controllers can be greatly improved using multiobjective optimization schemes. A set of Pareto optimal solutions are obtained using multiobjective optimization schemes; it is convenient for the

operator to select the most appropriate control parameters when the working condition changes or much more attention should be paid to the extremely low water head or high water head working conditions.

The effectiveness of the developed LCNSGA-III algorithm has been verified using the eight test functions which have been described in Section 5.1. In what follows the superiority of the developed LCNSGA-III algorithm is further demonstrated by applying it to PTGS. The Pareto fronts of PID and FOPID controllers optimized by the two algorithms have been illustrated in Figures 11(a) and 11(b), respectively.

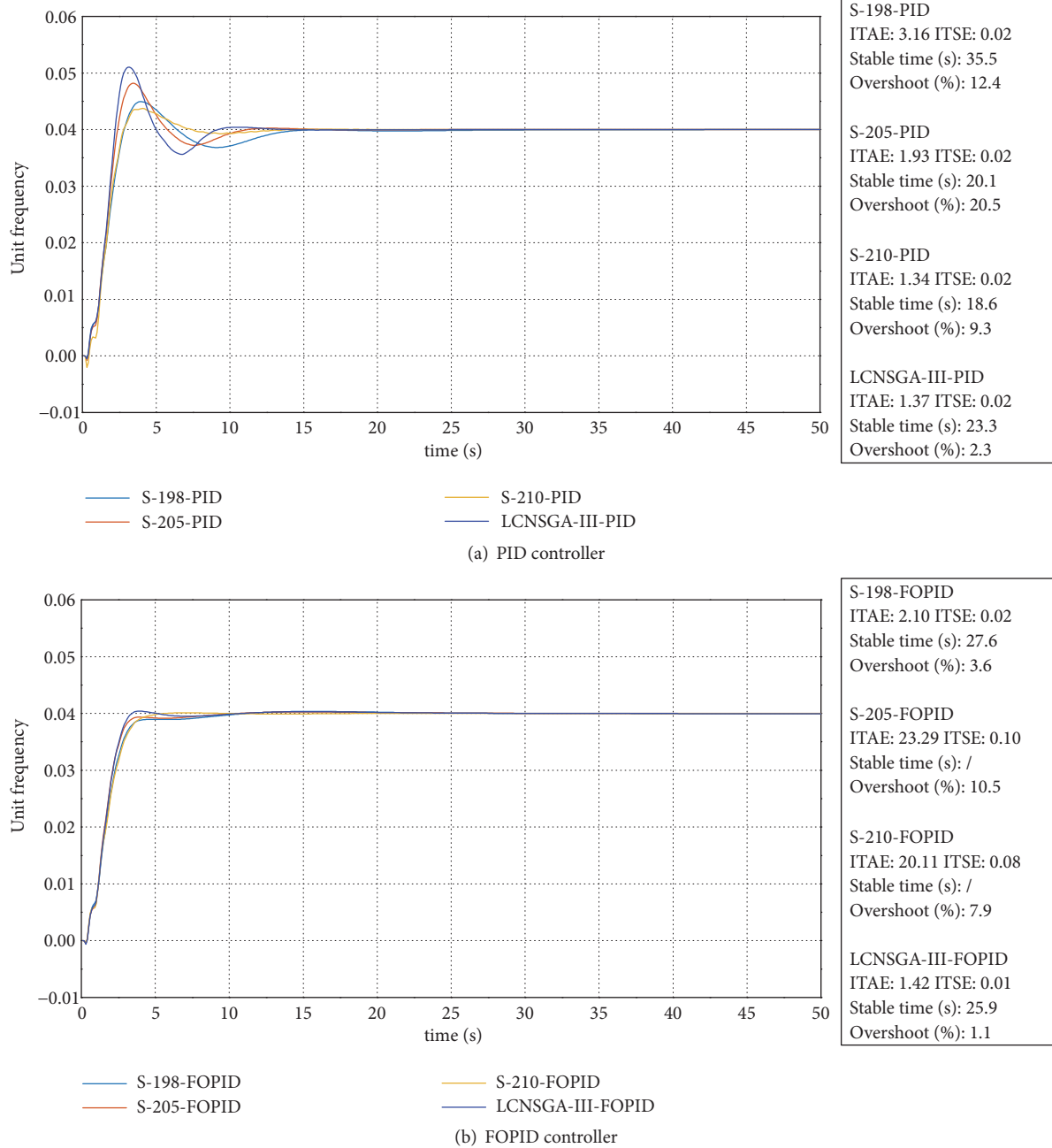


FIGURE 9: Unit frequency obtained at 210m working water head.

It can be observed from Figure 11 that the Pareto optimal solutions obtained by LCNSGA-III can dominate almost all of those obtained by NSGA-III. And the Pareto front obtained by LCNSGA-III distributes more uniformly and extensively. It can be found in Table 5 that the performances indices for the compromise Pareto optimal solution of LCNSGA-III are all smaller than NSGA-III, which further demonstrates the superiority of LCNSGA-III in optimizing the MO-FOPID problem. For example, the improved percentages of scheme LCNSGA-III-PID to scheme NSGA-III-PID are 62.9%, 50.0%, and 84.9% in terms of ITAE, ITSE, and OSO, respectively in the training stage (198m). The improved

percentages in the testing stage (205m) are 46.1%, 33.3%, and 91.3% in terms of ITAE, ITSE, and OSO, respectively.

6. Conclusions

In order to make PSUs adaptable to the changes of working environment and improve their control quality and stability, this study constructs a multiobjective optimization framework to optimize the FOPID controller for PTGS under multiworking conditions. An LCNSGA-III algorithm based on Latin-hypercube sampling and chaos theory is proposed to solve the MO-FOPID problem under multiworking

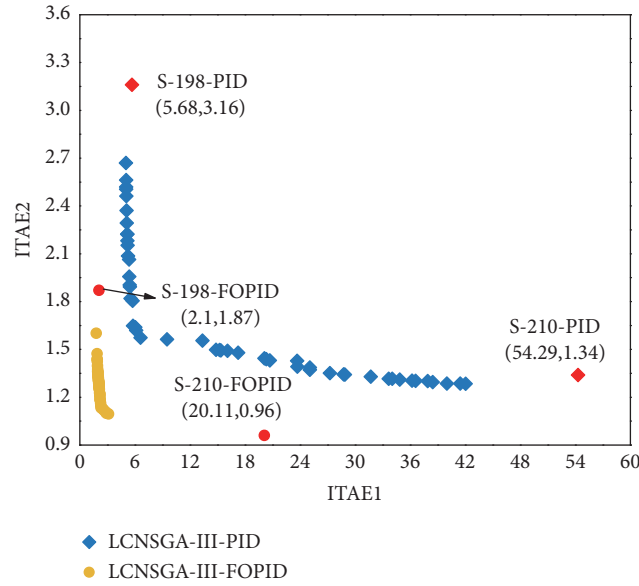


FIGURE 10: Pareto fronts obtained by LCNSGA-III-PID, LCNSGA-III-FOPID, and their comparison with single-objective solutions.

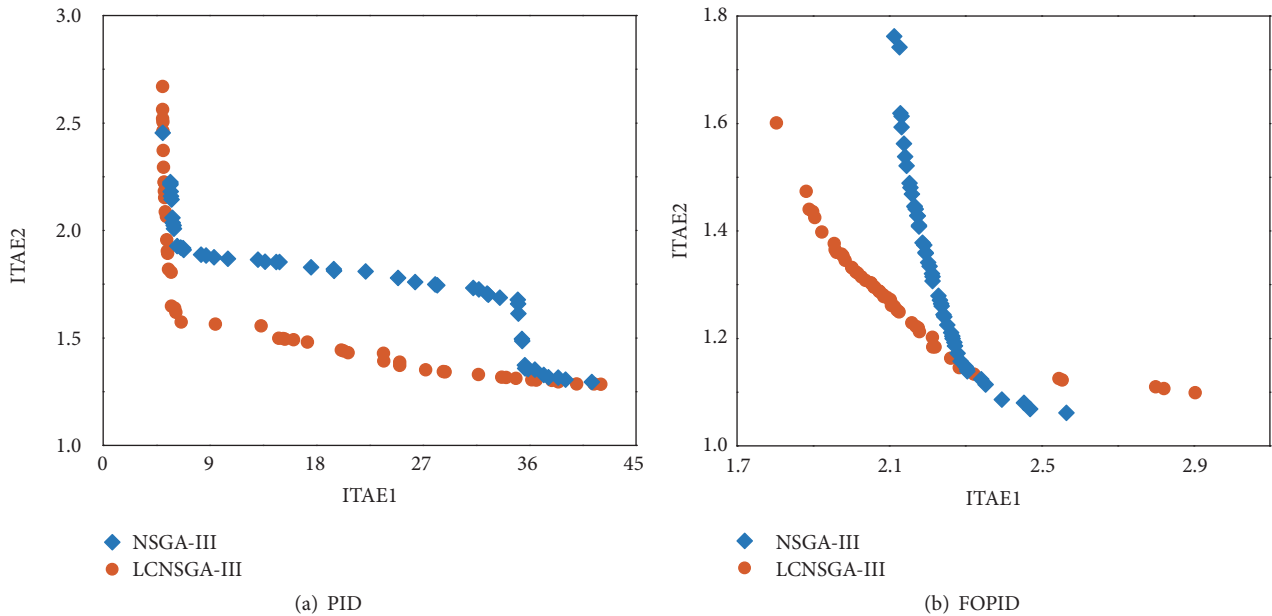


FIGURE 11: Comparison of Pareto fronts obtained by LCNSGA-III and NSGA-III for PID and FOPID controllers.

conditions. Implementation of the MO-FOPID controller optimized by LCNSGA-III relies on the simultaneous optimization of two complementary features: the ITAE index under low and high water heads. The experiment results indicate the following:

(1) The classical NSGA-III algorithm is improved using the Latin hypercube sampling- based initialization technique and the chaotic crossover and mutation operators. Experiments of the eight test functions show that the improvement strategies can effectively improve the convergence and diversity of the Pareto optimal front of the NSGA-III algorithm.

(2) Compared with the traditional PID controller, the FOPID can effectively suppress the frequency oscillation of PSUs in the “S” characteristic area running at middle or low working water heads and can enhance the dynamic response performance of PTGS.

(3) This study extends the single-objective optimization under single working conditions to the multiobjective optimization framework under multiworking conditions. The multiobjective framework has provided better dynamic performances than the single-objective optimization methods. The multiobjective implementation of FOPID makes it much more convenient for a operator to select the most

appropriate control parameters for a certain working condition.

This work sets a basis for research on multiobjective optimization of a FOPID controller of PTGS under multiworking conditions. The extension of the single-objective optimization under a single working-condition to the multiobjective framework under complex working conditions can provide new control law and optimization algorithms for the optimal control of PTGS. What is more, the proposed LCNSGA-III algorithm can be easily extended to optimization problems in other fields of scientific research and industrial application.

Data Availability

The data used to support the findings of this study are available from the corresponding author upon request.

Conflicts of Interest

The authors declare no conflicts of interest.

Acknowledgments

This work is supported by the National Natural Science Foundation of China (No. 51741907), the National Natural Science Foundation of China (NSFC) (No. 51709121), and the National Natural Science Foundation of China (No. 51709122).

References

- [1] R. N. Allan, R. Li, and M. M. Elkateb, "Modelling of pumped-storage generation in sequential Monte Carlo production simulation," *Generation, Transmission and Distribution, IEE Proceedings*, vol. 145, no. 5, pp. 611–615, 1998.
- [2] W. Wang, C. Li, X. Liao, and H. Qin, "Study on unit commitment problem considering pumped storage and renewable energy via a novel binary artificial sheep algorithm," *Applied Energy*, vol. 187, pp. 612–626, 2017.
- [3] J. Zhou, Z. Zhao, C. Zhang, C. Li, and Y. Xu, "A real-time accurate model and its predictive fuzzy PID controller for pumped storage unit via error compensation," *Energies*, vol. 11, no. 1, 2018.
- [4] J. Zhou, C. Zhang, T. Peng, and Y. Xu, "Parameter identification of pump turbine governing system using an improved backtracking search algorithm," *Energies*, vol. 11, no. 7, p. 1668, 2018.
- [5] C. Zhang, C. Li, T. Peng et al., "Modeling and synchronous optimization of pump turbine governing system using sparse robust least squares support vector machine and hybrid backtracking search algorithm," *Energies*, vol. 11, no. 11, p. 3108, 2018.
- [6] Y. Xu, Y. Zheng, Y. Du, W. Yang, X. Peng, and C. Li, "Adaptive condition predictive-fuzzy PID optimal control of start-up process for pumped storage unit at low head area," *Energy Conversion and Management*, vol. 177, pp. 592–604, 2018.
- [7] K. Natarajan, "Robust PID controller design for hydroturbines," *IEEE Transactions on Energy Conversion*, vol. 20, no. 3, pp. 661–667, 2005.
- [8] R.-E. Precup, A.-D. Balint, M.-B. Radac, and E. M. Petriu, "Backtracking search optimization algorithm-based approach to PID controller tuning for torque motor systems," in *Proceedings of the 2015 Annual IEEE Systems Conference*, pp. 127–132, IEEE, Vancouver, BC, Canada, 2015.
- [9] R.-E. Precup, A.-D. Balint, E. M. Petriu, M.-B. Radac, and E.-I. Voisan, "PI and PID controller tuning for an automotive application using backtracking search optimization algorithms," in *Proceedings of the IEEE Jubilee International Symposium on Applied Computational Intelligence and Informatics*, pp. 161–166, Timisoara, Romania, May 2015.
- [10] A. Khodabakhshian and R. Hooshmand, "A new PID controller design for automatic generation control of hydro power systems," *International Journal of Electrical Power & Energy Systems*, vol. 32, no. 5, pp. 375–382, 2010.
- [11] R. Melício, V. M. F. Mendes, and J. P. S. Catalão, "Fractional-order control and simulation of wind energy systems with PMSG/full-power converter topology," *Energy Conversion and Management*, vol. 51, no. 6, pp. 1250–1258, 2010.
- [12] V. Haji Haji and C. A. Monje, "Fractional order fuzzy-PID control of a combined cycle power plant using Particle Swarm Optimization algorithm with an improved dynamic parameters selection," *Applied Soft Computing*, vol. 58, pp. 256–264, 2017.
- [13] S. Zhang and L. Liu, "Normalized robust FOPID controller regulation based on small gain theorem," *Complexity*, vol. 2018, Article ID 5690630, 10 pages, 2018.
- [14] L. Liu and S. Zhang, "Robust fractional-order PID controller tuning based on bode's optimal loop shaping," *Complexity*, vol. 2018, Article ID 6570560, p. 14, 2018.
- [15] J.-W. Perng, G.-Y. Chen, and Y.-W. Hsu, "FOPID controller optimization based on SIWPSO-RBFNN algorithm for fractional-order time delay systems," *Soft Computing*, vol. 21, no. 14, pp. 4005–4018, 2017.
- [16] C. Li, N. Zhang, X. Lai, J. Zhou, and Y. Xu, "Design of a fractional-order PID controller for a pumped storage unit using a gravitational search algorithm based on the Cauchy and Gaussian mutation," *Information Sciences*, vol. 396, pp. 162–181, 2017.
- [17] Y. Xu, J. Zhou, Y. Zhang, W. Fu, Y. Zheng, and X. Zhang, "Parameter optimization of robust non-fragile fractional order pid controller for pump turbine governing system," in *Proceedings of the in Sixth International Conference on Instrumentation Measurement, Computer*, pp. 15–18, 2016.
- [18] Y. Xu, J. Zhou, X. Xue, W. Fu, W. Zhu, and C. Li, "An adaptively fast fuzzy fractional order PID control for pumped storage hydro unit using improved gravitational search algorithm," *Energy Conversion and Management*, vol. 111, pp. 67–78, 2016.
- [19] C. Jiang, Y. Ma, and C. Wang, "PID controller parameters optimization of hydro-turbine governing systems using deterministic-chaotic-mutation evolutionary programming (DCMEP)," *Energy Conversion and Management*, vol. 47, no. 9–10, pp. 1222–1230, 2006.
- [20] H. Fang, L. Chen, and Z. Shen, "Application of an improved PSO algorithm to optimal tuning of PID gains for water turbine governor," *Energy Conversion and Management*, vol. 52, no. 4, pp. 1763–1770, 2011.
- [21] P. G. Kou, J. Z. Zhou, H. E. Yao-Yao, X. Q. Xiang, and L. I. Chao-Shun, "Optimal PID governor tuning of hydraulic turbine generators with bacterial foraging particle swarm optimization algorithm," *Proceedings of the Csee*, vol. 29, no. 26, pp. 101–106, 2009.
- [22] Z. Wang, C. Li, X. Lai, N. Zhang, Y. Xu, and J. Hou, "An integrated start-up method for pumped storage units based on

- a novel artificial sheep algorithm,” *Energies*, vol. 11, no. 1, p. 151, 2018.
- [23] M. J. Mahmoodabadi and H. Jahanshahi, “Multi-objective optimized fuzzy-PID controllers for fourth order nonlinear systems,” *Engineering Science and Technology, an International Journal*, vol. 19, no. 2, pp. 1084–1098, 2016.
- [24] S. Panda, “Multi-objective PID controller tuning for a FACTS-based damping stabilizer using non-dominated sorting genetic algorithm-II,” *International Journal of Electrical Power & Energy Systems*, vol. 33, no. 7, pp. 1296–1308, 2011.
- [25] A.-A. Zamani, S. Tavakoli, and S. Etedali, “Fractional order PID control design for semi-active control of smart base-isolated structures: a multi-objective cuckoo search approach,” *ISA Transactions*, vol. 67, p. 222, 2017.
- [26] H. S. Sánchez, F. Padula, A. Visioli, and R. Vilanova, “Tuning rules for robust FOPID controllers based on multi-objective optimization with FOPDT models,” *ISA Transactions*, vol. 66, pp. 344–361, 2017.
- [27] S.-Z. Zhao, M. W. Iruthayarajan, S. Baskar, and P. N. Suganthan, “Multi-objective robust PID controller tuning using two lbests multi-objective particle swarm optimization,” *Information Sciences*, vol. 181, no. 16, pp. 3323–3335, 2011.
- [28] Z. Chen, X. Yuan, B. Ji, P. Wang, and H. Tian, “Design of a fractional order PID controller for hydraulic turbine regulating system using chaotic non-dominated sorting genetic algorithm II,” *Energy Conversion and Management*, vol. 84, pp. 390–404, 2014.
- [29] Z. Chen, Y. Yuan, X. Yuan, Y. Huang, X. Li, and W. Li, “Application of multi-objective controller to optimal tuning of PID gains for a hydraulic turbine regulating system using adaptive grid particle swarm optimization,” *ISA Transactions*, vol. 56, pp. 173–187, 2015.
- [30] T. Peng, J. Zhou, C. Zhang, and N. Sun, “Modeling and combined application of orthogonal chaotic NSGA-II and Improved TOPSIS to optimize a conceptual hydrological model,” *Water Resources Management*, pp. 1–19, 2018.
- [31] D. Xue, C. Zhao, and Y. Chen, “A modified approximation method of fractional order system,” in *Proceedings of the IEEE International Conference on Mechatronics and Automation*, pp. 1043–1048, 2006.
- [32] I. Podlubny, “Fractional-order systems and PIAD μ -controllers,” in *Proceedings of the IEEE Trans on Automatic Control*, vol. 44, 1999.
- [33] M. Zamani, M. Karimi-Ghartemani, N. Sadati, and M. Parniani, “Design of a fractional order PID controller for an AVR using particle swarm optimization,” *Control Engineering Practice*, vol. 17, no. 12, pp. 1380–1387, 2009.
- [34] C. Li, Y. Mao, J. Zhou, N. Zhang, and X. An, “Design of a fuzzy-PID controller for a nonlinear hydraulic turbine governing system by using a novel gravitational search algorithm based on Cauchy mutation and mass weighting,” *Applied Soft Computing*, vol. 52, pp. 290–305, 2017.
- [35] Y. Xu, C. Li, Z. Wang, N. Zhang, and B. Peng, “Load frequency control of a novel renewable energy integrated micro-grid containing pumped hydropower energy storage,” *IEEE Access*, vol. 6, pp. 29067–29077, 2018.
- [36] H. Jain and K. Deb, “An evolutionary many-objective optimization algorithm using reference-point based nondominated sorting approach, Part II: Handling constraints and extending to an adaptive approach,” *IEEE Transactions on Evolutionary Computation*, vol. 18, no. 4, pp. 602–622, 2014.
- [37] K. Deb, S. Agrawal, A. Pratap, and T. Meyarivan, “A fast elitist non-dominated sorting genetic algorithm for multi-objective optimization: NSGA-II,” in *Proceedings of the International Conference on Parallel Problem Solving From Nature*, vol. 1917, pp. 849–858.
- [38] S. Poles, Y. Fu, and E. Rigoni, *The effect of initial population sampling on the convergence of multi-objective genetic algorithms*, Springer, Berlin, German, 2009.
- [39] W. Fu, K. Wang, C. Li, X. Li, Y. Li, and H. Zhong, “Vibration trend measurement for a hydropower generator based on optimal variational mode decomposition and an LSSVM improved with chaotic sine cosine algorithm optimization,” *Measurement Science and Technology*, vol. 30, no. 1, p. 015012, 2019.
- [40] H. Lu, R. Niu, J. Liu, and Z. Zhu, “A chaotic non-dominated sorting genetic algorithm for the multi-objective automatic test task scheduling problem,” *Applied Soft Computing*, vol. 13, no. 5, pp. 2790–2802, 2013.
- [41] T. Habutsu, Y. Nishio, I. Sasase, and S. Mori, “A secret key cryptosystem by iterating a chaotic map,” in *International Conference on Theory and Application of Cryptographic Techniques*, pp. 127–140, 1991.
- [42] K. Deb, A. Pratap, S. Agarwal, and T. Meyarivan, “A fast and elitist multiobjective genetic algorithm: NSGA-II,” *IEEE Transactions on Evolutionary Computation*, vol. 6, no. 2, pp. 182–197, 2002.
- [43] K. Deb, L. Thiele, M. Laumanns, and E. Zitzler, “Scalable multi-objective optimization test problems,” in *Proceedings of the Congress on Evolutionary Computation (CEC ’02)*, pp. 825–830, May 2002.
- [44] X. Lai, C. Li, N. Zhang, and J. Zhou, “A multi-objective artificial sheep algorithm,” *Neural Computing and Applications*, 2018.
- [45] K. Deb and H. Jain, “An evolutionary many-objective optimization algorithm using reference-point-based nondominated sorting approach, part I: solving problems with box constraints,” *IEEE Transactions on Evolutionary Computation*, vol. 18, no. 4, pp. 577–601, 2014.
- [46] K. Deb, *Multiobjective Optimization Using Evolutionary Algorithms*, New York, NY, USA, Wiley, 2001.
- [47] C. Zhang, J. Zhou, C. Li, W. Fu, and T. Peng, “A compound structure of ELM based on feature selection and parameter optimization using hybrid backtracking search algorithm for wind speed forecasting,” *Energy Conversion and Management*, vol. 143, pp. 360–376, 2017.

Research Article

Estimation of Climatic Parameters of a PV System Based on Gradient Method

Rabiaa Gammoudi ¹, Houda Brahmi ² and Rachid Dhifaoui³

¹Department of Electrical Engineering, National High School of Engineering of Tunis (ENSIT), Avenue Taha Hussein Montfleury, 1008 Tunis, Unit of Research ERCO-INSAT, Tunisia

²University Tunis el Manar, Higher Institute of Medicals Technologies of Tunis (ISTMT), 9 Rue Zouhair Essafi, 1006 Tunis, Unit of Research ERCO-INSAT, Tunisia

³University of Carthage, National Institute of Applied Sciences and Technologies, Centre Urbain Nord BP 676, 1080 Tunis Cedex, Unit of Research ERCO-INSAT, Tunisia

Correspondence should be addressed to Houda Brahmi; houda.brahmi@istmt.utm.tn

Received 25 October 2018; Revised 2 January 2019; Accepted 28 January 2019; Published 18 February 2019

Guest Editor: Aitor J. Garrido

Copyright © 2019 Rabiaa Gammoudi et al. This is an open access article distributed under the Creative Commons Attribution License, which permits unrestricted use, distribution, and reproduction in any medium, provided the original work is properly cited.

The behavior of a photovoltaic generator is generally described by its current-voltage characteristic whose appearance depends on the climatic conditions (temperature and solar radiation). The aim of this work is to show the possibility of identifying the values of these two parameters from an experimental curve $I_{pv}(V_{pv})$ using numerical method. Subsequently, we will also estimate the series and shunt resistors of the equivalent scheme of a PVG. This estimate is certainly beneficial to properly evaluate its energy balance. The integration of these resistances allows us to obtain a new model. In this work, we will propose a mathematical calculation strategy to ensure the estimation of all the parameters.

1. Introduction

It is now recognized internationally that the supply of energy, in its various forms, contributes to the sustainable development of the countries. In this context, fossil fuels (oil, gas, uranium, etc.), despite their contributions, have disadvantages in terms of capacity that comes from the deterioration of the world's reserves and in terms of the impact on the environment. The latter is visible by the rejection of greenhouse gases that causes global warming. These disadvantages give rise to technologies that help the exploitation of inexhaustible clean natural energies. In recent decades, as a result of improved panel performance, photovoltaic, as well as the progression of benefits including subsidies, the profitability of a photovoltaic installation has become justified [1, 2].

The output characteristics of a photovoltaic panel depend essentially on the solar radiation to which it is subjected and its temperature, which makes the knowledge of these two parameters is very important. These two quantities can be

measured using sensors, also they can be estimated in order to minimize the number of sensors used which is a very important factor in the design of photovoltaic systems.

The model of a photovoltaic cell with a single diode is the most used thanks to the simplification of the equivalent electrical circuit which makes it possible to describe the behavior of the cell with the minimum of equations. For constant climatic conditions, this model has five parameters. In the case of variable climatic conditions, these parameters change in consequence. The estimation of the series and shunt resistance of the photovoltaic generator equivalent diagram is certainly beneficial to correctly evaluate its energy balance [3, 4].

In this work, in order to treat the characteristics and to analyze the impact of the variations of the quantities intervening from it from a practical point of view, we study the case of the photovoltaic panel TITAN-12-50 of ERCO-INSAT laboratory.

In the first part, we will be interested in the mathematical model of a photovoltaic cell, the developed model takes

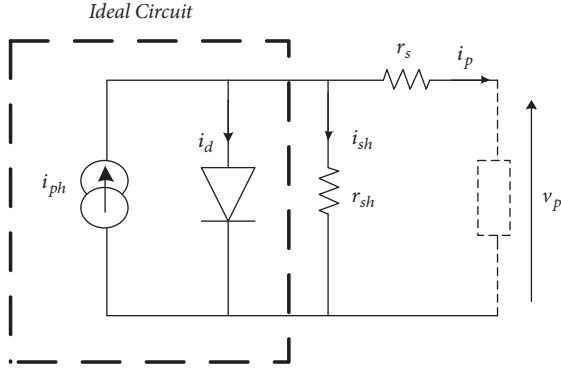


FIGURE 1: Equivalent circuit of real solar cell.

into account climatic variations such as temperature, solar radiation and wind speed. Support simulations are presented to show the dynamic behavior of the system. These simulations show that the shunt and series resistances are influenced by the climatic parameters or the interest of estimating them in real time. In the second part the expression of the two resistances has been developed. The efficiency of the new model has been validated experimentally while using a Dspace1104 card. The third part revolves around the estimation of two main parameters (solar radiation and temperature) through an algebraic strategy from an experimental curve $I_{pv}(V_{pv})$. Finally, we did a case study on the TITAN 12-50 panel installed on the roof of the ERCO-INSAT research unit.

2. Modeling of Solar Cell and Experimental Database

The equivalent circuit of a photovoltaic cell is given by Figure 1.

In the sense of this model, we can write the following relation:

$$i_{ph} = i_d + i_{pv} + i_{sh} = i_d + i_{pv} + \frac{v_{pv} + r_s i_{pv}}{r_{sh}} \quad (1)$$

with v_{pv} and i_{pv} being, respectively, the output voltage and the output current of PV cell. r_s and r_{sh} are the series and shunt resistors of the cell, i_{sh} is the current passing in the r_{sh} resistance, and i_d is the current of the diode.

The current of the diode i_d is strongly related to the temperature and the gap energy of the junction. It also depends on the voltage across the diode. It is given by the equation below:

$$i_d = i_s \left(\exp \left(\frac{v_{pv} + r_s i_{pv}}{v_t} \right) - 1 \right) \quad (2)$$

where i_s is the reverse saturation current of the diode and v_t is the solar cell thermal voltage.

The inverse saturation current and the thermal voltage are given by the following equations:

$$i_s = i_s(T_j) = i_{sr} \left(\frac{T_j}{T_{jr}} \right)^3 \exp \left(w_g \left(\frac{1}{v_{tr}} - \frac{1}{v_t} \right) \right) \quad (3)$$

$$v_t = \frac{\mathcal{K}_I \mathcal{K}_B T_j}{q}, \quad (4)$$

$$v_{tr} = \frac{\mathcal{K}_I \mathcal{K}_B T_{jr}}{q}$$

where $v_{tr} = \mathcal{K}_I \mathcal{K}_B / q$.

We note here that the index (r) used in this paper indicates that the value corresponds to the STC condition (Standard Test Condition: $E = E_s = 1000 \text{ W/m}^2$, $T_A = T_{Ar} = 25^\circ \text{C}$).

w_g is the energy of gap, \mathcal{K}_B Boltzmann constant, \mathcal{K}_I coefficient of ideality, and q the electron charge, and the main variable of this model is the temperature of the p-n junction of the diode T_j (expressed in $^\circ \text{K}$).

The following model was adopted taking into account variations in solar radiation, wind speed, and ambient temperature T_A .

$$T_j = T_A (^\circ \text{C}) + 273.15 + 33.75 E_s f_W(\vartheta_W) \quad (5)$$

The solar radiation E_s is expressed in W/m^2 and the function $f_W(\vartheta_W)$ introduces the effect of the wind speed.

$$f_W(\vartheta_W) = \exp(-\gamma(\vartheta_W - 1)) \quad \vartheta_W \geq 1 \quad (6)$$

The parameter γ must be positive for the function to vary in the opposite direction of the wind speed. Indeed the increase of the wind speed makes the solar cell cool [5].

The current of solar photons i_{ph} is strongly dominated by a variation of solar radiation and very slightly variable under the effect of the temperature. Given these properties, the current of photons is governed by the following model.

$$i_{ph} = i_{ph}(E_s, T_j) = E_s [i_{phr} + k_T (T_j - T_{jr})] \quad (7)$$

k_T is the temperature coefficient that depends a lot on the manufacturing technology and it is basically provided by the manufacturer.

Table 1 gives the values of the different quantities used in PVG model.

All the quantities related to the climatic conditions are defined. The electrical behavior in charge of the solar cell will be described by (8).

$$f(v_{pv}, i_{pv}) = i_{pv} - i_{ph} + i_s \left(\exp \left(\frac{v_{pv} + r_s i_{pv}}{v_t} \right) - 1 \right) + \frac{v_{pv} + r_s i_{pv}}{r_{sh}} \quad (8)$$

This function is a nonlinear function and involves several variables. In order to resolve it, we need a numerical method; in this work Newton-Raphson method is exploited [6].

The nominal powers of solar cells are always limited to a few watts. So the solution in this case is to switch to serial-parallel coupling of several cells. Solar energy is marketed in the form of panels or photovoltaic generator [7–9].

A PVG is a configuration comprising Np rows in parallel; each of the rows is formed by Ns panels in series, with each

TABLE 1: Quantities related to the physical model of the solar cell.

Notation	Designation	Numerical values
E_{sr}	Reference solar radiation (w/m ²) in STC	1000
T_{Ar}	Ambient temperature (°C) in STC	25
T_{jr}	Reference junction temperature (°K) in STC	298.15
w_g	Energy of gap (eV)	1.12
q	Electron charge (C)	1.602×10^{-19}
K_B	Boltzmann constant (J/°K)	1.38065×10^{-23}
K_I	Constant of ideality	1==>2
k_T	Temperature coefficient (A/°C)	0.0032

panel being itself formed of ns series cells. So we finally get the following.

$$\begin{aligned} I_{pv} &= i_{pv} \times N_p, \\ V_{pv} &= n_s \times N_s \times v_{pv} \end{aligned} \quad (9)$$

For this purpose, we denote, respectively, by I_{pv} and V_{pv} the current and the voltage of PVG.

So, finally we get for a photovoltaic generator the following mathematical model (10):

$$\begin{aligned} F(I_p, V_p) &= I_p - I_{ph} + I_s \left(\exp\left(\frac{V_p + R_s I_p}{V_t}\right) - 1 \right) \\ &+ \frac{V_p + R_s I_p}{R_{sh}} = 0 \end{aligned} \quad (10)$$

with

$$\begin{aligned} R_s &= \frac{N_s n_s r_s}{N_p} \\ R_{sh} &= N_s n_s r_{sh} \\ I_s &= N_p i_s \\ I_{ph} &= N_p i_{ph} \\ V_T &= N_s n_s v_T. \end{aligned} \quad (11)$$

2.1. Nonlinear Characteristic $I_{pv} = f(V_{pv})$. The mathematical model of a photovoltaic generator is expressed in the following form.

$$f = I_{pv} - I_{ph} - I_s + \mathcal{F}_s + \mathcal{F}_{sh} = 0 \quad (12)$$

To arrange the calculation in the simplest way and therefore as clear as possible, we will define the following quantities.

$$\mathcal{F}_s(V_{pv}, I_{pv}) = I_s \exp\left(\frac{V_{pv} + R_s I_{pv}}{V_T}\right) \quad (13)$$

$$\mathcal{F}_{sh}(V_{pv}, I_{pv}) = \frac{V_{pv} + R_s I_{pv}}{R_{sh}} = G_{sh}(V_{pv} + R_s I_{pv}) \quad (14)$$

We must solve the following system with two variables V_{pv} and I_{pv} .

$$f(V_{pv}, I_{pv}) = I_{pv} - I_{ph} - I_s + \mathcal{F}_s + \mathcal{F}_{sh} = 0 \quad (15)$$

This function is nonlinear; the most appropriate method for its resolution is the method of "Newton Raphson". This technique requires the development of the Jacobian matrix. The elements of this matrix are defined below.

$$J = \begin{bmatrix} \frac{\partial f}{\partial I_{pv}} & \frac{\partial f}{\partial V_{pv}} \end{bmatrix} \quad (16)$$

$$\frac{\partial f}{\partial I_{pv}} = 1 + \frac{R_s \mathcal{F}_s}{V_t} + R_s G_{sh} \quad (17)$$

$$\frac{\partial f}{\partial V_{pv}} = \frac{\mathcal{F}_s}{V_t} + G_{sh}$$

Table 2 gives the main data of the solar panel TITAN-12-50.

2.2. Influence of Solar Radiation on the Classic Model. To show the influence of solar radiation on the $I_{pv} = f(V_{pv})$ characteristic from the previously developed database, the characteristics are measured at the same constant temperature of 26°C and different solar radiation ranging from 200 to 900 W/m² as shown in Figure 2. It can be seen that the short-circuit current varies in the same direction as the solar radiation while the open circuit voltage varies slightly with the solar radiation.

2.3. Influence of Temperature on the Classic Model. For different temperatures and with a constant solar radiation equal to 600W/m², we acquire the voltage at the terminals of the PVG and the current flow as shown in Figure 3.

We notice that the short-circuit current is not sensitive to the variation of the temperature. On the other hand, the open circuit voltage varies in the opposite direction of the temperature.

3. Estimation of Series and Shunt Resistances

The estimation of the series and shunt resistances of the equivalent PVG scheme is certainly beneficial to correctly evaluate its energy balance.

3.1. Influence of Series Resistance on the Classic Model. For different values of the series resistance, the behavior of the PVG generator was simulated by plotting the $I_{pv} = f(V_{pv})$ characteristics. Figure 4 shows the evolution of the PV

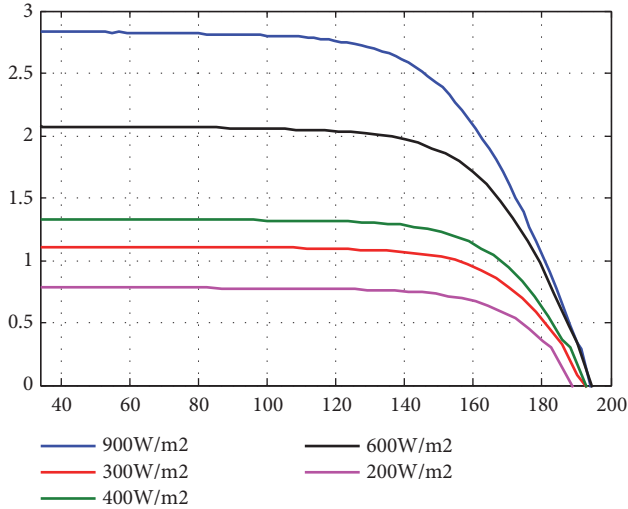


FIGURE 2: Influence of solar radiation on the $I_{pv} = f(V_{pv})$ characteristic.

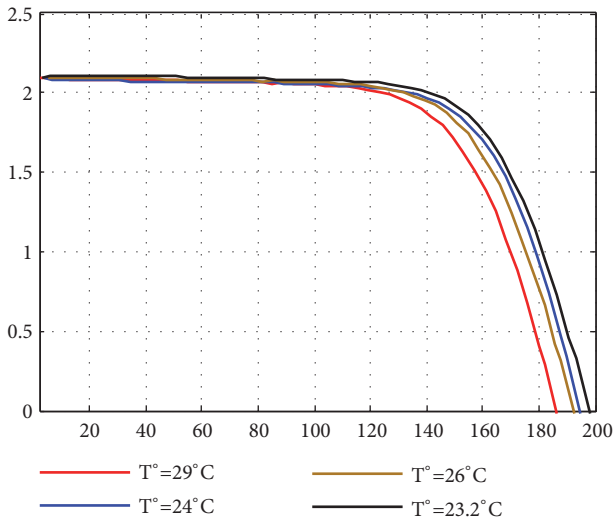


FIGURE 3: Influence of temperature on the $I_{pv} = f(V_{pv})$ characteristic.

current with the PV voltage for different values of series resistance.

It is noted that the short-circuit current and the open circuit voltage are not affected by the variation of the series resistance. On the other hand, the slope of the characteristic is very sensitive to this variation. The slope variation affects the maximum power as shown in Figure 5.

So, we can say here that the increase of the series resistance weakens the optimal power. This result is very obvious because a part of the power produced would be lost by Joule effect.

3.2. Influence of Shunt Resistance on the Classic Model. We will now set the value of the series resistance to see the influence of the shunt resistor, Figure 6.

TABLE 2: Electrical parameters of the solar panel TITAN-12-50.

Name	Manufacturer	TITAN
Description		STP-50-01
Cell types		Polycrystalline
Cell size		100cm ²
Cell number		36
Rated power		50Wc
Power tolerance		±5%
Optimal voltage		17.2V
Optimal current		2.9A
Open circuit voltage		21V
Short circuit current		3.4A
Efficiency		11.3%
Manufacturer's warranty		20 years

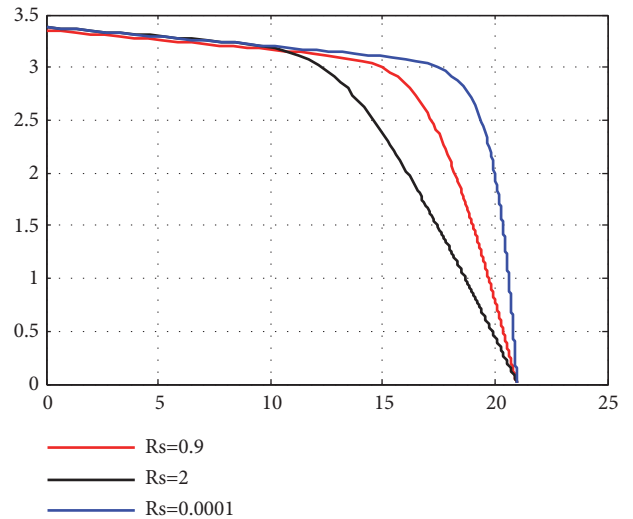


FIGURE 4: Influence of series resistance on the $I_{pv} = f(V_{pv})$ characteristic.

Like the series resistor, the shunt resistor also does not have an influence on the open circuit voltage and the short-circuit current. The effect of the shunt resistor is very focused on the optimum operating point of the PVG, Figure 7.

The increase in shunt resistance slightly weakens the optimal power. The joules losses due to the shunt resistor remain much lower than those due to the series resistance.

I_{phr} and I_{sr} are, respectively, the saturation and photons currents in the reference regime. The values of these quantities are usually evaluated from two particular regimes. For the open circuit and short-circuit regimes, the experience confirms that the effect of series and shunt resistances is almost negligible regardless of the weather conditions.

In open circuit regime, we have the following.

$$\begin{aligned} V_{pv} &= V_{oc} \\ I_{pv} &= 0 \end{aligned} \quad (18)$$

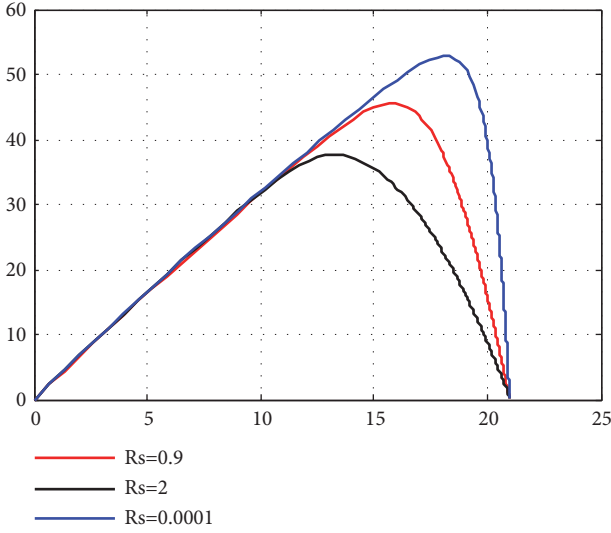


FIGURE 5: Influence of serie resistance on the $P_{pv} = f(V_{pv})$ characteristic.

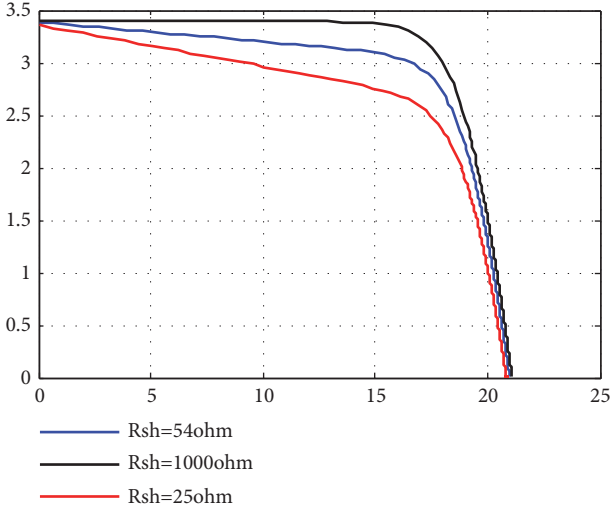


FIGURE 6: Influence of shunt resistance on the $I_{pv} = f(V_{pv})$ characteristic.

So, we obtain the following.

$$\begin{aligned}
 I_{ph} - I_d - I_{pv} - I_{sh} &= 0 \\
 I_{ph} - I_s \left(\exp\left(\frac{V_{oc}}{V_t}\right) - 1 \right) &= 0 \\
 I_{ph} &= I_s \left(\exp\left(\frac{V_{oc}}{V_t}\right) - 1 \right)
 \end{aligned} \tag{19}$$

In short-circuit regime, we have the following.

$$\begin{aligned}
 V_{pv} &= 0 \\
 I_{pv} &= I_{cc}
 \end{aligned} \tag{20}$$

So, we obtain the following.

$$I_{ph} = I_{cc} \tag{21}$$

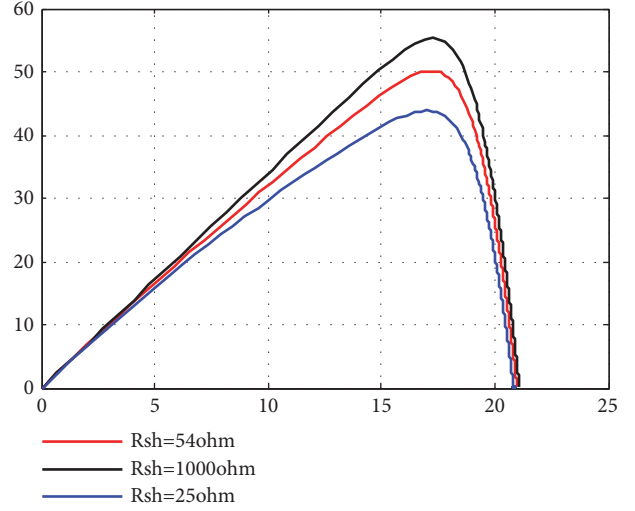


FIGURE 7: Influence of shunt resistance on the $P_{pv} = f(V_{pv})$ characteristic.

Back to the open circuit regime, we can write the following in reference climatic condition.

$$I_{sr} = \frac{I_{phr}}{\left(\exp(V_{ocr}/V_{tr}) - 1\right)} = I_{ccr} \exp\left(-\frac{V_{ocr}}{V_{tr}}\right) \tag{22}$$

3.3. Estimation of Series Resistance. The internal conductance of the photovoltaic generator in any mode satisfies the relation below.

$$G_{pv}(V_{pv}, I_{pv}) = \frac{\partial I_{pv}}{\partial V_{pv}} = -\frac{G_{sh}V_T + \mathcal{F}_s}{V_T + R_s \mathcal{F}_s + V_T R_s G_{sh}} \tag{23}$$

To estimate the value of the series resistor, it is necessary to carry out an open circuit test because the effect of the series resistance is manifested in the vicinity of the open circuit operation, unlike the effect of the shunt resistor, which remains insignificant. The value of the series resistance is estimated by the following relation.

$$R_s = -\frac{\partial V_{pv}}{\partial I_{pv}} \quad \text{when } I_{pv} = 0 \text{ and } V_{pv} = V_{oc} \tag{24}$$

By applying (23) in (24), we can deduce the following.

$$\begin{aligned}
 R_s &= -\frac{1}{G_{pv}(V_{oc}, 0)} = \frac{V_t}{I_s \exp(V_{oc}/V_t)} \\
 &= \frac{V_t}{I_s} \exp\left(-\frac{V_{oc}}{V_t}\right)
 \end{aligned} \tag{25}$$

Under Standard Test Conditions (STC), we consider the following peer relationship.

$$R_{sr} = \frac{V_{tr}}{I_{sr}} \exp\left(-\frac{V_{ocr}}{V_{tr}}\right) \tag{26}$$

Applying the expression of I_{sr} , we obtain the following.

$$R_{sr} = \frac{V_{tr}}{I_{ccr}} \left(1 - \exp\left(-\frac{V_{ocr}}{V_{tr}}\right)\right) \tag{27}$$

3.4. Estimation of Shunt Resistance. The effect of the shunt resistor is significant around the point of short-circuit operation, so it is necessary to perform a short-circuit test to estimate this resistance.

The conductance G_{sh} has the following expression:

$$G_{sh} = -\frac{\partial I_{pv}}{\partial V_{pv}} \quad \text{when } I_{pv} = I_{cc} \text{ and } V_{pv} = 0 \quad (28)$$

or, in other terms,

$$G_{sh} = -\mathcal{G}_{pv}(0, I_{cc}) = \frac{G_{sh}V_t + \mathcal{F}_{scc}}{V_t + R_s\mathcal{F}_{scc} + V_tR_sG_{sh}} \quad (29)$$

$$\mathcal{F}_{scc} = \mathcal{F}_s(0, I_{cc}) = I_s \exp\left(\frac{R_s I_{cc}}{V_t}\right)$$

so, finally we get (30).

$$\begin{aligned} V_t R_s G_{sh}^2 + \left(R_s I_s \exp\left(\frac{R_s I_{cc}}{V_t}\right)\right) G_{sh} \\ - I_s \exp\left(\frac{R_s I_{cc}}{V_t}\right) = 0 \end{aligned} \quad (30)$$

It is a second-order equation, and its solution passes by the computation of the discriminate, in which the square of the saturation current is involved, which is a very small quantity. We can thus eliminate the second term of this equation and estimate the shunt resistance by the following.

$$R_{sh} = \sqrt{\frac{R_s V_t}{I_s} \exp\left(-\frac{R_s I_{cc}}{V_t}\right)} \quad (31)$$

In STC, this relation becomes as follows.

$$R_{shr} = \sqrt{\frac{R_{sr} V_{tr}}{I_{sr}} \exp\left(-\frac{R_{sr} I_{ccr}}{V_{tr}}\right)} \quad (32)$$

This relation shows on one side a term proportional to the temperature and on the other side a second term, which decreases exponentially with the temperature.

3.5. Validation of the Proposed Model: Checking of the Evolution of Open Circuit Voltage with Temperature. The manufacturer supplies, under STC conditions, a coefficient of sensitivity of the open circuit voltage versus the value temperature. So, we can write the following.

$$\begin{aligned} V_{oc} &= V_{ocr} - 0.0798 (T_A - T_{Ar}) \\ &= 22.9950 - 0.0798 T_A \end{aligned} \quad (33)$$

Moreover, in the sense of the model, the open circuit voltage verifies.

$$V_{oc} = V_T \log\left(1 + \frac{I_{ph}}{I_s}\right) \quad (34)$$

The curves in Figure 8 correspond, respectively, to formula (33) given by constructor and to formula (34). The difference between the two curves is acceptable.

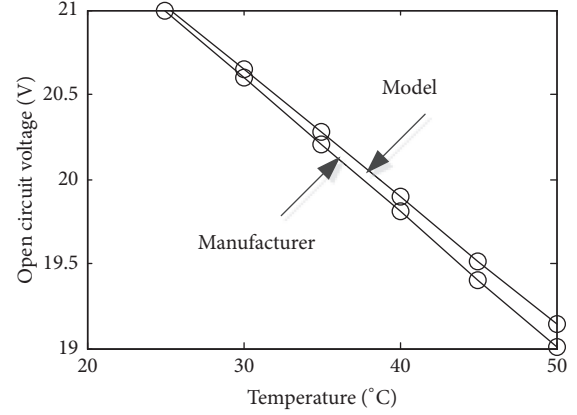


FIGURE 8: Variation of the open circuit voltage of the TITAN-12-50 panel with temperature.

3.6. Experimental Validation. To validate the previously proposed model, the photovoltaic panels installed at the research unit were exploited. The experimental installation comprises a photovoltaic generator whose characteristics are given in Table 2, a voltage sensor, a solar radiation sensor, and a temperature sensor. This experimental bench is controlled by a DS1104 dSPACE card.

The proposed strategy is implemented and tested in real time with a sampling frequency of 10 kHz. Figure 9 shows the complete configuration of the system described above.

Figures 10 and 11 show, respectively, the scenario of solar radiation and the comparison between the measured voltage and the voltage estimated by the developed model. It is constant that the tensions converge towards the same value whatever the variation of the solar radiation.

4. Estimation of Solar Radiation and Temperature

To measure the temperature, it is necessary to provide the solar panel with an integrated temperature sensor, which would greatly increase the cost on the one hand and complicate its manufacture on the other hand. A possible indirect solution for the junction temperature evaluation would be to identify it from the measurement results and establish a link with the ambient temperature.

With regard to solar radiation, the hardware solution of placing multiple solar radiation sensors would obviously increase the cost of installation [10–13]. The purpose of this section is to show the possibility of identifying the values of solar radiation and temperature from an experimental point of view.

Before going on to the method of the estimation of the solar radiation and the temperature for a photovoltaic system, we will present the notions of the adapted gradient method.

4.1. Quadratic Minimization by the Conjugate Gradient Method. The optimization, especially numerical optimization, has experienced a significant increase in recent years with the advent of the computer. It is often the last stage

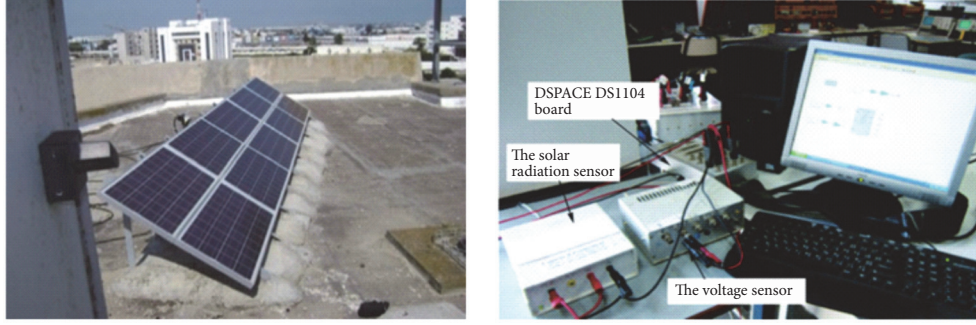


FIGURE 9: Configuration of the studied system.

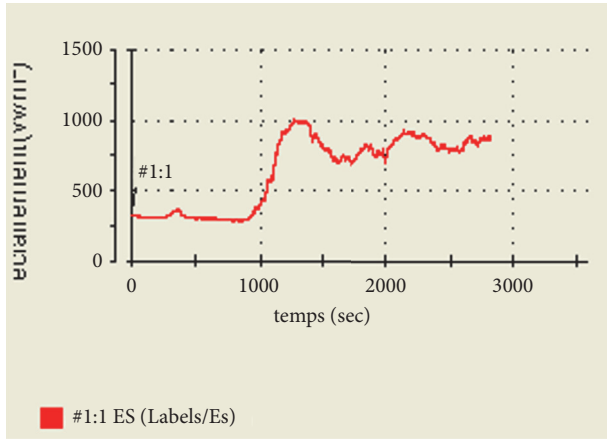
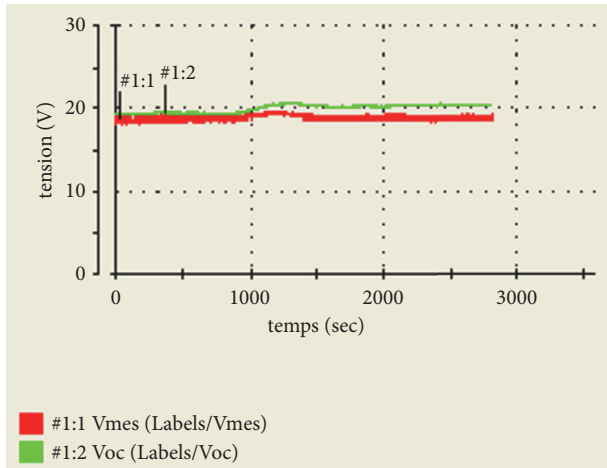


FIGURE 10: Variation of solar radiation.

FIGURE 11: Comparison between measured and estimated open circuit voltage (V_{oc} and V_{mes}).

of numerical analysis, where we have studied a physical phenomenon, put it into an equation, studied these equations, and shown that one could calculate the solutions with a computer. We begin to optimize the system by changing some parameters to change the solution in a desired direction.

Several methods are used for numerical optimization such as Newton's method, the quasi-Newton method, the conjugate gradient method, linear search, the regions of trust, and Nelder-Mead's method.

In this part, we will use the conjugate gradient method to minimize a nonlinear function $\Phi(\underline{X})$ differentiable at least twice.

The development of the Taylor series function $\Phi(\underline{X})$ around an initial condition \underline{X}_0 is expressed as follows.

$$\begin{aligned} \Phi(\underline{X}_0 + \underline{\Delta X}) \cong & \Phi(\underline{X}_0) + \sum_i \left. \frac{\partial \Phi}{\partial x_i} \right|_{\underline{X}_0} \Delta x_i \\ & + \frac{1}{2} \sum_{i,j} \left. \frac{\partial^2 \Phi}{\partial x_i \partial x_j} \right|_{\underline{X}_0} \Delta x_i \Delta x_j \end{aligned} \quad (35)$$

This equation can be further rewritten in the following form involving the gradient vector \underline{G} and the Hessian matrix H of the second derivatives evaluated in \underline{X}_0 . The Hessian matrix constitutes the Jacobian matrix of the gradient vector.

$$\Phi(\underline{X}_0 + \underline{\Delta X}) \cong \Phi(\underline{X}_0) + \underline{G}_0^T \underline{\Delta X} + \frac{1}{2} \underline{\Delta X}^T H_0 \underline{\Delta X} \quad (36)$$

$$\underline{G}_0 = \underline{G}(\underline{X}_0) = \left. \frac{\partial \Phi}{\partial \underline{X}} \right|_{\underline{X}_0} \quad (37)$$

$$H_0 = H(\underline{X}_0) = \left[\left. \frac{\partial \underline{G}(\underline{X})}{\partial \underline{X}} \right]_{\underline{X}_0}$$

In expanded form, the matrix $H(\underline{X})$ is symmetric and has the following expression.

$$h_{ij} = h_{ji} = \frac{\partial g_i}{\partial x_j} = \frac{\partial g_j}{\partial x_i} = \frac{\partial^2}{\partial x_i \partial x_j} = \frac{\partial^2}{\partial x_j \partial x_i} \quad (38)$$

The solution of minimizing a quadratic problem of the type below using the conjugate gradient method is given by the following system.

$$\begin{aligned} & \min_{\underline{X}} \Phi(\underline{X}) \\ \Phi(\underline{X}) = & \frac{1}{2} \underline{X}^T H \underline{X} + \underline{C}^T \underline{X} \end{aligned} \quad (39)$$

To minimize the function $\Phi(\underline{X})$ we could proceed to a local minimization in terms of $\Delta \underline{X}$ with \underline{G}_0 and H_0 constant and repeat the same calculation as many times as necessary by rectifying each time the initial condition, the gradient vector, and the Hessian matrix. Obviously, it is admitted here that the Hessian matrix remains positive, which is often the case.

4.2. Estimation of Solar Radiation and Temperature: Minimizing the $V_p(I_p)$ Function. In this section, we are interested in the identification of E_s and V_t parameters from a given (V_{pv}, I_{pv}) operating point.

As we have already presented in the first section, the model of a photovoltaic generator is described by the following.

$$f = I_p - I_{ph} - I_s + \mathcal{F}_s + \mathcal{F}_{sh} = 0 \quad (40)$$

The different terms of this model are defined as follows.

$$\begin{aligned} V_T &= \eta T_j \\ V_{Tr} &= \eta T_{jr} \\ I_{ph} &= E_s [I_{ccr} + K_{Tr} (V_T - V_{Tr})] \\ I_s &= I_{sr} \left(\frac{V_T}{V_{Tr}} \right)^3 \exp \left(\frac{W_g}{V_{Tr}} - \frac{W_g}{V_T} \right) \\ \mathcal{U}_p &= V_p + R_s I_p \\ \mathcal{F}_s &= I_s \exp \left(\frac{\mathcal{U}_p}{V_T} \right) \\ \mathcal{F}_{sh} &= G_{sh} \mathcal{U}_p \end{aligned} \quad (41)$$

The main variables of this model are, respectively, the voltage across the generator V_p and the current I_p delivered to the load. These quantities vary, of course, with the load, solar irradiance, and temperature. The solar radiation is denoted here as E_s . The junction temperature appears by the magnitude V_T , which is proportional to it, provided that the factor of constant ideality is considered. The parameters R_s and G_{sh} correspond, respectively, to the series resistance and the shunt conductance of the equivalent scheme. The other parameters are constants.

The mathematical model of a photovoltaic generator for a given operating point becomes as follows.

$$f(V_T, E_s) = 0 \quad (42)$$

Before exposing the identification technique used, it is necessary to develop the first and second derivatives of the terms of the function f of the model with respect to these parameters. We establish the following.

$$\begin{aligned} u_p &= V_{pv} + R_s I_{pv} \\ \frac{\partial I_{ph}}{\partial V_t} &= E_s K_{Tr} \\ \frac{\partial I_{ph}}{\partial E_s} &= I_{ccr} + K_{Tr} (V_t - V_{tr}) \end{aligned}$$

$$\frac{\partial I_s}{\partial V_t} = I_s \left(\frac{3V_t + W_g}{V_t^2} \right)$$

$$\frac{\partial \mathcal{F}_s}{\partial V_t} = \mathcal{F}_s \left(\frac{3V_t + W_g - u_p}{V_t^2} \right)$$

$$\frac{\partial^2 I_{ph}}{\partial E_s^2} = \frac{\partial^2 I_{ph}}{\partial V_t^2} = 0$$

$$\frac{\partial^2 I_s}{\partial V_t^2} = I_s \left(\frac{(2V_t + W_g)^2 + 2V_t^2}{V_t^4} \right)$$

$$\frac{\partial^2 \mathcal{F}_s}{\partial V_t^2} = \mathcal{F}_s \left(\frac{(2V_t + W_g - u_p)^2 + 2V_t^2}{V_t^4} \right)$$

(43)

Let us consider an experimental point (V_{pv}, I_{pv}) raised to solar radiation and temperature supposed unknown. The injection of this point into the function f of the mathematical model (40) would lead to a nonzero value because of the error between the real values of the parameters and the values used in the model.

By denoting by \underline{X} the vector of the parameters (V_t, E_s) to be identified, the function (40) of the model would be denoted accordingly by $f(\underline{X})$. The object is to determine the vector \underline{X} that makes $f(\underline{X})$ tend to zero.

In order to take advantage of the available digital quadratic programming tools, we perform the minimization of the following quadratic criterion.

$$\Phi(\underline{X}) = \frac{1}{2} f^2(\underline{X}) \quad (44)$$

The Taylor series development expresses $\Phi(\underline{X})$ as follows:

$$\Phi(\underline{X}_0 + \underline{x}) = \Phi(\underline{X}_0) + \underline{G}_0 \underline{x} + \frac{1}{2} \underline{x} H_0 \underline{x} \quad (45)$$

where \underline{G}_0 and H_0 are, respectively, the gradient vector and the Hessian matrix of $\Phi(\underline{X})$ around an initial condition \underline{X}_0 . The vector \underline{x} corresponds to the variation to be made around \underline{X}_0 .

The gradient vector and the Hessian matrix are expressed as follows.

$$\underline{G}(\underline{X}) = \frac{\partial \Phi}{\partial \underline{X}} = f(\underline{X}) \frac{\partial f(\underline{X})}{\partial \underline{X}} \quad (46)$$

$$H(\underline{X}) = \frac{\partial \underline{G}(\underline{X})}{\partial \underline{X}}$$

By involving the sensitivity relationships defined above, the gradient vector $\underline{G}(\underline{X})$ has for relation (47) the following.

$$\begin{aligned} \psi_1 &= \frac{\partial f}{\partial V_t} = \frac{\partial I_{pv}}{\partial V_t} - \frac{\partial I_{ph}}{\partial V_t} - \frac{\partial I_s}{\partial V_t} + \frac{\partial \mathcal{F}_s}{\partial V_t} + \frac{\partial \mathcal{F}_{sh}}{\partial V_t} \\ &= -\frac{\partial I_{ph}}{\partial V_t} - \frac{\partial I_s}{\partial V_t} + \frac{\partial \mathcal{F}_s}{\partial V_t} \end{aligned}$$

$$\begin{aligned}
&= -E_s K_{tr} - I_s \left(\frac{3V_t + W_g}{V_t^2} \right) \\
&\quad + \mathcal{F}_s \left(\frac{3V_t + W_g - u_p}{V_t^2} \right) \\
\psi_2 &= \frac{\partial f}{\partial E_s} = \frac{\partial I_{pv}}{\partial E_s} - \frac{\partial I_{ph}}{\partial E_s} - \frac{\partial I_s}{\partial E_s} + \frac{\partial \mathcal{F}_s}{\partial E_s} + \frac{\partial \mathcal{F}_{sh}}{\partial E_s} \\
&= -\frac{\partial I_{ph}}{\partial E_s} = -[I_{ccr} + K_{Tr}(V_t - V_{tr})] \\
\underline{G} &= \begin{bmatrix} \psi_1 \\ \psi_2 \end{bmatrix}
\end{aligned} \tag{47}$$

In order to simplify the calculation without losing too much on precision, the Hessian matrix could be expressed by the approximate Gaussian relation below.

$$H(\underline{X}) \simeq \left(\frac{\partial f(\underline{X})}{\partial \underline{X}} \right) \left(\frac{\partial f(\underline{X})}{\partial \underline{X}} \right)^T = \begin{bmatrix} \psi_1^2 & \psi_1 \psi_2 \\ \psi_1 \psi_2 & \psi_2^2 \end{bmatrix} \tag{48}$$

We can express exactly this matrix by the use of the following complete formula.

$$\begin{aligned}
H &= \begin{bmatrix} \psi_1 + \psi_3 f & \psi_1 \psi_2 - K_{Tr} f \\ \psi_1 \psi_2 - K_{Tr} f & \psi_2^2 \end{bmatrix} \\
\psi_3 &= \frac{\partial \psi_1}{\partial V_t} = \frac{\partial}{\partial V_t} \left(\frac{\partial f}{\partial V_t} \right) \\
&= \frac{\partial}{\partial V_t} \left(-\frac{\partial I_{ph}}{\partial V_t} - \frac{\partial I_s}{\partial V_t} + \frac{\partial \mathcal{F}_s}{\partial V_t} \right) = -\frac{\partial^2 I_s}{\partial V_t^2} + \frac{\partial^2 \mathcal{F}_s}{\partial V_t^2} \\
&= -I_s \left(\frac{(2V_t + W_g)^2 + 2V_t^2}{V_t^4} \right) \\
&\quad + \mathcal{F}_s \left(\frac{(2V_t + W_g - u_p)^2 + 2V_t^2}{V_t^4} \right)
\end{aligned} \tag{49}$$

The proposed technique is to iteratively apply the conjugate gradient method using $H(\underline{X})$ and $\underline{G}(\underline{X})$ as parameters of the quadratic problem. The algorithm consists of the following steps:

- (i) Give an initial condition \underline{X}_0 for the parameter vector \underline{X} .
- (ii) Calculate $\underline{G}(\underline{X}_0)$ and $H(\underline{X}_0)$ and readjust the limits of the variation vector \underline{x} .
- (iii) To seek the optimal solution of the quadratic problem by the constrained conjugate gradient technique to establish the correction \underline{x} necessary for the minimization of $\Phi(\underline{X})$ around \underline{X}_0 .

$$\min_{\underline{x}} \left(\frac{1}{2} \underline{x}^T H \underline{x} + \underline{G}^T \underline{x} \right) \tag{50}$$

$$\underline{x}_{min} \leq \underline{x} \leq \underline{x}_{max}$$

- (iv) Correct the parameter vector by $\underline{X}_0 = \underline{X}_0 + \underline{x}$ and return to step (ii).

TABLE 3: Different experimental values of the characteristics (V_{pv} , I_{pv}).

V_{pv}	I_{pv}
0	3.300
3.5353	3.2505
5.5500	3.2010
6.7962	3.1680
8.3215	3.1185
9.7205	3.0690
10.9567	3.0195
12.2502	2.9535
13.8727	2.8545
15.2266	2.7555
16.5322	2.5740
17.2528	2.4255
17.9818	2.1945
18.4340	1.9800
18.7883	1.7655
19.1226	1.5345
19.3951	1.3200
19.6467	1.1055
19.8972	0.8745
20.1202	0.6600
20.3465	0.4455
20.5306	0.2145
20.6500	0

4.3. Estimation of T_j and E_s (Application on the Photovoltaic Panel TITAN 12-50). Just to fix the ideas and check the relations, consider the constant parameters of the Table 1 and a function point corresponding to $V_p = 13.8727V$ and $I_p = 2.8545A$. Propose as initial conditions $\underline{X}_0 = [1.3 \ 1] = [V_T \ E_s]_0$.

With this initial condition, we calculate the following.

$$f_0 = -0.3045$$

$$\underline{G}_0 = \begin{bmatrix} -0.0580 \\ 0.9743 \end{bmatrix} \tag{51}$$

$$H_0 = \begin{bmatrix} 0.0362 & -0.6092 \\ -0.6092 & 10.2387 \end{bmatrix}$$

By completing the algorithm flow with the limits

$$\begin{bmatrix} 1 \\ 0.8 \end{bmatrix} \leq \underline{X} \leq \begin{bmatrix} 1.6 \\ 1.2 \end{bmatrix} \tag{52}$$

we reach the solution: $\underline{X} = [1.3056, 0.9052]$

$$V_T = 1.3056 \text{ and } E_s = 0.9052.$$

We note here that the estimated value of the solar radiation is divided by a ratio of 1000. Still as a test and validation of the developments made, consider the complete curve (V_{pv} , I_{pv}) given by Table 3 with the parameters of the TITAN-12-50 module already introduced in Table 2.

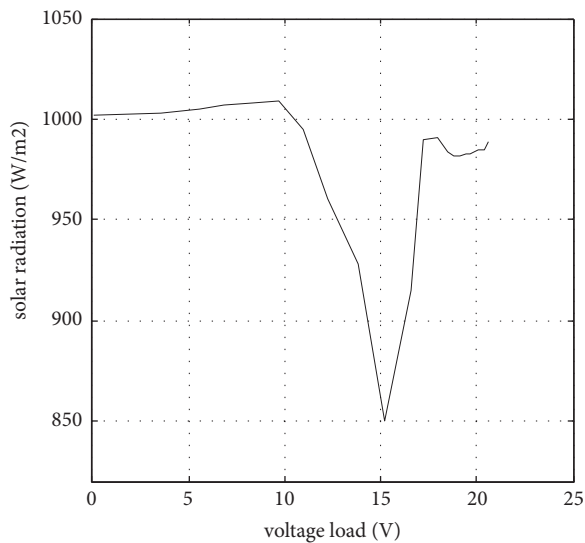


FIGURE 12: Variation of solar radiation with the load voltage.

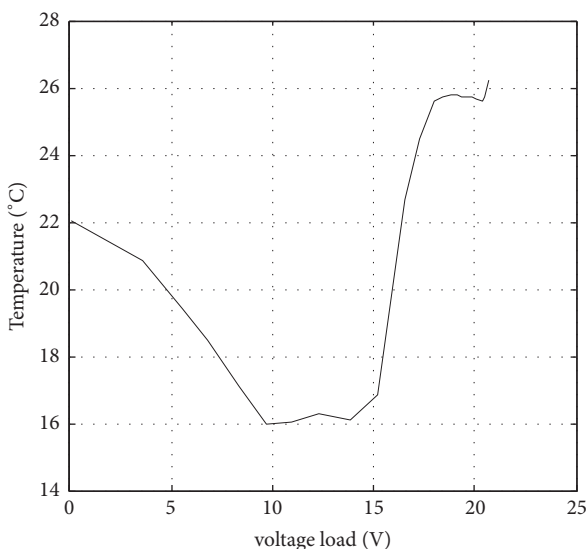


FIGURE 13: Variation of temperature with the load voltage.

Figures 12 and 13 give, respectively, the variation of solar radiation and the temperature with the load voltage

5. Conclusion

In this paper, we have proposed a method based on numerical development to estimate through an experimental curve the two main parameters influencing the operation of a PV system. In the same way, we estimated the two series and shunt resistors while showing the influence of the climatic conditions on these resistances, which allows us to develop a new model of a PVG. Finally, we showed the efficiency of this model experimentally using dSPACE 1104.

Data Availability

The parameters of the photovoltaic panel are included in the article, while the simulation programs used in the study are available from the corresponding author on request.

Conflicts of Interest

The authors declare that there are no conflicts of interest regarding the publication of this paper.

References

- [1] R. Gammoudi, N. Rebei, and O. Hasnaoui, "STM microcontroller implementation of MPPT algorithms for stand-alone PV Water Pumping System," *International Journal of Engineering and Technical Research (IJETR)*, 2015.
- [2] G. Lavidas and V. Venugopal, "Prospects and applicability of wave energy for South Africa," *International Journal of Solar Energy*, 2017.
- [3] R. A. M. Coetzee, A. Mwesigye, and Z. Huan, "A numerical model for optimal receiver array and mass flow rate in residential solar water heating systems," *International Journal of Sustainable Energy*, vol. 37, no. 9, pp. 902–918, 2017.
- [4] Y. V. Daus, I. V. Yudaev, and G. V. Stepanchuk, "Reducing the costs of paying for consumed electric energy by utilizing solar energy," *Applied Solar Energy*, vol. 54, no. 2, pp. 139–143, 2018.
- [5] N. Rebei, A. Hmidet, R. Gammoudi, and O. Hasnaoui, "Implementation of photovoltaic water pumping system with MPPT controls," *Frontiers in Energy*, vol. 9, no. 2, pp. 187–198, 2015.
- [6] H. Brahmi and R. Dhifaoui, "Dynamic characteristics and improved MPPT control of PV generator," *Frontiers in Energy*, vol. 7, no. 3, pp. 342–350, 2013.
- [7] R. H. Almeida, L. Narvarte, and E. Lorenzo, "PV arrays with delta structures for constant irradiance daily profiles," *Solar Energy*, vol. 171, pp. 23–30, 2018.
- [8] Y. V. Daus and V. V. Kharchenko, "Evaluating the applicability of data on total solar-radiation intensity derived from various sources of actinometric information," *Applied Solar Energy*, vol. 54, no. 1, pp. 71–76, 2018.
- [9] S. V. Kiseleva, O. S. Popel', A. B. Tarasenko, and R. R. Avezov, "Efficiency estimation for the grid-tie photovoltaic stations construction in some regions of Central Asia and Transcaucasia," *Applied Solar Energy*, vol. 53, no. 4, pp. 306–311, 2017.
- [10] F. dell'Isola, M. Cuomo, L. Greco, and A. Della Corte, "Bias extension test for pantographic sheets: numerical simulations based on second gradient shear energies," *Journal of Engineering Mathematics*, vol. 103, pp. 127–157, 2017.
- [11] J. Kaderli, J. Zweck, A. Safin, and S. E. Minkoff, "An analytic solution to the coupled pressure-temperature equations for modeling of photoacoustic trace gas sensors," *Journal of Engineering Mathematics*, vol. 103, pp. 173–193, 2017.
- [12] R. R. Avezov, E. Y. Rakhimov, and A. M. Mirzabaev, "Calculation of the temperature of the internal surface of the heat-removing channel wall of the ray-absorbing heat-exchange panels of flat-plate solar water-heating collectors," *Applied Solar Energy*, vol. 53, no. 4, pp. 312–315, 2017.
- [13] S. Franco, V. R. Mandla, and K. R. Mohan Rao, "Estimation of bright roof areas for large scale solar PV applications to meet the power demand of megacity Hyderabad," *Applied Solar Energy*, vol. 52, no. 4, pp. 284–289, 2016.

Research Article

Fuel Cell Output Current Prediction with a Hybrid Intelligent System

José-Luis Casteleiro-Roca ¹, Antonio Javier Barragán ², Francisca Segura ²,
José Luis Calvo-Rolle ¹ and José Manuel Andújar ²

¹University of A Coruña, Department of Industrial Engineering, Avda. 19 de febrero s/n, 15495 Ferrol, A Coruña, Spain

²University of Huelva, Department of Electronic Engineering, Computer Systems and Automatic, Campus de El Carmen, 21071 Huelva, Spain

Correspondence should be addressed to José-Luis Casteleiro-Roca; jose.luis.casteleiro@udc.es

Received 26 October 2018; Revised 23 December 2018; Accepted 29 January 2019; Published 12 February 2019

Guest Editor: Izaskun Garrido

Copyright © 2019 José-Luis Casteleiro-Roca et al. This is an open access article distributed under the Creative Commons Attribution License, which permits unrestricted use, distribution, and reproduction in any medium, provided the original work is properly cited.

A fuel cell is a complex system, which produces electricity through an electrochemical reaction. For the formal application of control strategies on a fuel cell, it is very important to have a precise dynamic model of it. In this paper, a dynamic model of a real hydrogen fuel cell is obtained to predict its response. The data used in this paper to obtain the model have been acquired from a real fuel cell subjected to different load patterns by means of a programmable electronic load. Using this data, a nonlinear model based on a hybrid intelligent system is obtained. This hybrid model uses artificial neural networks to predict the output current of the fuel cell in a very precise way. The use of a hybrid scheme improves the performance of neural networks reducing to half the mean squared error obtained for a global model of the fuel cell.

1. Introduction

The problems derived from pollution, and the increasingly alarming climate change, have led modern society to look for clean energy sources. One of the most promising technologies for accomplishing hybrid energy topologies is based on renewable sources centers on hydrogen, due to its possible generation by electrolyzers and then its storage. Subsequently, from this gas, the generation of electrical energy by fuel cells is absolutely feasible [1]. In this sense, fuel cell based systems are an energy source that appears as a hopeful choice as a result of their increased performance, high reliability in steady applications, and small environmental incidence, space and automotive applications [2].

A fuel cell is a complex system consisting of a series connection of individual cells (a stack), where the electric current is produced by an electrochemical reaction, combined with all other systems necessary for its operation, that is, filters and systems that condition the gases involved in the reaction (H_2 and O_2), a cooling system, and, of course,

a control system [3]. Compared to other clean technologies, such as wind or photovoltaic generation, fuel cells do not require a specific location to obtain higher performance. In addition, they are very respectful of the environment. Proton Exchange Membrane (PEM) fuel cells (PEMFC) offer high energy density and a number of advantages, such as their low volume and weight compared to other technologies. PEMFC operate at low temperatures (50°C – 100°C), which allow them to start more quickly (requiring less heating time), and result in less wear and tear on system components and better durability. PEMFC are commercially available in a large range of powers (from some watts to several MW), permitting their use in a large number of applications [2]. For example, in stationary applications, fuel cells can be connected to the electrical network [4], installed as separate generators [5], or operate in landfills and wastewater treatment plants [6]. Its use is also interesting in transport applications, owing to the scarcity of fossil fuels and their polluting effects [7, 8], or on other types of mobile stations [9].

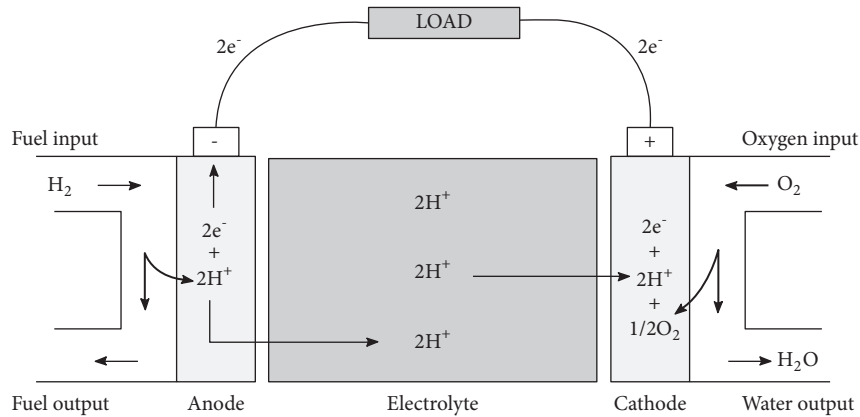


FIGURE 1: Fuel cell diagram.

A fuel cell behaves as a nonlinear dynamical system, which generates electrical energy through an electrochemical reaction. The energy generated by the fuel cell is not regulated; thus, a control system is necessary for its efficient use [10–13]. In this way, for the formal application of control strategies on a fuel cell, it is very important to have a model of its dynamic behaviour [1, 14–18]. Hou et al. [19] analysed stack voltage response to current steps measuring voltage variation rate, initial value of dynamic voltage, time to reach steady state and dynamic resistance factor. The results of this investigation show that the dynamic response of the stack voltage is different for increases and decreases in current [20], what must be taken into account when establishing a test pattern to obtain data from the fuel cell.

It is important to be able to predict the behaviour of fuel cells for their efficient use; hence, obtaining an accurate model is a very important task before designing a control strategy. Achieving an accurate model of a system is a fundamental part of its study; however, we do not always have enough information to obtain an acceptable mathematical model. Therefore, we must resort to modelling techniques based on input–output data [21–25]. In control systems this process is even more critical, since it requires a model as accurate as possible, both to perform analysis on the system [26–28] and to design a suitable and efficient controller for it [29–31].

For the current prediction in this paper, several regression techniques had been checked. The algorithms based on multiple regression analysis are accepted regression methods used in several applications [32–37]. Some previous works have shown the use of these methods despite its low performance [33, 38–40]. In this paper, to overcome this limitation, we propose to use hybrid intelligent system to accomplish the regression task, more specifically, an artificial neural network (ANN) hybrid system as the ones used in [41–46], since ANNs allow obtaining simple and very accurate nonlinear models [47–50].

This work is divided into the following sections. After to the current introduction, the case study is described in detail. Afterwards, the model approach and the employed algorithms are presented. The results section explains the

best achieved configuration of the hybrid model, and the validation of the accomplished prediction model. Lastly, conclusions are explained and future works are depicted.

2. Case of Study

A single fuel cell of a PEM stack consists of an electrolyte layer in contact with an anode and a cathode on both sides; see Figure 1. A PEM fuel cell produces electrochemical energy when a hydrogen-rich gas passes through the anode and a gas rich in oxygen (or air) passes through the cathode with an electrolyte between the anode and the cathode, which allows the exchange of electrical charge (ions) [51]. The dissociation of hydrogen molecules produces the flow of ions through the electrolyte and an electric current through an external circuit. The only residue generated is pure water. A usual single fuel cell produces approximately 1.2 V under normal operating conditions. For the creation of higher power systems, cells are connected in series forming a stack.

The data used for the realisation of the model were acquired through laboratory tests of an air-cooled polymer electrolyte fuel cell (AC-PEFC). Specifically, a PEM FCgen-1020AVS stack from Ballard was used [52]. This stack was built with 80 BAM4G cells [53] based on polymeric composition. The anode and cathode side are made of a porous carbon cloth with a catalyst based on platinum and platinum-ruthenium [54]. The stack was assembled with graphite plates and sandwiched between aluminium end plates by compression. The PEM FCgen-1020AVS stack is designed to provide up to 3.4 kW stable nonregulated electrical power with 45.33 V and 75 A. This stack is air-cooled, and a dead-ended configuration is used; thus, it does not require external humidification of the air or hydrogen. The inlet hydrogen pressure can vary from 1.16 to 1.56 bar. The oxidant and cooling subsystem were built based on the manufacturer's instructions [55]. The complete sequence to put into operation the individual devices that make up the stack, the oxidation and cooling subsystem, the electric subsystem, and the implementation of the balance of plant (BoP), whose schema is shown in Figure 2 and a real image of the laboratory in Figure 3, were thoroughly explained in [56].

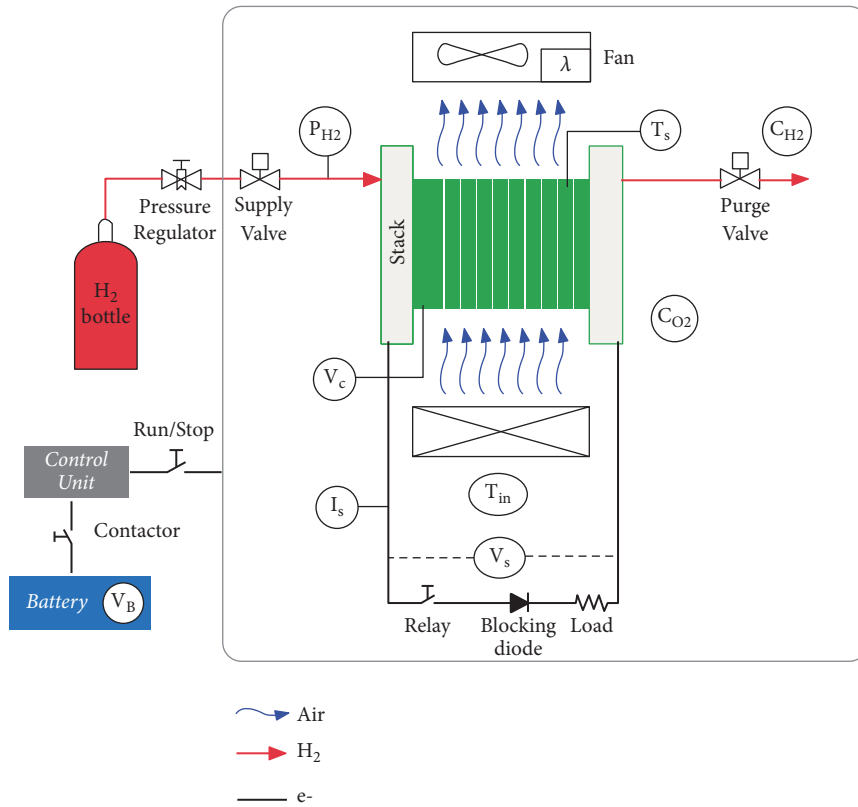


FIGURE 2: Stack + BoP to integrate the fuel cell.

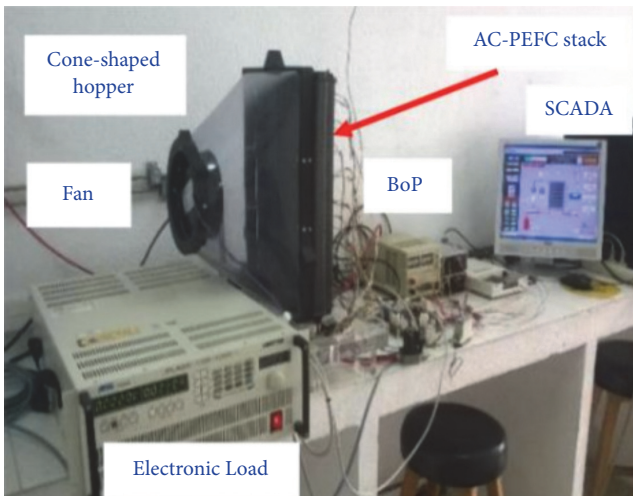


FIGURE 3: Laboratory implementations to test the fuel cell.

To test the system an Amrel PLA5K-120-1200 programmable electronic load was used. A system was implemented to monitor all the fuel cell systems and store the data resulting from the tests, which was described in [57, 58]. In [59], a detailed thermal model based on differential equations is established according to the conservation equations of mass and energy for a 16 cells PEMFC stack. In this work, the effects of the temperature on the operation of the cell are

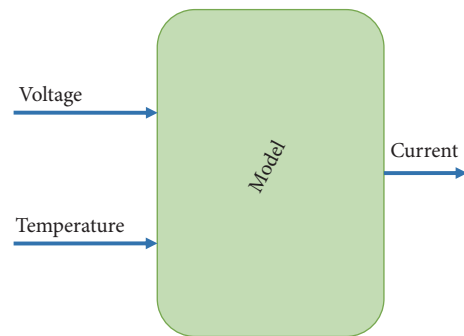


FIGURE 4: Basic schematic model.

demonstrated. In order to avoid these effects of operation, the used BoP includes a temperature control system to guarantee the maintenance of the fuel cell at its optimum value. In addition, it is necessary to keep in mind that the hydrogen gas should be vented periodically to the atmosphere and replaced with fresh hydrogen using a purge process according to [55].

3. Model Approach

The model proposal implemented in this work is illustrated in Figure 4, where the inputs are the voltage and the temperature measured at the BoP and the output is the present value of the current. To take into account the process dynamic, the inputs

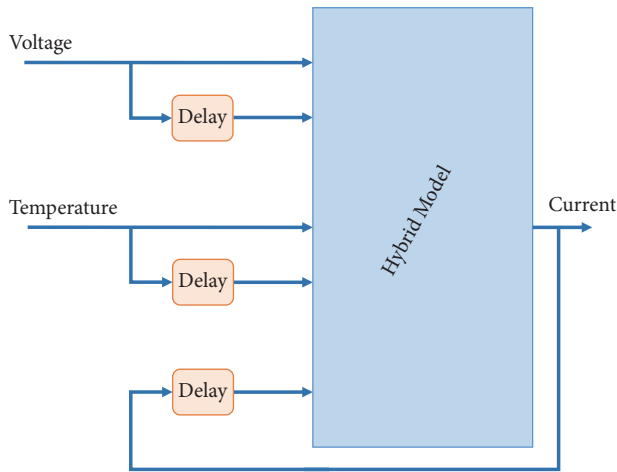


FIGURE 5: Model approach to predict actual current value.

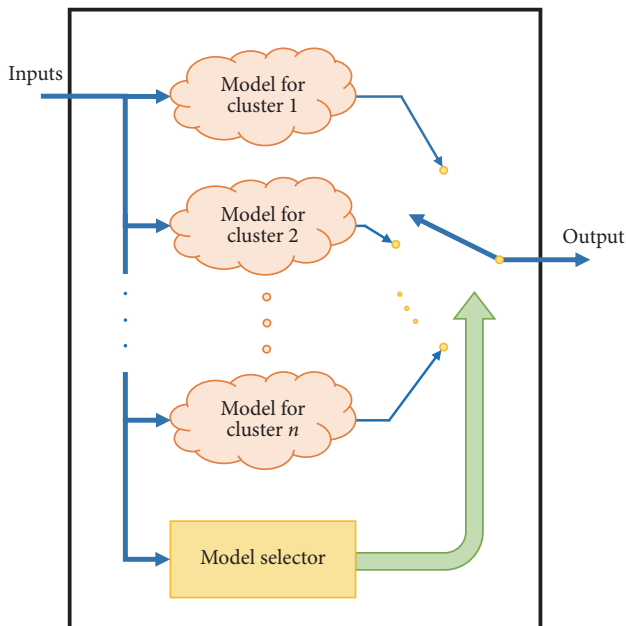


FIGURE 6: Internally schematic to achieve the hybrid model.

of the model include the previous measured values of voltage, temperature, and current.

An internal layout of the model with the mentioned previous variable values is shown in Figure 5, where the hybrid model is represented. Due to the possible nonlinear response, this hybrid model is built upon clustering; the modelling dataset is divided in groups with similar characteristics. A different regression model was created for each cluster with the objective to increase the whole model performance.

Figure 6 represents the operation of the hybrid model shown in Figure 5. The number of clusters is obtained by testing different topologies. This figure represents a general hybrid model, with n clusters and n models with the specific parameters for each one.

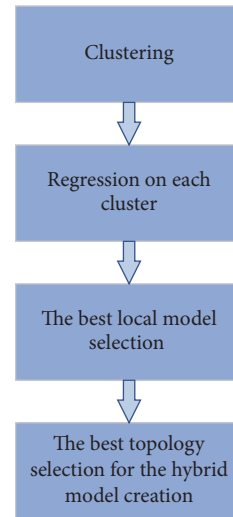


FIGURE 7: Flowchart of the hybrid model creation phases.

To create a hybrid model, the modelling process could be divided into the following steps (Figure 7):

- (1) Clustering phase
- (2) Regression modelling phase for each cluster
- (3) Selection of the best local model (by cluster)
- (4) Selection of the best topology for the hybrid model

For the clustering phase, the k-means algorithm has been used to achieve the groups with similar features. To perform the regression modelling phase, the ANN algorithm was chosen considering its capacity to predict the output of nonlinear systems with a simple internal configuration. Although this is a hybrid system, the model achieves better results if the regression algorithms are intelligent systems than if they are traditional regression methods. The regression modelling phase uses k-fold to achieve a more real approach in the model performance measurement. The k-fold testing method is explained in Figure 8. The data for each cluster is divided into k times and k models with the same configuration and are trained with different test data.

As it is shown in Figure 8, the errors values between the measured and the predicted output for each model are stored. When the k-fold process finished, all the data of a specific cluster is used to test the model, and the performance could be achieved. When all the different possible configurations for the models are tested, the best regression algorithm for each group is chosen based on the lowest error reached.

For the hybrid model topology definition, the number of clusters must be determined. This choice is done based on the global error considering the samples quantity for every cluster and estimating a weighted error. The best hybrid configuration is the one with the best whole performance.

3.1. K-Means Algorithm. The k-means method is used to create a certain number of groups in an unlabeled data set. The idea is to place centroids in the corresponding hyperspace, so that the data belonging to the same centroid

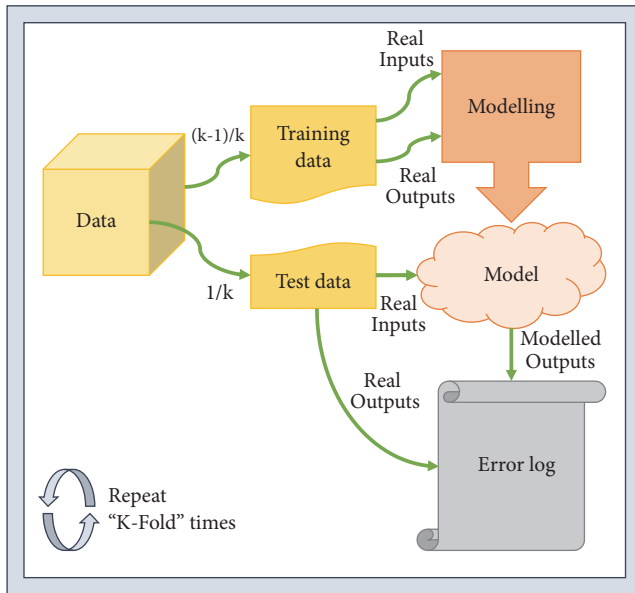


FIGURE 8: K-Fold training and test data selection.

have similar characteristics and represent a data cluster [60, 61].

Every new sample, once the centroids are trained and correctly placed in the hyperspace, is compared with them and is associated with the centroid that is closest in terms of the chosen distance, usually the Euclidean [62].

This algorithm has an initial training phase that needs to know the number of clusters to divide the data. This phase could be slow depending on the number of groups and the data size; however, once the training is finished, the cluster assignment is very fast for new data [63].

The initial location of the centroids is chosen randomly. Then, the location varies, until reaching the greatest distance between them, according to the following procedure:

- (i) Each sample is associated with the nearest centroid and is included in a specific list.
- (ii) After checking all the samples and being associated with the list of the corresponding centroid, the list of labelled samples will be available.
- (iii) The location of the centroid is recalculated obtaining the center of the set of samples that have been associated with it.
- (iv) The procedure is repeated until the centroids are no longer displaced in the successive calculations.

Moreover, as the initial centroids are randomly selected, the procedure is repeated several times until the largest distance between centroids is reached.

3.2. Artificial Neural Networks. The ANN is an intelligent algorithm that uses small processing units called neurons. These neurons are interconnected between each other through links, and each one calculates a function taking into account the different inputs. All the inputs to each neuron have its weight in the activation function inside the neuron [64].

The main specific characteristics of ANNs are that they can learn from experience through the generalization of cases [65]. The ANNs are adaptive intelligent systems that can carry out certain functions through training. The ANNs create their own internal representation of the problem with the training and respond according to the situations, although they had not previously learned a specific situation. Then, the ANNs are able to generalize from previous cases to new ones [66].

The activation function defines the new state, or output, of the neuron as level of excitation [67]. The activation degree of the artificial neuron can usually vary between a range (normally $[0, 1]$ or $[-1, 1]$). This value indicates the state of the neuron: inactive (0 or -1), active (1), or an intermediate state between these limits which indicates its activation degree.

The topology, or architecture, of an ANN is determined by the organization of the neurons, their arrangement, and their connections. The architecture depends on four main parameters: the layers quantity in the system, the number of neurons of every layer, the connectivity between neurons, and the activation functions [68].

The basic structure to interconnect neurons is the multilayer perceptron. This type of ANN is organized in several layers: input, intermediate or hidden and output. A layer is a set of neurons whose input information comes from the same source: the inputs of the ANN for the input layer or the previous layer for the rest of the layers. The output of the neurons in the same layer has the same destination too: the next layer or the output of the ANN (in the case of the output layer).

Normally, the output layer neurons use special activation functions depending on the use of the ANN; for regression, the typical is the linear function.

3.3. Data Processing. The data set in this research is collected using the BoP system described in the case study section. With this equipment, the samples from two different days were collected. A total of 774391 samples were recorded from these tests and, after discarding the bad measurements, the data sets were reduced to 774,385. As the model used previous values, it was necessary to eliminate the samples that did not have all the inputs values to model.

Although there were 774,379 valid samples, only 1/5 of them were used to train the hybrid model; they were selected randomly to ensure the generalization of the model. Then, only 154,875 samples were used in the modelling phase.

In addition, the samples of another different day were used to validate the hybrid model achieved. 4,832 samples, which were not used in the modelling phase, were recorded from two separate tests (1,489 and 3,343 samples each), and they were used in the validation phase of the research.

4. Results

The results of this research could be divided into three different parts: the clustering, the modelling, and the validation.

4.1. Clustering Results. The clusters were created with the explained k-means algorithm. Nine hybrid systems were created with different number of clusters (between 2 and 9),

TABLE 1: Number of samples in each created cluster.

	CI-1	CI-2	CI-3	CI-4	CI-5	CI-6	CI-7	CI-8	CI-9	CI-10
Global	154,875									
Hybrid 2	75,814	79,061								
Hybrid 3	47,719	50,414	56,742							
Hybrid 4	10,699	37,213	50,414	56,549						
Hybrid 5	10,699	28,324	30,251	37,020	48,581					
Hybrid 6	10,699	22,194	28,058	28,324	28,580	37,020				
Hybrid 7	285	10,699	22,194	28,084	28,273	28,320	37,020			
Hybrid 8	285	2,627	10,475	22,194	28,084	28,273	28,320	34,617		
Hybrid 9	285	2,627	5,375	8,161	22,194	27,538	28,084	28,250	32,361	
Hybrid 10	285	2,027	2,627	5,099	8,161	22,194	26,447	27,533	28,139	32,363

TABLE 2: Configuration for each individual hybrid model.

	CI-1	CI-2	CI-3	CI-4	CI-5	CI-6	CI-7	CI-8	CI-9	CI-10
Global	ANN15									
Hybrid 2	ANN15	ANN12								
Hybrid 3	ANN14	ANN11	ANN12							
Hybrid 4	ANN14	ANN15	ANN14	ANN11						
Hybrid 5	ANN11	ANN13	ANN11	ANN14	ANN15					
Hybrid 6	ANN12	ANN13	ANN15	ANN12	ANN15	ANN12				
Hybrid 7	ANN11	ANN14	ANN12	ANN12	ANN11	ANN12	ANN13			
Hybrid 8	ANN11	ANN15	ANN11	ANN11	ANN11	ANN11	ANN12	ANN14		
Hybrid 9	ANN11	ANN15	ANN13	ANN11	ANN12	ANN13	ANN11	ANN12	ANN15	
Hybrid 10	ANN11	ANN13	ANN11	ANN13	ANN11	ANN12	ANN12	ANN15	ANN11	ANN15

TABLE 3: Mean square error for each individual hybrid model.

	CI-1	CI-2	CI-3	CI-4	CI-5	CI-6	CI-7	CI-8	CI-9	CI-10
Global	0.0043									
Hybrid 2	0.0014	0.0028								
Hybrid 3	0.0012	0.0046	0.0030							
Hybrid 4	0.0000	0.0010	0.0069	0.0046						
Hybrid 5	0.0000	0.0000	0.0102	0.0032	0.0144					
Hybrid 6	0.0000	0.0146	0.0037	0.0000	0.0085	0.0010				
Hybrid 7	0.0000	0.0000	0.0147	0.0034	0.0058	0.0000	0.0014			
Hybrid 8	0.0000	0.0075	0.0000	0.0184	0.0031	0.0017	0.0000	0.0003		
Hybrid 9	0.0000	0.0075	0.0000	0.0000	0.0171	0.0000	0.0030	0.0082	0.0002	
Hybrid 10	0.0000	0.0000	0.0075	0.0000	0.0000	0.0041	0.0000	0.0074	0.0019	0.0000

as the optimal number of groups was previously unknown. The algorithm was trained with random initialisation of the centroids, and the training was repeated 20 times to ensure the best divisions, the furthest centroids. The number of samples used in the modelling phase for each cluster is shown in Table 1.

4.2. Modelling Results. The ANN regression algorithm is configured with only a single hidden layer. The input layer has 5 inputs, one for each variable explained in the model approach section, and only 1 output in the last layer. Several configurations of the ANNs for each cluster were trained, all of them with tan-sigmoid activation function

for the internal neurons (in the hidden layer) and, in the output layer, a linear activation function was used. The difference in the several configurations was the hidden layer neurons' quantity. This layer size varied from 1 to 15 neurons.

To train each ANN configuration, the Levenberg-Marquardt optimization algorithm was used. Moreover, to finish the training phase, gradient descent was used base on the MSE (mean squared error). The best ANN configurations for each cluster are indicated in Table 2.

The selection of these advantageous configurations uses the MSE as a performance measurement for the created models. In Table 3 it is possible to see the lowest error for

TABLE 4: Mean squared error for each model.

	Global	Hybrid model (local models)								
		2	3	4	5	6	7	8	9	10
MSE	0.0043	0.0021	0.0030	0.0042	0.0073	0.0046	0.0041	0.0037	0.0047	0.0024

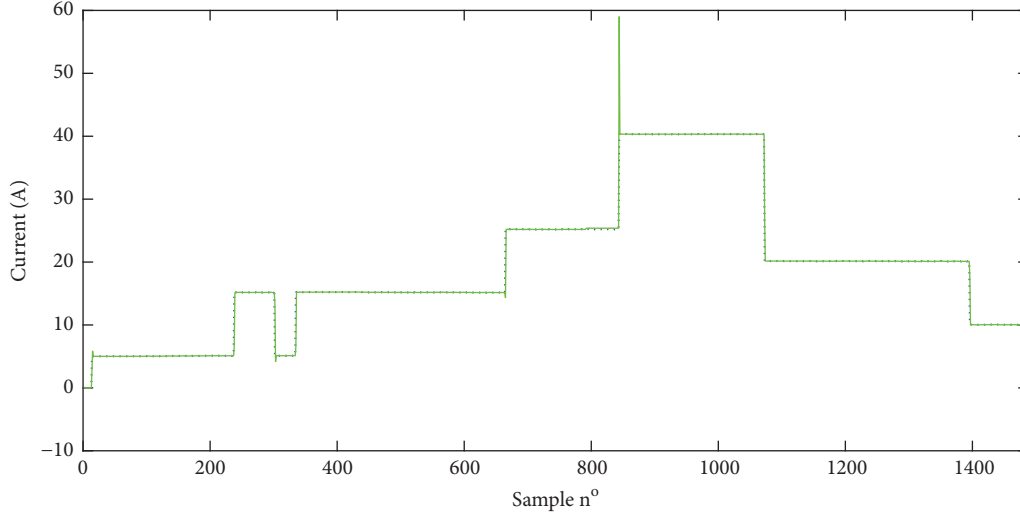


FIGURE 9: Validation test 1.

TABLE 5: Performance values for the validation tests.

	MSE	NMSE	MAE	MAPE
Validation test 1	0.5327	0.0043	0.0704	1.9414
Validation test 2	0.4384	8.4272e-4	0.1889	3.7677

each cluster achieved with the configuration that is shown in Table 2.

To calculate the best hybrid configuration for the whole model, as explained, the number of samples was considered. The performance of the different hybrids and the global model is presented in Table 4. It is shown that the best configuration implies a hybrid model with two clusters, and the error using a global model is more than the double.

4.3. Validation Procedure. Two validation data sets were used to check the final hybrid model accomplished with 2 clusters and configurations of 15 and 12 internal neurons. The first test is shown in Figure 9, where the current has few changes, but it is possible to appreciate that the real data (blue dotted line) and the output of the model (green continuous line) are very close all the time.

The second validation data set (Figure 10) shows a usual test for the fuel cells. In this case, the current is increased until its maximum and, then, reduced gradually. The predicted value in this case shows the biggest error in the middle of the test when the current has the highest values.

In Table 5 different error values are shown for the validation data: MSE, NMSE (normalize mean square error), MAE (mean absolute error), and MAPE (mean absolute percentage error). Despite the graphical error shown for the second

validation data in Figure 10, the error values are very good. The worst value is the MAE because, in the test, the current has very high values; however, the other error values are lower than the ones obtained in the first validation data. This fact could be confirmed with Figure 11, where the percentage absolute error of the second validation data is in the worst part of the test (the central part of Figure 10).

5. Conclusions

A model of a fuel cell based on hydrogen has been developed in this work. The model predicts the current in the fuel cell under different working points, and it could be used in several ways as control or fault detection. As an example, in the fault detection field, the model output must be similar to the real measure of a current sensor, and if the measured value deviates from the modelled one, a sensor failure or a system malfunction could be represented.

Since the fuel cell is a nonlinear system, a hybrid model instead of a global is selected. In this paper, ANNs are used as regression algorithm due to its accuracy. Furthermore, with the hybrid model, the performance of the ANNs is increased up reducing to half the MSE obtained with a global model.

Very good results are obtained in terms of error in the predicted current considering that the MSE value is 0.0021 for the hybrid model with 2 clusters. One of them used an ANN with 15 internal neurons and the other an ANN with 12 neurons. To validate the model, two different data sets were used and, although the maximum MAE was 0.1889, the maximum NMSE was only 0.0043.

As for future works, the possibility of predicting the future values of the current will be examined. This future prediction

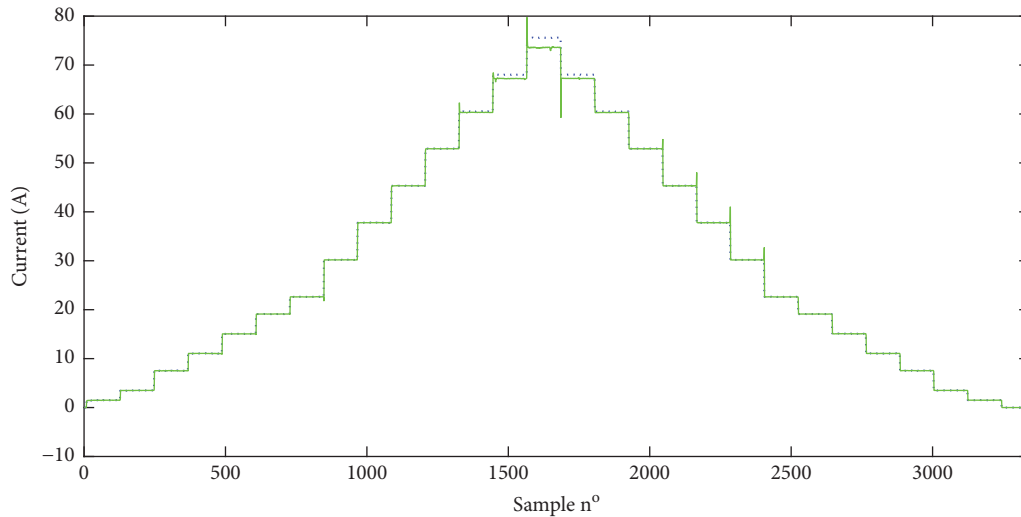


FIGURE 10: Validation test 2.

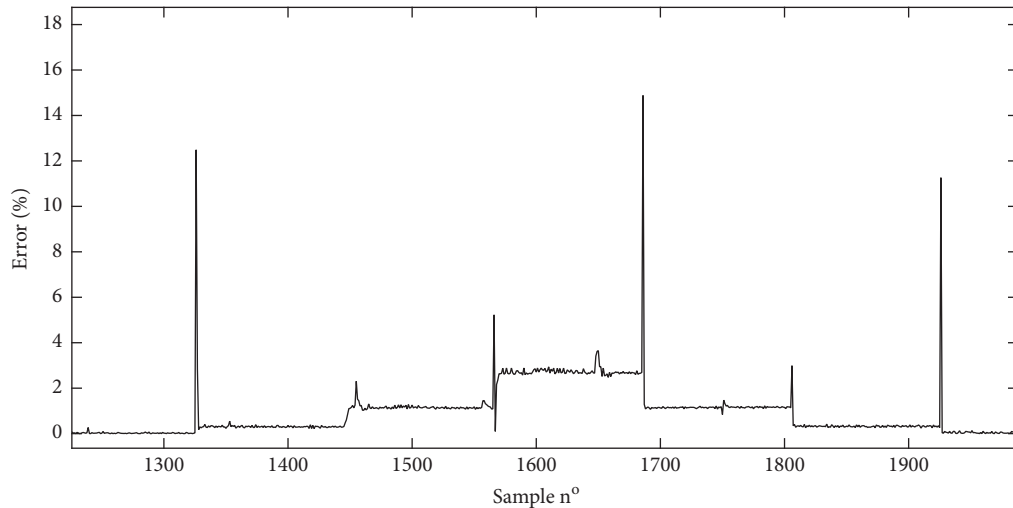


FIGURE 11: Percentage absolute error in the worst part of the validation test 2.

would increase the fuel cell performance, since it could be adapted faster to new working points.

Data Availability

The data used to support the findings of this study are available from the corresponding author upon request.

Conflicts of Interest

The authors declare that they have no conflicts of interest.

Acknowledgments

This work has been funded by the Spanish Ministry of Economy Industry and Competitiveness through the H2SMART- μ GRID (DPI2017-85540-R) project.

References

- [1] F. Vivas, A. De las Heras, F. Segura, and J. Andújar, "A review of energy management strategies for renewable hybrid energy systems with hydrogen backup," *Renewable & Sustainable Energy Reviews*, vol. 82, pp. 126–155, 2018.
- [2] J. Andújar and F. Segura, "Fuel cells: History and updating. A walk along two centuries," *Renewable & Sustainable Energy Reviews*, vol. 13, no. 9, pp. 2309–2322, 2009.
- [3] A. De las Heras, F. Vivas, F. Segura, and J. Andújar, "From the cell to the stack. A chronological walk through the techniques to manufacture the PEFCs core," *Renewable & Sustainable Energy Reviews*, vol. 96, pp. 29–45, 2018.
- [4] M. V. Moreira and G. E. da Silva, "A practical model for evaluating the performance of proton exchange membrane fuel cells," *Journal of Renewable Energy*, vol. 34, no. 7, pp. 1734–1741, 2009.

- [5] A. Kirubakaran, S. Jain, and R. K. Nema, "A review on fuel cell technologies and power electronic interface," *Renewable and Sustainable Energy Reviews*, vol. 13, no. 9, pp. 2430–2440, 2009.
- [6] J. Paska, P. Biczek, and M. Kłos, "Hybrid power systems – An effective way of utilising primary energy sources," *Journal of Renewable Energy*, vol. 34, no. 11, pp. 2414–2421, 2009.
- [7] M. Bertoluzzo and G. Buja, "Development of electric propulsion systems for light electric vehicles," *IEEE Transactions on Industrial Informatics*, vol. 7, no. 3, pp. 428–435, 2011.
- [8] A. De las Heras, F. Vivas, F. Segura et al., "Air-cooled fuel cells: Keys to design and build the oxidant/cooling system," *Journal of Renewable Energy*, vol. 125, pp. 1–20, 2018.
- [9] D. Ross, "Power struggle [power supplies for portable equipment]," *IEE Review*, vol. 49, no. 7, pp. 34–38, 2003.
- [10] J. Andújar, F. Segura, E. Durán, and L. Rentería, "Optimal interface based on power electronics in distributed generation systems for fuel cells," *Journal of Renewable Energy*, vol. 36, no. 11, pp. 2759–2770, 2011.
- [11] F. Segura, J. M. Andújar, and E. Durán, "Analog current control techniques for power control in PEM fuel-cell hybrid systems: A critical review and a practical application," *IEEE Transactions on Industrial Electronics*, vol. 58, no. 4, pp. 1171–1184, 2011.
- [12] J. Lekube, A. J. Garrido, I. Garrido, and E. Otaola, "Output power improvement in oscillating water column-based wave power plants," *Revista Iberoamericana de Automática e Informática Industrial (RIAI)*, vol. 15, no. 2, pp. 145–155, 2018.
- [13] J.-L. Casteleiro-Roca, E. Jove, F. Sánchez-Lasheras et al., "Power cell SOC modelling for intelligent virtual sensor implementation," *Journal of Sensors*, vol. 2017, Article ID 9640546, 10 pages, 2017.
- [14] J. C. Amphlett, R. M. Baumert, R. F. Mann et al., "Performance modeling of the ballard Mark IV solid polymer electrolyte fuel cell I. mechanistic model development," *Journal of The Electrochemical Society*, vol. 142, no. 1, pp. 1–8, 1995.
- [15] J. C. Amphlett, R. F. Mann, B. A. Peppley et al., "A model predicting transient responses of proton exchange membrane fuel cells," *Journal of Power Sources*, vol. 61, no. 1-2, pp. 183–188, 1996.
- [16] P. Famouri and R. Gemmen, "Electrochemical circuit model of a PEM fuel cell," in *Proceedings of the IEEE Power Engineering Society General Meeting*, vol. 3, pp. 1436–1440, IEEE, Toronto, Canada, 2003.
- [17] J. Kim, S.-M. Lee, S. Srinivasan, and C. E. Chamberlin, "Modeling of proton exchange membrane fuel cell performance with an empirical equation," *Journal of The Electrochemical Society*, vol. 142, no. 8, pp. 2670–2674, 1995.
- [18] H. P. van Bussel, F. G. Koene, and R. K. Mallant, "Dynamic model of solid polymer fuel cell water management," *Journal of Power Sources*, vol. 71, no. 1-2, pp. 218–222, 1998.
- [19] Y. Hou, Z. Yang, and X. Fang, "An experimental study on the dynamic process of PEM fuel cell stack voltage," *Journal of Renewable Energy*, vol. 36, no. 1, pp. 325–329, 2011.
- [20] C. Ziogou, S. Voutetakis, S. Papadopoulou, and M. C. Georgiadis, "Modeling, simulation and experimental validation of a PEM fuel cell system," *Computers & Chemical Engineering*, vol. 35, no. 9, pp. 1886–1900, 2011.
- [21] A. J. Barragán, B. M. Al-Hadithi, A. Jiménez, and J. M. Andújar, "A general methodology for online TS fuzzy modeling by the extended Kalman filter," *Applied Soft Computing*, vol. 18, pp. 277–289, 2014.
- [22] M. J. López-Baldán, A. García-Cerezo, J. M. López, and A. R. Gallego, "Fuzzy modeling of a thermal solar plant," *International Journal of Intelligent Systems*, vol. 17, no. 4, pp. 369–379, 2002.
- [23] S. O. T. Ogaji, R. Singh, P. Pilidis, and M. Diacakis, "Modelling fuel cell performance using artificial intelligence," *Journal of Power Sources*, vol. 154, no. 1, pp. 192–197, 2006.
- [24] S. Wojciechowski, "A comparison of classification strategies in rule-based classifiers," *Logic Journal of the IGPL*, vol. 26, no. 1, pp. 29–46, 2018.
- [25] F. Segovia, J. M. Górriz, J. Ramírez et al., "Using deep neural networks along with dimensionality reduction techniques to assist the diagnosis of neurodegenerative disorders," *Logic Journal of the IGPL*, vol. 26, no. 6, pp. 618–628, 2018.
- [26] A. J. Barragán, B. M. Al-Hadithi, J. M. Andújar, and A. Jiménez, "Formal methodology for analyzing the dynamic behavior of nonlinear systems using fuzzy logic," *Revista Iberoamericana de Automática e Informática Industrial (RIAI)*, vol. 12, no. 4, pp. 434–445, 2015.
- [27] F. Gordillo, J. Aracil, and T. Alamo, "Determining limit cycles in fuzzy control systems," in *Proceedings of the 6th International Fuzzy Systems Conference*, vol. 1, pp. 193–198, IEEE, Barcelona, Spain, 1997.
- [28] X. M. Vilar-Martínez, J. A. Montero-Sousa, J. L. Calvo-Rolle, and J. L. Casteleiro-Roca, "Expert system development to assist on the verification of "tacan" system performance," *Dyna*, vol. 89, no. 1, pp. 112–121, 2014.
- [29] J. G. Fontanet, A. L. Cervantes, and I. B. Ortiz, "Alternatives of control for a furuta's pendulum," *Revista Iberoamericana de Automática e Informática Industrial RIAI*, vol. 13, no. 4, pp. 410–420, 2016.
- [30] E. Irigoyen and G. Miñano, "A NARX neural network model for enhancing cardiovascular rehabilitation therapies," *Neurocomputing*, vol. 109, pp. 9–15, 2013.
- [31] J. Marquez, A. Pina, and M. Arias, "A general and formal methodology to design stable nonlinear fuzzy control systems," *IEEE Transactions on Fuzzy Systems*, vol. 17, no. 5, pp. 1081–1091, 2009.
- [32] A. Ghanghermeh, G. Roshan, J. Orosa et al., "New climatic indicators for improving urban sprawl: A case study of tehran city," *Entropy*, vol. 15, no. 3, pp. 999–1013, 2013.
- [33] J. L. Calvo-Rolle, H. Quintian-Pardo, E. Corchado, M. del Carmen Meizoso-López, and R. Ferreiro García, "Simplified method based on an intelligent model to obtain the extinction angle of the current for a single-phase half wave controlled rectifier with resistive and inductive load," *Journal of Applied Logic*, vol. 13, no. 1, pp. 37–47, 2015.
- [34] J. L. Calvo-Rolle, O. Fontenla-Romero, B. Pérez-Sánchez, and B. Guijarro-Berdinas, "Adaptive inverse control using an online learning algorithm for neural networks," *Informatica*, vol. 25, no. 3, pp. 401–414, 2014.
- [35] E. Jove, J. M. Gonzalez-Cava, J. Casteleiro-Roca et al., "Modelling the hypnotic patient response in general anaesthesia using intelligent models," *Logic Journal of the IGPL*, 2018.
- [36] E. Jove, J. A. Lopez-Vazquez, M. I. Fernandez-Ibanez et al., "Hybrid intelligent system to predict the individual academic performance of engineering students," *International Journal of Engineering Education*, vol. 34, no. 3, pp. 895–904, 2018.

- [37] E. Jove, P. Blanco-Rodríguez, J. L. Casteleiro-Roca et al., "Attempts prediction by missing data imputation in engineering degree," in *Proceeding of the International Joint Conference SOCO'17-CISIS'17-ICEUTE'17*, pp. 167–176, Springer, León, Spain, 2017.
- [38] J. L. Casteleiro-Roca, J. L. Calvo-Rolle, M. C. Meizoso-López, A. J. Piñón-Pazos, and B. A. Rodríguez-Gómez, "Bio-inspired model of ground temperature behavior on the horizontal geothermal exchanger of an installation based on a heat pump," *Neurocomputing*, vol. 150, pp. 90–98, 2015.
- [39] I. Machón-González, H. López-García, and J. L. Calvo-Rolle, "A hybrid batch SOM-NG algorithm," in *Proceedings of the International Joint Conference on Neural Networks (IJCNN)*, pp. 1–5, IEEE, Barcelona, Spain, 2010.
- [40] J. A. Rincon, V. Julian, C. Carrascosa et al., "Detecting emotions through non-invasive wearables," *Logic Journal of the IGPL*, vol. 26, no. 6, pp. 605–617, 2018.
- [41] R. F. Garcia, J. L. Rolle, M. R. Gomez, and A. D. Catoira, "Expert condition monitoring on hydrostatic self-levitating bearings," *Expert Systems with Applications*, vol. 40, no. 8, pp. 2975–2984, 2013.
- [42] J. L. Calvo-Rolle, J. L. Casteleiro-Roca, H. Quintián, and M. Del Carmen Meizoso-Lopez, "A hybrid intelligent system for PID controller using in a steel rolling process," *Expert Systems with Applications*, vol. 40, no. 13, pp. 5188–5196, 2013.
- [43] R. Ferreiro Garcia, J. L. Rolle, J. P. Castelo, and M. R. Gomez, "On the monitoring task of solar thermal fluid transfer systems using NN based models and rule based techniques," *Engineering Applications of Artificial Intelligence*, vol. 27, pp. 129–136, 2014.
- [44] H. Quintián, J. L. Calvo-Rolle, and E. Corchado, "A hybrid regression system based on local models for solar energy prediction," *Informatica*, vol. 25, no. 2, pp. 265–282, 2014.
- [45] H. Q. Pardo, J. L. C. Rolle, and O. F. Romero, "Application of a low cost commercial robot in tasks of tracking of objects," *Dyna*, vol. 79, no. 175, pp. 24–33, 2012.
- [46] A. Moreno-Fernandez-de Leceta, J. M. Lopez-Guede, L. Ezquerro Insagurbe et al., "A novel methodology for clinical semantic annotations assessment," *Logic Journal of the IGPL*, vol. 26, no. 6, pp. 569–580, 2018.
- [47] H. Alaiz Moretón, J. L. Calvo Rolle, I. García, and A. Alonso Alvarez, "Formalization and practical implementation of a conceptual model for PID controller tuning," *Asian Journal of Control*, vol. 13, no. 6, pp. 773–784, 2011.
- [48] J. Rolle, I. Gonzalez, and H. Garcia, "Neuro-robust controller for non-linear systems," *Dyna*, vol. 86, no. 3, pp. 308–317, 2011.
- [49] J. L. Casteleiro-Roca, J. A. M. Pérez, A. J. Piñón-Pazos et al., "Modeling the electromyogram (emg) of patients undergoing anesthesia during surgery," in *Proceeding of the International Conference on Soft Computing Models in Industrial and Environmental Applications*, pp. 273–283, Springer, 2015.
- [50] R. F. Garcia, J. L. C. Rolle, J. P. Castelo, and M. R. Gomez, "On the monitoring task of solar thermal fluid transfer systems using NN based models and rule based techniques," *Engineering Applications of Artificial Intelligence*, vol. 27, pp. 129–136, 2014.
- [51] J. Andújar, F. Segura, and M. Vasallo, "A suitable model plant for control of the set fuel cell–DC/DC converter," *Journal of Renewable Energy*, vol. 33, no. 4, pp. 813–826, 2008.
- [52] Ballard, "FCgen1020-ACS fuel cell from Ballard Power Systems," <http://www.ballard.com/docs/default-source/backup-power-documents/fcgen-1020acs.pdf>, 2018.
- [53] V. Mehta and J. S. Cooper, "Review and analysis of PEM fuel cell design and manufacturing," *Journal of Power Sources*, vol. 114, no. 1, pp. 32–53, 2003.
- [54] T. R. Ralph, G. A. Hards, J. E. Keating et al., "Low cost electrodes for proton exchange membrane fuel cells: Performance in single cells and ballard stacks," *Journal of The Electrochemical Society*, vol. 144, no. 11, pp. 3845–3857, 1997.
- [55] Ballard, "FCgenTM-1020ACS/FCvelocityTM-1020ACS Fuel Cell Stack. Ballard Product Manual and Integration Guide," Document Number MAN5100192-0GS, 2009.
- [56] F. Segura and J. Andújar, "Step by step development of a real fuel cell system. Design, implementation, control and monitoring," *International Journal of Hydrogen Energy*, vol. 40, no. 15, pp. 5496–5508, 2015.
- [57] F. Segura and J. Andújar, "Modular pem fuel cell scada & simulator system," *Resources*, vol. 4, no. 3, pp. 692–712, 2015.
- [58] F. Segura, V. Bartolucci, and J. Andújar, "Hardware/software data acquisition system for real time cell temperature monitoring in air-cooled polymer electrolyte fuel cells," *Sensors*, vol. 17, no. 7, article no. 1600, 2017.
- [59] X. Li, Z. Deng, D. Wei et al., "Parameter optimization of thermal-model-oriented control law for PEM fuel cell stack via novel genetic algorithm," *Energy Conversion and Management*, vol. 52, no. 11, pp. 3290–3300, 2011.
- [60] J. MacQueen, "Some methods for classification and analysis of multivariate observations," in *Proceedings of the Berkeley Symposium on Mathematical Statistics and Probability, Volume 1: Statistics*, vol. 1, pp. 281–297, 1967.
- [61] J. Moody and C. J. Darken, "Fast learning in networks of locally-tuned processing units," *Neural Computation*, vol. 1, no. 2, pp. 281–294, 1989.
- [62] J. Orallo, M. Quintana, and C. Ramírez, *Introducción a la Minería de Datos*, Editorial Alhambra, S.A., 2004.
- [63] P. Viñuela and I. León, *Redes De Neuronas Artificiales: Un Enfoque Práctico*, Pearson Educación - Prentice Hall, 2004.
- [64] M. Galipienso, M. Quevedo, O. Pardo et al., *Inteligencia Artificial. Modelos, Técnicas Y Áreas De Aplicación*, Editorial Paraninfo, 2003.
- [65] J. González and V. Hernando, *Redes Neuronales Artificiales: Fundamentos, Modelos Y Aplicaciones*, RA-MA, 1995.
- [66] A. M. C. Harston and R. Pap, *Handbook of Neural Computing Applications*, Elsevier, 2014.
- [67] B. Del Brío and A. Molina, *Redes Neuronales Y Sistemas Borrosos*, RA-MA, 2006.
- [68] R. López and J. Fernández, *Las Redes Neuronales Artificiales*, Netbiblo, 2008.

Research Article

A Comparative Analysis of Self-Rectifying Turbines for the Mutriku Oscillating Water Column Energy Plant

Erlantz Otaola ¹, Aitor J. Garrido ², Jon Lekube,³ and Izaskun Garrido²

¹*Tecnalia Electric Aircraft, Tecnalia Research and Innovation, 20009 San Sebastian, Spain*

²*Automatic Control Group (ACG), Institute of Research and Development of Processes, Dept. Aut. Control and Systems Eng., University of the Basque Country (UPV/EHU), P^o Rafael Moreno 3, Bilbao 48013, Spain*

³*Promotion and Subsidies Area, Basque Energy Board (EVE), 48011 Bilbao, Spain*

Correspondence should be addressed to Erlantz Otaola; otaola06@gmail.com

Received 31 October 2018; Accepted 30 December 2018; Published 23 January 2019

Academic Editor: Marcin Mrugalski

Copyright © 2019 Erlantz Otaola et al. This is an open access article distributed under the Creative Commons Attribution License, which permits unrestricted use, distribution, and reproduction in any medium, provided the original work is properly cited.

Oscillating Water Column (OWC) based devices are arising as one of the most promising technologies for wave energy harnessing. However, the most widely used turbine comprising its power take-off (PTO) module, the Wells turbine, presents some drawbacks that require special attention. Notwithstanding different control strategies are being followed to overcome these issues; the use of other self-rectifying turbines could directly achieve this goal at the expense of some extra construction, maintenance, and operation costs. However, these newly developed turbines in turn show diverse behaviours that should be compared for each case. This paper aims to analyse this comparison for the Mutriku wave energy power plant.

1. Introduction

1.1. Energy Problem. An increase in the energy consumers' environmental awareness seems to be driving a decrease on the fossil fuels and nuclear fission consumption, currently the most used energy resources [1–3]. This realization is pressuring into pushing renewable energy technology and its sources beating out other nonrenewables [4–6], as the 2020 climate and energy package reflects [7]. Renewable energy evolves around the natural resources that provide practically inexhaustible amounts of energy [8], either through the massive latent energy or through regenerative capabilities within the human time-scale. The most studied renewable energies today are solar, wind, wave, hydraulic, biomass, geothermic, and tidal [9].

Delucchi and Jacobson state that the total energy requirements could be fulfilled from solar, wind, and wave energy [10–12]. However, wave energy has lagged behind, even though the power density analysis stands up for the opposite [4]. According to this concept, when solar radiation heats air masses to different temperatures, it forces them to move and thus creates wind. Therefore, wind pools solar energy

and increases the power density. In turn, the ocean allows transferring energy from the wind to mechanical energy within the waves. Through this principle, at about 15-degree latitude, where the sun radiation is of 0.17 kW/m², the wind power density rises to 0.58 kW/m² and the wave power density climbs up to 8.42 kW/m² [4].

Additionally, the power density increment of the waves means that a sudden sun radiation stop would not suppose a wave activity decrease until many hours later. Besides, the sun could have easily come back by then, generating new powerful waves. This makes wave energy a precious and available resource. An analysis of the wave energy available to be harnessed estimates an annual total production around 100,000 kWh, compared to the 16,000 kWh annual consumption [13].

Consequently, hundreds of patents have been developed all around the globe to harness wave energy [14, 15]. Their classification divides them into on-shore or off-shore devices [16]. On-shore machines are easily manufactured and maintained, but harness less energy and there are fewer locations for installation. Oscillating vanes [17], tapering canals [18], and oscillating wave column (OWC) [19] are the most



FIGURE 1: The OWC power plant of Mutriku.

widely used types. Off-shore devices quite often require to be affixed to the seabed and are not as developed as on-shore ones. Mighty Whale [20], Wave Dragon [21], Wave Plane [22], Pelamis [23], Archimedes [24], Wave Star [25], and Power Buoy [26] technologies are examples of such type of technology. Oscillating wave column technology is nowadays deemed as the most promising candidate, due to it having the largest development rate compared to the rest [27–29].

1.2. Background. An OWC-technology-based device converts wave energy into an oscillating air flow, which in turn makes a turbine rotate. With the turbine attached to a power induction generator, energy is harnessed [19]. It can be understood as two main subassemblies: the capture chamber and the power take-off (PTO) system.

The capture chamber [30] consists of a hollow structure with an aperture placed in such a way that it stays below the sea water level (SWL) regardless of the tide. This configuration allows the water in and out of the cavity, which compresses and decompresses the air inside the cavity as the waves enter and leave. The air pressure variation forces an upwards and downwards air stream.

This air stream acts upon the PTO system composed of a turbine and a power induction generator [31]. It flows through the turbine, forcing it to spin and generating a pressure drop as a result. The spin creates a torque that turns the generator. The oscillating airflow would make a common turbine spin in a different direction each time. To optimize the turbine for unidirectional movement, a valve-based rectifying system could be used [19] or, in a more straightforward way, self-rectifying turbines.

Based on this technology, the Basque Energy Board (EVE) has built a ground-breaking power plant known as NEREIDA MOWC [32] in the Basque town of Mutriku (Figure 1), which consists of 16 turbo-generator modules rated at 18.5 kWh each with self-rectifying turbines coupled to a DFIG generator. This power plant makes use of 5-blade Wells turbines from the series NACA00XX [33–35]. The

Wells turbine, invented by Alan A. Wells in 1976, is regarded as the first of its kind [33, 34, 36–38]. Its rotor is made up of a number of blades symmetric in the direction normal to the airflow, allowing the tangential force to keep constant regardless of the airflow direction, making them spin always in the same direction [39]. However, this symmetry presents an inherent drawback, the stalling effect, which makes the turbine stall when the airflow through the turbine goes over a certain value. This sharply drops the efficiency of the turbine [40, 41].

There are many methods oriented towards the solution of this issue [42–45]:

- (i) relief valves
- (ii) air valve control
- (iii) rotational speed control

Relief valves permit some airflow to be bypassed to reduce the incoming air stream into the turbine [5, 46].

Air valve control allows for the regulation of the airflow input to the turbine so that it never reaches the airflow limit value, thus avoiding the stall effect. Several control methods have been developed for this model, such as artificial-neural-networks-based controllers [47] or robust sliding-mode controllers [48], but PID type controller is still considered the most efficient one [49].

The turbine can also be prevented from stalling by controlling its rotational speed which involves accelerating the turbine to a sufficient speed (Figure 2). In this case, the slip of the DFIG generator is set to vary so that higher speeds can be reached [47, 50]. This approach tends to calculate the maximum pressure drop throughout the turbine without stalling to determine the slip of the DFIG and modify the turbine rotational speed [49] (Figure 3).

As it can be observed, solving the stalling effect requires sufficient control mechanisms. However, it could be avoided directly by using a turbine without this issue. This substitution would additionally allow the focus of the control only on increasing the torque output of the system. There are many turbines that have been developed since Wells was created which could yield promising results. Pitch-controlled Wells, impulse, and radial with pitch-controlled guide vanes and biradial turbines are compared to the Wells turbine installed in Mutriku throughout this paper.

2. Materials and Methods

2.1. Turbines Description. Pitch-controlled Wells turbines (Figure 4) consist of endowing the Wells turbine with the capability of modifying the pitch angle between two extreme angles, $\pm\gamma$, to convert the incoming airflow more efficiently into rotational motion [51]. This increase in efficiency stems from the ability to diminish the hysteresis of a vane due to the influence of the vanes in close proximity [52]. This turbine also enhances the performance when starting up or at low speeds [53], allowing reaching higher speeds in a shorter amount of time, a desirable feature in OWC-based devices [54].

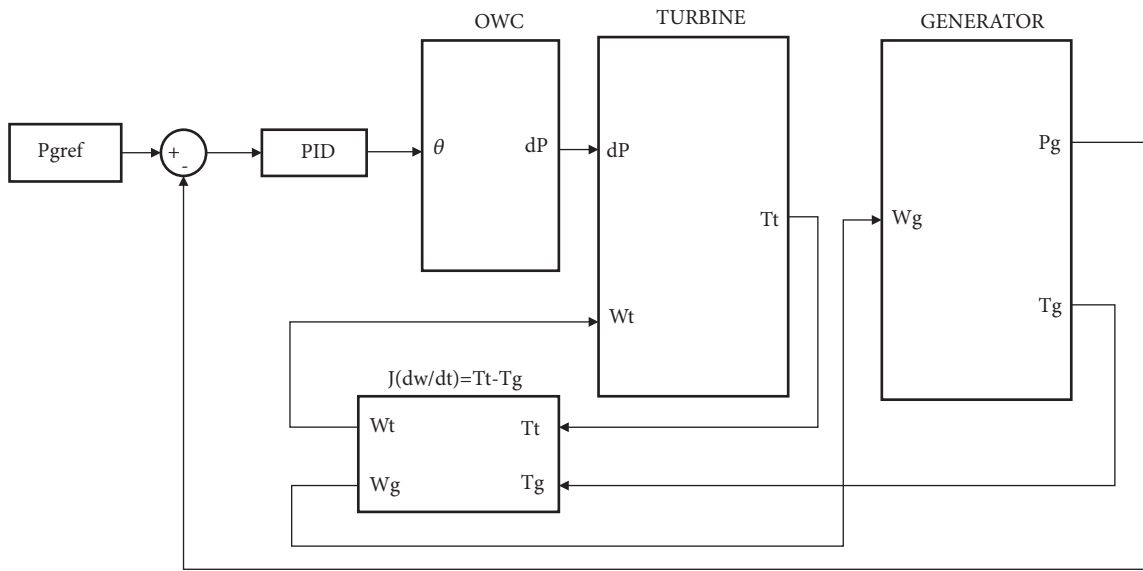


FIGURE 2: Rotational speed control diagram.

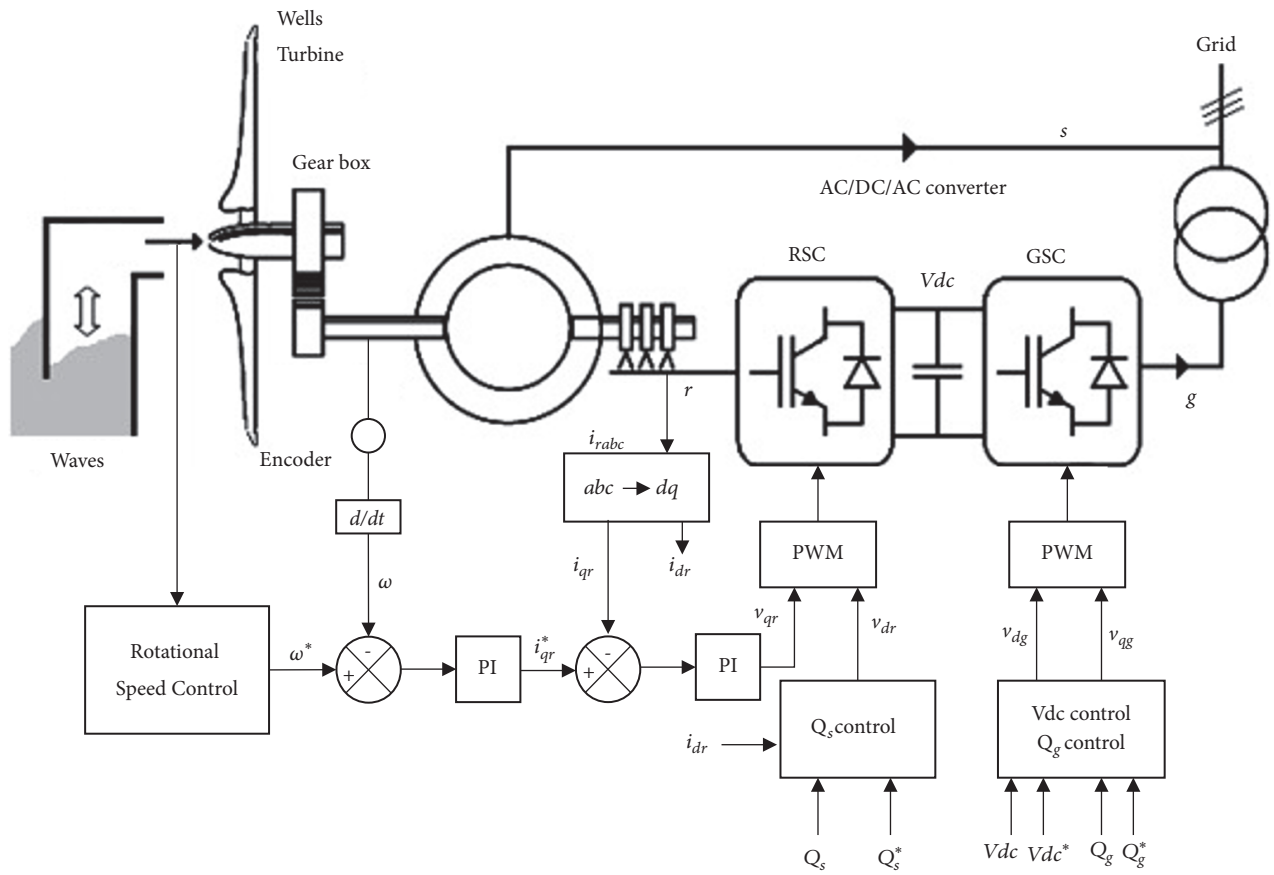


FIGURE 3: DFIG control strategy diagram.

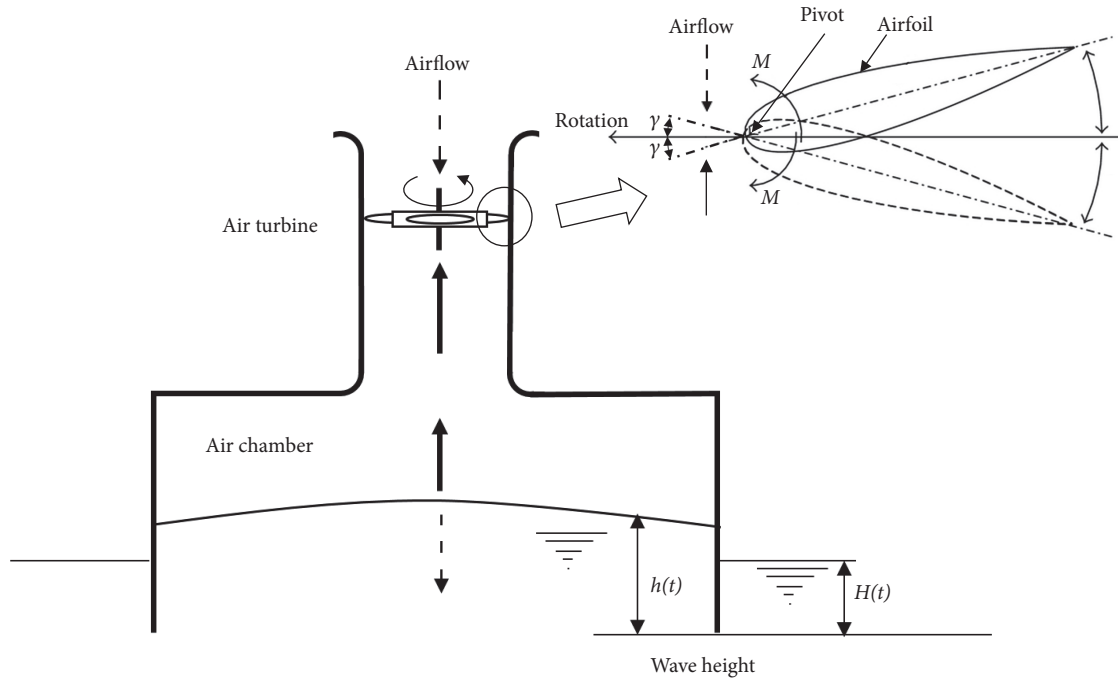


FIGURE 4: Wells turbine with pitch control.

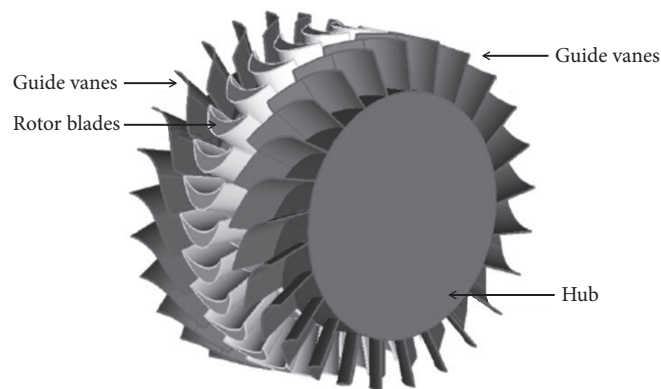


FIGURE 5: Impulse turbine.

Impulse turbines (Figure 5) solve the stalling problem, are capable of starting in a short period of time and of working at low speeds [55]. Setoguchi et al. [56–63] developed a variation of this turbine adding two rows of guide vanes, one upstream and other downstream, whose pitch is controlled to increase its efficiency. These guide vanes are mechanically coupled so that the one in the outgoing path does not obstruct the airflow when controlling the ingoing vane to optimize the energy conversion [64].

Radial turbines with pitch-controlled guide vanes (Figure 6) are similar to impulse turbines with the difference that the airflow enters the turbine radially and not axially [65–71]. They also include two rows of guide vanes, one upstream and other downstream, whose pitch is controlled between two extreme angles [70]. These turbines reduce the mechanical requirements of the impulse turbines but maintain all their benefits, such as the removal of the stall effect [72]. However,

the trade-off requires an extra system forcing the air in the radial direction.

Biradial turbines (Figure 7) are a new kind of a radially attacking turbine [73]. This turbine is also equipped with two rows of mechanically coupled guide vanes, which are axially displaced to guide the input airflow without obstructing the outgoing airflow. Obstructing the airflow would make the vanes stall [74]. Since these turbines use impulse-type vanes, all the drawbacks from the Wells turbines are solved. Additionally, their mechanical design allows them to convert wave energy more efficiently [73].

The data obtained by different sensors placed in the Mutriku wave power plant is used to compare these turbines, along with the Wells variant. From the data, inputs for the different turbine models can be created and therefore compute their outputs when subjected to the same inputs. This way, the most adequate turbine can be determined.

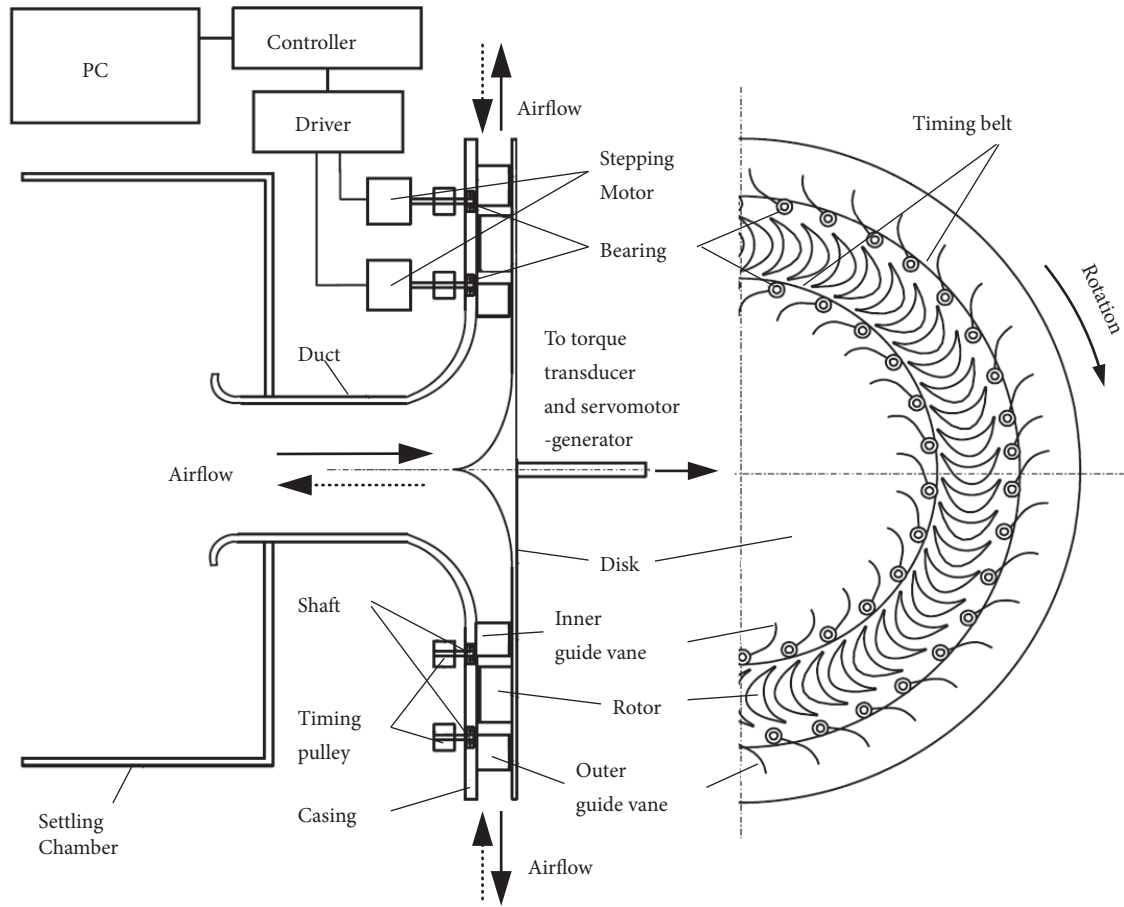


FIGURE 6: Radial turbine with pitch-controlled guide vanes.

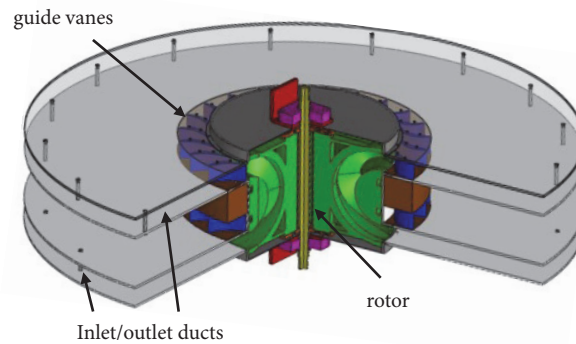


FIGURE 7: Biradial turbine.

2.2. *Sensors Description and Data Treatment.* The data used to simulate the environment and the control of the turbines comes from three different sources:

- (i) Basque Energy Board (EVE)
- (ii) AZTI-Tecnalia
- (iii) State harbours (website)

The following variables are provided by the EVE, from January 1st 2014 to May 15th 2014, with half second resolution:

- (i) Pressure (Pa)
- (ii) Air valve angle (degree)
- (iii) Rotational speed (rpm)
- (iv) System extracted power (kW)

From the aforementioned data, rotational speed and valve angle depend on the control strategy, whose parameters vary from one turbine to another. Therefore, these values depend

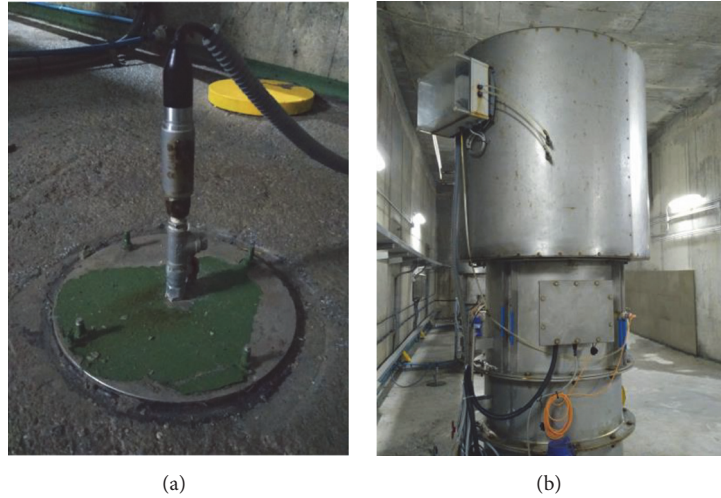


FIGURE 8: Pressure sensors in Mutriku. (a) Capture chamber static pressure sensor. (b) Pressure drop along the PTO sensor.

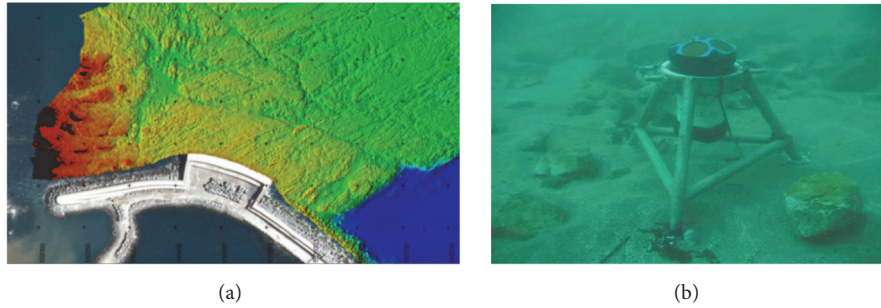


FIGURE 9: (a) Wave spectrum record. (b) RDI 600kHz.

on each turbine and the ones provided by the EVE are related to the Wells turbine use case.

The pressure and the extracted torque outputs are extensively used to compare against the outputs from the other turbines' models and hence determine the turbine whose response would best fit in Mutriku.

There are two types of pressure sensors in the power plant of Mutriku: one to measure the static pressure of the capture chamber and the other for the pressure drop along the turbo-generator module. The pressure of the capture chamber is measured by means of a *PTX 7355* type *Druck* sensor installed at the base of the power plant (Figure 8(a)). However, in order to obtain the pressure drop through the turbo-generator, two CMR controls P-sensors for low air pressure are employed, one at the inlet of the turbine and the second at the top of the turbo-generator module (Figure 8(b)) [75].

AZTI-Tecnalia provided the average height and period of the wave trains that took place during a period of 20 mins every 2 hours on May 12th 2014. From the wave fundamental parameters, two half-a-second resolutions vectors are generated, one for the amplitude and another for the period. Those vectors are used as inputs for all the models of the different turbines to objectively compare their response for the exact same conditions.

The sensor used to acquire this information is the Teledyne RDI 600kHz, an Acoustic Doppler Current Profiler (Figure 9).

This sensor measures water depth ranging from 0.7m to 90m. Laying in the seabed next to Mutriku, where the water depth is around 5m, this sensor allows measuring all the different wave heights. In order to harness the data, this can be done well via a serial/DC/computer cable well storing it in an internal memory card and then recovering it in the PC.

2.3. Turbine Models Development. The expression obtained in [76] to work out the pressure drop through the Wells turbine installed in Mutriku is a function of a parameter depending on the turbine itself, the power coefficient (C_a),

$$dp = C_a \frac{\rho b l_1 n}{2} \frac{1}{a_1} (v_t^2 + \omega_t^2 r^2), \quad (1)$$

The definition of this parameter may however vary from one turbine to another, making the expression of the pressure drop through the turbine change. Therefore, to make use of the previous unaltered expression, it is necessary to obtain an equation that relates the power coefficient in (1) to the power coefficient definition for each turbine.

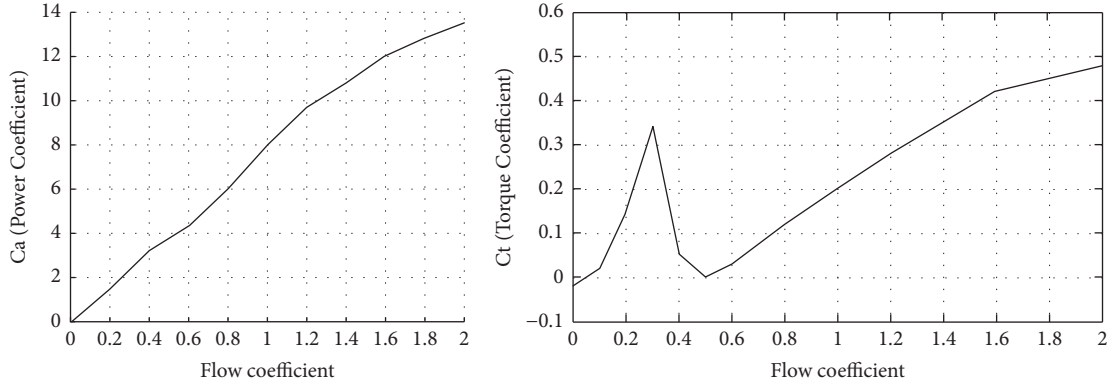


FIGURE 10: Relationship between flow coefficient-power coefficient and flow coefficient-torque coefficient.

Additionally, to benchmark the different turbines a comparison of the corresponding output torque directly linked to the output power is needed. According to [76], the output torque of the Wells turbine is defined as

$$T_t = \frac{dp \cdot C_t \cdot r \cdot a_1}{C_a} \quad (2)$$

Integrating (1) into (2), the output torque can also be defined as

$$T_t = C_t \frac{\rho b l_1 n}{2} r (v_t^2 + \omega_t^2 r^2) \quad (3)$$

This equation also depends on a coefficient of the turbine in use, the torque coefficient (C_t). Hence, as expected, this expression may differ from one turbine to another. Consequently, it is necessary to find an expression relating the torque coefficient in (3) and the torque coefficient for each turbine to compare.

Both previous parameters, power and torque coefficient, depend in turn on the flow coefficient, defined as

$$\Phi = \frac{v_t}{\omega_t r} \quad (4)$$

This definition may differ for some turbines, too. An expression relating this expression to the one defined for each turbine may thus also be necessary in those situations.

The relationships between flow coefficient and power coefficient and flow coefficient and torque coefficient relationships for the case of the Wells turbine are described in Figure 10.

In this sense, adapting the Wells turbine model for the case of Mutriku [76] to the different definitions of the torque coefficients, the pressure drop and output torque can be obtained for all the turbines and, therefore, determine which turbine would be the most appropriate for the case at Mutriku.

A convergence of the expressions for the different turbines is developed in the following way. The flow coefficients of the turbines to be compared are written as a function of the flow coefficient of the Wells turbine. The power and torque coefficients are in turn expressed reversely, writing the

TABLE 1: Parameters of the pitch-controlled Wells turbine.

Blade profile	NACA0021
Blade number	20
Cord length	75 mm
Solidity	0.75
Hub to tip ratio	0.7
Aspect ratio	0.6
Diameter	750 mm
Gap between rotor and casing	1 mm
Angle range	0-12°

coefficients for the Wells as a function of the coefficients of the new turbines.

This stems from the fact that the new turbines' expressions are integrated within a model devoted to the Wells. So to obtain the power or torque coefficients, the flow coefficient is used as an input. Therefore, once the flow coefficient (4) is calculated by the model for the different turbines, this serves as the input for the graph relating the flow coefficient to the other two (Figure 10 for the Wells turbine in Mutriku). Once the power and torque coefficients are obtained from the graphs, both are rewritten into the same form as the coefficients defined for the Wells turbine and then implemented in the model.

Pitch-Controlled Wells. The pitch-controlled Wells turbine analysed in this section is an adaptation to the duct diameter in Mutriku of the turbine defined in [54]. The main features of this turbine can be summarised in Table 1.

Regarding the turbine parameters, they are defined as

$$C_{a_{pW}} = \frac{dp_{pW} Q}{(\rho b l_1 v_a n (v_t^2 + \omega_t^2 r^2)) / 2}, \quad (5)$$

$$C_{t_{pW}} = \frac{T_{t_{pW}}}{(\rho b l_1 r n (v_t^2 + \omega_t^2 r^2)) / 2}, \quad (6)$$

$$\Phi_{pW} = \frac{v_t}{\omega_t r} \quad (7)$$

TABLE 2: Parameters of the biradial turbine.

Rotor	
Diameter	244 mm
Input/output width	53.7 mm
Blade number	3
Width	3.7 mm
Input/output angle	40°
Gap between rotor and casing	1 mm
Guide vanes	
Vane number	23
Geometry	Aerofoil
Rotor axis -vane distance	274 mm
Rotor end-vane distance	30 mm
Duct	
Diameter	750 mm

After a few modifications, it can be obtained that, for this turbine,

$$dp_{pW} = C_a \frac{\rho b l_1 n}{2} \frac{1}{a_1} (v_t^2 + \omega_t^2 r^2), \quad (8)$$

$$T_{t_{pW}} = C_t \frac{\rho b l_1 n}{2} r (v_t^2 + \omega_t^2 r^2) \quad (9)$$

Hence, the power and torque coefficient defined for this turbine can be directly used within the model developed for the Wells turbine [76] without further modifications.

Biradial. The biradial turbine analysed in this section is an adaptation to the duct diameter in Mutriku of the turbine described in [74]. The main features of this turbine can be summarised in Table 2.

Regarding the turbine parameters, they are defined as

$$C_{a_B} = \frac{dp_B}{\rho \omega_t^2 D^2} = \frac{dp_B}{4\rho \omega_t^2 r^2}, \quad (10)$$

$$C_{t_B} = \frac{T_{t_B}}{\rho \omega_t^2 D^5}, \quad (11)$$

$$\Phi_B = \frac{Q}{\omega_t D^2} \quad (12)$$

It can be observed how all parameters vary with respect to the ones defined for the Wells turbine used in Mutriku. In this scenario, an expression to convert them into the type used in the Wells turbine model [76] must be worked out.

In the case of the power coefficient, (1) and (10) have been compared and, since the expression is equivalent,

$$dp = dp_B, \quad (13)$$

$$C_a \frac{\rho b l_1 n}{2} \frac{1}{a_1} (v_t^2 + \omega_t^2 r^2) = 4C_{a_B} \cdot \rho \omega_t^2 r^2, \quad (14)$$

$$C_a = \frac{4C_{a_B} \cdot \rho \omega_t^2 r^2 \cdot 2a_1}{\rho b l_1 n (v_t^2 + \omega_t^2 r^2)}$$

$$C_a = C_{a_B} \cdot \frac{8a_1}{b l_1 n (\Phi^2 + 1)} \quad (15)$$

In this way, once the power coefficient has been worked out via the graphs in [76], it is adequately transformed into the power coefficient defined for the Wells turbine by means of (15) so that it can be used in the pressure drop calculation.

Regarding the torque coefficient, since the torque output must be equal regardless of the equation used, (3) and (11) have to be compared and equal.

$$T_t = T_{t_B}, \quad (16)$$

$$C_t \frac{\rho b l_1 n}{2} r (v_t^2 + \omega_t^2 r^2) = C_{t_B} \rho \omega_t^2 D^5 = 32C_{t_B} \rho \omega_t^2 r^5, \quad (17)$$

$$C_t = \frac{32C_{t_B} \rho \omega_t^2 r^5 \cdot 2}{\rho b l_1 n r (v_t^2 + \omega_t^2 r^2)}$$

$$C_t = C_{t_B} \cdot \frac{64r^2}{b l_1 n (\Phi^2 + 1)} \quad (18)$$

Analogous to the power coefficient, once the torque coefficient is determined, it is rewritten in an expression compatible with (3), which is then implemented in the model to obtain the output torque.

Finally, prior to the power and torque coefficient, the flow coefficient defined for the Wells turbine (implemented in the model) must be rewritten as a function of the type defined for the biradial (input of the graph). Therefore,

$$\begin{aligned} \Phi_B &= \frac{Q}{\omega_t D^3} = \frac{v_t a_1}{8\omega_t r^3} = \frac{v_t \pi r^2}{8\omega_t r^3} = \frac{v_t \pi}{8\omega_t r} = \frac{\pi}{8} \frac{v_t}{\omega_t r} \\ &= \frac{\pi}{8} \Phi \end{aligned} \quad (19)$$

Now, all the necessary modifications have been obtained for the model to work properly for the Biradial, which is now ready for implementation.

Impulse. The impulse turbine analysed in this section is adapted to the duct diameter in Mutriku for the turbine defined in [64]. The main features of this turbine can be summarised in Table 3.

TABLE 3: Parameters of the impulse turbine.

Rotor	
Geometry	Circular arc ($r = 30.2$ mm) and ellipse
Cord length	54 mm
Edge radius	0.5 mm
Gap between rotor and casing	1 mm
Blade number	38
Radius	375 mm
Hub radius	210 mm
Angle	60°
Blade height	16.1 mm
Guide vanes	
Vane number	26
Straight line and circular arc ($r = 32$ mm)	
Geometry	
Cord length	70 mm
Angle	15°

Regarding the turbine parameters, they are defined as

$$C_{a_i} = \frac{dp_I Q}{(\rho b l_1 v_a n (v_t^2 + \omega_t^2 r^2)) / 2}, \quad (20)$$

$$C_{t_i} = \frac{T_{t_i}}{(\rho b l_1 r n (v_t^2 + \omega_t^2 r^2)) / 2}, \quad (21)$$

$$\Phi_I = \frac{v_t}{\omega_t r} \quad (22)$$

After a few modifications, it can be obtained that, for this turbine,

$$dp_I = C_{a_i} \frac{\rho b l_1 n}{2} \frac{1}{a_1} (v_t^2 + \omega_t^2 r^2), \quad (23)$$

$$T_{t_i} = C_{t_i} \frac{\rho b l_1 n}{2} r (v_t^2 + \omega_t^2 r^2), \quad (24)$$

and, hence, that the power and torque coefficient defined for this turbine can be directly used within the model developed for the Wells turbine [76] without further modifications.

Radial with Pitch-Controlled Guide Vanes. The radial with pitch-controlled guide vanes turbine analysed in this section is adapted to the duct diameter in Mutriku for the turbine defined in [71]. The main features of this turbine can be summarised in Table 4.

TABLE 4: Parameters of the radial turbine.

Rotor	
Geometry	Circular arc ($r = 30.2$ mm) and ellipse
Cord length	54 mm
Edge radius	0.5 mm
Blade number	88
Radius	375 mm
Angle	60°
Solidity	2.02
Guide vanes	
Vane number	26
Straight line and circular arc ($r = 24.8$ mm)	
Geometry	
Cord length	50 mm
Outer vane solidity	2.31
Inner vane solidity	2.29
Input angle	15°

Regarding the turbine parameters, they are defined as

$$C_{a_R} = \frac{dp_R}{(\rho (v_t^2 + \omega_t^2 r^2)) / 2}, \quad (25)$$

$$C_{t_R} = \frac{T_{t_R}}{(\rho a_1 r (v_t^2 + \omega_t^2 r^2)) / 2}, \quad (26)$$

$$\Phi_R = \frac{v_t}{\omega_t r} \quad (27)$$

It can be seen directly how the first two parameters, power and torque coefficient, vary with respect to the ones defined for the Wells turbine used in Mutriku. In this scenario, an expression to convert the previous two into the type used in the Wells turbine model [76] has to be worked out.

As in the biradial case, both output pressure and torque have to be the same regardless of the equation used to work it out. Equalling (1) and (25),

$$dp = dp_R, \quad (28)$$

$$C_a \frac{\rho b l_1 n}{2} \frac{1}{a_1} (v_t^2 + \omega_t^2 r^2) = C_{a_R} \cdot \frac{\rho}{2} (v_t^2 + \omega_t^2 r^2), \quad (29)$$

$$C_a = C_{a_R} \cdot \frac{a_1}{b l_1 n} \quad (30)$$

Equalling (3) and (26), the expression to modify the torque coefficient is obtained.

$$T_t = T_{t_R}, \quad (31)$$

$$C_t \frac{\rho b l_1 n}{2} r (v_t^2 + \omega_t^2 r^2) = C_{t_R} \cdot \frac{\rho a_1 r}{2} (v_t^2 + \omega_t^2 r^2), \quad (32)$$

$$C_t = C_{t_R} \cdot \frac{a_1}{b l_1 n} \quad (33)$$

Now, all the necessary modifications have been obtained for the model to work properly with the radial with pitch-controlled guide vanes turbine and the model is ready to be implemented.

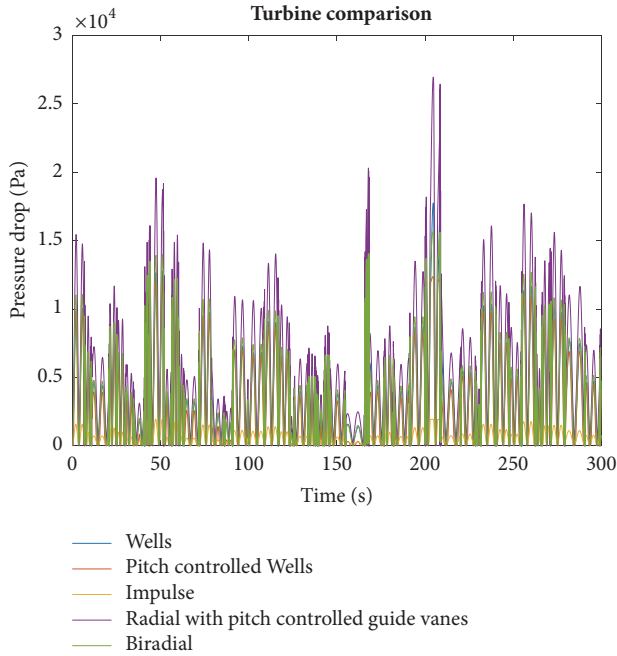


FIGURE 11: Model pressure drop output for the different turbines.

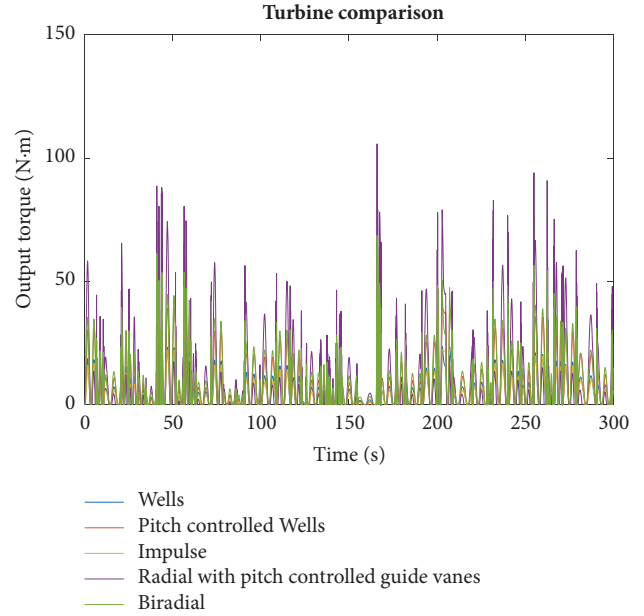


FIGURE 12: Model torque output for the different turbines.

3. Results

3.1. Models Modifications. In [76], a mathematical model was developed for the complete capture chamber of an OWC system including the turbine by determining both the pressure drop and the output torque of the turbine from the input wave parameters. For that, a Wells turbine was modelled and was validated with data from the Mutriku facility where a Wells turbine is installed. Then, [75] integrated this partial model into a complete wave-to-grid model. This complete model allowed modifying the control strategy obtaining the pressure drop and output torque for each control case study and thus implementing a control strategy to make the most of each turbine. Comparing the output torque of each turbine, the most adequate one can be chosen.

Taking that into account, the part of the model regarding the capture chamber along with the expressions obtained in the previous section, the turbine equation can be rewritten to suit the different definitions of flow, power, and torque coefficients whenever these modifications are needed, as in the case of the biradial and the radial with pitch-controlled guide vanes.

For pitch-controlled Wells and impulse turbines, each of them has proven that no expression modifications are needed. Therefore, only power and torque coefficients curves for each turbine have to be modified.

3.2. Models Outputs. Once the models are ready, the data in Section 2.1 is used to run the models and determine the pressure drop and output torque for the five studied turbines. Besides, the parameters of the turbines, such as radius and cord length are obtained from the turbines' data presented in Section 2.2.

This way, every turbine is tested within the exact same test environment (same wave parameters and same capture chamber geometry) but with its own attributes (turbine geometry and optimized control parameters). This allows for a comparison the response of the turbines in an unbiased way, thus extracting the most accurate conclusions when it comes to determining the most appropriate turbine for the case of Mutriku.

The pressure drop and output torque for the different turbines are as shown in Figures 11 and 12.

As it can be outlined from the previous figures, according to the pressure drop the radial turbine with pitch-controlled guide vanes seems to be the most appropriate for the case of Mutriku, for its pressure values exceed all others. Impulse turbines are the ones with the lowest pressure drop and therefore it seems not to be a well suited turbine for Mutriku.

However, this way to choose the most suitable turbine is regarding the output power that the turbine can provide, a feature related to the output torque that the turbine applies on the generator over time. Therefore, analysing the output torque of each turbine allows for the election of the one that provides the highest torque for the case of Mutriku disregarding the cost of manufacture, maintenance, and operation. Besides, even though the biradial turbine seems to provide the largest output torque, some uncertainty exists because the radial turbine presents the greatest peak value. Therefore, a more thorough analysis may be necessary, to work out the mean output torque, since this variable is one decisive feature to determine the best turbine for this case study (Table 5).

From the results above, the biradial turbine is deemed the most suitable option for the Mutriku wave power plant installation when considering only the output torque. It generates the largest pressure drop and mean output torque,

TABLE 5: Output torque mean values.

Wells	4.9428
Wells with pitch control	8.1732
Impulse	4.1148
Radial with pitch controlled guide vanes	7.0273
Biradial	9.7282

a 136% above the one that provides the lowest torque and a 19% above the second one, the Wells turbine with pitch control. This leaves the radial turbine with pitch-controlled guide vanes in the third place. Finally, Wells turbine and impulse turbine lag behind with results close to the others.

4. Conclusions

The results obtained throughout the present paper show how new self-rectifying turbines invented along the recent past years since the Wells invention have suffered an enormous enhancement. This upgrade has provided not only OWC technology-based power plants with a larger energy harnessing capability, but also additional benefits such as a slighter computational load since the stall effect control is avoided. This former fact allows for the development of more complex control algorithms that result in an increase of the amount of energy harnessed from the waves.

This way, it is evinced how, even if the current trends are prone to relate all the upcoming upgrades of OWC technology-based devices to software advancement, research on mechanical components shows how mechanical parts, such as self-rectifying turbines, also play an important role in it. This fact stands up for making progress on both research branches in parallel, one feeding the other, to achieve a faster, more advantageous, and more successful evolution of OWC technology-based devices.

Besides, this article is proof of how the model-based methodology is a good choice when carrying out analytic studies both of controllers and mechanical components and so. Following this approach, adapting the turbine model and adjusting the control for the particularities for each turbine, a systematic comparative analysis procedure has been performed for the different turbines in a reliable and low-cost effective manner.

Nomenclature

a : Wave amplitude
 a_1 : Capture chamber area
 b : Blade's height
 c : Wave propagation speed
 C_a : Power coefficient
 C_t : Torque coefficient
 dp : Pressure drop
 D : Diameter of the duct
 l : Length of the capture chamber
 l_1 : Length of blade's chord
 n : Number of blades
 Q : Air flow

r : Turbine's mean diameter
 t : Time variable
 T : Wave period
 T_t : Output torque
 v_t : Airflow linear speed
 ω : Wave angular frequency
 ω_t : Turbine rotation speed
 x : Space variable
 y : Wave instantaneous height
 λ : Wavelength
 ρ : Air density
 ϕ : Flow coefficient

Superscripts

B: Biradial turbine
I: Impulse turbine
R: Radial turbine with pitch-controlled guide vanes
pW: Pitch-controlled Wells turbine.

Data Availability

The data used to support the findings of this study are available from the corresponding author upon request.

Conflicts of Interest

The authors declare that there are no conflicts of interest regarding the publication of this article.

Acknowledgments

This work was supported by the MINECO through the Research Project DPI2015-70075-R (MINECO/FEDER, UE) and in part by the University of the Basque Country (UPV/EHU) through PPG17/33. The authors would like to thank the collaboration of the Basque Energy Agency (EVE) through Agreement UPV/EHUEVE23/6/2011, the Spanish National Fusion Laboratory (EURATOM-CIEMAT) through Agreement UPV/EHUCIEMAT08/190, and EUSKAMPUS-Campus of International Excellence.

References

- [1] I. Garrido, A. J. Garrido, J. A. Romero, E. Carrascal, G. Sevillano-Berasategui, and O. Barambones, "Low effort L_i nuclear fusion plasma control using model predictive control laws," *Mathematical Problems in Engineering*, vol. 2015, Article ID 527420, 8 pages, 2015.
- [2] I. Garrido, A. J. Garrido, M. G. Sevillano, and J. A. Romero, "Robust Sliding Mode Control for Tokamaks," *Mathematical Problems in Engineering*, vol. 2012, Article ID 341405, 14 pages, 2012.
- [3] A. J. Garrido, I. Garrido, O. Barambones, P. Alkorta, and F. J. Maseda, "Simple linear models for plasma control in tokamak reactors," in *Proceedings of the 2008 International Conference on Control, Automation and Systems, (ICCAS '08)*, pp. 2429–2432, 2008.

- [4] J. Lekube, A. J. Garrido, I. Garrido, and E. Otaola, "Output power improvement in oscillating water column-based wave power plants," *Revista Iberoamericana de Automatica e Informatica Industrial*, vol. 15, no. 2, pp. 145–155, 2018.
- [5] A. J. Garrido, I. Garrido, M. Amundarain, M. Alberdi, and M. De La Sen, "Sliding-mode control of wave power generation plants," *IEEE Transactions on Industry Applications*, vol. 48, no. 6, pp. 2372–2381, 2012.
- [6] I. Garrido, A. J. Garrido, M. Alberdi, M. Amundarain, and O. Barambones, "Performance of an ocean energy conversion system with DFIG sensorless control," *Mathematical Problems in Engineering*, vol. 2013, Article ID 260514, 14 pages, 2013.
- [7] Ministerio de Agricultura, Alimentación y Medio Ambiente, "Paquete de Energía y Cambio Climático 2013-2020". Available in: <http://www.magrama.gob.es/es/cambio-climatico/temas/el-proceso-internacional-de-lucha-contra-el-cambio-climatico/la-union-europea/>.
- [8] Intergovernmental Panel on Climate Change, "Renewable Energy Sources and Climate Change Mitigation". Available in: http://srren.ipcc-wg3.de/report/IPCC_SRREN_Full_Report.pdf.
- [9] F. Fusco, G. Nolan, and J. V. Ringwood, "Variability reduction through optimal combination of wind/wave resources - An Irish case study," *Energy*, vol. 35, no. 1, pp. 314–325, 2009.
- [10] M. Delucchi, "Wind, water and solar power for the world," *IEEE Spectrum*, 2011.
- [11] M. Z. Jacobson and M. A. Delucchi, "Providing all global energy with wind, water, and solar power, part I: technologies, energy resources, quantities and areas of infrastructure, and materials," *Energy Policy*, vol. 39, no. 3, pp. 1154–1169, 2011.
- [12] M. Z. Jacobson and M. A. Delucchi, "Providing all global energy with wind, water, and solar power, part II: reliability, system and transmission costs, and policies," *Energy Policy*, vol. 39, no. 3, pp. 1170–1190, 2011.
- [13] European Ocean Energy Association, 2013 Industry Vision Paper. Available in: http://www.oceanenergy-europe.eu/images/Publications/European_Ocean_Energy-Industry_Vision_Paper_2013.pdf (last accessed April 2015).
- [14] D. Y. Goswami and F. Kreith, *Energy Conversion*, CRC Press, 2007.
- [15] H. Polinder and M. Scuotto, "Wave energy converters and their impact on power systems," in *Proceedings of the 2005 International Conference on Future Power Systems*, pp. 62–70, Amsterdam, The Netherlands, November 2005.
- [16] J. A. Carta González, R. Calero Pérez, A. Colmenar Santos, and M. A. Castro Gil, "Clasificación de los dispositivos de captación," in *Centrales de energías renovables: Generación eléctrica con energías renovables*, pp. 586–604, Madrid, España: Pearson Educación, 1st edition, 2009.
- [17] J. A. Carta González, R. Calero Pérez, A. Colmenar Santos, and M. A. Castro Gil, "Los alerones oscilantes," in *Centrales de energías renovables: Generación eléctrica con energías renovables*, pp. 593–594, Madrid, España: Pearson Educación, 1st edition, 2009.
- [18] J. A. Carta González, R. Calero Pérez, A. Colmenar Santos, and M. A. Castro Gil, "Los canales ahusados," in *Centrales de energías renovables: Generación eléctrica con energías renovables*, pp. 594–595, Madrid, España: Pearson Educación, 1st edition, 2009.
- [19] J. A. Carta González, R. Calero Pérez, A. Colmenar Santos, and M. A. Castro Gil, "Las columnas oscilantes de agua (OWC)," in *Centrales de energías renovables: Generación eléctrica con energías renovables*, pp. 588–593, Madrid, España: Pearson Educación, 1st edition, 2009.
- [20] J. A. Carta González, R. Calero Pérez, A. Colmenar Santos, and M. A. Castro Gil, "Mighty Whale (Poderosa Ballena)," in *Centrales de energías renovables: Generación eléctrica con energías renovables*, pp. 596–597, Madrid, España: Pearson Educación, 1st edition, 2009.
- [21] J. A. Carta González, R. Calero Pérez, A. Colmenar Santos, and M. A. Castro Gil, "Wave Dragon (Dragón de olas)," in *Centrales de energías renovables: Generación eléctrica con energías renovables*, pp. 597–598, Madrid, España: Pearson Educación, 1st edition, 2009.
- [22] J. A. Carta González, R. Calero Pérez, A. Colmenar Santos et al., "WavePlane (Plano de olas)," in *Centrales de energías renovables: Generación eléctrica con energías renovables*, pp. 598–600, Madrid, España: Pearson Educación, 1st edition, 2009.
- [23] J. A. Carta González, R. Calero Pérez, A. Colmenar Santos et al., "Pelamis," in *Centrales de energías renovables: Generación eléctrica con energías renovables*, pp. 600–601, Madrid, España: Pearson Educación, 1st edition, 2009.
- [24] J. A. Carta González, R. Calero Pérez, A. Colmenar Santos et al., "Archimedes," in *Centrales de energías renovables: Generación eléctrica con energías renovables*, p. 601, Madrid, España: Pearson Educación, 1st edition, 2009.
- [25] J. A. Carta González, R. Calero Pérez, A. Colmenar Santos et al., "Wave Star (Estrella de las olas)," in *Centrales de energías renovables: Generación eléctrica con energías renovables*, pp. 601–603, Madrid, España: Pearson Educación, 1st edition, 2009.
- [26] J. A. Carta González, R. Calero Pérez, A. Colmenar Santos et al., "PowerBuoy," in *Centrales de energías renovables: Generación eléctrica con energías renovables*, pp. 603–604, Madrid, España: Pearson Educación, 1st edition, 2009.
- [27] M. A. Ormaza, M. A. Goitia, A. J. G. Hernández, I. G. Hernández et al., "Neural control of the Wells turbine-generator module," in *Proceedings of the 2009 IEEE Conference on Decision and Control*, pp. 7315–7320, IEEE, 2009.
- [28] M. de la Sen, A. J. Garrido, J. C. Soto, O. Barambones, and I. Garrido, "Suboptimal Regulation of a Class of Bilinear Interconnected Systems with Finite-Time Sliding Planning Horizons," *Mathematical Problems in Engineering*, vol. 2008, Article ID 817063, 26 pages, 2008.
- [29] A. J. Garrido, I. Garrido, M. Alberdi, M. Amundarain, O. Barambones, and J. A. Romero, "Robust control of oscillating water column (OWC) devices: Power generation improvement," *OCEANS 2013 MTS/IEEE - San Diego: An Ocean in Common*, art. no. 6740982, 2013.
- [30] Y. Torre-Encino, I. Ortubia, de López Aguilera, and L. I. J. Marqués, "Mutriku wave power plant: From the thinking out the reality," in *Proceedings of 8th European Wave Tidal Energy Conference*, pp. 319–329, 2009.
- [31] A. El Marjani, F. Castro Ruiz, M. A. Rodriguez, and M. T. Parra Santos, "Numerical modelling in wave energy conversion systems," *Energy*, vol. 33, no. 8, pp. 1246–1253, 2008.
- [32] Y. Torre-Encino, "Mutriku Wave Power Plant: From Conception to Reality," in *European Federation Of Regional Energy and Environmental Agencies (FEDARENE)*, Brussels, Belgium, 2009.
- [33] T. Setoguchi and M. Takao, "Current status of self rectifying air turbines for wave energy conversion," *Energy Conversion and Management*, vol. 47, no. 15–16, pp. 2382–2396, 2006.

- [34] S. Raghunathan, "Performance of the Wells self-rectifying turbine," *The Aeronautical Journal*, vol. 89, no. 890, pp. 369–379, 1985.
- [35] V. Jayashankar, S. Anand, T. Geetha et al., "A twin unidirectional impulse turbine topology for OWC based wave energy plants," *Journal of Renewable Energy*, vol. 34, no. 3, pp. 692–698, 2009.
- [36] L. Gato and V. Warfield, "Performance of a high-solidity Wells turbine for an OWC wave power plant," in *Proceedings of the European Wave Energy Symposium*, pp. 181–190, 1994.
- [37] M. Inoue, K. Kaneko, T. Setoguchi, and T. Saruwatari, "Studies on the Wells Turbine for Wave Power Generator (Turbine Characteristics and Design Parameter for Irregular Wave)," *JSME International Journal*, vol. 31, no. 4, pp. 676–682, 1988.
- [38] S. Shaaban, "Insight analysis of biplane wells turbine performance," *Energy Conversion and Management*, vol. 59, pp. 50–57, 2012.
- [39] A. Thakker and R. Abdulhadi, "Effect of blade profile on the performance of wells turbine under unidirectional sinusoidal and real sea flow conditions," *International Journal of Rotating Machinery*, vol. 2007, Article ID 51598, 9 pages, 2007.
- [40] V. Jayashankar, S. Anand, T. Geetha et al., "A twin unidirectional impulse turbine topology for OWC based wave energy plants," *Journal of Renewable Energy*, vol. 34, no. 3, pp. 692–698, 2008.
- [41] S. Raghunathan, T. Setoguchi, and K. Kaneko, "The wells air turbine subjected to inlet flow distortion and high levels of turbulence," *International Journal of Heat and Fluid Flow*, vol. 8, no. 2, pp. 165–167, 1987.
- [42] J. Klamka, "Controllability and minimum energy control of linear fractional discrete-time infinite-dimensional systems," in *Proceedings of the 11th IEEE International Conference on Control & Automation*, vol. 162, pp. 1210–1214, Taichung, Taiwan.
- [43] A. Babiarz et al., "Controllability of discrete-time linear switched systems with constraints on switching signal," in *Proceedings of the 7th Asian Conference on Intelligent Information and Database Systems (ACIIDS '15)*, vol. 9011, Part I of *Lecture Notes in Artificial Intelligence*, pp. 304–312, Bali, Indonesia, 2015.
- [44] A. Czornik and M. Niezabitowski, "Alternative formulae for lower general exponent of discrete linear time-varying systems," *Journal of The Franklin Institute*, vol. 352, no. 1, pp. 399–419, 2015.
- [45] J. Klamka et al., "Trajectory controllability of semilinear systems with delay," in *Proceedings of the 7th Asian Conference on Intelligent Information and Database Systems (ACIIDS '15)*, vol. 9011, Part I of *Lecture Notes in Artificial Intelligence*, pp. 313–323, Bali, Indonesia, 2015.
- [46] A. F. D. O. Falcao, L. C. Vieira, P. A. P. Justino, and J. M. C. S. André, "By-pass air-valve control of an OWC wave power plant," *Journal of Offshore Mechanics and Arctic Engineering*, vol. 125, no. 3, pp. 205–210, 2003.
- [47] M. Amundarain, M. Alberdi, A. J. Garrido, and I. Garrido, "Neural control of the Wells turbine-generator module," in *Proceedings of the 48th IEEE Conference on Decision and Control*, pp. 7315–7320, 2009.
- [48] O. Barambones and A. J. Garrido, "Adaptive sensorless robust control of AC drives based on sliding mode control theory," *International Journal of Robust and Nonlinear Control*, vol. 17, no. 9, pp. 862–879, 2007.
- [49] M. Amundarain, M. Alberdi, A. J. Garrido, and I. Garrido, "Modeling and simulation of wave energy generation plants: Output power control," *IEEE Transactions on Industrial Electronics*, vol. 58, no. 1, pp. 105–117, 2011.
- [50] V. Jayashankar, K. Udayakumar, B. Karthikeyan, K. Manivannan, N. Venkatraman, and S. Rangaprasad, "Maximizing power output from a wave energy plant," in *Proceedings of the IEEE Power Engineering Society Winter Meeting*, vol. 3, pp. 1796–1801, 2000.
- [51] T. Setoguchi et al., "Air-Turbine with Self-Pitch-Controlled Blades for Wave Energy Conversion (Estimation of Performances in Periodically Oscillating Flow)," *International Journal of Rotating Machinery*, vol. 3, no. 4, pp. 233–238, 1997.
- [52] T. Setoguchi, K. Kaneko, H. Hamakawa, and M. Inoue, "Measurement of hysteresis on Wells turbine characteristics in reciprocating flow," in *Proceedings of the 1st International Symposium on Experimental and Computational Aerothermodynamics of Internal Flows*, pp. 537–543, 1990.
- [53] M. Inoue, K. Kaneko, T. Setoguchi, and H. Hamakawa, "Air turbine with self-pitch-controlled blades for wave energy generator," *JSME International Journal*, vol. 32, no. 1, pp. 19–24, 1989.
- [54] T. H. Kim, T. Setoguchi, K. Kaneko, and M. Takao, "The optimization of blade pitch settings of an air turbine using self-pitch-controlled blades for wave energy conversion," *Journal of Solar Energy Engineering*, vol. 123, no. 4, pp. 382–386, 2001.
- [55] K. Kaneko, T. Setoguchi, and S. Raghunathan, "Self-rectifying turbines for wave energy conversion," in *Proceedings of the 1st International Offshore and Polar Engineering Conference 1991*, vol. 1, pp. 385–392, 1991.
- [56] T. W. Kim, K. Kaneko, T. Setoguchi, and M. Inoue, "Aerodynamic performance of an impulse turbine with self-pitch-controlled guide vanes for wave power generator," in *Proceedings of the 1st KSME-JSME Thermal and Fluid Engineering Conference 1988*, vol. 2, pp. 133–137, 1988.
- [57] T. W. Kim, K. Kaneko, T. Setoguchi, E. Matsuki, and M. Inoue, "Impulse turbine with self-pitch-controlled guide vanes for wave power generator (effects of rotor blade profile and sweep angle)," in *Proceedings of the 2nd KSME-JSME Thermal and Fluid Engineering Conference 1990*, vol. 1, pp. 277–281, 1990.
- [58] T. Setoguchi, K. Kaneko, H. Maeda, T. W. Kim, and M. Inoue, "Impulse turbine with self-pitch-controlled guide vanes for wave power conversion: Performance of mono-vane type," *International Journal of Offshore and Polar Engineering*, vol. 3, no. 1, pp. 73–78, 1993.
- [59] T. Setoguchi, K. Kaneko, H. Maeda, T. W. Kim, and M. Inoue, "Impulse turbine with self-pitch-controlled guide vanes for wave power conversion," in *Proceedings of the 3rd International Offshore and Polar Engineering Conference 1993*, vol. 1, pp. 161–166, 1993.
- [60] H. Maeda, T. Setoguchi, K. Kaneko, T. W. Kim, and M. Inoue, "The effect of turbine geometry on the performance of impulse turbine with self-pitch-controlled guide vanes for wave power conversion," in *Proceedings of the 4th International Offshore and Polar Engineering Conference 1994*, vol. 1, pp. 378–382, 1994.
- [61] T. Setoguchi, K. Kaneko, H. Maeda, T. W. Kim, and M. Inoue, "Impulse turbine with self-pitch-controlled tandem guide vanes for wave power conversion," *International Journal of Offshore and Polar Engineering*, vol. 4, no. 1, pp. 76–80, 1994.
- [62] H. Maeda, T. Setoguchi, K. Kaneko, T. W. Kim, and M. Inoue, "Effect of turbine geometry on the performance of impulse turbine with self-pitch-controlled guide vanes for wave power conversion," *International Journal of Offshore and Polar Engineering*, vol. 5, no. 1, pp. 72–74, 1995.
- [63] T. Setoguchi, K. Kaneko, H. Taniyama, H. Maeda, and M. Inoue, "Impulse turbine with self-pitch-controlled guide vanes for wave power conversion: Guide vanes connected by links,"

- International Journal of Offshore and Polar Engineering*, vol. 6, no. 1, pp. 76–80, 1996.
- [64] T. Setoguchi, S. Santhakumar, H. Maeda, M. Takao, and K. Kaneko, “A review of impulse turbines for wave energy conversion,” *Journal of Renewable Energy*, vol. 23, no. 2, pp. 261–292, 2001.
- [65] K. Kaneko, T. Setoguchi, and S. Raghunathan, “Self-rectifying turbines for wave energy conversion,” *International Journal of Offshore and Polar Engineering*, vol. 2, no. 3, pp. 238–240, 1992.
- [66] M. E. McCormick and B. Cochran, “A Performance Study of a Radial Turbine,” in *Proceedings of the First European Wave Energy Conference 1993*, pp. 443–448, 1993.
- [67] M. E. McCormick, J. G. Rehak, and B. D. Williams, “An Experimental Study of a Bi-directional Radial Turbine for Pneumatic Energy Conversion,” in *Proceedings of the Mastering Ocean through Technology*, vol. 2, pp. 866–870, 1992.
- [68] T. N. Veziroglu, Ed., *Alternative Energy Sources VI, Wind/Ocean/Nuclear/Hydrogen*, vol. 3, Hemisphere Publishing Corporation, 1985.
- [69] T. Setoguchi, S. Santhakumar, M. Takao, T. H. Kim, and K. Kaneko, “A performance study of a radial turbe for wave energy conversion,” *Journal of Power and Energy*, vol. 216, no. A1, pp. 15–22, 2002.
- [70] M. Takao, Y. Fujioka, H. Homma, T. Kim, and T. Setoguchi, “Experimental Study of a Radial Turbine Using Pitch-Controlled Guide Vanes for Wave Energy Conversion,” *International Journal of Rotating Machinery*, vol. 2006, pp. 1–7, 2005.
- [71] T. Setoguchi, M. Takao, Y. Kinoue, K. Kaneko, S. Santhakumar, and M. Inoue, “Study on an impulse turbine for wave energy conversion,” *International Journal of Offshore and Polar Engineering*, vol. 10, no. 2, pp. 145–152, 2000.
- [72] A. El Marjani, F. Castro Ruiz, M. A. Rodriguez, and M. T. Parra Santos, “Numerical modelling in wave energy conversion systems,” *Energy*, vol. 33, pp. 1246–1253, 2008.
- [73] A. F. O. Falcão, L. M. C. Gato, and E. P. A. S. Nunes, “A novel radial self-rectifying air turbine for use in wave energy converters,” *Journal of Renewable Energy*, vol. 50, pp. 289–298, 2013.
- [74] A. F. O. Falcão, L. M. C. Gato, and E. P. A. S. Nunes, “A novel radial self-rectifying air turbine for use in wave energy converters. Part 2. Results from model testing,” *Journal of Renewable Energy*, vol. 53, pp. 159–164, 2013.
- [75] J. Lekube, A. J. Garrido, I. Garrido, E. Otaola, and J. Maseda, “Flow control in wells turbines for harnessing maximum wave power,” *Sensors*, vol. 18, no. 2, 2018.
- [76] A. J. Garrido, E. Otaola, I. Garrido et al., “Mathematical modeling of oscillating water columns wave-structure interaction in ocean energy plants,” *Mathematical Problems in Engineering*, vol. 2015, Article ID 727982, 11 pages, 2015.

Research Article

Meteorological Data-Based Optimal Control Strategy for Microalgae Cultivation in Open Pond Systems

Riccardo De-Luca,¹ Fabrizio Bezzo,¹ Quentin Béchet,² and Olivier Bernard ²

¹CAPE-Lab Computer-Aided Process Engineering Laboratory, Department of Industrial Engineering, Università di Padova, Via Marzolo 9, 35131 Padova, Italy

²BIOCORE, INRIA, Université Côte d'Azur, BP 93, 06902 Sophia-Antipolis Cedex, France

Correspondence should be addressed to Olivier Bernard; olivier.bernard@inria.fr

Received 11 September 2018; Accepted 16 December 2018; Published 8 January 2019

Guest Editor: Izaskun Garrido

Copyright © 2019 Riccardo De-Luca et al. This is an open access article distributed under the Creative Commons Attribution License, which permits unrestricted use, distribution, and reproduction in any medium, provided the original work is properly cited.

Outdoor biofuel production from microalgae is a complex dynamical process submitted to climatic variations. Controlling and optimizing such a nonlinear process strongly influenced by weather conditions is therefore tricky, but it is crucial to make this process economically sustainable. The strategy investigated in this study uses weather forecast coupled to a detailed predictive model of algal productivity for online optimization of the rates of fresh medium injection and culture removal into and from the pond. This optimization strategy was applied at various climatic conditions and significantly increased productivity compared to a standard operation with constant pond depth and dilution rate, by up to a factor of 2.2 in a Mediterranean climate in summer. A thorough analysis of the optimizer strategy revealed that the increase of productivity in summer was achieved by finding a trade-off between algal concentration to optimally distribute light and pond temperature to get closer to optimal growth temperature. This study also revealed that maintaining the temperature as high as possible is the best strategy to maximize productivity in cold climatic conditions.

1. Introduction

Microalgae cultivation for biofuel and food production has been the focus of many studies for the past 20 years [1]. Several environmental [2, 3] and techno-economic assessments [4–6] aimed to quantify the profitability of algal cultivation systems and compare algal fuel to other biofuels.

It turns out that culturing process optimization is required to reduce the energy need, reduce the environmental footprint, and make algal biofuel cleaner and profit earning. Among the strategies to reduce impacts and costs while increasing productivity, online control and optimization has proven to be very efficient [7]. However, it becomes very challenging for microalgae which receive their energy from the sun. In particular, the combination of light and temperature both influencing the system dynamics must be anticipated to maintain the process in adequate production domains. Regulating the temperature by heating and cooling, or lighting the process to maintain the algae closer to their

optimum would increase the productivity, but it would immediately jeopardize the benefit of this clean energy source [8], and there is a need for a passive strategy to avoid any additional energetic inputs.

Several models have been published in the last decade, which can accurately predict algal yields at full-scale depending on the species, weather conditions, system design, and operation [9–11]. Some studies have even proposed full scale validation when weather fluctuations were recorded [12, 13].

When assuming rudimentary weather patterns, these models were used to support the optimization of the system design [14, 15] and operation [16, 17]. With the development and the miniaturization of computational power, it is now conceivable to locally compute an advanced control strategy based on weather forecasts to optimize system operation maximizing algal productivity.

Model Predictive Control (MPC) has already been applied to microalgae culture for controlling pH [18], optimization of CO₂ fixation [19, 20], or optimization of more

specific criteria including microalgal products [21, 22]. The MPC approach revealed efficient to manage the complexity of the model, but these approaches implicitly admitted that light pattern was perfectly known well in advance. Recently, [23, 24] proposed an online control strategy based on the knowledge of future weather conditions to online optimization system operation, namely, the inflow and outflow rates of the photobioreactor. The MPC strategy consisted of determining iteratively the optimal inflow and outflow hourly rates for an entire week based on the weekly weather forecasts. Unlike in [16], the culture depth could vary and thus thermal inertia of the cultivation system could be modified to optimize system temperature fluctuations. The benefits of this approach were briefly assessed on the basis of a week of cultivation in Nice (France) in summer.

The objective of this new study is first to more extensively investigate how this MPC framework can, without additional energy input, manage different climates (given by different seasons and locations). Furthermore, with a reverse engineering approach, a second goal is to analyse the strategies of the MPC and derive a reduced number of operational rules. Such simplified framework may be applied even without the need of implementing advanced automatic control/optimisation techniques. Finally, we compute the water need associated with each control strategy, and we identify paths to reduce the water use and tailor it to the local water availability.

This work is organised as follows: in Section 2 a brief description of the model used for describing microalgae productivity in open ponds is given; moreover, the description of the cultivation system and the definition of the adopted optimisation function are reported at the end of this section. Section 3 deals with the productivity results obtained with different climatic conditions in Nice and Rennes (France); then, after a brief discussion about the theoretical control logic ensuring the highest possible productivity, a detailed analysis of the optimization strategy is reported. The analysis of the optimization scheme, split into four phases, aims to extract a reduced set of 'rules to be used as a future practical guideline. Finally, Section 4 presents a brief discussion of the key aspect of the resulting control logic, whereas Section 5 presents the main conclusions and some hints for future research.

2. Materials and Methods

The optimization strategy investigated in this study requires a model predicting algal productivity in outdoor open ponds. The selected model combines three submodels predicting (i) the temperature fluctuations in an open pond [9], (ii) the light distribution in the culture medium, and (iii) the algal productivity as a function of temperature fluctuations and light distribution. The model equations are presented and described in the following two paragraphs.

2.1. Productivity Model. The high rate open pond is a standard process to grow microalgae with reduced energy inputs. It consists of a raceway shaped reactor mixed with a paddle wheel. In general, medium depth is fixed between 0.1 m and 0.5 m (typically 0.3 m). Here, we consider possible

fluctuations of depth between these bounds. The reactor is modeled as an ideally mixed system, with a fresh medium inflow (flow rate q^{in} , in $\text{m}^3 \text{s}^{-1}$) and a culture outflow for extraction (q^{out} , in $\text{m}^3 \text{s}^{-1}$). The pond is inoculated at the beginning of the cultivation period. The evolution of the biomass concentration can be expressed from the following mass balance:

$$\frac{d(x(t)V(t))}{dt} = -x(t)q^{out}(t) + G(\cdot)V(t) - R(\cdot)V(t), \quad (1)$$

where t is the time variable (s), $x(t)$ is the algal biomass concentration (kg m^{-3}), $G(\cdot)$ is the algal specific growth rate ($\text{kg m}^{-3} \text{s}^{-1}$), $R(\cdot)$ is the respiration rate ($\text{kg m}^{-3} \text{s}^{-1}$), and $V(t)$ is the pond volume (m^3). $V(t)$ varies over time according to the following equation:

$$\frac{dV(t)}{dt} = q^{in}(t) - q^{out}(t) + v_r(t)S - \frac{m_e(t)S}{\rho_w}, \quad (2)$$

where S is the pond surface area (m^2), ρ_w is water density (kg m^{-3}), $v_r(t)$ is the rainwater flow (m s^{-1}), and $m_e(t)$ is the mass flux caused by evaporation at the pond surface ($\text{kg m}^{-2} \text{s}^{-1}$). Changes in pond volume are associated with changes in pond depth $l_p(t) = V(t)/S$. The specific growth rate $G(\cdot)$ in (1) depends on the biomass concentration $x(t)$, the solar irradiance at the pond top surface $H_s(t)$ (W m^{-2}), and the pond temperature $T_p(t)$. By using a modified Beer-Lambert law to model light distribution within the algal culture, $G(t, x(t), H_s(t), T_p(t))$ was expressed as [25]

$$G(t, x(t), H_s(t), T_p(t)) = \frac{1}{l_p(t)} \int_0^{l_p(t)} \mu_m x(t) \frac{\sigma \eta_H H_s(t) e^{-\sigma x(t)z}}{K_I + \sigma \eta_H H_s(t) e^{-\sigma x(t)z}} dz \quad (3)$$

where μ_m is the maximum specific growth rate (s^{-1}), σ is the extinction coefficient (set at $120 \text{ m}^2 \text{ kg}^{-1}$; see [9]), η_H is the photosynthetically active radiation (PAR) fraction of solar light (set at 0.47), z is the local depth (m), and K_I is a half-saturation parameter (W kg^{-1}). The specific respiration rate $R(\cdot)$ in (1) depends on pond temperature $T_p(t)$ and biomass concentration $x(t)$ through the following equation [25]:

$$R(t, x(t), T_p(t)) = \lambda_r x(t), \quad (4)$$

where λ_r is the respiration coefficient (s^{-1}). As μ_m , K_I , and λ_r values change with temperature (see [25]), these three parameters were henceforth renamed $\mu_m(T_p(t))$, $K_I(T_p(t))$, and $\lambda_r(T_p(t))$, respectively. Reference [26] showed that the evolution of parameter $\mu_m(T_p(t))$ with temperature could be fitted to the following function:

$$\mu_m(T_p(t)) = \mu_{m,max} \phi_T(T_p(t)), \quad (5)$$

where $\mu_{m,max}$ is the maximum value of $\mu_m(T_p(t))$ (s^{-1}) and $\phi_T(T_p(t))$ is the temperature-dependent function reported in the following equation [26]:

$$\phi_T(T_p(t)) = 0 \quad \text{if } T_p \leq T_{min} \text{ or if } T_p(t) \geq T_{max}$$

otherwise

$$\phi_T(T_p(t)) = \frac{(T_p(t) - T_{max})(T_p(t) - T_{min})^2}{(T_{opt} - T_{min})[(T_{opt} - T_{min})(T_p(t) - T_{min}) - (T_{opt} - T_{max})(T_{opt} + T_{min} - 2T_p(t))]} \quad (6)$$

where T_{min} is the temperature below which the growth is assumed to be zero, T_{max} is the temperature above which there is no growth nor respiration, and T_{opt} is the temperature at which $\mu_m(T_p(t)) = \mu_{m,max}$. This model does not explicitly represent mortality for temperatures above T_{max} [27]. As it will be discussed later on, the optimisation strategy will always maintain temperature below T_{max} , so that mortality will eventually not occur.

Experimental values of $\mu_m(T_p(t))$, $K_I(T_p(t))$, and $\lambda_r(T_p(t))$ were extracted from the study of [25] conducted on *Chlorella vulgaris* as the model of [25] was shown to accurately predict algal productivity in outdoor photobioreactors under various weather conditions [28]. As $\lambda_r(T_p(t))$ and $K_I(T_p(t))$ exhibited similar evolution with temperature, the same function $\phi_T(T_p(t))$ was used for fitting the behavior of these two parameters at different temperatures:

$$\begin{aligned} K_I(T_p(t)) &= K_{I,max} \phi_T(T_p(t)), \\ \lambda_r(T_p(t)) &= \lambda_{r,max} \phi_T(T_p(t)). \end{aligned} \quad (7)$$

Fitting these parameters was performed by using the Maximum Likelihood method included in the entity *Parameter estimation* of the gPROMS™ software (4.1 version). The complete set of the parameter values used to describe the temperature function ϕ_T is reported in Table 1.

2.2. Temperature Model. The universal model for temperature prediction in shallow algal ponds developed by [29] has been used in this work. This model was validated against data collected from a high rate algal pond [13, 25]. The temperature model, valid for any opaque water body having a uniform temperature profile, is based on eight heat fluxes that can be expressed from available meteorological data/system design parameters. Pond temperature obeys the following equation [29]:

$$\begin{aligned} \rho_w V(t) c_{p_w} \frac{dT_p(t)}{dt} &= Q_{ra,p}(t) + Q_{ra,s}(t) + Q_{ra,a}(t) \\ &+ Q_{ev}(t) + Q_{conv}(t) + Q_{cond}(t) \\ &+ Q_i(t) + Q_r(t), \end{aligned} \quad (8)$$

where c_{p_w} is the specific heat capacity of water ($\text{J kg}^{-1}\text{K}^{-1}$), $Q_{ra,p}(t)$ is the radiation flow from the pond surface (W), $Q_{ra,s}(t)$ is the global (direct and diffuse) solar irradiance (W), $Q_{ra,a}(t)$ is the radiation flow from the air to the pond

(W), $Q_{ev}(t)$ is the evaporation heat flow (W), $Q_{conv}(t)$ is the convective heat flow at the pond surface (W), $Q_{cond}(t)$ is the conductive heat flow with the ground at the pond bottom (W), $Q_i(t)$ is the heat flow associated with the water inflow (W), and $Q_r(t)$ is the heat flow associated with rainfall (W). A detailed description of the equations used to describe each heat flux can be found in the supplementary material (S1.1).

2.3. Weather Data. Weather data originates from the European Centre for Medium-Range Weather Forecast (ECMWF) website (year 2012). This data, available every 6 hours, includes the air temperature T_a , the relative humidity RH , the wind velocity v_w , the rain volumetric flux v_r , and the sky cloudiness CC (see supplementary material (S2) for complete description). The solar irradiance at the ground level, H_s , was determined combining the solar irradiance at the top of the atmosphere (determined by the latitude and the solar declination angle) with the sky cloudiness CC (see supplementary material (S1.2) for further details).

2.4. System Description. The optimization strategy was investigated at two different locations in France, representing two very different climates: a Mediterranean climate in Nice ($43^\circ 42' 11''\text{N}$, $7^\circ 15' 57''\text{E}$) and a temperate climate in Rennes ($48^\circ 06' 53''\text{N}$, $1^\circ 40' 46''\text{W}$). Simulations were performed over one week at three different seasons at each location (winter: January; spring: March; summer: July). The pond surface area S was 100 m^2 . The initial conditions were as follows:

- (i) The initial pond temperature $T_p(t=0)$ was set at the average value of air temperature $T_{a,avg}$ over the period τ of simulation as a reasonable estimation of T_p in the absence of actual measurements.
- (ii) the initial biomass concentration x was set to 0.4 kg/m^3 .
- (iii) the initial pond depth l_p was set to the typical value of 0.3 m [30].
- (iv) the inflow temperature T^{in} was set at a value equal to $T_{a,avg}$.

Standard pond operation consisted of maintaining the pond depth and dilution rates at typical values during the entire cultivation period (depth of 0.25 m and dilution rate of 0.1 day^{-1} , as discussed in [31–33]).

2.5. Numerical Optimization. The optimization strategy consisted of permanently adjusting inflow and outflow rates (q^{in}

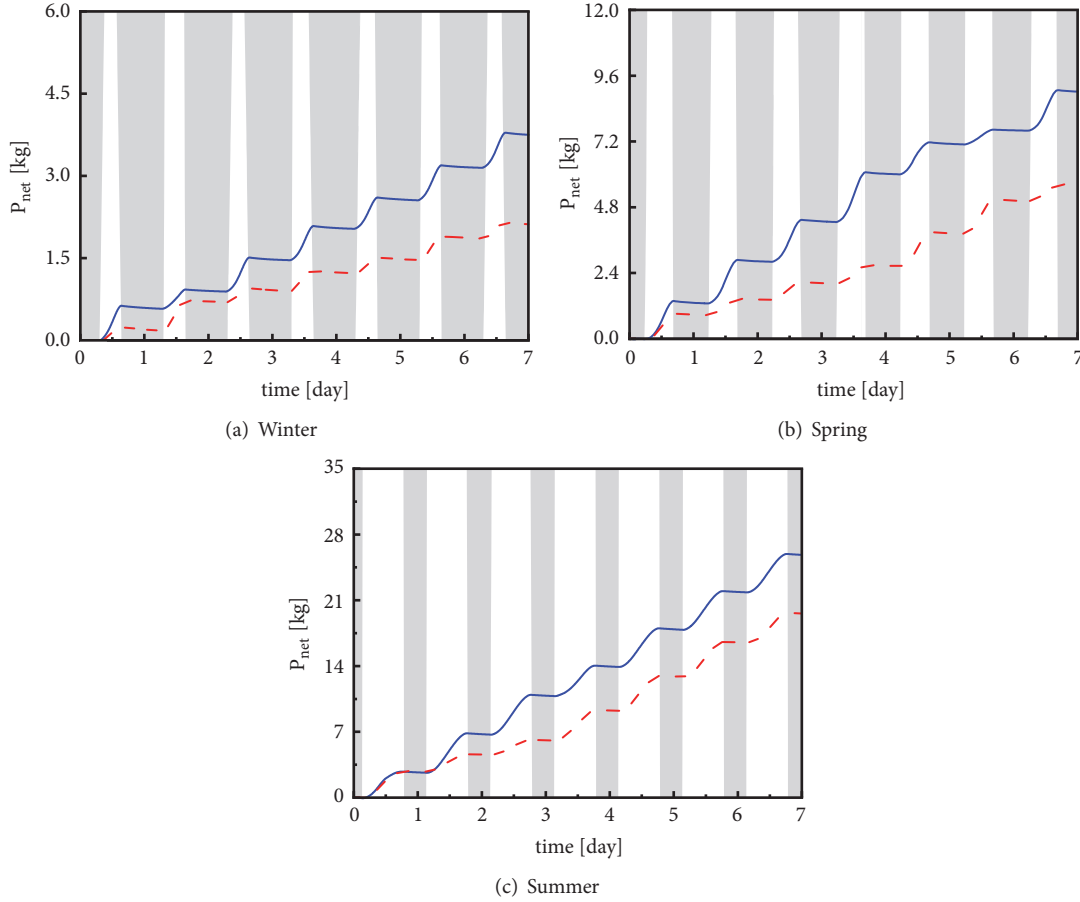


FIGURE 1: P_{net} obtained with the optimal control strategy (blue continuous line: Nice; dashed red line: Rennes. The background is colored in white at daytime and in grey at nighttime).

and q^{out} , respectively) to maximize the productivity over the period of time considered (1 week), defined by the following equation (see [34]):

$$P_{net}(t) = \int_0^\tau (G(t, x(t), H_s(t), T_p(t)) - R(t, x(t), T_p(t))) V(t) dt. \quad (9)$$

The pond depth changed with time since q^{in} and q^{out} were not identical. These two control inputs were taken as piecewise constant variables within the range $[0 \div 1]$ m^3/s . The pond depth was constrained between 0.05 m and 0.5 m. The optimization was implemented through the gPROMS™ software (4.1 version) by using the default optimization solver NLPSQP, which uses a sequential quadratic programming method for the solution of nonlinear programming problems.

2.6. Water Demand. The net water demand ($WD(t)$) associated with algal cultivation was calculated as follows:

$$WD(t) = \int_0^\tau q^{in}(t) dt + \max(0, V_0 - V_\tau), \quad (10)$$

where V_0 and V_τ are, respectively, the pond volume at the beginning and at the end of the cultivation period. This

TABLE 1: Values of the parameters used in the temperature function ϕ_T .

Parameter	Description	Value
T_{min}	Minimum growth temperature	-10.0 (°C)
T_{max}	Maximum growth temperature	42.1 (°C)
T_{opt}	Optimum growth temperature	35.8 (°C)
$\lambda_{r,max}$	Max. respiration coefficient	$2.01 \cdot 10^{-6}$ (s^{-1})
$\mu_{m,max}$	Max. specific growth rate	$6.48 \cdot 10^{-5}$ (s^{-1})
$K_{L,max}$	Max. half-saturation constant	7192.92 ($W \text{ kg}^{-1}$)

expression accounts for both water use for fresh water injection and change in pond volume between initial and final times.

3. Results

3.1. Strategy Impact on Productivity. Figure 1 shows the algal productivity obtained during optimized and standard cultivation, at Nice and Rennes for three seasons (winter, spring, and summer). The reported results (see Table 2) show that the optimization strategy significantly increased productivity compared to standard operation, by up to a

TABLE 2: Standard cultivation versus optimal control strategy: productivity and water demand.

Case studies		Productivity (kg·week ⁻¹)		Water demand (m ³ ·week ⁻¹)	
		Nice	Rennes	Nice	Rennes
Winter	Standard cultivation strategy	2.59	1.25	17.53	17.53
	Optimal control strategy	3.73	2.12	26.83	25.02
Spring	Standard cultivation strategy	5.60	3.96	17.53	17.33
	Optimal control strategy	9.02	5.61	32.60	27.48
Summer	Standard cultivation strategy	11.62	12.71	17.53	17.53
	Optimal control strategy	25.83	19.59	122.98	45.97

factor of 2.2 for the summer case in Nice. Interestingly, Table 2 shows that productivity was slightly higher in Rennes than in Nice in summer under standard operation. This result is explained by the high temperature peaks in Nice, which cause productivity to significantly drop. Figure 2 shows the optimal q^{in} and q^{out} profiles maximizing algal productivity over the entire cultivation period.

Figure 2 reveals that medium injection or culture extraction only occurred at day time. Although the resulting control strategy was different for the two locations, a qualitatively recurrent behavior can be identified despite the weather variability along cultivation and for the different periods of the year. The behavior of the optimizer was therefore analyzed on a time window of three cultivation days only.

3.2. Optimal Operation Strategy: Key Features. The ideal control logic to enhance productivity should result from several considerations.

Firstly, algal concentration must be optimized at daytime by accounting for two processes: (1) biomass losses through respiration linearly increase with the algal concentration, and (2) the amount of light intensity captured by algal cells, hence photosynthetic rate, increases with algal concentration. As a result, there is an optimal algal concentration that should ensure that most of the light entering the pond is captured by algae while still maintaining respiration rates at a low value. Previous studies show that this optimal concentration is reached when the specific rate of photosynthesis at the pond bottom equals the specific rate of respiration [35]. Mathematically, these conditions are reached when the ‘compensation function’ defined below is equal to 1 [35]:

$$f_{comp}(t) = \mu_{m,max} \frac{\sigma \eta_{H_s} H_s(t) e^{-\sigma x(t) l_p(t)} / (K_{I,max} \phi_T(t) + \sigma \eta_{H_s} H_s(t) e^{-\sigma x(t) l_p(t)})}{\lambda_{r,max}} \quad (11)$$

If this function is higher than 1, the pond productivity could be improved by increasing biomass in the system. Conversely, values lower than 1 indicate that the net rate of growth at the pond bottom is negative: diluting the system would increase productivity. In summary, the ideal optimal biomass concentration at daytime $x_{opt}(t)$ is the algal concentration that guarantees that the compensation function defined in (11) equals 1.

Secondly, maximal productivity is achieved when the pond temperature $T_p(t)$ is maintained at T_{opt} at daytime. At nighttime, the pond temperature $T_p(t)$ and the biomass concentration $x(t)$ should be maintained as low as possible in order to minimize respiration rates, hence biomass losses. The ideal optimal pond operation would therefore require a drastic change of the algal concentration and pond temperature at sunrise and sunset to stay optimal at daytime and nighttime. Such drastic changes are in practice difficult to achieve and the next paragraph discusses how they are handled by the optimization scheme.

3.3. Detailed Analysis of the Optimization Scheme. The analysis of the optimization scheme is split into four phases, from morning to night.

Morning. Focusing first on the summer case study, Figures 3(a) and 3(b) show that no water was injected to or extracted from the pond in the morning ($q^{in}(t), q^{out}(t) = 0$), to maintain the pond depth in Rennes at a constant and low value ($l_p(t) = 0.05$ m; see Figure 3(c)). Very small depths indeed minimize the thermal inertia of the pond and thus allow a fast increase of the pond temperature $T_p(t)$ (see Figure 3(d)), hence a greater productivity increase. The same control strategy was used in Nice although the pond depth in Nice was slightly above its minimal constraint (see Figure 3(c)). Removing culture from the pond would lead to lower the biomass content and therefore increase the compensation function which is already significantly higher than 1 (Figure 3(f)). Removing more biomass would thus cause productivity losses.

The morning control strategies in spring and winter were similar (Figures 4(a), 4(b), 5(a), and 5(b)), except for Nice in winter. In this particular case, a fraction of the culture was replaced by fresh medium at sunrise of days 4 and 5. It slightly increased temperature (see Figure 4(d)) as injected medium was hotter than the algal culture.

Based on these observations, the optimizer behavior in the *Morning* phase can be schematized by the following simple rules:

- (i) During the morning the pond depth is maintained as low as possible in order to rapidly reach both optimal pond temperature and biomass concentration.
- (ii) In winter, if pond temperature is lower than inflow temperature and if the biomass content in the pond

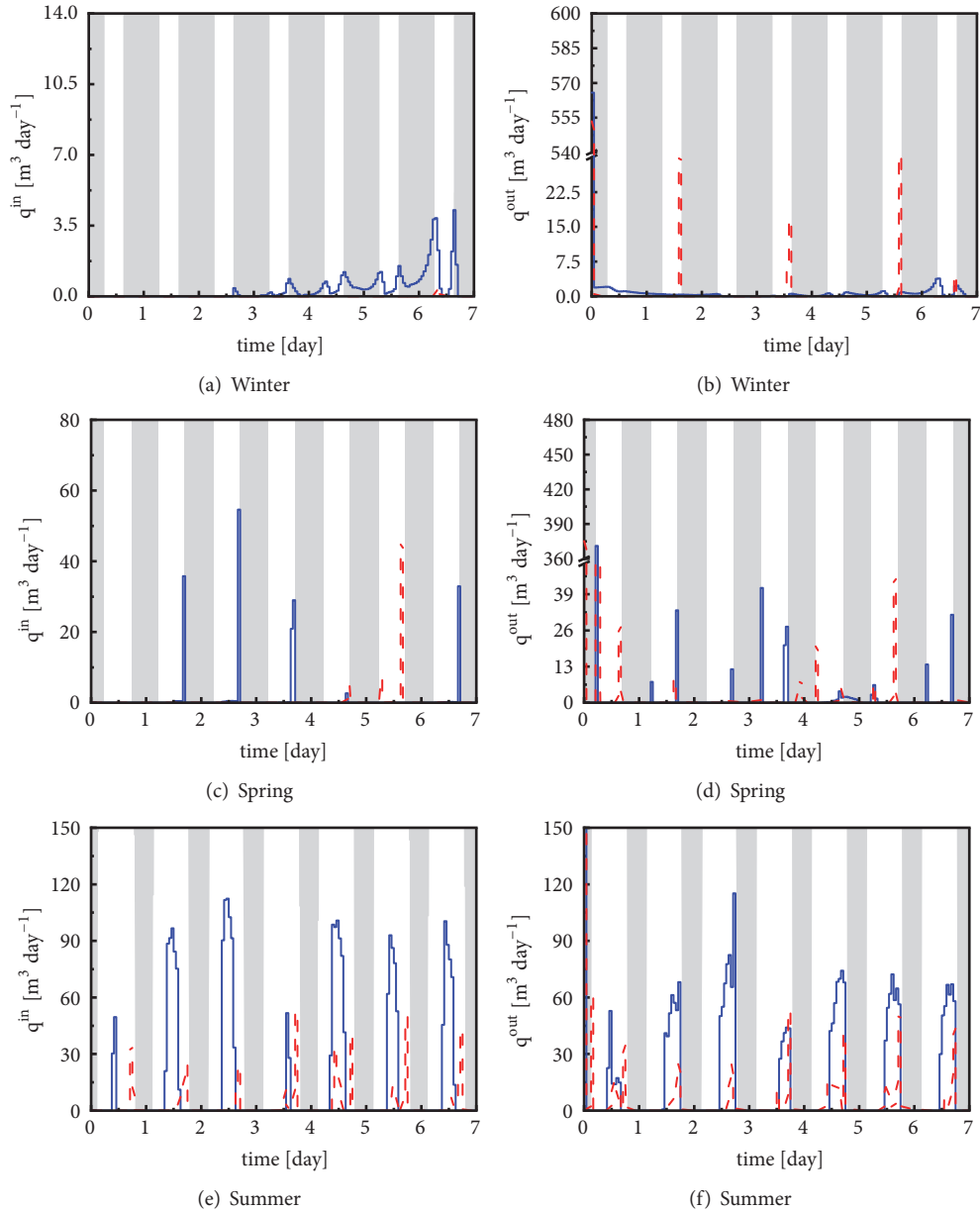


FIGURE 2: q^{in} and q^{out} optimized profile (blue continuous line: Nice; dashed red line: Rennes. The background is colored in white at daytime and in grey at nighttime).

is high enough to avoid ‘washout’ conditions, the culture can be partially replaced with fresh medium to increase temperature.

Afternoon. Figures 3(a) and 3(b) show that the inflow rate $q^{in}(t)$ in Nice exhibits a ‘bell curve’ profile from midday until late afternoon in summer. $q^{out}(t)$ followed the same dynamics but started slightly later in the day. In other words, the control strategy was mainly based on replacing the pond culture by fresh medium (‘flushing’ strategy). This culture replacement had two main consequences. Firstly, as shown in Figure 3(f), the compensation function $f_{comp}(t)$ was maintained at a value close to 1 during the afternoon, indicating that the algal

concentration was kept at its optimal value $x_{opt}(t)$. Secondly (‘flushing strategy’), replacing algal culture by relatively cold fresh medium helped maintaining pond temperature close to optimal level T_{opt} (35.8°C , Figure 3(d)). Figure 3(c) shows that the pond depth l_p in Nice increased until mid-afternoon and then decreased, which indicates that culture replacement was not sufficient to maintain pond temperature at the optimal level. Increasing the pond depth increased its thermal inertia and eventually limited temperature increase (‘depth strategy’). Figures 3(a), 3(b), and 3(c) show that the same ‘flushing’ and ‘depth’ strategies were used in Rennes in summer during day 5, but not during days 3 and 4. As Figure 3(f) shows that the compensation function was significantly lower than

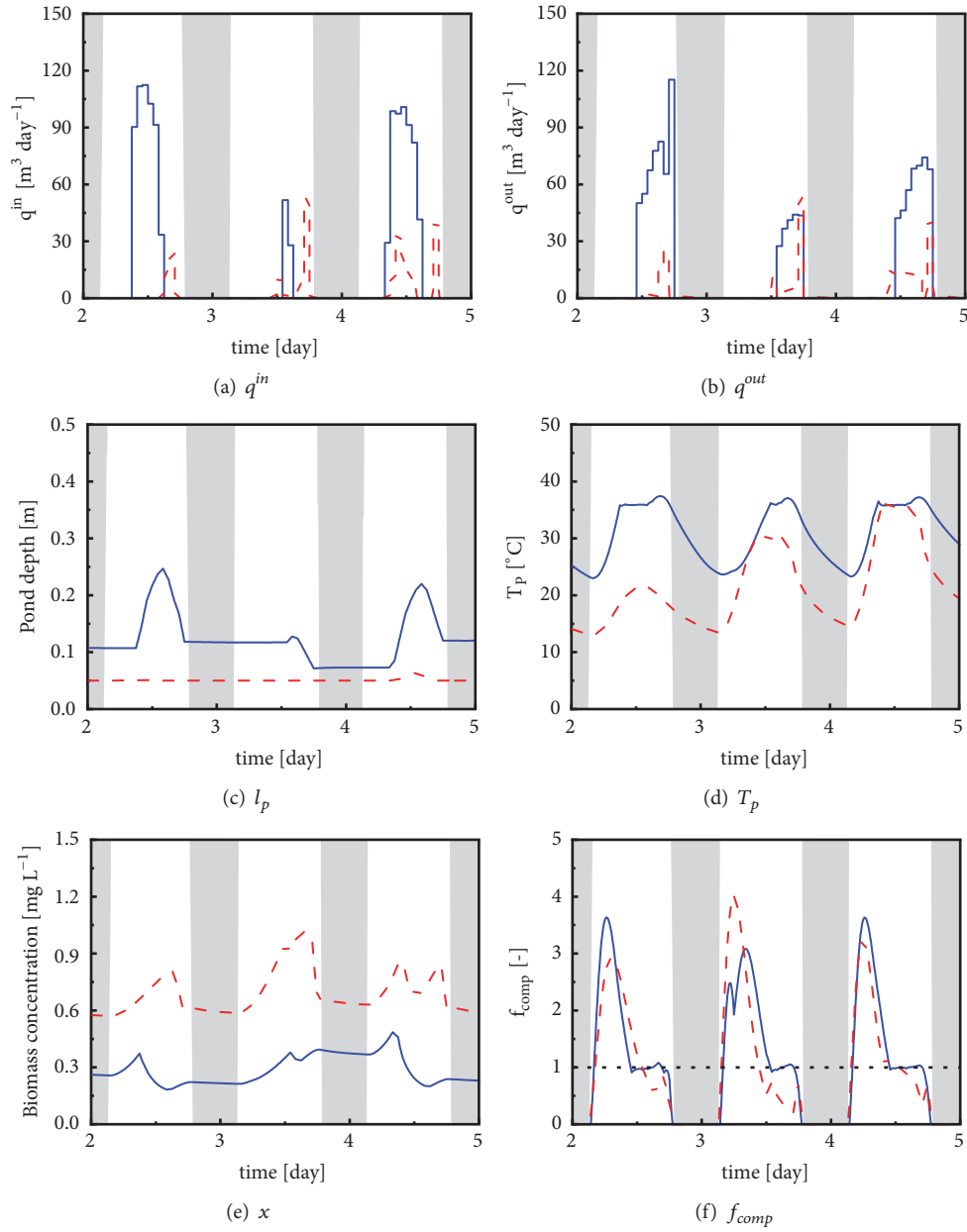


FIGURE 3: July. Three-day zoom of the optimized profiles (blue continuous line: Nice; dashed red line: Rennes. The background is colored in white at daytime and in grey at nighttime).

1 during the afternoons of days 3 and 4, further culture replacement could have theoretically been used to maintain the biomass concentration at its optimal value. Yet, replacing the culture by colder fresh medium would have significantly decreased the pond temperature and therefore lower biomass productivity. Figure 3(d) shows indeed that days 3 and 4 were relatively cold, differently from day 5 in which the pond temperature reached its optimal value. In other words, the optimizer found the best trade-off between optimal biomass concentration and optimal temperature conditions in the case of warm but not hot weather conditions. In addition,

Figure 3(c) shows that in Rennes the depth was maintained at its lowest value in the afternoon of days 3 and 4 (warm days) in order to maximize the temperature increase. Figures 4(a), 4(b), 5(a), and 5(b) show that both $q^{in}(t)$ and $q^{out}(t)$ were maintained at 0 in winter and spring in Rennes and Nice. As a result, the biomass concentration slightly increased at daytime (Figures 4(e) and 5(e)). In addition, the depth was left at its lowest value (0.05 m) all day long. These observations indicate that the optimal strategy during cold days consists of maintaining the pond temperature as high as possible even if biomass concentration is significantly higher than

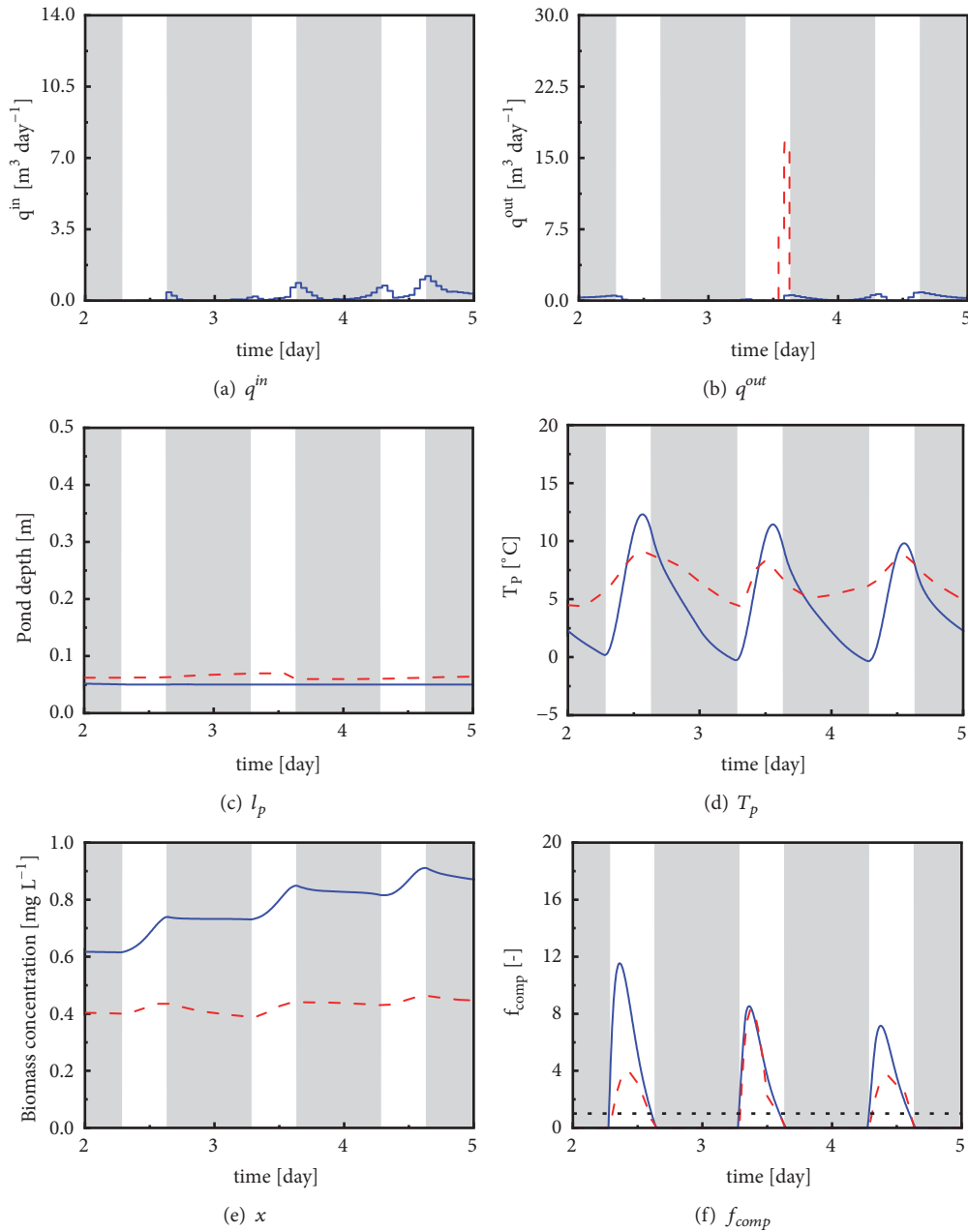


FIGURE 4: January. Three-day zoom of the optimized profiles (blue continuous line: Nice; dashed red line: Rennes. The background is colored in white at daytime and in grey at nighttime).

the optimal concentration. The optimizer behavior in the *Afternoon* phase can be schematized by the following simple rule:

- (i) In the afternoon the culture can be flushed to maintain the algal concentration at its optimal level. In summer, this ‘flushing strategy’ can be combined with depth increase strategy to control temperature at its optimal level. In spring and winter, the optimal strategy consists in staying in batch at daytime while maintaining the pond depth at a minimal value, to

ensure that pond temperature reaches the highest possible value.

Sunset. In summer, Figures 3(a) and 3(b) show that a high fraction of the culture was replaced by fresh medium at sunset in Rennes. ‘Flushing’ the system at sunset both lowered pond temperature (see Figure 3(d)) and biomass concentration (see Figure 3(e)), which in turn limited respiration rates at nighttime. The alternative strategy used in Nice was based on decreasing the pond depth when approaching sunset (Figure 3(c)), to remove a significant fraction of the biomass.

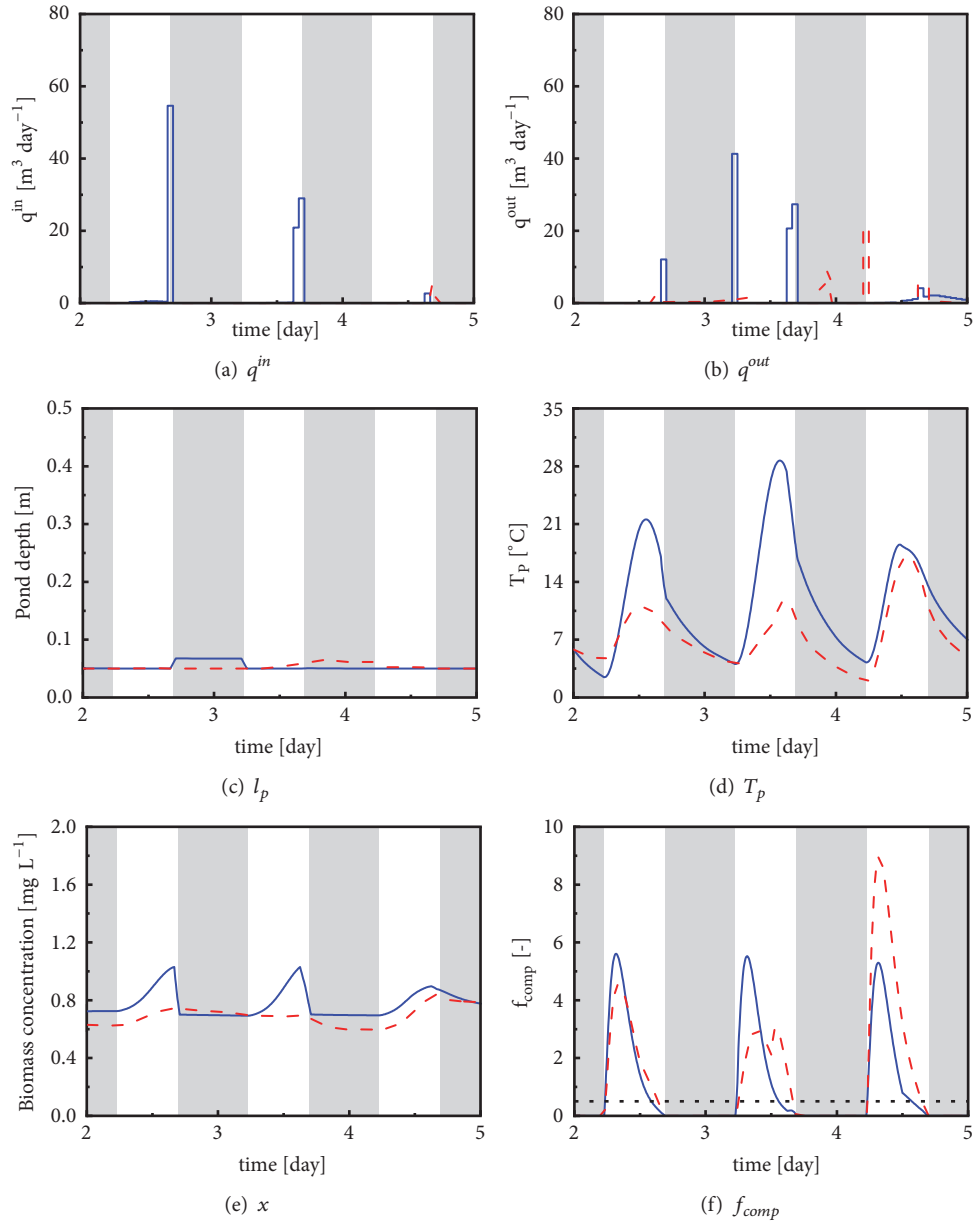


FIGURE 5: March. Three-day zoom of the optimized profiles (blue continuous line: Nice; dashed red line: Rennes. The background is colored in white at daytime and in grey at nighttime).

In addition, decreasing pond depth accelerates the pond temperature decrease at night. Similarly to the ‘flushing’ strategy used in Rennes, this ‘depth-decrease’ control strategy reduced respiration at nighttime. Removing too much biomass from the system would reduce respiration at nighttime but this would also cause the productivity to be low the day after. As a result, the optimizer finds the optimal algal concentration ensuring both low respiration rates at nighttime and sustained productivities the following morning. In winter only a small fraction of the culture was replaced by fresh medium in Nice (Figures 4(a) and 4(b)) as night-time respiration rates were limited by cold temperatures (Figure 3(d)). In Rennes the ‘flushing strategy’ at sunset was not applied, mostly

because inflow temperature was higher (9.2°C) than pond temperature $T_p(t)$ at sunset. Injecting relatively warm water at sunset would therefore enhance respiration at nighttime. The optimal strategy at Nice in spring consisted on partly ‘flushing’ the system at sunset similarly to the summer case. In Rennes, culture was not replaced at sunset in spring, mostly because maintaining temperatures as high as possible was the best strategy to optimize productivity (Figures 5(a) and 5(b)). The optimizer behavior at *Sunset* can be schematized by the following simple rule:

- (i) During hot days, a fraction of the culture is replaced with fresh medium at sunset to minimize nighttime

respiration rates. Pond depth is also maintained at a low level to faster decrease temperatures at nighttime. In winter or in colder climates, culture is not replaced by fresh medium at sunset to maximize temperature during the following day.

Night. The pond depth was maintained at its sunset value all night long independently on the season (Figures 3(c), 4(c), and 5(c)). In addition, Figures 3(a), 3(b), 4(a), 4(b), 5(a), and 5(b) show that, in general, no ‘flushing’ was used at nighttime ($q^{in} = 0$ and $q^{out} = 0$). The only exceptions were in spring at day 4 for Rennes and at day 5 for Nice, which correspond to culture extraction just after rainfall to maintain the pond depth at its lowest possible value. In summer, temperatures are minimized at nighttime. In winter, low thermal inertia and therefore low depth must be maintained at daytime to increase temperature and this constrains pond depths to be low at nighttime. The optimizer behavior at *Night* can be schematized by the following simple rule:

- (i) The pond stays in batch and thus depth is maintained at the sunset value.

4. Discussion

The optimization technique significantly increased the productivity at the two locations and three seasons considered. The productivity boost in summer mainly results from the optimizer ability to maintain, during large periods of daytime, ideal growth conditions, i.e., providing efficient trade-off between optimal concentration and temperature (via the ‘flushing’ and ‘depth’ strategies). In spring and winter, the optimal temperature for the species *C. vulgaris* (35.8°C) cannot be reached, so the optimal strategy consists of limiting culture replacement to ensure higher temperatures, even if it leads to relatively high biomass concentrations. Because of relatively low temperatures, respiration rates are indeed relatively low, so these higher biomass concentrations is not too penalized by respiration.

The knowledge of future weather is crucial to optimize the process inflows and outflows, and this can be illustrated in several cases. Firstly, in hot days, slowly increasing the pond depth can help to maintain the pond temperature at its optimal value during daytime. As temperature dynamics is relatively slow due to the high thermal inertia of water, only an accurate knowledge of future weather conditions and their impact on pond temperature can help to maintain pond temperature as close as possible to its optimal value. Secondly, a fraction of the algal culture is replaced by fresh medium at sunset to minimize respiration losses at nighttime. However, removing too much biomass from the pond would lead to low productivity values the morning after, and especially if the day after is particularly sunny. Determining the optimal fraction of culture to remove from the pond at sunset therefore requires knowing the weather conditions of the following day. Sensitivity of the management strategy to accuracy in the future weather was assessed in [23]. It was shown that, especially for hot periods, biases in weather predictions can deeply affect the productivity. Higher frequency weather data acquisition will mitigate this risk. Weather predictions at

short term should also be combined with actual measurements of water temperature and solar fluxes. Also, the main rules guiding the optimisation can be used to check that the logic of the control action stay coherent and possibly limit the controller action in case of conflict. These rules must also be used to initialize the MPC strategy with reasonable profile inflow and outflow profiles. It will reduce the risk of local minima in the determination of the optimal strategy.

This study covers most of the possible combinations of light and temperature ranges. Having in depth examined the control strategy has provided the keys for understanding the control under most of the possible climates. The study in [23] was focused on a hot climate. It proposed a first picture, but it is crucial to better understand how to manage the trade-off between light access and optimal temperature for a larger variety of seasons and latitudes. This MPC strategy must still be tested for a larger range of locations at all seasons. But the study with the climates of Rennes and Nice through all the seasons provide hints that it might stay efficient in many other locations. In the most extreme cases, complementary strategies could be jointly used to more efficiently heat water in winter or decrease temperature in summer. Heat exchangers have a potential here, provided that the unavoidable energy consumption (at least for pumps) is compensated by the productivity gain.

Temperature control by playing on thermal inertia and culture replacement by fresh medium is central in the optimization strategy. This point was so far never considered in the previous optimization studies which focused on optimizing algal access to light by playing on the compensation function. *Chlorella vulgaris* is relatively resistant to high temperatures ($T_{max} = 42^\circ\text{C}$). However, for a cold-adapted algae species, the possibility of culture crashes due to temperatures above T_{max} triggering cell mortality [27, 36] would increase further the impact of temperature on productivity. In this case, the optimizer would likely place temperature control above concentration control in summer to avoid culture crashes.

In this study, we did not include the water cost in the optimization criterion. However, the optimal management induces high dilution rates, especially in summer, both to reduce temperature and to dilute culture at high density. Water demands were consequently higher than the standard management procedure (Table 2) which required a significantly lower amount of water (only 17.53 m³ week⁻¹ for all the seasons). This shows that the management of process temperature must be designed to have a limited impact on water consumption.

In particular, the optimized control strategy increased the *WD* at Nice in summer up to a factor of 7.7, which means an increase by a factor of 3.2 per kg of produced algae: from 1.25 m³ kg⁻¹ up to 4 m³ kg⁻¹. This computation also highlights the necessity to recycle water after biomass extraction to reduce the water need.

As a perspective, the same optimisation strategy should be studied when constraining the maximum amount of water that can be used in the process (based for example on the availability on rainwater at the location considered) and

assuming that an important fraction of the water can be recycled, as suggested by [37].

5. Conclusions

The MPC scheme based on a complex dynamical model able to describe the algal growth in open ponds through meteorological data allows significant increase of the productivity efficiency compared to standard operation. Productivity gain was achieved via two main mechanisms: culture replacement (compensation condition) and pond depth control (thermal optimization). A short list of simple rules was extracted for simplified operation. Temperature control turns out to be a key factor to achieve maximal productivity. The drawback of this strategy is a relatively high water demand, especially in sunny and hot climates. Further research needs to address water recycling implementation and include it in the cost criterion to reach a compromise between maximizing productivity while reducing the water demand. The analysis of the optimal strategy for a diversity of heat fluxes and temperature conditions offer a general strategy which is likely to be efficient in many other locations. More extensive simulations must now consider other production sites to consolidate the management strategy and further generalise it.

Data Availability

The data used to support the findings of this study are available from the corresponding author upon request.

Conflicts of Interest

The authors declare that they have no conflicts of interest.

Acknowledgments

The authors acknowledge the support of the ANR Phycover project (ANR-14-CE04-0011) and Inria Project Lab *Algae in silico*. Riccardo De-Luca and Fabrizio Bezzo acknowledge the support of Project PRIN 2012 Improving Biofuels and High Added Value Molecules Production from Unicellular Algae (2012XSAWYM).

Supplementary Materials

The supplementary material contains details about the physical model for computing medium temperature and local illumination. It also presents the meteorological data used for the simulations. (*Supplementary Materials*)

References

- [1] T. M. Mata, A. A. Martins, and N. S. Caetano, "Microalgae for biodiesel production and other applications: a review," *Renewable & Sustainable Energy Reviews*, vol. 14, no. 1, pp. 217–232, 2010.
- [2] L. Lardon, A. Helias, B. Sialve, J. P. Steyer, and O. Bernard, "Life-cycle assessment of biodiesel production from microalgae," *Environmental Science & Technology*, vol. 43, no. 17, pp. 6475–6481, 2009.
- [3] P. Collet, L. Lardon, A. Hélias et al., "Biodiesel from microalgae—life cycle assessment and recommendations for potential improvements," *Journal of Renewable Energy*, vol. 71, pp. 525–533, 2014.
- [4] M. S. Wigmosta, A. M. Coleman, R. J. Skaggs, M. H. Huesemann, and L. J. Lane, "National microalgae biofuel production potential and resource demand," *Water Resources Research*, vol. 47, no. 3, 2011.
- [5] J. Yang, M. Xu, X. Zhang, Q. Hu, M. Sommerfeld, and Y. Chen, "Life-cycle analysis on biodiesel production from microalgae: Water footprint and nutrients balance," *Bioresource Technology*, vol. 102, no. 1, pp. 159–165, 2011.
- [6] J. W. Moody, C. M. McGinty, and J. C. Quinn, "Global evaluation of biofuel potential from microalgae," *Proceedings of the National Academy of Sciences of the United States of America*, vol. 111, no. 23, pp. 8691–8696, 2014.
- [7] J. S. Alford, "Bioprocess control: advances and challenges," *Computers & Chemical Engineering*, vol. 30, no. 10–12, pp. 1464–1475, 2006.
- [8] Q. Béchet, A. Shilton, O. B. Fringer, R. Munoz, and B. Guieysse, "Mechanistic modeling of broth temperature in outdoor photobioreactors," *Environmental Science & Technology*, vol. 44, no. 6, pp. 2197–2203, 2010.
- [9] Q. Béchet, A. Shilton, and B. Guieysse, "Modeling the effects of light and temperature on algae growth: State of the art and critical assessment for productivity prediction during outdoor cultivation," *Biotechnology Advances*, vol. 31, no. 8, pp. 1648–1663, 2013.
- [10] O. Bernard, F. Mairet, and B. Chachuat, "Modelling of Microalgae Culture Systems with Applications to Control and Optimization," in *Microalgae Biotechnology*, vol. 153 of *Advances in Biochemical Engineering/Biotechnology*, pp. 59–87, Springer International Publishing, Cham, 2016.
- [11] E. Lee, M. Jalalizadeh, and Q. Zhang, "Growth kinetic models for microalgae cultivation: A review," *Algal Research*, vol. 12, pp. 497–512, 2015.
- [12] M. Huesemann, B. Crowe, P. Waller et al., "A validated model to predict microalgae growth in outdoor pond cultures subjected to fluctuating light intensities and water temperatures," *Algal Research*, vol. 13, pp. 195–206, 2016.
- [13] Q. Béchet, N. Coulombier, C. Vasseur, T. Lasserre, L. Le Dean, and O. Bernard, "Full-scale validation of an algal productivity model including nitrogen limitation," *Algal Research*, vol. 31, pp. 377–386, 2018.
- [14] R. J. Ritchie and A. W. Larkum, "Modelling photosynthesis in shallow algal production ponds," *Photosynthetica*, vol. 50, no. 4, pp. 481–500, 2012.
- [15] P. Slegers, P. van Beveren, R. Wijffels, G. van Straten, and A. van Boxtel, "Scenario analysis of large scale algae production in tubular photobioreactors," *Applied Energy*, vol. 105, pp. 395–406, 2013.
- [16] R. Muñoz-Tamayo, F. Mairet, and O. Bernard, "Optimizing microalgal production in raceway systems," *Biotechnology Progress*, vol. 29, no. 2, pp. 543–552, 2013.
- [17] A. Rarrek, M. Mostertz, H. Kistenmacher, S. Rehfeldt, and H. Klein, "Simulation and optimization of large open algae ponds," *Chemical Engineering Research and Design*, vol. 114, pp. 220–235, 2016.

- [18] M. Berenguel, F. Rodríguez, F. G. Acién, and J. L. García, "Model predictive control of pH in tubular photobioreactors," *Journal of Process Control*, vol. 14, no. 4, pp. 377–387, 2004.
- [19] J. L. García Sánchez, M. Berenguel, F. Rodríguez, J. M. Fernández Sevilla, C. Brindley Alias, and F. G. Acién Fernández, "Minimization of Carbon Losses in Pilot-Scale Outdoor Photobioreactors by Model-Based Predictive Control," *Biotechnology and Bioengineering*, vol. 84, no. 5, pp. 533–543, 2003.
- [20] S. Tebbani, F. Lopes, R. Filali, D. Dumur, and D. Pareau, "Nonlinear predictive control for maximization of CO₂ biofixation by microalgae in a photobioreactor," *Bioprocess and Biosystems Engineering*, vol. 37, no. 1, pp. 83–97, 2014.
- [21] S. Benattia, S. Tebbani, and D. Dumur, "Nonlinear Model Predictive Control for regulation of microalgae culture in a continuous photobioreactor," in *Proceedings of the 22nd Mediterranean Conference on Control and Automation, MED 2014*, pp. 469–474, IEEE, 2014.
- [22] A. Juneja and G. S. Murthy, "Model predictive control coupled with economic and environmental constraints for optimum algal production," *Bioresource Technology*, vol. 250, pp. 556–563, 2018.
- [23] R. De-Luca, F. Bezzo, Q. Béchet, and O. Bernard, "Exploiting meteorological forecasts for the optimal operation of algal ponds," *Journal of Process Control*, vol. 55, pp. 55–65, 2017.
- [24] R. De-Luca, *An investigation on microalgae growth at different scales: from photosynthetic mechanisms modelling to operation optimisation in open pond cultivation systems [PhD Thesis]*, University of Padova, 2017.
- [25] Q. Béchet, P. Chambonnière, A. Shilton, G. Guizard, and B. Guieysse, "Algal productivity modeling: A step toward accurate assessments of full-scale algal cultivation," *Biotechnology and Bioengineering*, vol. 112, no. 5, pp. 987–996, 2015.
- [26] O. Bernard and B. Rémond, "Validation of a simple model accounting for light and temperature effect on microalgal growth," *Bioresource Technology*, vol. 123, pp. 520–527, 2012.
- [27] R. Serra-Maia, O. Bernard, A. Gonçalves, S. Bensalem, and F. Lopes, "Influence of temperature on *Chlorella vulgaris* growth and mortality rates in a photobioreactor," *Algal Research*, vol. 18, pp. 352–359, 2016.
- [28] Q. Béchet, A. Shilton, and B. Guieysse, "Full-Scale Validation of a Model of Algal Productivity," *Environmental Science & Technology*, vol. 48, no. 23, pp. 13826–13833, 2014.
- [29] Q. Béchet, A. Shilton, J. B. K. Park, R. J. Craggs, and B. Guieysse, "Universal Temperature Model for Shallow Algal Ponds Provides Improved Accuracy," *Environmental Science & Technology*, vol. 45, no. 8, pp. 3702–3709, 2011.
- [30] Y. Chisti, "Biodiesel from microalgae," *Biotechnology Advances*, vol. 25, no. 3, pp. 294–306, 2007.
- [31] O. Jorquera, A. Kiperstok, E. A. Sales, M. Embiruçu, and M. L. Ghirardi, "Comparative energy life-cycle analyses of microalgal biomass production in open ponds and photobioreactors," *Bioresource Technology*, vol. 101, no. 4, pp. 1406–1413, 2010.
- [32] R. Davis, A. Aden, and P. T. Pienkos, "Techno-economic analysis of autotrophic microalgae for fuel production," *Applied Energy*, vol. 88, no. 10, pp. 3524–3531, 2011.
- [33] J. N. Rogers, J. N. Rosenberg, B. J. Guzman et al., "A critical analysis of paddlewheel-driven raceway ponds for algal biofuel production at commercial scales," *Algal Research*, vol. 4, pp. 76–88, 2014.
- [34] R. De-Luca, Q. Béchet, F. Bezzo, and O. Bernard, "Optimal operation of algal ponds accounting for future meteorology," *IFAC-PapersOnLine*, vol. 49, no. 7, pp. 1062–1067, 2016.
- [35] H. Takache, G. Christophe, J. F. Cornet, and J. Pruvost, "Experimental and theoretical assessment of maximum productivities for the microalgae *Chlamydomonas reinhardtii* in two different geometries of photobioreactors," *Biotechnology Progress*, vol. 26, no. 2, pp. 431–440, 2010.
- [36] Q. Béchet, M. Laviale, N. Arsapin, H. Bonnefond, and O. Bernard, "Modeling the impact of high temperatures on microalgal viability and photosynthetic activity," *Biotechnology for Biofuels*, vol. 10, no. 1, p. 136, 2017.
- [37] R. L. White and R. A. Ryan, "Long-Term Cultivation of Algae in Open-Raceway Ponds: Lessons from the Field," *Industrial Biotechnology*, vol. 11, no. 4, pp. 213–220, 2015.